FZD-482

Experiments on upwards gas/liquid flow in vertical pipes

H.-M. Prasser, M. Beyer, H. Carl,
A. Manera, H. Pietruske, P. Schütz

September 2007

Wissenschaftlich-Technische Berichte
FZD-482 2007 · ISSN 1437-322X

WISSENSCHAFTLICH-TECHNISCHE BERICHTE

Forschungszentrum
Dresden Rossendorf

Wissenschaftlich-Technische Berichte
FZD-482
September 2007

H.-M. Prasser, M. Beyer, H. Carl, A. Manera,
H. Pietruske, P. Schütz

Experiments on upwards gas/liquid flow in vertical pipes

Technical Report

Forschungszentrum
Dresden Rossendorf

Technischer Fachbericht

Experimente zu aufwärtsgerichteten Gas/Flüssigkeitsströmungen in vertikalen Rohren

Technical Report

Experiments on upwards gas/liquid flow in vertical pipes

Reaktorsicherheitsforschung-Vorhaben-Nr./
Reactor Safety Research-project No.: 150 1265

Vorhabenstitel: **Aufbau und Durchführung von Experimenten an der Mehrzweck-Thermohydraulikversuchsanlage TOPFLOW für generische Untersuchungen von Zweiphasenströmungen und die Weiterentwicklung und Validierung von CFD-Codes.**

Project Title: **Construction and execution of experiments at the multi-purpose thermal hydraulic test facility TOPFLOW for generic investigations of two-phase flows and the development and validation of CFD codes.**

Autoren / Author(s): **H.-M. Prasser, M. Beyer, H. Carl, A. Manera, H. Pietruske, P. Schütz**

Dienststelle der Autoren /
Performing Organisation: **Forschungszentrum Dresden-Rossendorf e.V.**
Institut für Sicherheitsforschung

Berichtsdatum /
Publication Date: **September 2007**

Berichts-Nr. / Report-No.: **FZD-482**

Das diesem Bericht zugrundeliegende Vorhaben wurde mit Mitteln des Bundesministeriums für Wirtschaft und Technologie unter dem Förderkennzeichen 150 1265 gefördert. Die Verantwortung für den Inhalt dieser Veröffentlichung liegt bei den Autoren.

Berichtsblatt

1. ISBN oder ISSN	2. Berichtsart Technischer Fachbericht
3a. Titel des Berichts Experimente zu aufwärtsgerichteten Gas/Flüssigkeitsströmungen in vertikalen Rohren	
3b. Titel der Publikation	
4a. Autoren des Berichts (Name, Vorname(n)) H.-M. Prasser, M. Beyer, H. Carl, A. Manera, H. Pietruske, P. Schütz	5. Abschlussdatum des Vorhabens 30.09.2006
	6. Veröffentlichungsdatum September 2007
4b. Autoren der Publikation (Name, Vorname(n))	7. Form der Publikation Broschüre
8. Durchführende Institution(en) (Name, Adresse) Forschungszentrum Dresden-Rossendorf e.V. Institut für Sicherheitsforschung Postfach 510119 01314 Dresden	9. Ber.Nr. Durchführende Institution
	10. Förderkennzeichen *) 150 1265
	11a. Seitenzahl Bericht
	11b. Seitenzahl Publikation 143
13. Fördernde Institution (Name, Adresse) Bundesministeriums für Wirtschaft und Technologie (BMWi) 11019 Berlin	12. Literaturangaben 61
	14. Tabellen 4
	15. Abbildungen 102
16. Zusätzliche Angaben	
17. Vorgelegt bei (Titel, Ort, Datum)	

18. Kurzreferat

Zweiphasenmessungen in senkrechten Rohrleitungen sind gut geeignet, um die Wirkung verschiedener Konstitutivgesetze zu untersuchen, die den Impulsaustausch an der Phasengrenze sowie das dynamische Verhalten der Phasengrenze selbst beschreiben. Die Strömung wird in ihrer Bewegung entlang der Rohrleitung und im speziellen im Scheerfeld in Wandnähe über eine relativ große vertikale Lauflänge der Beobachtung zugänglich, ohne dass sofort eine Separation von Gas und Flüssigkeit erfolgt.

Gittersensoren, die das Arbeitspferd bei den beschriebenen Experimenten darstellen, lieferten Serien von momentanen, zweidimensionalen Gasgehaltsverteilungen mit hoher zeitlicher und räumlicher Auflösung. Sie erlauben nicht nur die Ermittlung von Gasgehalts- und Geschwindigkeitsprofilen, sondern auch die Bestimmung von Blasengrößenverteilungen und nach Blasengrößen aufgelösten Gasgehaltsprofilen sowie deren Entwicklung in Strömungsrichtung. Für die Messung der Zwischenphasengrenzfläche wurde ein neuartiger Algorithmus entwickelt. Die Sensoren wurden für einen Einsatz nahe den Betriebsparametern von Leichtwasserreaktoren ertüchtigt. Die meisten Versuche konnten so sowohl für eine Luft/Wasser- als auch für eine Dampf/Wasser-Strömung bei bis zu 6.5 MPa bei identischen Strömungsrandbedingungen durchgeführt werden, was die Möglichkeit bietet, den Einfluss der Stoffwerte zu ermitteln.

19. Schlagwörter
Zweiphasenströmung, Gasblasen, Gasgehaltsverteilungen, Geschwindigkeitsfelder

20. Verlag	21. Preis

Document Control Sheet

1. ISBN or ISSN	2. Type of Report Technical Report
3a. Report Title Experiments on upwards gas/liquid flow in vertical pipes	
3b. Title of Publication	
4a. Author(s) of the Report (Family Name, First Name(s)) H.-M. Prasser, M. Beyer, H. Carl, A. Manera, H. Pietruske, P. Schütz	5. End of Project 30.09.2006
4b. Author(s) of the Publication (Family Name, First Name(s))	6. Publication Date September 2007
	7. Form of Publication Booklet
8. Performing Organisation(s) (Name, Address) Forschungszentrum Dresden-Rossendorf e.V. Institut für Sicherheitsforschung Postfach 510119 01314 Dresden	9. Originator's Report No.
	10. Reference No.*) 150 1265
	11a. No. of Pages Report
	11b. No. of Pages Publication 143
13. Sponsoring Agency (Name, Address) Bundesministeriums für Wirtschaft und Technologie (BMWi) 11019 Berlin	12. No. of References 61
	14. No. of Tables 4
	15. No. of Figures 102
16. Supplementary Notes	
17. Presented at (Title, Place, Date)	

18. Abstract

Two-phase flow experiments at vertical pipes are much suitable for studying the action of different constitutive relations characterizing the momentum exchange at the gas/liquid interface as well as the dynamic behaviour of the gas/liquid interface itself. The flow can be observed in its movement along the pipe and, in particular, within the shear field close to the pipe wall over a considerable vertical distance and, consequently, over a comparatively long time without the immediate separation of gas and liquid characteristic for horizontal flows.

Wire-mesh sensors, which were the working horse in the described experiments, supplied sequences of instantaneous two-dimensional gas fraction distributions with a high-resolution in space and time. This allows to derive from the data not only void fraction and bubble velocity profiles, but also bubble size distributions, bubble-size resolved radial gas fraction profiles as well as the axial evolution of these distributions. An interfacial surface reconstruction algorithm was developed in order to extract the extension of interfacial area from the wire-mesh sensor data. The sensors were upgraded to withstand parameters that are close to nuclear reactor conditions. Most of the experiments were performed for both air/water flow at ambient pressure and steam/water flow of up to 6.5 MPa at identical combinations of the gas and liquid superficial velocities. This offers excellent conditions for studying the influence of the fluid properties.

19. Keywords
Two-Phase Flow, Gas bubbles, Gas volume fraction distribution, velocity fields

20. Publisher	21. Price

This report is part of a series, which comprise following reports:

- Construction and execution of experiments at the multi-purpose thermal hydraulic test facility TOPFLOW for generic investigations of two-phase flows and the development and validation of CFD codes (Final project report), FZD-481,
- Experiments on upwards gas-liquid flow in vertical pipes, FZD-482,
- Experiments on two-phase flow in a vertical tube with a moveable obstacle, FZD-483,
- Experimental investigation of stratified air/water flows in a horizontal channel, FZD-484,
- Experimental investigation and CFD simulation of slug flow in horizontal channels, FZD-485,
- CFD models for polydispersed bubbly flows, FZD-486,
- Turbulent Dispersion of Bubbles in Poly-dispersed Gas-Liquid Flows in a Vertical Pipe, FZD-487,
- Validation of the Multiple Velocity Multiple Size Group (CFX10.0 N x M MUSIG) Model for Poly-dispersed Multiphase Flows, FZD-487.

All these reports are published as reports of the Forschungszentrum Dresden-Rossendorf.

Dieser Bericht ist Teil einer Serie, die folgende Einzelberichte umfasst:

- Aufbau und Durchführung von Experimenten an der Mehrzweck-Thermohydraulikversuchsanlage TOPFLOW für generische Untersuchungen von Zweiphasenströmungen und die Weiterentwicklung und Validierung von CFD-Codes (Abschlussbericht), FZD-480,
- Experimente zu aufwärtsgerichteten Gas-Flüssig Strömungen in vertikalen Rohren, FZD-482,
- Experimente zur Zweiphasenströmung in einem vertikalen Rohr mit verschiebbarem Hindernis, FZD-483,
- Experimentelle Untersuchung von geschichteten Luft/Wasser Strömungen in einem horizontalen Kanal, FZD-484,
- Experimentelle Untersuchung und CFD-Simulation von Schwallströmung in horizontalen Kanälen, FZD-485,
- CFD Modelle für polydisperse Blasenströmungen, FZD-486,
- Turbulente Blasendispersion in einer polydispersen Rohrströmung, FZD-487,
- Validierung des N x M MUSIG Modells für polydisperse Mehrphasen-strömungen, FZD-487.

Alle Berichte sind als Berichte des Forschungszentrums Dresden-Rossendorf veröffentlicht.

Content

1. Introduction

The present report is dedicated to the two-phase flow experiments, which were carried out at the vertical test sections of the TOPFLOW test facility within the research project "Construction and execution of experiments at the multi-purpose thermal hydraulic test facility TOPFLOW for generic investigations of two-phase flows and the development and validation of CFD codes". The project was funded by the Federal Ministry Economics and Technology of Germany in the framework of the reactor safety research. The TOPFLOW experiments are embedded in the activities of the German CFD Alliance that aims at the development and validation of CFD codes for the application in the field of nuclear reactor safety. The growing interest in CFD in the field of reactor safety is explained by the necessity to increase the independence of accident and transient analyses from empirical correlations, scaling effects and the influence of geometry factors. It belongs to the merits of the thermal fluid dynamic test facility TOPFLOW to offer the opportunity for studying a gas/liquid two-phase flow in large pipes in a wide range of void fractions and fluid parameters.

The report focuses on those experiments that where performed at the straight vertical test sections without internals. The experiments with the movable obstacle, which were carried out at the test section DN200, are described in a separate report.

Two-phase flow experiments at vertical pipes were chosen as the object of the present research, because they are very suitable for studying the action of different constitutive equations characterizing the momentum exchange at the gas/liquid interface as well as the dynamic behaviour of the gas/liquid interface itself. The flow can be observed in its movement along the pipe and, in particular, within the velocity gradient close to the pipe wall over a considerable vertical distance and, consequently, over a comparatively long time without the immediate separation of gas and liquid characteristic for horizontal flows.

Most of the experimental data that represents the basis for today available models for upwards two-phase flow origin from vertical pipes that have a diameter or, respectively, hydraulic diameter of 50 mm or below. Tests at large diameter pipes are rare, especially if we speak about high-temperature / high-pressure measurements. For this reason, most of the available large diameter pipes in literature are operated with air/water (Table 1.1).

Most of the authors use either electrical or optical local probes for the characterisation of the flow structure. The first insights into the flow structure in large diameter pipes was made by Ohnuki & Akimoto (1996, 2000), who found that a slug flow with Taylor bubbles typical for small pipes is not found in large pipes. Instead, a direct transition from bubbly to churn-turbulent flow takes place. Delfos et al. (2001) study the air entrainment in a Taylor bubble kept at rest in a downwards flow. The test pipe was used by Kockx et al. (2005) for studies of the liquid film around Taylor bubbles, which was measured using a Laser Induced Fluorescence technique. Sun et al. (2002) validated the one-dimensional one-group interfacial area transport equation using the measuring data from electrical four-tip probes. Misawa et al. (2004) used our wire-mesh sensors in pipes of up-to 200 mm diameter. Since the sensors had always a measuring matrix of 32x32 points, the resolution decreased with growing diameter from 3 mm at 42 mm diameter down to 12 mm at 200 mm diameter, which does no more allows capturing smaller bubbles present in the flow. Furthermore, the

pipes were quite limited in length. The work was therefore concentrated at the scaling effect with respect to the formation and geometry of large bubbles.

Tab. 1.1 Test facilities for studying the evolution of the structure of an upwards gas/ liquid flow in pipes of 100 mm inner diameter and more in comparison with TOPFLOW

Reference	D_i mm	L/D_{max} -	$J_{L,max}$ m/s	$J_{G,max}$ m/s	Gas -	p_{max} MPa	Instrumentation -
Ohnuki & Akimoto (1996)	480	4.2	0.2	0.78	air	0.1	1 tip optical probes
Okawa et al. (1999)	155.2	10	0.583	0.258	steam	0.5	2 tip optical probe
Ohnuki & Akimoto (2002)	200	61.5	1.06	4.7	air	0.1	1 tip optical probes 2 tip electrical probe
Delfos et al. (2001)	100	55	slug flow		air	0.1	video observation
Sun et al. (2002)	101.6	33	1.0	0.12	air	0.1	4 tip electrical probe
Misawa et al. (2004)	42	30.3	4.8	6.0	air	0.1	mesh sensor (3 mm)
	100	13.3	0.85	1.06	air	0.1	mesh sensor (6 mm)
	200	6.95	0.21	0.26	air	0.1	mesh sensor (12 mm)
Kobayashi et al. (2004)	230	35	0.56	0.24	air	0.1	fast gate valves
Shen et al. (2005)	200	113	0.277	0.372	air	0.1[1]	2/4 tip optical probes
TOPFLOW (present study)	195.3	40	1.6 1.6	7.8 0.84	air steam	0.1 6.5	mesh sensor (3 mm)

[1] significant hydrostatic pressure built-up in the pipe due to large height (24 m)

Shen et al. (2005) used two and four tip probes to measure gas fraction and gas velocity profiles as well as radial Sauter diameter distributions and bubble chord length PDFs in a 200 mm diameter pipe. The length of the pipe was 24 m, which allowed to experiment with a maximum inlet length of up to L/D = 113. Attention was given to the transition from wall peak to central peak gas fraction distributions.

Only one test facility unites the features of a large diameter with a steam/water flow at elevated pressures: Okawa et al. (1999) used a vertical pipe of 155.2 mm and 1.5 m height to perform a validation of their novel interfacial drag model, i.e. L/D is limited to 4.2. The facility is equipped with a heater to produce steam at pressures between 0.2 and 0.5 MPa with a maximum superficial velocity of about 1.5 m/s (at 0.2 MPa). Three measuring planes at different heights are equipped with double-tip optical void probes that are operated in parallel, which allows obtaining radial void fraction profiles with a statistical accuracy of 1 % within 30 s of signal acquisition.

The formulation and validation of geometry independent constitutive relations on the level of the calculation cell of the CFD code require instrumentation, which is capable in resolving the relevant structures. Furthermore, it is of great advantage, if measuring information is supplied from the entire cross-section of the duct. In case of relevance to nuclear reactor safety, an additional criterion is the applicability to a wide range of void fractions and fluid thermodynamic parameters. These requirements are fulfilled by the wire-mesh sensors, which were the working horse in the described experiments. They supply sequences of instantaneous two-dimensional gas fraction distributions with a high-resolution in space and time sufficient to characterize large amounts of individual bubbles. This allows to derive from the data not only void fraction and bubble velocity profiles, but also bubble size distributions, bubble-size resolved radial gas fraction profiles as well as the axial evolution of these distributions.

A novel evaluation technique, based on an interfacial surface reconstruction algorithm, was developed in order to extract the extension of interfacial area from the

wire-mesh sensor data. This method was applied to measurements at the large vertical test pipe, which is outlined in an individual section.

Furthermore, within the project, the sensors were upgraded to withstand parameters that are close to nuclear reactor conditions. Most of the experiments were performed for both air/water flow at ambient pressure and steam/water flow of up to 6.5 MPa at identical combinations of the gas and liquid superficial velocities. This offers excellent conditions for studying the influence of the fluid properties. A special series of tests was dedicated to interfacial steam condensation cause by a slight sub-cooling of the liquid phase. The results are presented in a separate section of the report.

It was the goal of the experiments at the vertical test sections to supply the basis for the theoretical work package directed towards a multi-disperse two-fluid model for an adiabatic gas/liquid flow at gas fractions, at which the liquid phase can be envisaged as continuous. The main flow regimes tackled were bubbly flow, slug flow and the transition towards churn-turbulent flow. These flow patterns are characterized by a gas phase that is represented by bubbles of different size and shape. The momentum exchange between gas and liquid is described by so-called bubble forces, which act either in the main flow direction, like the drag force, or perpendicular to the main flow in the present of a gradient of the liquid velocity field, which is built-up by the non-slip conditions at the pipe wall. The latter ones are the so-called non-drag forces. Correlations for the bubble forces are tested by measuring the change of radial gas fraction profiles along the flow path and comparing them to the predictions of fluid dynamic models containing the force correlations to be tested. Since all bubble forces are bubble-size dependent, the ability of the mesh sensors to deliver bubble-size resolved gas fraction profiles was a necessary precondition for the analyses. This kind of model validation reveals information on the correctness and soundness of the model correlations in an integral way, i.e. individual bubble force correlations, e.g. for the lift or the wall lubrication forces, cannot be directly tested.

An exception is the turbulent dispersion force, which was accessed separately from other forces by a cross-correlation technique using the signals of a pair of wire-mesh sensors put in the flow in a small distance behind each other. Also in this case, a direct measurement of the force itself was not feasible. The turbulent dispersion was characterised indirectly by a statistic evaluation of the lateral stochastic motion of bubbles on the path between both sensors. A separate section of the report is dedicated to these studies.

In case of bubbly, slug and churn-turbulent flow regimes, the dynamics of the interfacial area are described by correlations for the bubble coalescence and break-up. Elementary events of neither coalescence nor bubble break-up can be observed directly except by video observation in a much diluted two-phase flow. The strategy of the TOPFLOW experiments with respect to these phenomena is therefore similar to the validation of the bubble forces: The evolution of bubble-size distributions along the flow path is used to calibrate the model coefficients of the corresponding constitutive equations that are solved embedded into a CFD code or a simplified flow solver.

At TOPFLOW, two vertical test sections with different inner diameters are available. This allowed studying the influence of the scaling on the flow structure. The small test section has a nominal diameter of DN50, while the large one is a DN200 pipe. It is well-known that there is a limit diameter, below which the average gas fraction is diameter dependent. At larger diameters, a further increase does no more cause a

change of the void fraction, when the superficial velocities are kept constant. The dimensions of both vertical test sections were selected in the given way to perform measurements both below and above this critical diameter. Another important feature is the capability to run tests at high pressure and temperature, which allows studying the influence of the fluid parameters on the flow patterns.

2. TOPFLOW vertical test sections

2.1 Aim and general scheme of TOPFLOW

TOPFLOW is an acronym standing for **T**ransient **T**w**O** **P**hase **FLOW** Test Facility (Schaffrath et al., 2001). It is designed for generic and applied studies of transient two phase flow phenomena in power and process industries. The fluid is either steam/water or air/water mixture.

The facility was constructed using parts of NOKO, a test facility, which was successfully operated at the Forschungszentrum Jülich (Hicken et al., 2002). NOKO was dismantled in 2001. The electrical heater and the condenser tank were transferred to the new site in Rossendorf (FZD) and completed by new components and instrumentation. TOPFLOW is accommodated in the building of two former nuclear critical assemblies which were decommissioned by VKTA Rossendorf. By end of 1999 the reactors were dismantled and the building was released from nuclear law and made available to FZD for a new use. In the end of 2002 the facility was completed and reached nominal working parameters of 7 MPa and the corresponding saturation temperature of 286 °C. The final licence to operate TOPFLOW at high pressure was granted in September 2003. During the final stage of commissioning, the facility was already used for air/water tests. In parallel, the development of instrumentation was continued. The first scientific steam/water experiments at nominal pressure were started in May 2004 with tests in the small test section of DN50. In September 2004 the tests were extended to the DN200 pipe. A compact overview on TOPFLOW and the experiments carried out in the frame of the presented project is given by Prasser et al. (2006a).

The research project entitled "Construction and execution of experiments at the multipurpose thermal hydraulic test facility TOPFLOW for generic investigations of two-phase flows and the development and validation of CFD codes" was started in April 2002 and lasted for 4 years and 6 months. Beside basic studies at the vertical test sections, an experiment on the flow structure in the hot-leg of the primary circuit of a pressurised water reactor (PWR) was planned. In October 2003 it was decided to significantly extend TOPFLOW for this test, for which a new wing had to be added to the building. The construction was immediately started and the new building was erected in summer 2003. The basic equipment of the new part, a pressure vessel to accommodate the hot-leg test and auxiliary systems for cooling and media supply, was successfully commissioned in 2005. An accident during preliminary tests of the PWR hot-leg model in May 2006 led to the termination of these experiments. After the repair of the damages, TOPFLOW is again available for experiments. The hot-leg tests were postponed to the successor project.

An electrical steam generator with a power of 4 MW representing the heat source of the facility and a heat sink consisting of blow-down tank to quench the exhaust steam, cooling circuit and dry cooling tower system are two main infrastructural com-

ponents of TOPFLOW. Between these to ends the flow passes through various test rigs, which makes up a multi-purpose test facility (Fig. 2.1).

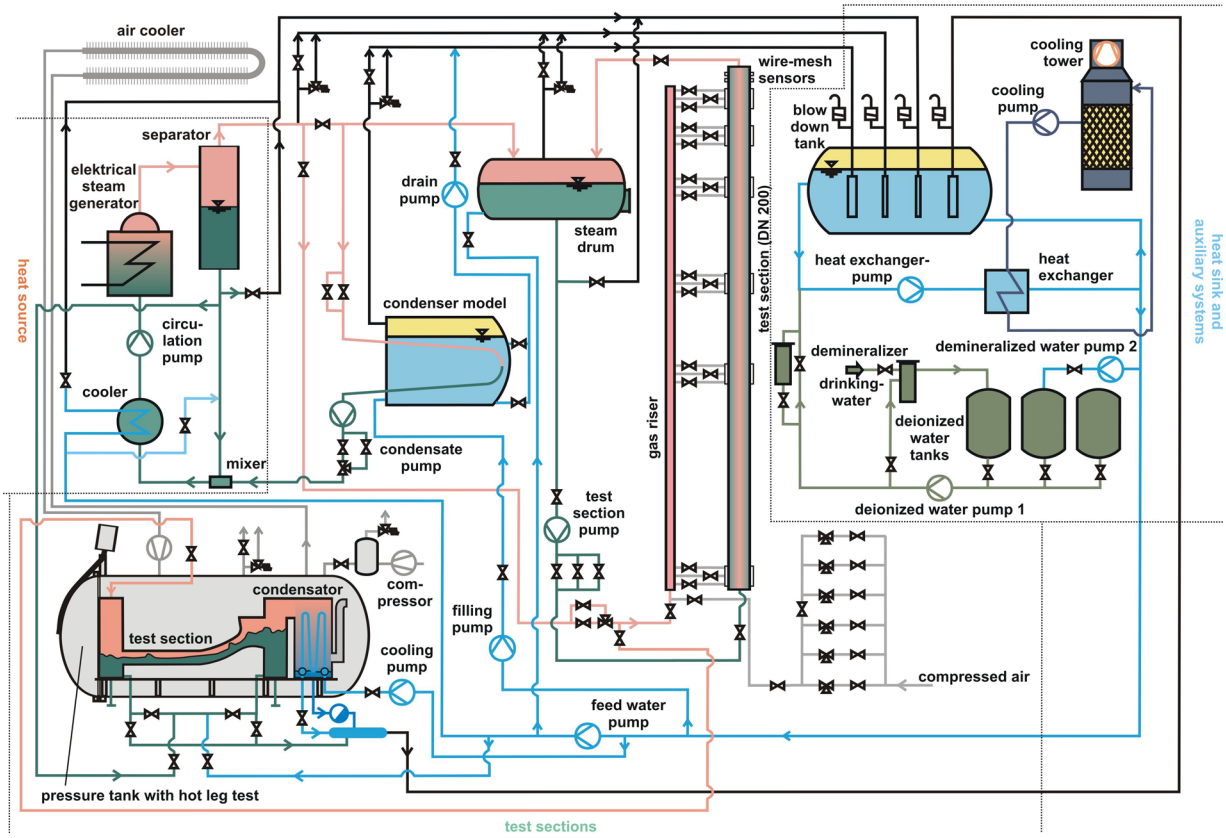

Fig. 2.1 General scheme of the thermal-hydraulic test facility TOPFLOW

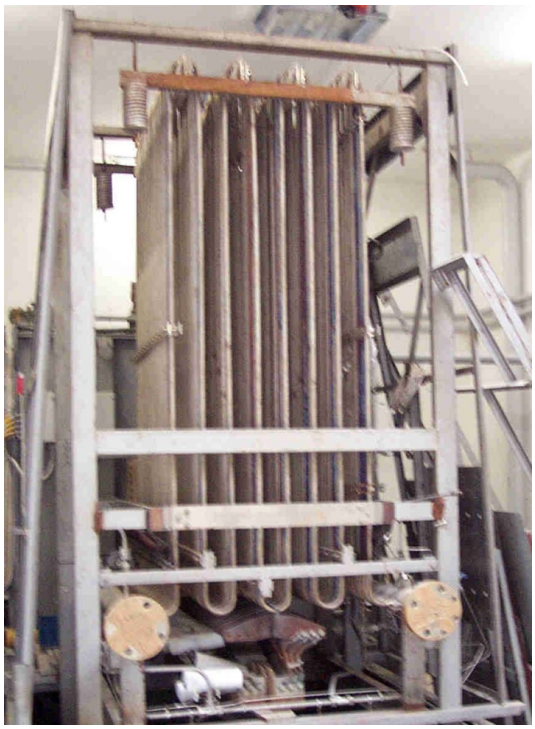

Fig. 2.2 Electrically heated tubes of the TOPFLOW steam generator

The steam is generated in 24 directly electrically heated stainless steel pipes (Fig. 2.2), supplied from a power transformer. The heater circuit can be operated up to a pressure of 10 MPa and generate about 1.4 kg/s saturated steam at this pressure. It was decided to limit operation to 7 MPa and 286 °C because these are the maximum operation conditions for some of the components. In later stages, an extension of the operational range is feasible. In order to achieve 7 MPa in the test sections, the license for the heater circuit was later upgraded to an operation at 7.5 MPa. The dry cooling system can be seen on top of the roof of the mechanical shop of TOPFLOW (Fig. 2.3), while the other components except the pressure chamber for the PWR hot-leg test are located in the central part of the building. On the right side the new wing for the pressure chamber of the PWR hot leg test is attached.

Fig. 2.3 TOPFLOW building with dry cooling system on top of the roof of the left wing

Fig. 2.4 Vertical test sections DN50 (left) and DN200 (right) in the TOPFLOW hall

Between the heat source and the heat sink different test sections can be operated. Presently, TOPFLOW is equipped with four main experimental components. These are:

- Two vertical pipes, nominal diameter DN50 and DN200 (Fig. 2.4 to Fig. 2.6), both 9 m tall, the achieved maximum values of the L/D-ratios are correspondingly 45 for DN200 and 180 for DN50;
- The condenser (Fig. 2.7), which can used to study the behaviour of passive safety systems for nuclear reactors. This vessel is 6 m long, the diameter is about 2 m, it has a volume of 18 m³, the condenser tube bundle can transfer the full heater power;
- the steam drum (L = 5 m, D = 1.5 m, V = 8 m³, p_{max} = 7 MPa);
- The pressure tank for the hot-leg tests (L = 7 m, D = 2.5 m, p_{max} = 5 MPa), equipped with a compressor station to supply pressurized air and an over-roof cooling system with a circulation fan. The pressure tank has a full-size quick-lock port on one end, through which a test facility inside can be accessed. The test rig can be extracted from the tank via a rail system and a mounting platform in front of the port.

Fig. 2.5 Upper end of the vertical test sections with a part of the connecting pipe towards the steam drum

Fig. 2.6 Valves and piping at the steam injector of the large vertical test pipe DN200

Fig. 2.7 View of TOPFLOW with the BWR emergency condenser test in the fore-ground

In the vertical pipe with DN200 the following superficial phase velocities can be reached: J_{steam} < 1.4 m/s at 7 MPa and J_{steam} < 9.2 m/s at 1 MPa, J_{water} < 2.3 m/s. The water flow is generated by test section pump (Fig. 2.8), which is circulating the water through the test sections and the steam drum (Fig. 2.1). The steam is supplied by the steam generating system consisting of the electrical heater, the circulation pump and the cyclone separator. The two-phase flow is generated by injecting the steam at the bottom of the test sections (Fig. 2.6). After leaving the vertical test sections, the two-phase mixture is separated in the steam drum. The steam is condensed in a blow down tank (Fig. 2.1).

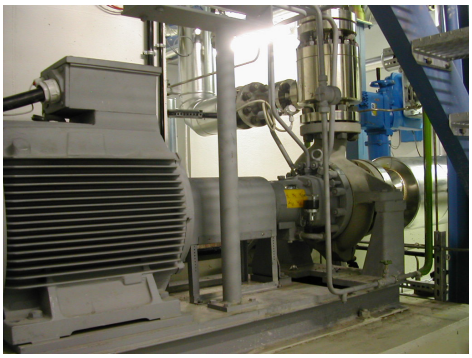

Fig. 2.8 Test section pump for the circulation of water

Big attention was paid to accurate steam and water mass flow measurements, which are performed by multi-strand standard nozzle meters that have an accuracy of 1 % over a mass flow range of 5 decades. Additionally to the high pressure operation it is possible to perform experiments with an air/water flow. For this purpose, TOPFLOW is equipped with an air supply and metering station with a capacity of 750 m³/h at nominal conditions, which corresponds to maximum superficial air velocities of 6.9 m/s in the large pipe. The filtered air is taken from the central pressurised air network of the research centre. The accuracy of the air supply system is better then 1 % of the measuring value. This measuring error also applies to the other measuring technique on TOPFLOW.

2.2 Vertical test sections

The facility is equipped with two vertical test sections, which are stainless steel pipes with inner diameters of 194.1 mm (DN200) or, respectively, 195.3 mm in case of the variable gas injection as well as 52.3 mm (DN50). Both test sections have a total height of 9 m (Fig. 2.9).

Between the test section pump (Fig. 2.1) and the control valves with the multi-strand standard nozzle meters (liquid flow control) a Y-shaped sieve is included in the pipe that serves as a dirt catcher. At the inlet of each test section isolating valves are installed, which direct the liquid mass flow to the corresponding vertical pipe. Upstream of these valves are mounted pipe bends that direct the liquid flow into the vertical pipes. At the upper end of the test section there is a pair of second pipe bend installed, leading the gas/liquid mixture into the piping that connects the test section with the steam drum that serves as a separator vessel (Fig. 2.1).

At a distance of ca. 500 mm above the bends a gas injector is located (for DN200 shown in Fig. 2.10). It consists in a tube of an outer diameter of 60.3 mm which enters the test section from the side. The tube is bended into the main flow direction, forming a coaxial tube segment. At its end, a thread is cut for screwing a gas injection head on top.

Two types of gas injection heads were used. Type K (Fig. 2.11) has three rings with 20 orifices of 6 mm diameter each, which are drilled into the cylindrical part of the head. This injector produces quite large primary bubbles. Gas injection type I is shown in Fig. 2.12. In this case, 16 perforated tubes were welded to the cylindrical part. The total number of injection orifices is 152, their diameter is 0.8 mm.

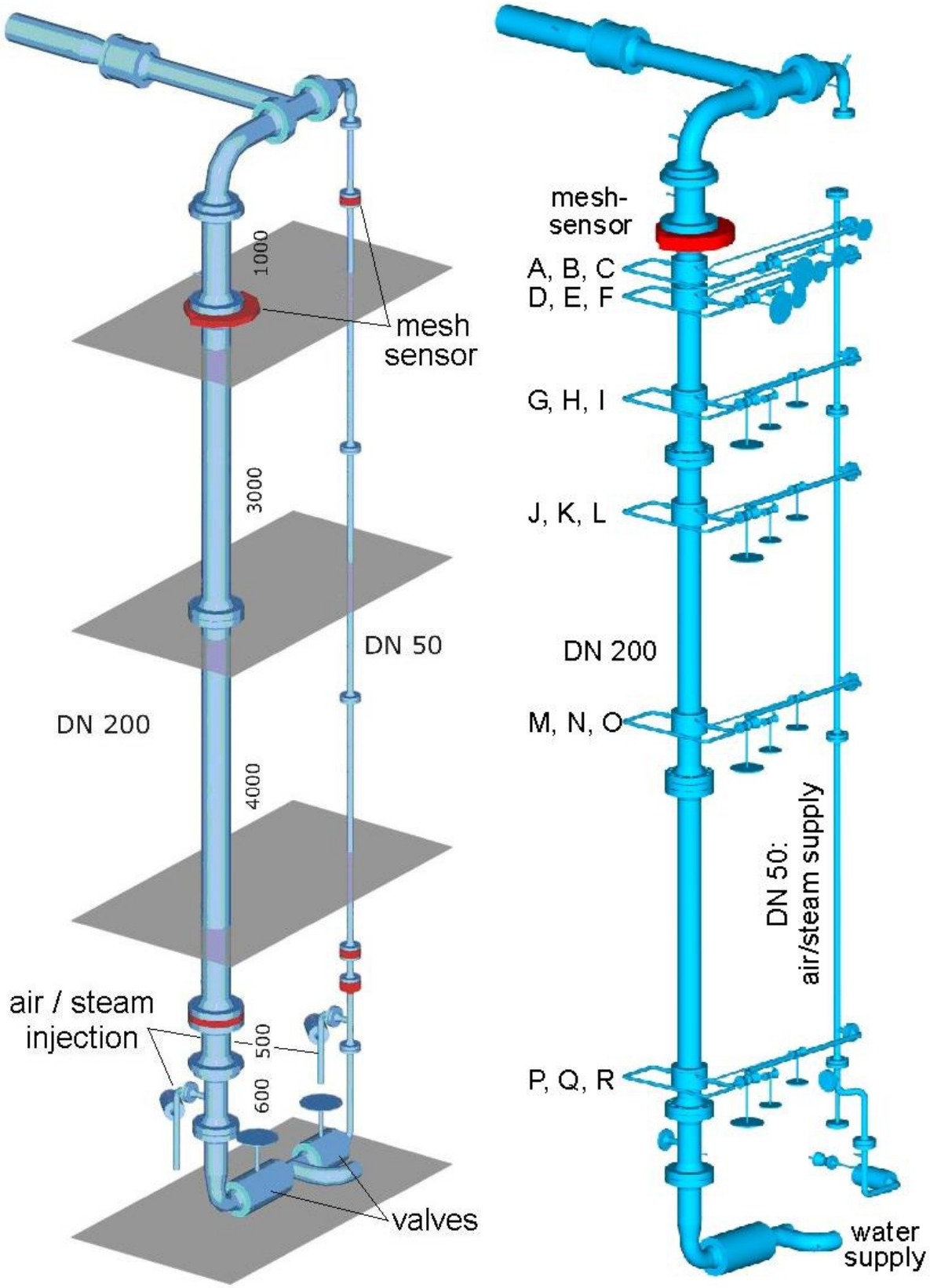

Fig. 2.9 Vertical test sections of the TOPFLOW facility, left: DN50: inner diameter 52.3 mm, DN200: inner diameter 194.1 mm, right: DN200 with variable gas injection system, inner diameter 195.3 mm;
both systems: max. pressure: 7 MPa, max. temperature: 286 °C

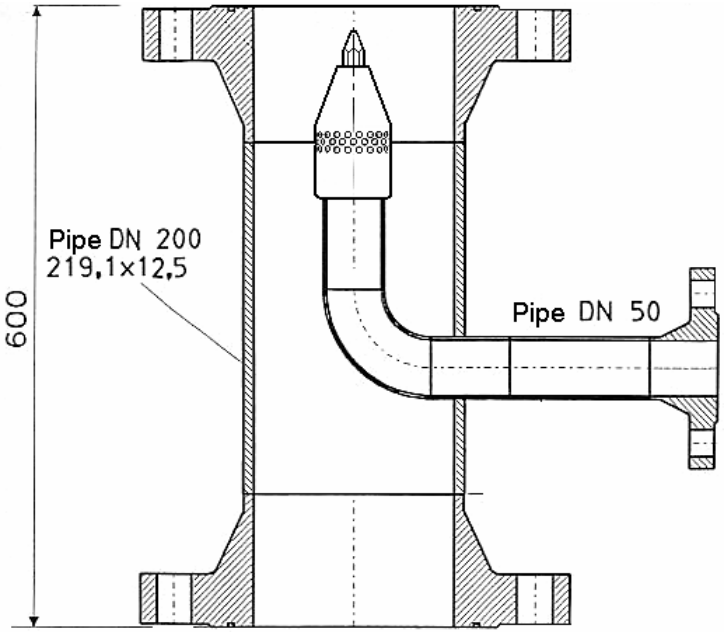

Fig. 2.10 Gas injection device in the DN200 test section

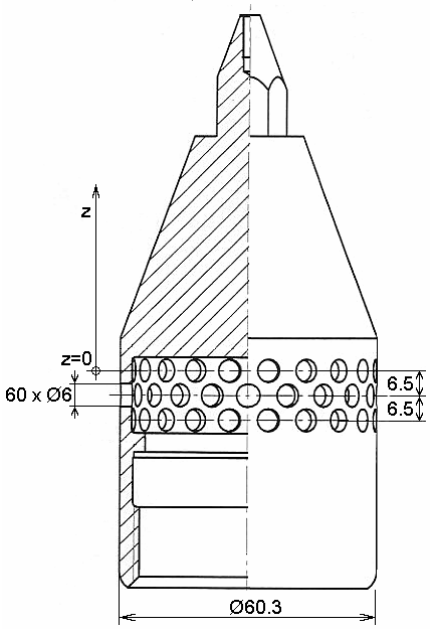

Fig. 2.11 Gas injection head type K for the large pipe DN200

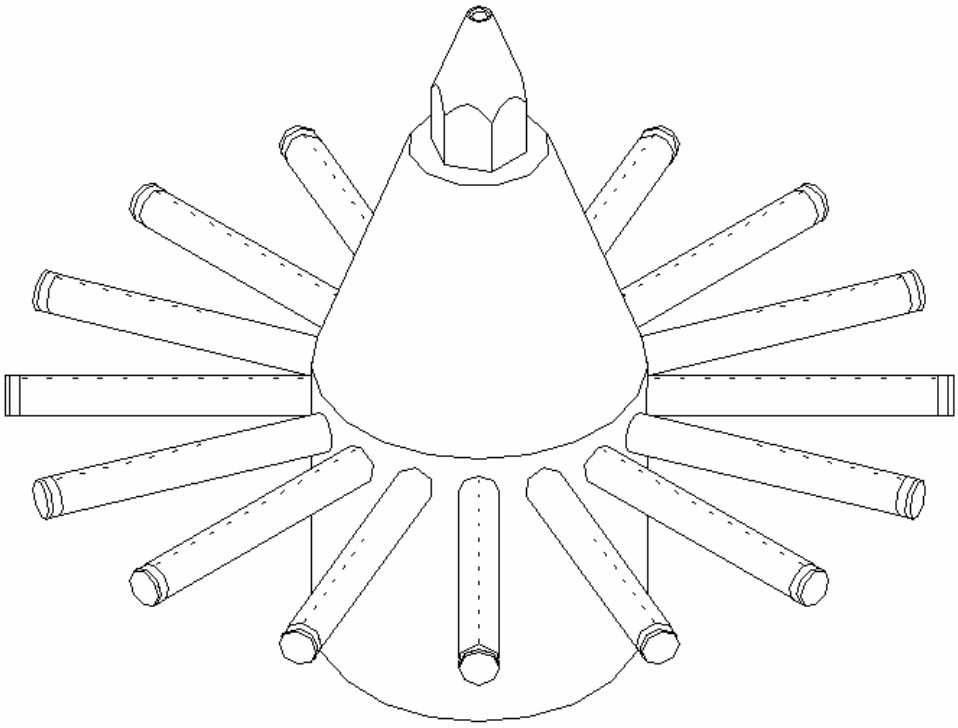

Fig. 2.12 Gas injection head type I for the large pipe DN200

For the DN50 pipe, similar gas injection devices are used. The gas injection head (Fig. 2.13) disposes of 8 orifices with a diameter of 4 mm. Its performance is close to the one of type K for the large pipe. Similar to the injection head type I in the DN200 test section was built a device for the DN50 tube. Fig. 2.14 shows this head with 24 holes of ø 0.8 mm. Both type I devices inject into the test pipes small bubbles. That is an advantage for analyse of bubbly flows, but on the other side the gas mass flow rates are limited. Above the perforated region all injector heads have conical parts in order to reduce the formation of vortices due to flow separation effects. The upper row of injection orifices or, respectively, the perforated tubes, are taken as origin for the z-axis (z = 0).

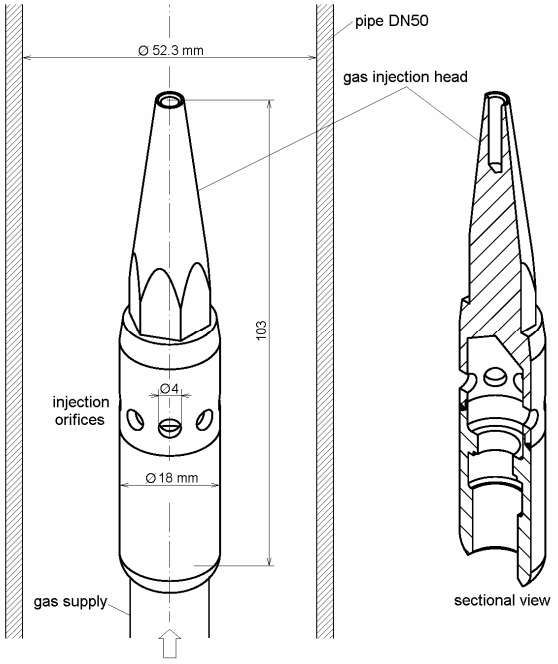

Fig. 2.13 Gas injection head of the small pipe DN50, injection through 8 orifices of 4 mm diameter

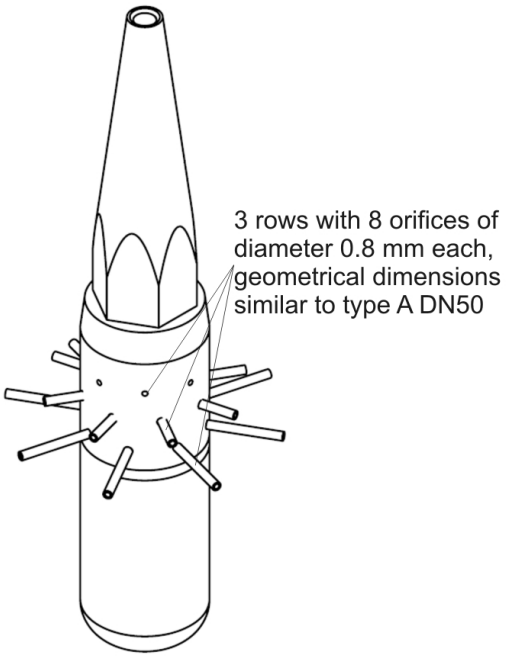

Fig. 2.14 Gas injection device for the small pipe DN50 (24 orifices of 0.8 mm diameter)

At the upper end both test sections join together and the two-phase mixture is directed towards the steam drum, to separate it. An overall isometric scheme of the test sections is shown in Fig. 2.9, left side. All components and pipes of TOPFLOW are designed for an operation with steam/water mixture at pressures of up to 7 MPa and 286 °C.

The wire-mesh sensors are mounted into one of the flange connections of the given pipe. During air/water tests at the pipe DN200 and in all experiments at the small pipe DN50, two sensors were used, which were mounted in a short distance (65 mm) behind each other. High-pressure tests at the test section DN200 were only carried out with a single sensor, since a second sensor was not available.

Both test sections consist of pipe shoots of different lengths. The position of the sensors can be changed by re-arranging the shoots in different sequences. This technique was used to vary the distance between gas injection and sensor position in the experiments at the small pipe (DN50). In both pipes the minimum distance between the measuring plane of the first sensor in flow direction and the upper bend was 1000 mm. Therefore, in case of measurements with one of the injection heads

described above, the distance between the first measuring plane and the gas injection was constant.

The actual distance between gas injection and the measuring plane of the first wire-mesh sensor as well as the distance between the first and the second sensor are given in Tab. 2.1 arranged according to test runs. Detailed information about the experiments carried out on each test run contains appendix A1. In case of the small pipe DN50, up to four different inlet lengths were realized. The largest distance in the DN50 was kept close to the conditions of the DN200 tests. In order to change the distance between gas injection and the sensor at the large pipe was not used the rearranging of pipe shoots, but for this was availed a new construction of the vertical test section described in the next section.

Tab. 2.1 Test runs at the vertical test sections DN50 and DN200

Test run	Test section	Medium	Type of injection device	Distance between:	
				gas injection and measuring plane [mm]	measuring planes of the two sensors [mm]
LD01	DN200	a/w[1]	K	7606	63
LD02	DN200	a/w	I	7606	63
L03	DN50	a/w	I	7910	16
L04	DN50	a/w	I	7910	16
L05	DN50	a/w	K	7910	16
L20	DN50	a/w	K	100, 1600, 3100, 7910	16
D10	DN50	s/w[2]	I	7910	63
D11	DN50	s/w	K	7910	63

[1] a/w - air/water two-phase flow; [2] s/w – steam/water mixture

2.3 Variable gas injection system

One of the important tasks of the experiments at the vertical test sections is the derivation of geometry-independent closure relations for forces acting on bubbles as well as for bubble coalescence and fragmentation rates. Both phenomena are reflected by the evolution of the gas fraction profiles and the bubble size distribution along the flow path. In a previous project, the distance between the gas injection and the mesh sensors was varied at identical superficial air and water velocities and bubble size distributions were measured (Prasser et al., 2003). This was done by a cumbersome disassembling the facility each time when the distance was changed. In case of the large test section of TOPFLOW a more efficient solution was necessary.
To that end the so-called "variable gas injection system" was constructed. The new test section is equipped with gas injection units at six different heights. Each unit has three annular distributing chambers, from which gas or steam enters the test section via a number of orifices in the pipe wall (Fig. 2.15). In order to avoid an obstruction of the cross-section by the gas injection device for the flow coming from another gas injection port located upstream, there is no alternative to wall orifices. Injection devices like those shown in Fig. 2.10 - Fig. 2.14, cannot be used here. The influence of gas injection on void fraction profiles and bubble size distributions is discussed in Prasser (2004).

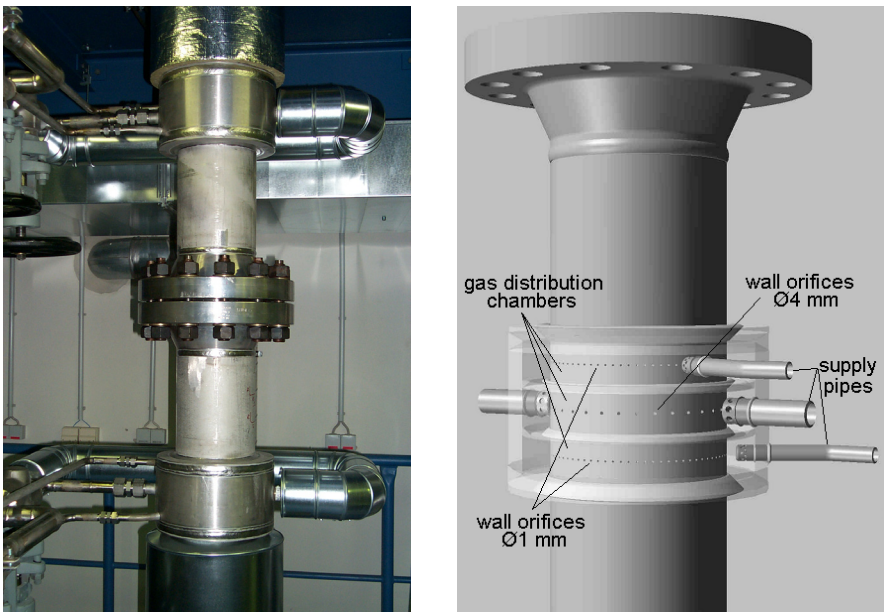

Fig. 2.15 Injection unit of the variable gas injection system at the vertical test section DN200 of TOPFLOW

Two different injection diameters allow to change the primary bubble size and to study its influence on the flow structure. In particular, the upper and the lower chambers have 72 orifices of 1 mm diameter, the central chamber has 32 orifices of 4 mm. This solution makes it possible to vary the distance between gas injection and measuring position, the so-called "inlet length" in 6 steps for the orifices of 4 mm and in 12 steps for the small orifices of 1 mm diameter. The latter is an advantage especially close to the sensor position, where the axial distance between two rings with 1 mm orifices in one and the same injection unit is still comparable to the distance of the unit from the sensor. For the lower injection units the distance between both rings of 1 mm orifices becomes insignificant.

The axial positions of the units are following an approximately logarithmic function, i.e. with growing distance from the sensor, the distance between neighbouring gas injection units are also increasing. The geometrical parameters are shown in Fig. 2.16. In this way, the fact is considered, that the intensity of the changes of the flow structure decreases with growing distance downstream of the gas injection. Another important option of-

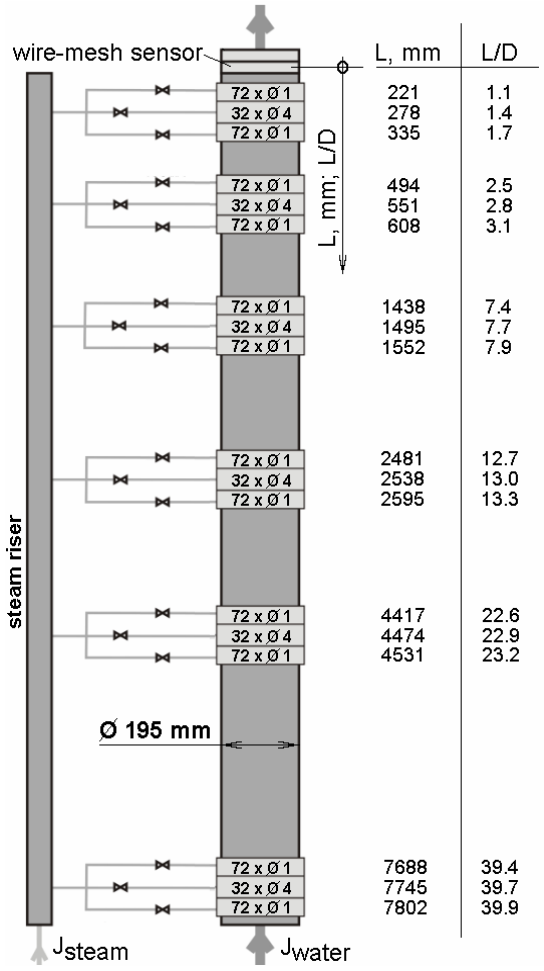

Fig. 2.16 Vertical test section with variable gas injection for studying the evolution of the flow structure in a large pipe of 195 mm inner diameter

fered by the presence of two rings with 1 mm orifices in each unit is the fact that gas flow rates above the limit flow rate for one ring can be achieved by a parallel operation of both rings. The whole system is designed for an operation at 7 MPa and the corresponding saturation temperature, which allows performing both air/water and steam/water tests under identical boundary conditions.

The steam supply for the injection units comes from a riser pipe of 50 mm nominal diameter, which replaced the small test section. Experiments at the DN50 test section were therefore not possible during the use of the variable gas injection system. For an isometric view of the entire test section with variable gas injection system, see Fig. 2.9, right picture. The general scheme of TOPFLOW with the variable gas injection system is shown in Fig. 2.1. In this modification of the test section DN200 are performed the following test runs: L01, L02, L06, L08, L10, D12 and D13 described in appendix A2. For the air/water tests (L) were used 2 low-temperature sensors with a distance between the measurement planes of 63 mm. The steam/water experiments (D) were carried out with the single high-temperature sensor.

3. Test conditions and assessment of experimental uncertainties

The flow rates were varied according to a unified test matrix, which was introduced in the predecessor project to define the superficial velocities in the MTLoop experiments. Independently from the pipe diameter and the properties of the fluid, the matrix defines pairs of values of both superficial air and water velocities. Each matrix point is identified by a test number of 3 digits ranging from 001 to 231 (Tab. 3.1). The mass flows that have to be set up during the tests are calculated from the superficial velocities given in the matrix and the actual pipe diameter as well as the densities of the gaseous and the liquid phases.

Tab. 3.1 Assignment of combinations of the liquid and the gas superficial velocities to identifier of the experiment runs

Superficial water velocity J_W, m/s \ Superficial velocity of the gaseous phase J_G, m/s	0.0025	0.0040	0.0062	0.0096	0.0151	0.0235	0.0368	0.0574	0.0898	0.140	0.219	0.342	0.534	0.835	1.305	2.038	3.185	4.975	7.772	12.14	18.97
4.047	011	022	033	044	055	066	077	088	099	110	121	132	143	154	165	176	187	198	209	220	231
2.554	010	021	032	043	054	065	076	087	098	109	120	131	142	153	164	175	186	197	208	219	230
1.611	009	020	031	042	053	064	075	086	097	108	119	130	141	152	163	174	185	196	207	218	229
1.017	008	019	030	041	052	063	074	085	096	107	118	129	140	151	162	173	184	195	206	217	228
0.641	007	018	029	040	051	062	073	084	095	106	117	128	139	150	161	172	183	194	205	216	227
0.405	006	017	028	039	050	061	072	083	094	105	116	127	138	149	160	171	182	193	204	215	226
0.255	005	016	027	038	049	060	071	082	093	104	115	126	137	148	159	170	181	192	203	214	225
0.161	004	015	026	037	048	059	070	081	092	103	114	125	136	147	158	169	180	191	202	213	224
0.102	003	014	025	036	047	058	069	080	091	102	113	124	135	146	157	168	179	190	201	212	223
0.0641	002	013	024	035	046	057	068	079	090	101	112	123	134	145	156	167	178	189	200	211	222
0.0405	001	012	023	034	045	056	067	078	089	100	111	122	133	144	155	166	177	188	199	210	221

In the test section DN200 (pipe of 194.1 or 195.3 mm diameter), the superficial air velocity (J_N) range was limited to the interval from 0.0025 to 7.772 m/s, the superficial liquid velocity ranged from 0.0405 to 1.61 m/s, while in the small test section the full matrix can be covered.

Desalinated water with a conductivity of about 2 – 5 µS/cm was used for the experiments. Measurements were taken after stable mass flow rates were established. The measuring time was usually set to 10 s. For the tests in the small pipe of 52.3 mm inner diameter, combinations of the superficial gas and liquid velocities were adjusted, which are identical to those one used in the large pipe. In this way the direct comparison of the flow structure established in two different pipe scales can be carried out.

Experiments were carried out both with an air/water two-phase flow and a steam/ water flow. Beside the superficial velocities, each test point is characterised by the thermodynamic conditions in the test section loop and of the injected gas.

The air/water tests are well defined by the pressure and the temperature at a fixed position in the vertical test sections. The pressure and the temperature are measured at a position close to the mesh sensors (see chapter 2.1). Because the length of the test section is about 9 m, the effect of hydrostatic and dynamic pressure drop has to be taken into account during the evaluation and interpretation of the measured data. The metering system for the injected air flow supplies volumetric flow rates related to standard conditions (p = 1.013 bar, T = 0 °C). The temperature of the arriving air is unknown. It was assumed that the air temperature reaches equilibrium with the liquid temperature soon downstream of the injection location, and that the thermal capacity of the air can be neglected in comparison to the thermal capacity of the water. Due to the fact that the liquid temperature is different from the standard temperature for which the flow rate is given, and the pressure is also different from the standard pressure, the real superficial gas velocity differs from the set value that is related to standard conditions. For an accurate analysis, the superficial air velocity has to be corrected according to the equation of state of the ideal gas. In most of the experiments, the correction is small.

Another source of uncertainty is the unknown humidity of the air flow arriving via the centralised pressurized air network. In the extreme case, the air is completely dry and saturates with steam, when it comes into contact with the water at the injection site. This leads to a slight increase of the superficial air velocity compared to the ideal value. An assessment of the maximum uncertainty is achieved by the assumption of the extreme cases of 0 and 100 % relative humidity of the air supply and the calculation of the evaporation rate on basis of the partial pressure under equilibrium conditions at the given water temperature. The change of the water temperature and the water mass flow due to this minor evaporation effect was neglected.

In the steam/water experiments, steam arrives under saturation conditions for the pressure in the heater circuit. This steam is reduced to the pressure at the location of the injection device. The pressure drop is caused by the piping, the control valves, the steam mass flow meters and, finally, the orifices of the injection device itself. This is an isenthalpic process, i.e. the enthalpy of the injected steam is known; it is given by the saturation conditions in the steam separator of the TOPFLOW heater circuit (Fig. 2.1). When the steam comes in contact with the liquid in the vertical test section, the local static pressure, that especially in case of the variable gas injection system may vary with the injection height, is the quantity determining the sub-cooling of the liquid phase. Even in adiabatic experiments, mass and energy exchange at the gas/ liquid interface cannot be neglected for this reason. The interpretation of experimental results obtained with a steam/water mixture requires a thermal hydraulic modelling of the test section circuit.

4. Wire-mesh sensors

4.1 General information

Electrode-mesh sensors are based on a measurement of the local instantaneous conductivity of the two-phase mixture. In case of a gas/liquid two-phase flow, the liquid phase is slightly conducting, while the gas phase is practically an ideal insulator. Mesh sensors were introduced by Johnson (1987), who used them to measure the integral gas fraction in a cross section. Reinecke *et al.* (1998) presented a device visualizing sequences of gas fraction distributions with a rate of about 100 frames per second for the first time. It consists of three layers of electrode grids. Three independent projections of the gas fraction distribution in the sensor cross section are obtained by measuring the impedance between two adjacent parallel wires. The imaging is carried out applying tomographic reconstruction algorithms. Later, the sensor was used to study flashing during depressurization of chemical reactors (Schmitz & Mewes, 2000). Our own development was aimed at a direct conductivity measurement between pairs of crossing wires to avoid tomographic reconstruction algorithms (Prasser et al., 1998) and to increase time resolution.

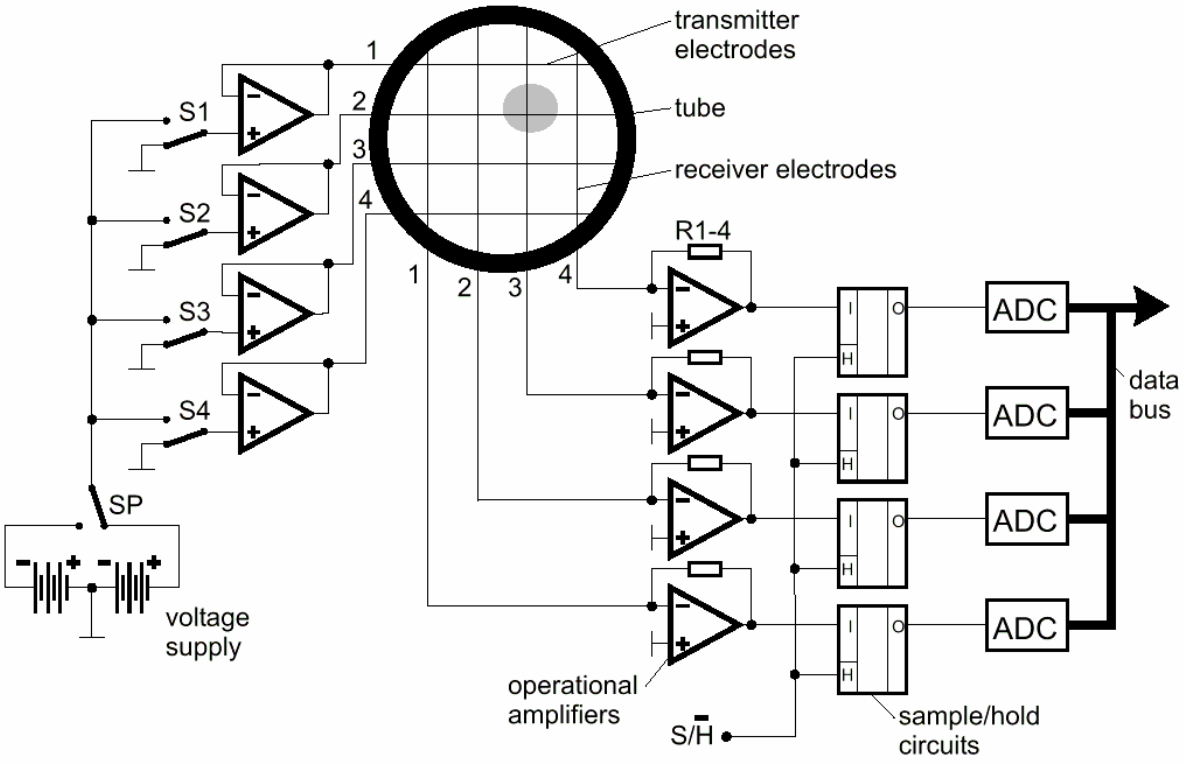

Fig. 4.1 Measuring principal of wire-mesh sensors, simplified scheme of a wire-mesh sensor with 2x4 electrode wires

From the point of view of the general arrangement of electrode wires, our sensors are quite similar to the ones described by Johnson (1987). The sensor consists of two grids of parallel wires which span over the measuring cross section. The wires of both planes cross under an angle of 90 deg.

Our first generation of sensors signal acquisition units worked at a framing rate of 1024 Hz, later 1200 Hz. A second generation has reached a time resolution of 10 000 frames per second (Peters et al., 1999). During the signal acquisition, one

grid of electrode wires is used as transmitter, the other as receiver plane (Fig. 4.1). The transmitter electrodes are activated by supplying them with voltage pulses in a successive order. The current at a receiver wire resulting from the activation of a given transmitter wire is a measure of the conductivity of the fluid in the corresponding control volume close to the crossing point of the two wires. The currents from all receiver wires are sampled simultaneously. This procedure is repeated for all transmitter electrodes. After activating the last transmitter wire, a complete matrix of measured values is stored in the computer, which represents the complete two-dimensional conductivity distribution in the sensor cross section at the time of measurement.

4.2 Low-pressure sensors

4.2.1 Sensors DN50

The sensors used for air/water experiments at the small test section DN50 were taken from previous experiments at the predecessor facility MTLoop (Prasser et al., 2003). Two sensors with a matrix of 16x16 measuring positions and an inner diameter of 51.2 mm were still available (Fig. 4.2). The wire diameter was 0.12 mm, the lateral pitch 3 mm and the distance between transmitter and receiver grids was about 1.8 mm. In order to adapt the slightly smaller inner diameter of the sensor to the inner diameter of the test pipe of 52.3 mm, conical connection pieces were manufactured and put between the sensors and the flanges. From this follows an axial distance between the measuring planes of both sensors of 16 mm. Measurements were carried out with frame rates of 2.5 kHz and 10 kHz. Signal sequences were recorded over a measuring period of 10 s.

4.2.2 Sensors DN200

For the measurements in the large pipe, two sensors with 64 receiver and 64 transmitter wires of 120 µm diameter were used. Correspondingly, the measuring matrix has the dimension of 2x64x64. Two electronic units, working in parallel, are able to perform 2500 samples per second (Prasser et al., 2002a). Since a measuring time of 10 s was chosen, each run resulted in 25000 two-dimensional gas fraction distributions consisting of 64x64 values for each sensor, i.e. the data array of each measurement has the dimension of 25000x64x64. One sensor is shown in Fig. 4.3 and Fig. 4.4. The inner diameter is identical with that of the test section. The lateral pitch of the wires is 3 mm, while the axial distance between the two grids is 2 mm. To compare the measurements in the DN50 and DN200 pipes, it makes sense that both types of sensors were constructed with the same lateral pith of 3 mm.

A successful application of wire-mesh sensors to perform high-speed visualization, bubble size distribution measurements and a decomposition of radial gas fraction profiles according to bubble size classes was published in a number of papers (Prasser et al., 2001, 2002b). These experiments, performed in a pipe of 51.2 mm diameter, resulted in valuable data for testing and adjusting basic models of bubble forces as well as coalescence and fragmentation correlations (Prasser et al., 2003).

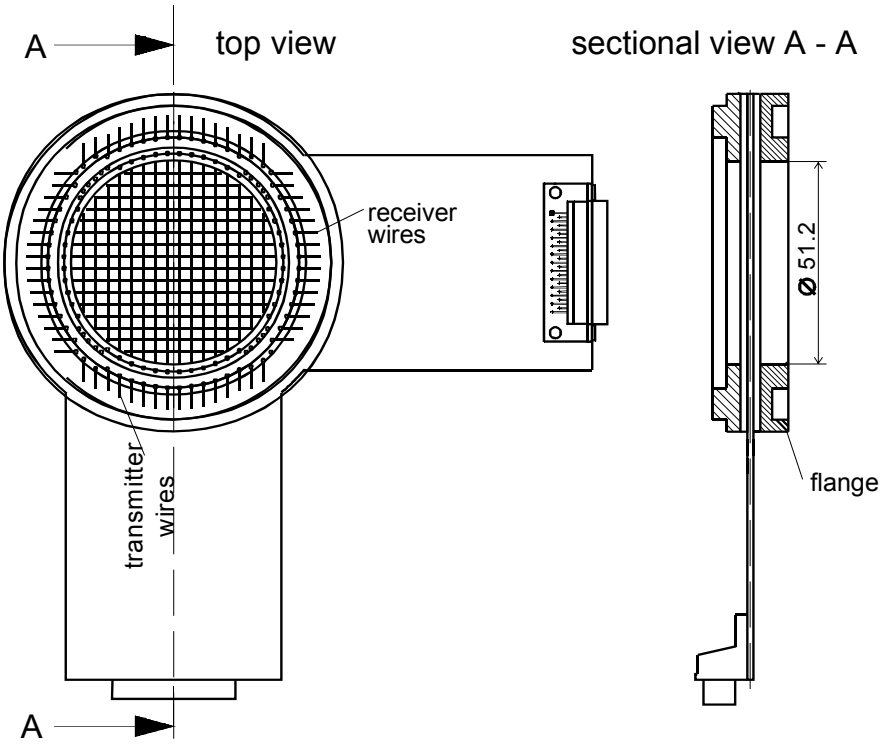

Fig. 4.2 Wire-mesh sensor for air/water experiments at ambient temperature with a measuring matrix of 16x16 on a cross-section of 51.2 mm diameter

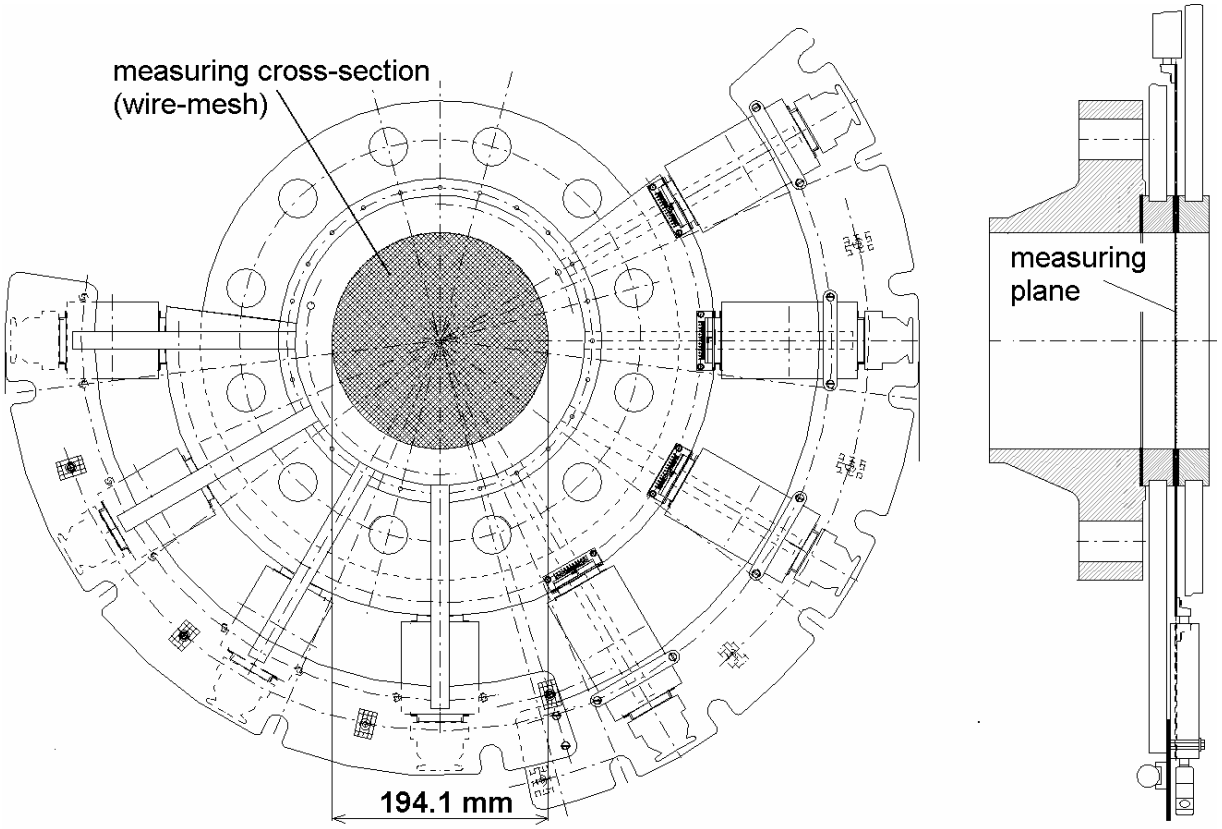

Fig. 4.3 Wire-mesh sensor for air/water tests in the DN200 test pipe with a measuring matrix of 64x64 points

In case of the presented experiments two wire-mesh sensors with a matrix of 64x64 measuring points each were applied. Each of these devices delivers 2500 instantaneous gas fraction distributions (frames) per second. A cross-correlation of the data of the first and the second sensor allowed obtaining gas velocity profiles. Bubble size distributions can be derived using described in Prasser et al. (2001) bubble recognition techniques. In this way new insight was brought into the structure of the two-phase flow in large pipes. Furthermore, it was possible to study the influence of scaling effects by comparing the results with measurements at the second test section (DN50).

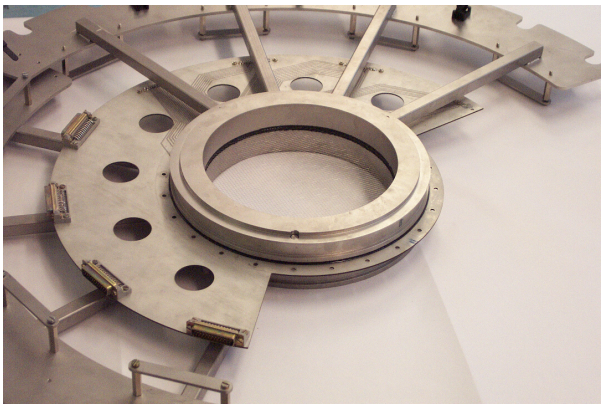

Fig. 4.4 Photograph of the wire-mesh sensor for air/water tests in the DN200 test pipe with a measuring matrix of 64x64 points

The merits of the wire-mesh sensor consist in the registration of instantaneous gas fraction distributions over the entire cross section. This allows obtaining gas fraction and bubble size profiles in a very efficient way. The sensor can obtain information on shape and size also for large and highly deformed bubbles, while local probes can only supply information about the length of the chord on which the bubble was penetrated.

4.3 High-pressure sensors

For the execution of the project sensors for an application in a hot steam/water mixture were required. Such sensors were developed for both test section: (1) a sensor with an inner diameter of 52.3 mm with a measuring matrix of 16x16 and (2) a sensor of 195 mm inner diameter with 64x64 measuring points. Both devices can be operated at 7 MPa and a temperature of max. 286 °C (Pietruske & Prasser, 2007). The spatial and temporal resolutions are equal to earlier used sensors for air/water flow at ambient conditions (3 mm, 2500 Hz or, alternatively, 10 kHz in case of the DN50 sensors).

Problems the development of high-pressure / high-temperature sensors had to face were:

- The sensor body must be designed for the overpressure and has to meet the requirements towards pressurized equipment.
- The construction has to withstand temperature transients without deformations of the electrode wires due to thermal dilation. Sensors for cold air/water flow, like the one shown in Fig. 4.2, have electrodes soldered to fixing points at both ends. Such sensors were shown to be applicable in boiling steam/water flows at temperatures of about 120 °C (Manera et al., 2001). At higher parameters, thermal dilation, especially a fast temperature drop, can cause plastic shrinking. Without appropriate measures, the wires lose their tension and become floppy.
- For contacting the electrodes from outside, a large number of pressure-resistant bushings has to be organised in a small available space.

- Additionally, it is desirable to create the possibility for repairing or, respectively, replacing broken wires, which is essential in view of the high costs of the high pressure sensor.
- First attempts to build high-pressure sensors led to a construction with electrode rods (Prasser et al., 1999 and 2000) that are fixed at one end and slide in a PTFE bearing on the other end, used in the WAHALoads project (Giot & Seynhaeve, 2004). In this way, the electrodes can perform thermal dilation without being deformed. The main disadvantage is the higher disturbance of the flow caused by the electrode rods, though the electrodes are manufactured with a wing-shaped cross-section in order to reduce their drag and the resulting pressure drop. Therefore, the task was set to return to thin electrode wires also for high-pressure / high-temperature sensors.

To compensate thermal dilation, the electrodes of the new sensors are stretched by springs. Each wire is equipped with its own spiral spring. In view of the small available space at the desired electrode pitch of 3 mm these springs have to be very small. They have an outer diameter of only 2 mm. Nevertheless, it has to be avoided that the springs disturb the flow. For this reason, the springs are put into blind holes at the inside of the sensor (Fig. 4.5). The holes must have a diameter smaller than the lateral pitch of the wires, therefore it cannot be excluded that the springs come in contact with the walls. To maintain electrical insulation, a ceramic pearl is inserted between spring and wire.

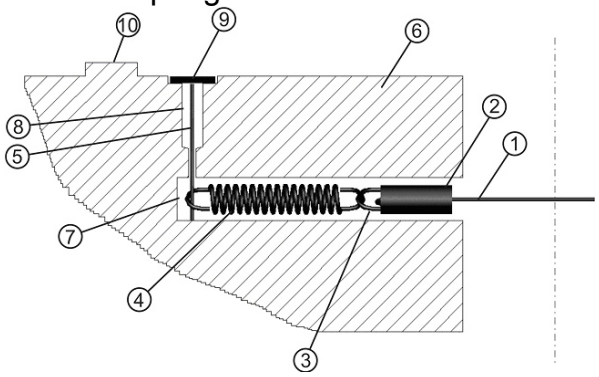

Fig. 4.5 Fixing and stretching of the electrode wires:
1 - electrode wire, 2 - ceramic insulation pearl, 3 - eye,
4 - spring, 5 - pin, 6 - sensor body, 7 - blind hole, 8 - guide hole, 9 - cover ring,
10 - sealing surface of flange connection

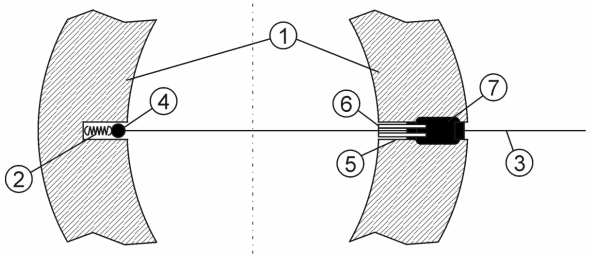

Fig. 4.6 Fixing of electrode wires in the sensor
1 - sensor body, 2 - spring,
3 - electrode wire, 4 - ceramic insulation pearl, 5 - channel,
6 - ceramic tube, 7 - cavern with epoxy resin

Springs are placed only on one end of the wires (Fig. 4.6). The second end is led through a channel on the opposite side of the sensor body to the outside. In this channel, the wire has again to be insulated from the grounded sensor body. This is done by a ceramic tube, which is interrupted in a cavern filled with high-temperature epoxy resin for sealing (Fig. 4.7). Available resins with the necessary strength have working temperatures of up to 180 °C. Since the fluid can be at higher temperature, the sealing is placed in elongations (see Fig. 4.9, pos. 3) of the sensor, at the outside of which cooling bodies are fixed.

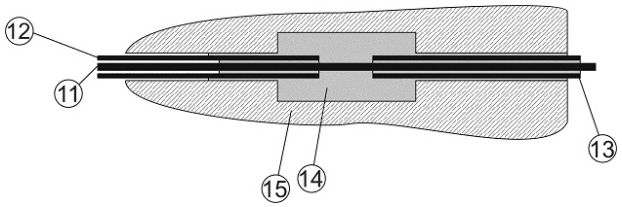

Fig. 4.7 Bushing of the electrode wire:
11 - electrode wire,
12, 13 - ceramic insulation tubes,
14 - cavern with epoxy resin,
15 - sensor body

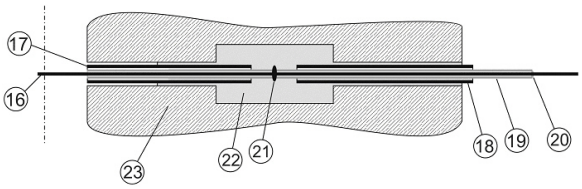

Fig. 4.8 Construction with additional steel capillary to allow for the repair of broken wires:
16 - electrode wire,
17, 18 - ceramic insulation tubes, 19 - stainless steel capillary, 20 - sealing by brazing, 21 - fixing point for better contact with resin,
22 - cavern with epoxy resin,
23 - sensor body

The possibility to repair broken wires is achieved by two features: (a) The wires are not directly put into the ceramic insulation tubes, but into capillary tubes made from steel (Fig. 4.8). At the outside, wires and capillary tubes are brazed together to seal the system completely. (b) The springs are fixed by pins (Fig. 4.5), guided in holes drilled in direction parallel to the sensor axis. These pins can be removed to unfix a broken wire. The brazing between wire and capillary tube is cut of and a new wire can be placed into the sensor.

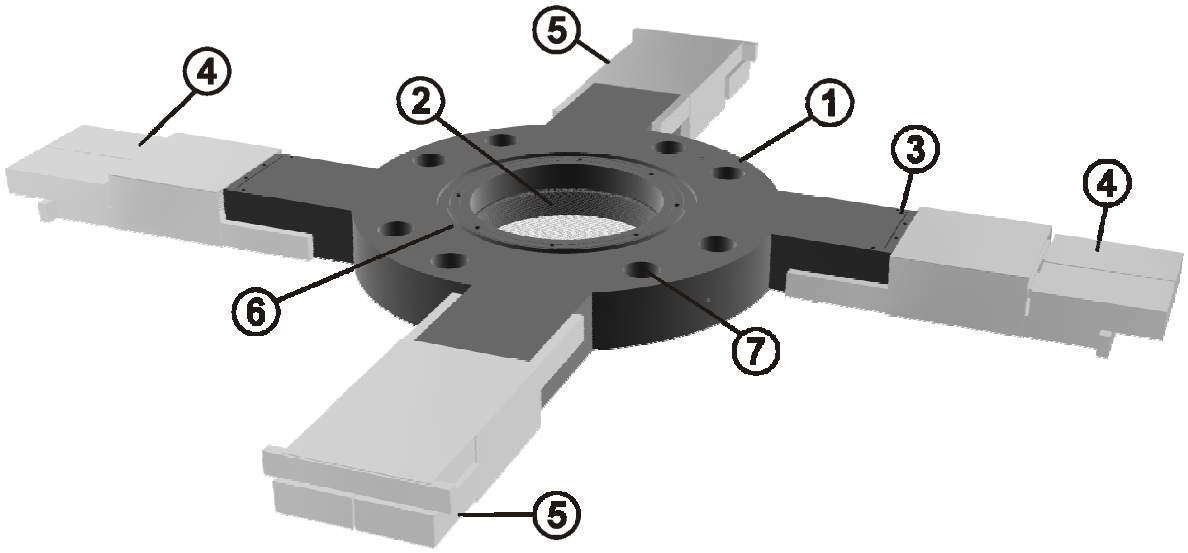

Fig. 4.9 CAD image of the complete sensor for a 195 mm inner diameter pipe, 64x64 electrodes:
1 - sensor body, 2 - measuring plane with wires, 3 - location of sealed bushings (without cooling bodies), 4 - driver unit, 5 - receiver pre-amplifier, 6 - cover ring, 7 - bolt hole of flange connection

The construction of the sensor body with all necessary holes and caverns is extremely complicated. It was manufactured from two half-shells, which were joint by vacuum brazing. The hidden channels were milled into the faces before put together. Both half-shells were treated in the same way to create the channels for each of the

two electrode grids. A stainless steel foil was put between the shells to separate the channels at the crossing points.

The described technology was used to build a sensor of 195 mm inner diameter with 64x64 wires (Fig. 4.9). The resulting pitch of the wires and the axial distance between the two grids are 3 mm. The wires have a diameter of 250 µm, which will be reduced to 100 µm in the next realizations to be manufactured.

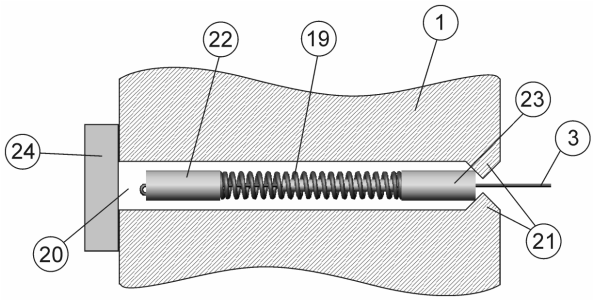

Fig. 4.10 Construction with additional steel capillary to allow for the repair of broken wires:
1 - sensor body, 3 - electrode wire, 19 - compression spring, 20 - orifice, 21 – edge, 22, 23, ceramic insulation pearls, 24 – cap

Sensors for a test pipe of 52.3 mm inner diameter are equipped with a matrix of 16x16 wires. Here, the construction is slightly different, because of geometric constraints. Wires are stretched by compression springs that rest on an edge in the orifices close to the inner surface of the sensor body (Fig. 4.10). Again, measures have to be taken to avoid a direct contact of the electrode wire with the sensor body.

A CAD view of a sensor of 52.3 mm inner diameter is shown in Fig. 4.11. Two identical sensors of this kind were manufactured and placed into the test pipe in a distance of 63 mm behind each other. This allowed to additionally measure steam velocities by cross-correlating the signals of both sensors.

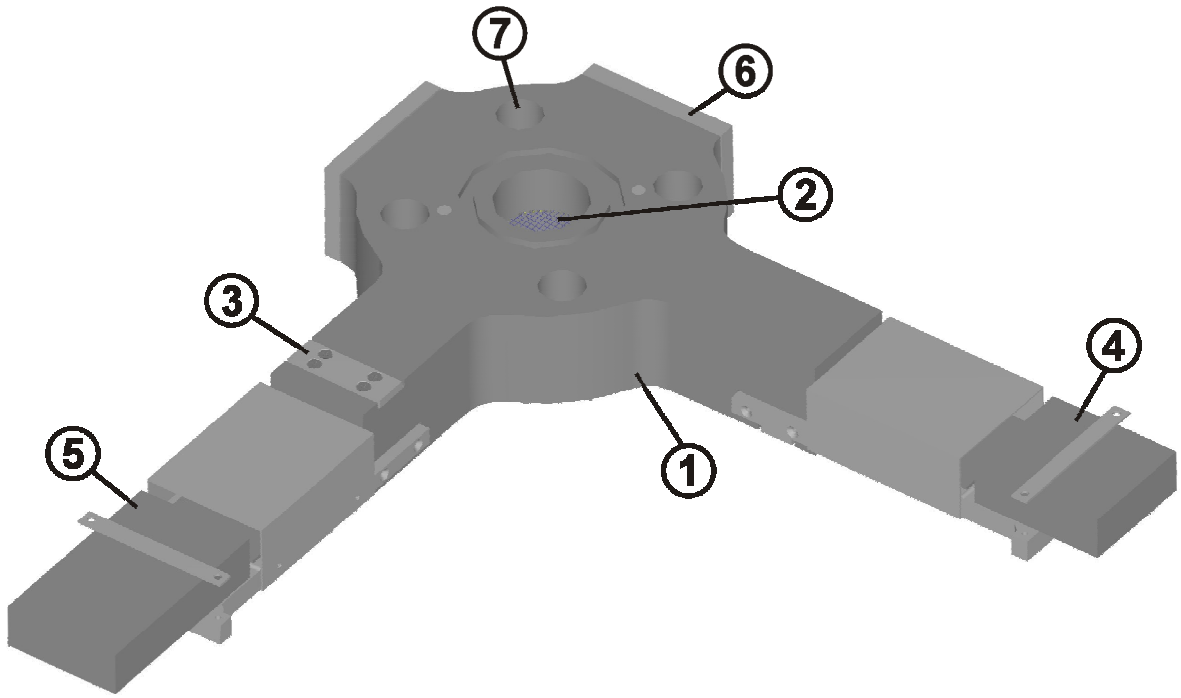

Fig. 4.11 CAD view of the complete sensor for a 52.3 mm inner diameter pipe, 16x16 electrodes:
1 - sensor body, 2 - measuring plane with wires, 3 - location of sealed bushings (without cooling bodies), 4 - driver unit, 5 - receiver pre-amplifier, 6 - cap, 7 - bolt hole of flange connection

Cooling bodies were fixed to the elongated parts (see Fig. 4.11, pos. 3) of the sensor in order to limit the temperature at the epoxy sealings. The electronic driver and pre-amplifier units were fixed directly to connections at the sensor to keep electrical noise low.

For the DN50 test section, a pair of high-pressure sensors was manufactured, while for the large pipe only a single sensor was available.

4.4 Data evaluation

4.4.1 Visualization

The data evaluation starts from the transformation of the measured electrical signals into local instantaneous gas fractions. At each measuring location the instantaneous conductivity signal is related to the signal characteristic for plain water. The result is a matrix of local instantaneous volumetric gas fractions $\varepsilon_{i,j,k}$, where k is the number of the current measurement and i, j are the two indexes of the location in the sensor plane. This data are used to calculate cross-section averaged gas fractions as well as radial gas fraction profiles.

Three different methods were applied to visualize the resulting gas fraction matrix $\varepsilon_{i,j,k}$: (1) instantaneous gas fraction distributions in the measuring plane, (2) virtual sectional side views and (3) virtual side projections (Prasser et al., 2005a). The first is generated by plotting two-dimensional distributions in the directions of i and j for a fixed value of index k. Sequences of these distributions obtained by stepwise incrementing index k can be viewed as animated images.

In case of virtual sectional side views, a distribution either from the plane i,k or j,k is plotted on the two-dimensional canvas in the way that the time axis is oriented downwards. The third index is kept constant, usually at a value representing an electrode wire in the centre of the cross section. Such image obtains the character of a side view to the flow on a vertical plane cut through the pipe along its axis. Originally, the vertical axis is a time axis, which can be transformed into a virtual z-axis, when it is scaled according to the velocity of the gaseous phase. If the drawing scale for the lateral axis (x or y) is kept identical to the scale of the virtual z-axis, bubbles are displayed in correct length-to-width relation. Often, individual bubble velocities are not available. In this case the average phase velocity calculated from the known superficial gas velocity divided by the measured average gas fraction is used as an approximation. This leads to certain distortions, since the velocity differs from bubble to bubble. The scaling according to the average velocity is nevertheless a helpful procedure to obtain an approximate visualization of the real shape of the bubbles. The method of constructing a virtual z-axis has the advantage that sectional plots obtained at different air flow rates can be compared directly.

The third method applied is the calculation of virtual side projections using a simplified ray-tracking algorithm. The virtual propagation of light through the three-dimensional column of elements filled with gas respectively liquid according to the gas fraction matrix $\varepsilon_{i,j,k}$ is simulated numerically. The procedure starts with the assumption of parallel white light arriving in the direction of the x-axis:

$$\vec{\Phi}_{x,0,j} = \vec{\Phi}_{white} = \left(\varphi_{red}, \varphi_{green}, \varphi_{blue}\right) = \left(255,255,255\right) \tag{1}$$

The light flux is treated like a vector consisting of three intensities for red, green and blue. In true-colour bitmap images, the white value is 255 for all three components. It

is used as initial value. When the light propagates through the column, its red, green and blue components are partially absorbed. The attenuation is assumed to be different for gas and liquid:

$$\vec{\Phi}_{x,i,j} = \vec{\Phi}_{x,i-1,j} \cdot \left[1 - \vec{\Lambda}_{gas} \cdot \varepsilon_{i,j} - \vec{\Lambda}_{liquid} \cdot \left(1 - \varepsilon_{i,j}\right)\right] \quad for \quad i \geq 0 \quad and \quad i \leq n_{el} \tag{2}$$

Virtual absorption coefficients are defined for each component both for gas and liquid phases individually, being components of the vectors $\vec{\Lambda}_{\text{gas}}$ and $\vec{\Lambda}_{\text{liquid}}$. In the result of illumination and absorption, there is light of a certain intensity and colour present in each location. In the next step it is assumed that gas and liquid scatter a portion of this intensity towards the observer, which looks at the column from the side under an angle of 90 deg compared to the illumination. This is reflected by a source term for the light propagating along the y-axis:

$$\vec{Q}_{i,j} = \vec{\Phi}_{x,i,j} \cdot \left[\vec{\Omega}_{gas} \cdot \varepsilon_{i,j} - \vec{\Omega}_{liquid} \cdot \left(1 - \varepsilon_{i,j}\right)\right] \tag{3}$$

In the direction towards the observer the flux resulting from these sources accumulates. Depending on the location of the source, the light has to propagate through more or less layers of two-phase medium, i.e. absorption has again to be considered. Accumulation and absorption in direction of the y-axis are described as follows:

$$\vec{\Phi}_{y,i,j} = \vec{\Phi}_{y,i,j-1} \cdot \left[1 - \vec{\Lambda}_{gas} \cdot \varepsilon_{i,j} - \vec{\Lambda}_{liquid} \cdot \left(1 - \varepsilon_{i,j}\right)\right] + \vec{Q}_{i,j} \quad for \quad j \geq 0 \quad and \quad j \leq n_{el} \tag{4}$$

The initial value for the flux in y-direction is “black”, i.e.:

$$\vec{\Phi}_{y,i,0} = \vec{\Phi}_{black} = \left(\varphi_{red}, \varphi_{green}, \varphi_{blue}\right) = (0,0,0) \tag{5}$$

The light flux distributions calculated for j = n_{el} are plotted in the same way as it was done to create virtual sectional side views. The result is a life-like image of the flow pattern, which is close to a visual observation through a transparent pipe wall.

The virtual absorption coefficients given by the vectors $\vec{\Lambda}_{\text{gas}}, \vec{\Lambda}_{\text{liquid}}$ as well as the virtual scattering coefficients in the vectors $\vec{\text{Q}}_{\text{gas}}, \vec{\text{Q}}_{\text{liquid}}$ were chosen empirically by optimizing the visual impression of the achieved imaging. The selected values ensure that the gaseous phase is painted from yellow to red and the liquid phase remains dark blue. Due to the virtual absorption of the light, portions of the given phase become fainter when they are more distant from the observer or, respectively, from the virtual light source. This effect generates the plastic three-dimensional impression of the obtained projection images.

4.4.2 Void fraction profiles

Local instantaneous gas fractions can be averaged over different domains to obtain time averaged void fraction profiles or spatially averaged void fraction time sequences (Prasser et al., 2002b). The averaging is based on weight coefficients that define the contribution of each crossing point of wires in the sensor matrix to the size of the domain, over which the averaging has to be performed. The definition of the weight coefficients necessary to obtain a cross-section averaged void fraction is shown in Fig. 4.12. The average can be calculated for each sampling period individually:

$$\bar{\varepsilon}_k = \varepsilon(t) = \sum_i \sum_j a_{i,j} \cdot \varepsilon_{i,j,k} \qquad (6)$$

In this way, a sequence of instantaneous average void fractions is obtained, available with the full measuring speed of the sensor. Another option is the averaging in time. Two-dimensional void fraction distributions are provided by the following averaging:

$$\bar{\varepsilon}_{i,j} = \frac{1}{k_{max}} \sum_{k=1}^{k_{max}} \varepsilon_{i,j,k} \qquad (7)$$

An average void fraction for the total measuring cross-section can be obtained as follows:

$$\bar{\varepsilon} = \sum_i \sum_j a_{i,j} \cdot \bar{\varepsilon}_{i,j} = \frac{1}{k_{max}} \sum_{k=1}^{k_{max}} \bar{\varepsilon}_k \qquad (8)$$

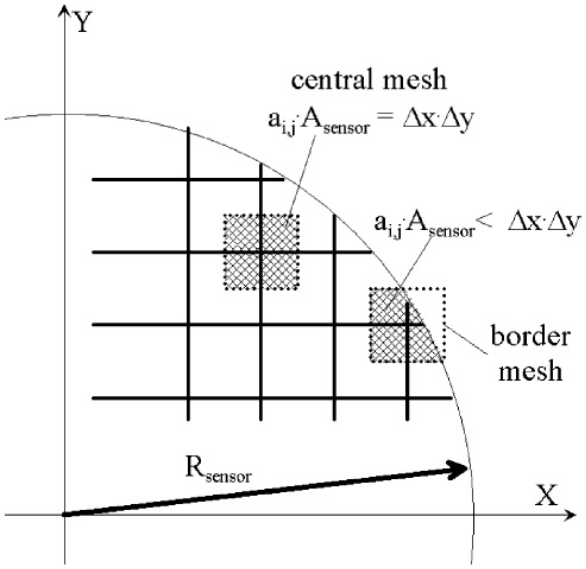

Fig. 4.12 Wight coefficients for the cross-section averaging of local gas fractions measured by the wire-mesh sensor

Radial gas fraction profiles can be calculated by averaging the local instantaneous gas fractions over the measuring period of 10 s and over a number of ring-shaped domains. The latter is done by the following equation:

$$\bar{\varepsilon}_m = \frac{1}{k_{max}} \sum_k \sum_i \sum_j a_{i,j,m} \cdot \varepsilon_{i,j,k} \,, \qquad (9)$$

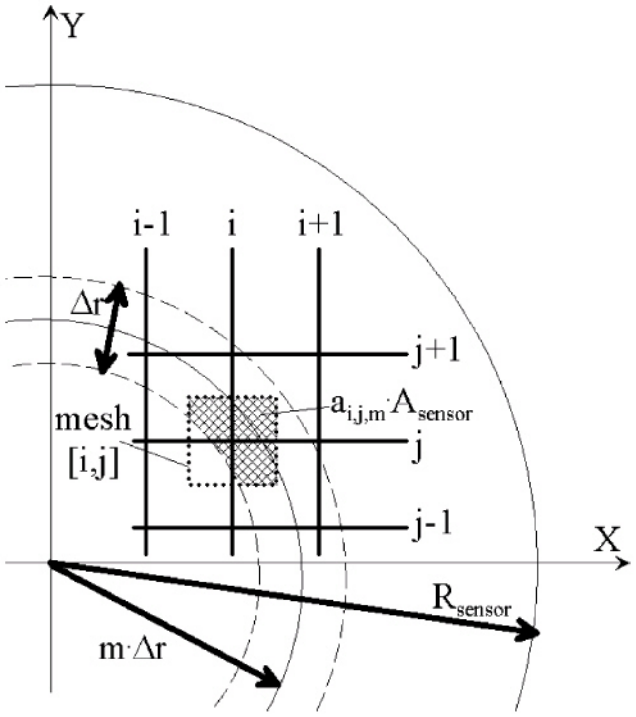

Fig. 4.13 Wight coefficients for the cross-section averaging of local gas fractions over a number of ring-shaped domains

where $a_{i,j,m}$ are weight coefficients denoting the contribution of each measuring point with the indexes i,j to a ring of the number m (see Fig. 4.13). This ring-shaped averaging domain covers a given radial distance from the centre of the sensor:

$$(m-1) \cdot \frac{R_{sensor}}{m_{max}} \le r \le m \cdot \frac{R_{sensor}}{m_{max}} \,, \qquad (10)$$

where m_{max} is the total number of radial steps (m_{max} = 20 for DN50, m_{max} = 80 for DN200).

Additionally, gas fraction profiles can be obtained for a limited range of the bubble-size. This requires a bubble identification and -size measurement, described in section 4.4.4. With the output of the bubble size measurement, the averaging of the void fraction can be performed selectively for certain bubble sizes (Prasser et al. 2002b).

4.4.3 Gas velocity profiles

The use of two wire-mesh sensors allows to measure gas velocity profiles. This was done by calculating cross-correlation functions for each couple of measuring points of sensor 1 and sensor 2 which are located above each other. For time-discrete series of the fluctuation component of the local instantaneous gas fractions from sensor 1 ($\varepsilon'_{1,i,j,k}$) and sensor 2 ($\varepsilon'_{2,i,j,k}$) the cross-correlation can be defined as follows:

$$F_{i,j,\Delta k} = \frac{\sum_k \varepsilon'_{1,i,j,k} \cdot \varepsilon'_{2,i,j,k+\Delta k}}{\sqrt{\sum_k \varepsilon'^2_{1,i,j,k}} \cdot \sqrt{\sum_k \varepsilon'^2_{2,i,j,k}}} \tag{11}$$

The index Δk corresponds to a time-shift of $\Delta t = \Delta k / f_{meas}$. Fluctuation components were calculated by subtracting the time-average from the instantaneous value: $\varepsilon'_{i,j,k} = \varepsilon_{i,j,k} - \overline{\varepsilon}_{i,j}$. The cross-correlation was carried out by means of Fast Fourier Transformation (FFT). The obtained cross-correlation functions were averaged in circumferential direction for different radii using the same weight coefficients allied for the calculation of radial gas fraction profiles:

$$F_{m,\Delta k} = \frac{1}{k_{max}} \sum_i \sum_j a_{i,j,m} \cdot F_{i,j,\Delta k} \tag{12}$$

In the next step the location of the maximum in the cross-correlation functions averaged by eq. (12) was found. The average gas phase velocity for the given radius is calculated from the corresponding time shift:

$$v_{air,m} = \frac{\Delta L}{\Delta k_{max}} \cdot f_{meas} \quad with \quad F_{m,\Delta k_{max}} = \max\left(F_{m,\Delta k}\right) \tag{13}$$

Here, ΔL is the axial distance between the two mesh sensors. The technique of averaging the cross-correlation functions before searching for the maximum has proven to supply more stable velocity values, than the velocities directly deduced from the result of a point-to-point cross-correlation according to eq. (11), which suffers from a high scattering of the results.

Due to constructional constraints, the measuring grids of both sensors used in the air/water experiments at the large pipe (DN200) are not coherent, i.e. the sensor matrix of the upper sensor is rotated by an angle of 60 deg compared to the matrix of lower one. For this, a direct calculation of cross-correlation functions between identical measuring positions in both sensors is not possible. Therefore, it is necessary to numerically rotate and flip the instantaneous gas fraction distribution of the second sensor to bring the indices i and j to a match. This is done by a coordinate transformation considering the necessary rotation. The coordinates of a measuring position in the second sensor plane in general do not fall exactly on positions of those in the first sensor plane in case of a rotation by 60 deg. Signals of four closest points of the rotated matrix of sensor 2 are interpolated to obtain the signal at the position within the first sensor.

4.4.4 Bubble size distributions

Bubble size distributions are extracted from the measuring data using the algorithm of Prasser et al. (2001). It starts from an identification of bubbles. A bubble is defined as a region of connected gas-containing elements in gas fraction data $\varepsilon_{i,j,k}$ that is completely surrounded by elements containing the liquid phase. Each element of

such a region obtains a common number that is unique for the detected bubble. These numbers are stored in the elements $b_{i,j,k}$ of a second array. This array has the same dimensions as the gas fraction array. After the bubble recognition algorithm is completed, each element $b_{i,j,k}$ carries the number of the bubble to which the given element with the indexes i,j,k belongs.

Local instantaneous gas fractions adopt intermediate values between 100 % (gas) and 0 % (liquid), when the corresponding control volume formed by two crossing wires contains both gas and liquid in the same time. Furthermore, signal noise may also lead to such intermediate values. Consequently, a sharp definition for elements filled with gas cannot be given and the introduction of a threshold is inevitable. The choice of the threshold influences the result of the bubble identification. A low threshold leads to unrealistic unification of bubbles since the fill procedure can jump from one bubble to another through elements that are shared by neighbouring bubbles. On the other hand, a high threshold may lead to the division of a bubble into unrealistic fragments, when the fill algorithm stops in elements where the gas fraction is decreased due to the signal noise. It was found that a combination of a recursive fill algorithm with a subsequent agglomeration of peripheral elements insures the best results (Prasser et al. 2001).

The fill procedure is started at a local maximum of the gas fraction and stops when the local gas fraction falls below the threshold. Best results were obtained by defining the threshold for the termination of the fill process for each bubble individually. This is done by subtracting a fixed value called “differential threshold” from the value of the gas fraction in the start element. Each start of the recursive fill procedure creates a new bubble. When no more start elements are found the agglomeration part of the algorithm is started. In this stage new bubbles are not added. The agglomeration aims at the consideration of elements at the periphery of bubbles, the gas fraction in which is less than the threshold. These elements get the same number that was already assigned to the bubble to which they are being linked, i.e. the areas in the array of $b_{i,j,k}$ marked with the same bubble number is extended towards the real boundary of the bubble.

After the bubble identification, the volume of the bubble with the number n is obtained by integrating the local gas fraction over elements owning the given bubble number:

$$V_{bub,n} = \Delta x \Delta y \Delta t \cdot w_{bub} \sum_{i,j,k} \varepsilon_{i,j,k} \qquad \forall [i,j,k] : b_{i,j,k} = n \tag{14}$$

The sum of gas fractions is multiplied by the extension of the control volume, which is the product of the lateral electrode pitch in x and y directions and the sampling period multiplied by the bubble velocity. In case of the sensors used in the present study, the control volume is defined by the pitch of the electrode wires being 3 mm in both directions and the sampling frequency of 2500 Hz:

$$\Delta x = \Delta y = 3 \text{ mm and } \Delta t = \frac{1}{f_{sample}} \tag{15}$$

Since the individual velocities of bubbles are not known, the gas phase velocity obtained by cross-correlation at the location of the centre of mass of the given bubble is taken as an approximation.

$$w_{bub} = w_G(r) \text{ with } r_n = \sqrt{(x_{CM,n} - x_0)^2 + (y_{CM,n} - y_0)^2} \tag{16}$$

The equivalent diameter of the bubble is defined as the diameter of a sphere that has the volume calculated according to eq. (14):

$$D_{bub,n} = \sqrt[3]{\frac{6V_{bub,n}}{\pi}} \tag{17}$$

The coordinates of the centre of mass can be obtained by averaging the coordinates of all grid elements belonging to the selected bubble using the local gas fraction values as a weight function:

$$x_{CM,n} = \frac{\sum_{i,j,k} i \cdot \Delta x \cdot \varepsilon_{i,j,k}}{\sum_{i,j,k} \varepsilon_{i,j,k}}; \quad y_{CM,n} = \frac{\sum_{i,j,k} j \cdot \Delta y \cdot \varepsilon_{i,j,k}}{\sum_{i,j,k} \varepsilon_{i,j,k}}; \quad \forall [i,j,k] : b_{i,j,k} = n \tag{18}$$

Information on the distortion of the bubble can be obtained by calculating the equivalent diameter in the x-y plane. For this matter, the area occupied by the bubble in the x-y plane is calculated by multiplying the sum of the local instantaneous gas fractions for the elements of the bubble by the area of the control volume in the x-y plane. The procedure is done for each single sampling time characterised by index k:

$$A_{xy,n,k} = \Delta x \Delta y \sum_{i,j} \varepsilon_{i,j,k} \quad \forall [i,j,k] : b_{i,j,k} = n \tag{19}$$

Afterwards, the maximum area is found and converted into the diameter of an equivalent circle:

$$D_{xy,n} = \sqrt{\frac{4A_{xy,n,max}}{\pi}} \quad \text{where} \quad A_{xy,n,max} = \max\left(A_{xy,n,k}\right) \tag{20}$$

This method is applicable to characterise the bubble size even in case, if velocity information is not available (see Prasser et al. 2005a).

4.5 Discussion of uncertainty of wire-mesh sensor measurements

4.5.1 Previous work

The measuring errors of the wire-mesh sensors have to be discussed with respect to different aspects. Due to the complexity of the interaction between gas bubbles and the electrode grids, errors are difficult to assess. In this section, a summary of the results obtained until now on this subject is given.

4.5.2 Accuracy of local instantaneous gas fractions

The accuracy of the gas fractions was checked by comparing the wire-mesh data with gamma-transmission measurements and ultra-fast X-ray tomography. Gamma-transmission measurements need integration periods much longer than the time resolution of the sensor. Therefore only time-averaged gas fractions can be compared. Such studies were performed with a single beam gamma-densitometer (0.48 GBq Cs-137, beam diameter 5 mm, NaI scintillation crystal, measuring period 120 s) in an air/water flow in a pipe of 51.2 mm inner diameter (MTLoop). The superficial velocities were varied in the ranges of $0.0025 \leq J_{N,air} \leq 12.1$ m/s and $0.043 \leq J_{water} \leq 4$ m/s. In order to enable a comparison with the line average supplied by the gamma device, the sensor data was averaged along the pipe diameter. The gas fraction

varied from nearly 0 % to almost 100 %. The line averages measured by both methods correspond within absolute error bands of ±5 % gas fraction.

A second study of this kind was performed at the CIRCUS test facility of TU Delft, which is a model of a natural circulation boiling water reactor used for flashing investigations in the start-up phase of the reactor. The signals of a wire-mesh sensor located in the riser (D = 47 mm) of the facility were compared to the readings of two gamma-transmission set-ups placed 170 mm upstream and downstream of the sensor. Again, line averages were compared and a good agreement was found for transient void fractions during the observed flow instabilities (Manera et al., 2001). The results confirm the applicability of the sensors in a boiling flow at temperatures around 100 - 120 °C.

Extensive studies in an air/water flow in a vertical pipe of 42 mm inner diameter were performed using the ultra-fast X-ray tomograph of AIST Tsukuba, Japan (Misawa et al., 2003). The tests were performed with two different gas injection modes: (A) 4 orifices of 5 mm diameter for creating large Taylor bubbles and (B) a sintered plate with a pore size of 100 µm for generating small bubbles. A wire-mesh sensor with 16x16 measuring points was placed 15 mm downstream of the measuring plane of the X-ray device, which consists in 18 pulsed X-ray tubes and a ring of 256 Cadmium Telluride (CdTe) detectors. The duration of a complete sampling cycle of the device is 3.8 ms, i.e. the framing rate is 263 Hz. Since the wire-mesh sensor allows higher sampling frequencies, it was operated at 1052 Hz, i.e. each frame delivered by the X-ray tomograph corresponds to a series of four frames of the mesh sensor. A comparison with reconstructed tomographic data revealed that the mesh sensor tends to distort large Taylor bubbles at low liquid velocities. Gas plugs become waisted and obtain a mushroom-like shape. This effect vanishes at liquid velocities greater than 0.2 m/s and both measuring methods start to show Taylor bubbles of similar shapes. The cross-section averaged void fractions show a satisfactory agreement for the slug flow. In case of the bubbly flow a strong underestimation by the X-ray tomography was observed, for the reason that small bubbles are not reconstructed properly by the X-ray tomography, since they travel through the measuring plane in less time than needed for a complete scan.

Later, a more detailed evaluation that involved the calculation of void fractions calculated directly from the radiation attenuation along the chords between X-ray tubes and detectors has shown a very good agreement between mesh sensor and the X-ray device (Prasser et al., 2005b). In the bubble flow regime the deviation of the absolute cross-section averaged gas fractions is less than 1 %. In case of the large Taylor bubbles a systematic underestimation of the gas fraction of up-to 4 % (absolute) was observed. It was therefore concluded that the earlier found big deviations (Misawa et. al., 2003) are caused by the applied image reconstruction technique used for the X-ray tomography that deserves future improvements.

4.5.3 Shape of the gas/liquid interface, feed-back of the sensor to the flow

A transparent channel with a square cross section (50 x 50 mm) was used to visually observe the interaction of gas bubbles with a wire-mesh sensor (Prasser et al., 2001). Electrode wires were directly fixed in small drillings in the acrylic glass walls of the channel and the interaction of bubbles with the wire-meshes was observed using a high speed video camera at 1000 frames per second. It was found that bubbles are broken up when they come in contact with the wires. Nevertheless it was demonstrated that the sensor signal still represents the correct shape of the undisturbed

bubbles with the accuracy given by the lateral pitch of the wires. The main disturbance influencing the measuring signal are water films formed in the wake of the wires and running in flow direction from the first electrode plane to the perpendicular wires of the second plane. As long as these films exist, the electrical current does not drop down completely to zero even at crossing points that are completely enclosed by gas. It was concluded, that these films are the probable reason for the slight underestimation of the gas fraction inside Taylor bubbles reported for the comparison with the X-ray tomography (Prasser et al., 2005b).

4.5.4 Bubble size measurement

The high-speed video sequences obtained at the transparent test channel mentioned above were used to assess the volume of individual bubbles during their passage through the sensor plane. Since the bubbles were observed only from one side, a rotational symmetry in the cross section plane was assumed. The calculated equivalent bubble diameters were compared to the bubble sizes measured by the wire-mesh sensor. The size of the generated bubbles was varied by using different capillaries for the air injection. Liquid velocities ranged from 0 to 0.8 m/s. Individual bubble diameters measured by the two methods correspond within bands of $\pm$20 %. At liquid velocities below 0.2 m/s some points the mesh sensor produces an overestimation of up-to 50 %. In general, the scattering of the diameters obtained by the image processing for bubbles generated under constant conditions is significantly higher than for the wire-mesh sensor. Studies with a more accurate reference method are underway.

The comparison of bubble size distributions obtained by two wire-mesh sensors put on a distance of 34 mm behind each other in a vertical pipe of 51.2 mm inner diameter has shown the effect of the bubble break-down caused by the first sensor to the signal of the second one (Prasser et al., 2001). In general, a decrease in the bubble sizes is observed (e.g. at J_{water} = 0.26 m/s and J_{air} = 0.052 m/s the peak of the small bubble fraction is shifted from 5.5 mm to approximately 4.7 mm), while the general shape of the distributions remains unchanged. With growing superficial water velocity the distorting effect becomes smaller.

The lowest detectable bubble size depends on the pitch of the electrode wires and the signal-to-noise ratio. The drop of the electrical current during a bubble passage depends on the bubble size and on the position of the centre of the bubble relative to the crossing point of the wires. The bubble produces the highest signal amplitude, when it hits the crossing point (e.g. in this case a 3 mm bubble shows a maximum local instantaneous gas fraction of about 70 %), the lowest signal when it passes through a mesh (here the same bubble of 3 mm shows a maximum gas fraction of less then 20 %). Assuming 5 % electrical noise and an electrode pitch of 3 mm, bubbles of about 1.7 mm diameter can still be recognized with a probability of 100 % (Scholz & Zippe, 2000).

4.5.5 Accuracy checks on basis of the signals available from the two wire-mesh sensors

4.5.5.1 Accuracy of gas fraction and gas velocity measurement

The fact that both gas fraction and gas velocity profiles are available allows calculating a value for the superficial gas velocity by averaging the product of gas fraction and velocity over the measuring cross section:

$$J_{air,meas} = \frac{1}{A_{pipe}} \cdot \int_0^R \varepsilon(r) \cdot v_{air}(r) \cdot 2\pi r \cdot dr = < \varepsilon \cdot v_{air} > \quad (21)$$

The results are compared to the superficial velocities known from the injected gas flow rate (Fig. 4.14). In both small and large pipes the agreement is good. There is a growing tendency to underestimate the superficial velocity with growing air flow rate. The average relative deviation is about 7 %. At the highest superficial air velocity of 1.16 m/s it reaches nearly 18 %. This is a rather good result, since we have to keep in mind that the first wire-mesh sensor leads to a significant bubble break-up, and, consequently, the cross-correlation method delivers velocities that are characteristic for the flow structure with a disturbed bubble-size distribution.

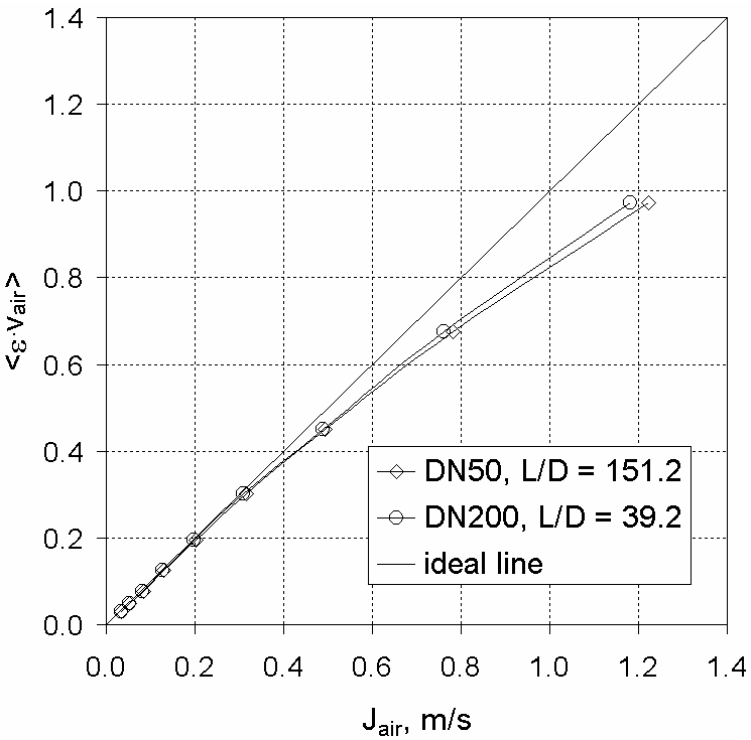

Fig. 4.14 Comparison between the superficial gas velocities calculated from the injected gas flow rate and the one reconstructed from radial gas fraction and gas velocity profiles

4.5.5.2 Bubble fragmentation caused by the wire-mesh sensor

The mentioned influence of the wire-mesh sensor on the flow structure can be studied by comparing bubble-size distributions calculated on basis of signals from both first and second sensor. Since it was found that bubble-size distributions supplied by wire-mesh sensors reflect the state upstream of the given sensor position (Prasser et al., 2005b), the second sensor shows the flow structure change caused by the first one. The result is shown in Fig. 4.15 for selected experimental points. At lower superficial gas velocities a significant bubble fragmentation caused by the first sensor leads to a shift of the peak of the bubble size distribution towards smaller equivalent diameters. With growing superficial gas velocity (see example at $J_{R,air}$ = 0.48 m/s) the distributions measured by the two sensors converge. Again, it has to be remarked that the earlier performed high-speed camera observations have shown that the first sensor still delivers bubble size distributions that reflect the undisturbed flow.

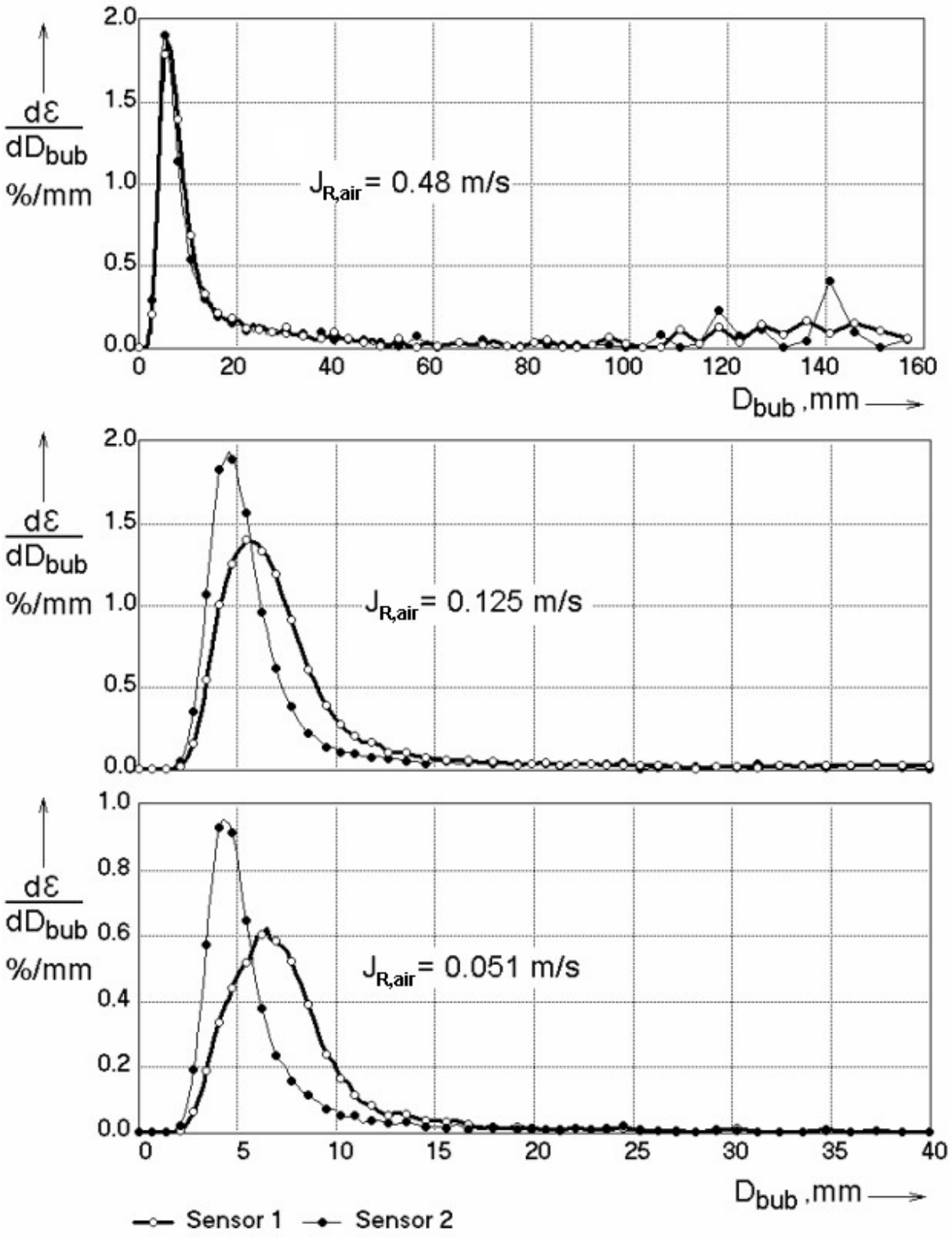

Fig. 4.15 Fragmentation of bubbles by the first wire-mesh sensor reflected in the signal of the second one, superficial velocity: J_{water} = 1.015 m/s

4.5.6 Choice of the differential threshold for the bubble-size measurement

Fig. 4.16 shows the result of a sensibility study to clarify the influence of the differential threshold used in the bubble identification algorithm. As result of this analysis, a value of 10 % was chosen as an optimum for the differential threshold.

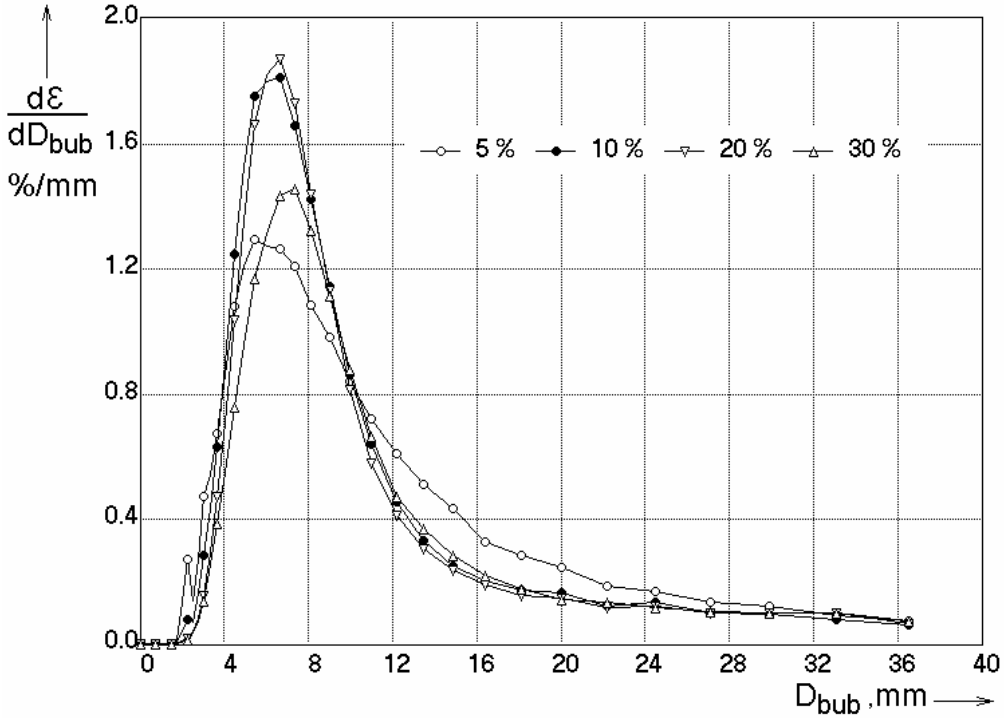

Fig. 4.16 Sensibility of bubble size distributions (small bubble peak region) to changes of the differential threshold (parameter) for the bubble recognition algorithm, superficial velocities: $J_{R,air}$ = 0.48 m/s and J_{water} = 1.015 m/s

This means that the recursive fill process for the bubble detection, which starts at an element of the measured distribution of local instantaneous gas fractions $\varepsilon_{i,j,k}$ where a local maximum is found, is continued as long as the adjoined elements have a gas fraction that is not more then 10 % below the value of the maximum in the starting point. Using this value for the differential threshold, the small bubble peak is obtained with the biggest possible resolution, i.e. the peak becomes wider and less pronounced either when the threshold is increased and when it is decreased. This finding is illustrated in Fig. 4.16 on the example of $J_{R,air}$ = 0.48 m/s, but similar behaviour was found also for other superficial velocities. The threshold of 10 % was therefore chosen to be used for the calculation of all bubble size distributions presented in the following chapters.

4.5.7 Conclusion on accuracy

Although there is still more work on accuracy assessment to be performed, it can be concluded, that the wire-mesh sensor reflects the correct shape of the gas/liquid interface. Despite of the effect, that the interface is distorted, the signal still represents the situation upstream of the sensor. Distortions may be especially large, when the liquid velocity is low. In air/water systems at room temperature a liquid velocity of about 0.2 m/s is sufficient to overcome the surface tension and viscosity dominated effects at the electrode wires and the distortions decrease. Gamma and X-ray transmission measurements have shown that gas fractions are measured with a good accuracy.

5. Characteristic void fraction, gas velocity and bubble size profiles

5.1 Appearance of a wall peak in the gas fraction profiles

Gas fraction profiles measured for different superficial gas velocities at a constant liquid flow rate are shown in Fig. 5.1. The profiles were obtained by averaging the wire-mesh data (comp. section 4.4.2) over the measuring period of 10 s and over the circumference at different radial positions. In case of gas injection through the orifices of 6 mm, all distributions show a central peak. This was found for the entire studied range of superficial velocities ($0.0025 \leq J_{N,G} \leq 4.98$ m/s, $0.102 \leq J_L \leq 1.61$ m/s; tests see appendix A1: LD01 and LD02). The profiles show some distortions close to the centre of the pipe, which are still reflecting the rather complicated geometry of the gas injection device. They are probably caused by the wake generated by the gas injection head.

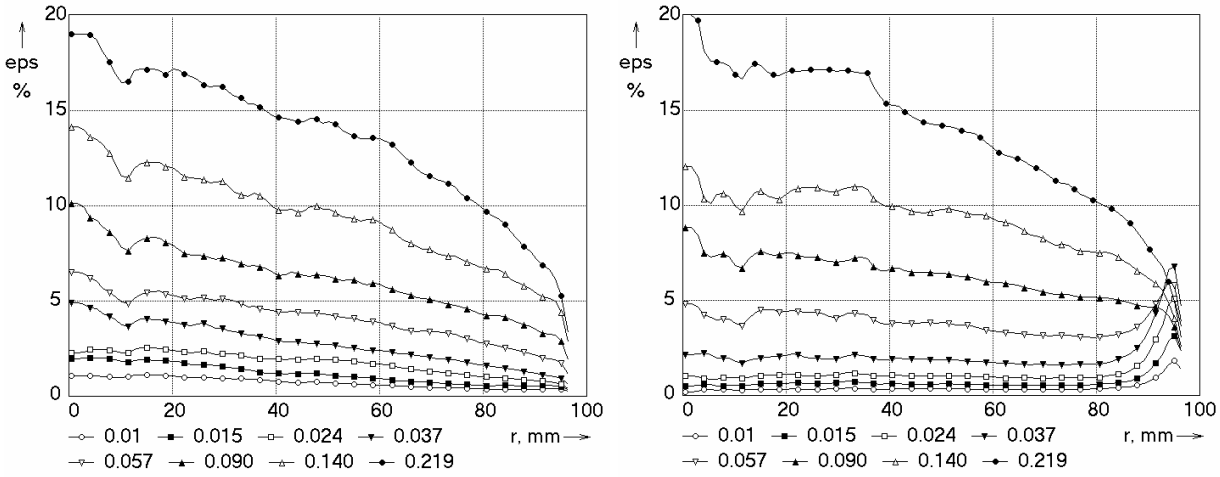

Injection geometry K (60 orifices, ∅ 6 mm) Injection geometry I (152 orifices, ∅ 0.8 mm)

Fig. 5.1 Radial gas fraction profiles in the 194.1 mm pipe, J_L = 1.02 m/s, varied parameter: $J_{N,G}$, m/s, L/D = 39.2

In the large pipe of 194.1 mm diameter a wall peak appeared only in tests with the gas injection geometry I (Fig. 5.1, right side). The wall peak vanishes when a certain superficial air velocity is exceeded. The measured bubble size distributions explain why the wall peak appears only with the small injection nozzles (Fig. 5.2). In case of the gas injection through the orifices on 0.8 mm diameter most of the gas fraction is still concentrated in the bubble size class with an equivalent diameter less than 5.5 - 5.8 mm, which is the characteristic diameter for the change of the sign of the lift force according to Tomiyama (1998). For bubbles smaller than this diameter, the lift force points towards the wall and is therefore responsible for the appearance of the wall peak.

As it can be seen from Fig. 5.2, the vanishing of the wall peak with growing superficial gas velocity corresponds with a shift of the peak in the bubble size distribution towards larger bubble diameters. In case of the gas injection head K, most of the bubbles are bigger than 5.5 - 5.8 mm, consequently a wall peak is not observed. As shown in Fig. 5.3, the wall peak disappears also with decreasing liquid velocity. This is mainly due to the fact that the liquid velocity gradient decreases with decreasing liquid flow rate. As a consequence the lift force decreases, since it is proportional to the local gradient of the liquid velocity. At a certain point, the lift force in

no more sufficient to create the wall peak. A second tendency is again connected with the bubble size. Since the gas fraction grows with decreasing superficial liquid velocity (at a constant air injection rate), the bubble size increases and more bubbles exceed the critical diameter for the lift force inverse.

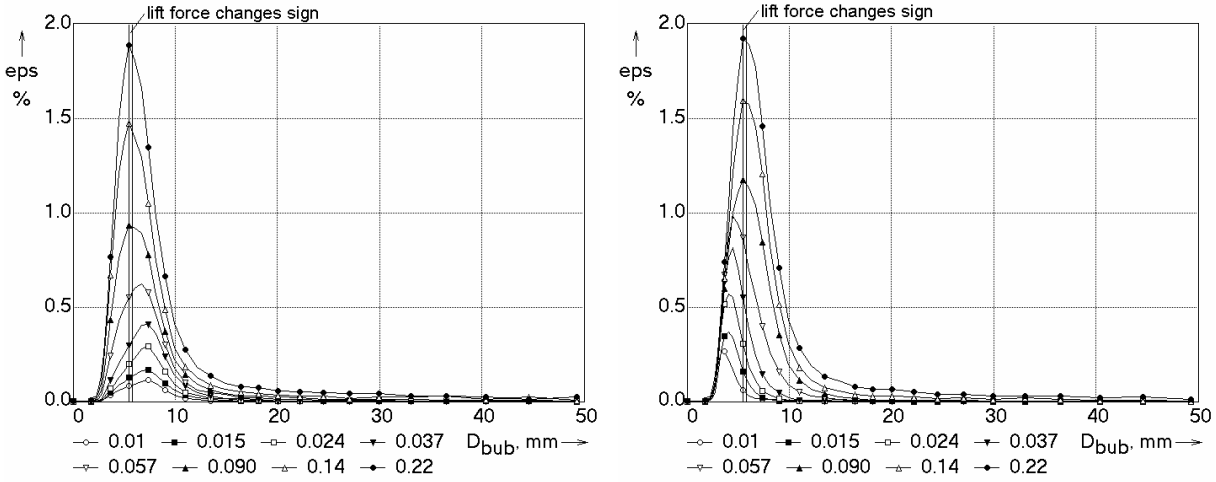

Injection geometry K (60 orifices, ∅ 6 mm) Injection geometry I (152 orifices, ∅ 0.8 mm)

Fig. 5.2 Bubble size distributions (part of gas fraction represented by a given bubble size class) in the 194.1 mm pipe, J_L = 1.02 m/s, varied parameter: $J_{N,G}$, m/s, L/D = 39.2

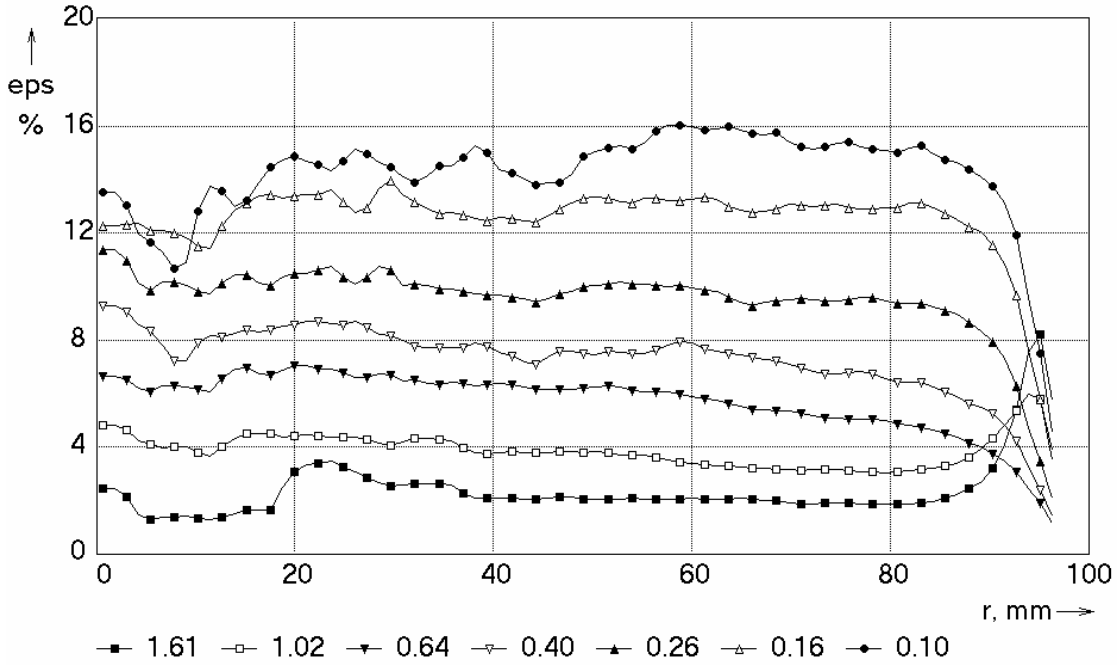

Fig. 5.3 Radial gas fraction profiles in the 194.1 mm pipe, $J_{N,G}$ = 0.057 m/s, varied parameter: J_L, m/s

The global situation is shown in Fig. 5.4, where the occurrence of the wall peak is mapped as a function of both gas and liquid superficial velocities. The wall peak is observed in a region that is bordered towards high superficial gas velocities and low superficial liquid velocities. This behaviour is well-known from studies of two-phase flow in small pipes. In earlier studies of our own (Prasser at al., 2003) performed in a pipe of 51.2 mm at the test facility MTLoop, we found a wall peak, too, when the air

was injected through 19 capillaries of 0.8 mm inner diameter (see also Fig. 5.4). However, the wall-peak region was significantly extended towards lower superficial liquid velocities. We believe that this is mainly explained by the fact that the liquid velocity gradient is greater in a small pipe compared to a large pipe with the same superficial liquid velocity.

J_{Water} m/s \ J_{Air} m/s	0.0025	0.0040	0.0062	0.0096	0.0151	0.0235	0.0368	0.0574	0.0898	0.140	0.219	0.342
1.611	9	20	31	42	53	64	75	86	97	108	119	130
1.017	8	19	30	41	52	63	74	85	96	107	118	129
0.641	7	18	29	40	51	62	73	84	95	106	117	128
0.405	6	17	28	39	50	61	72	83	94	105	116	127
0.255	5	16	27	38	49	60	71	82	93	104	115	126
0.161	4	15	26	37	48	59	70	81	92	103	114	125
0.102	3	14	25	36	47	58	69	80	91	102	113	124

wall peak in 51.2 and 194.1 mm pipe

wall peak in 51.2 mm pipe only

Numbers: Test points

Fig. 5.4 Flow map indicating the appearance of a wall peak in the radial gas fraction profiles for pipes of 51.2 mm and 194.1 mm diameter (gas injection orifices: ∅ 0.8 mm)

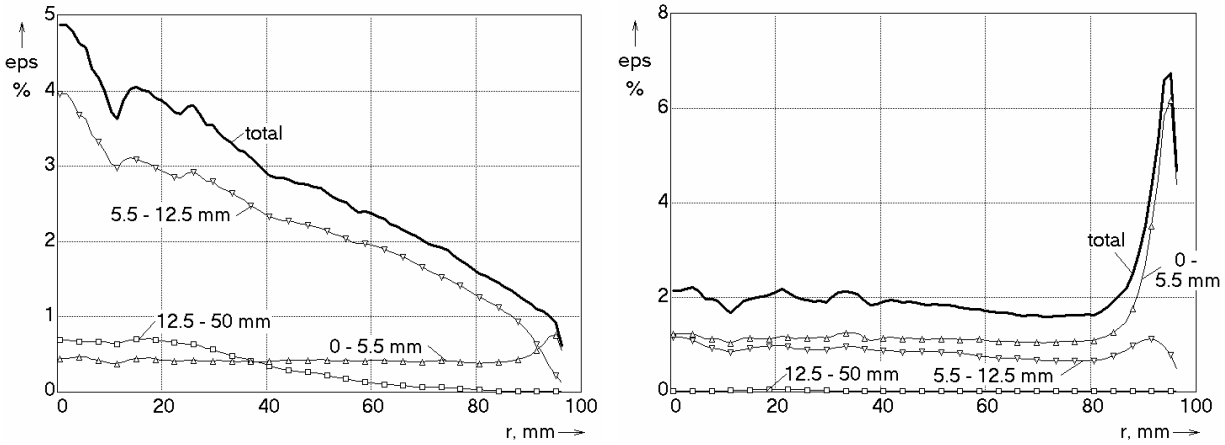

Injection geometry K (60 orifices, ∅ 6 mm) Injection geometry I (152 orifices, ∅ 0.8 mm)

Fig. 5.5 Radial gas fraction profiles decomposed according to bubble-size classes D_{pipe} = 194.1 mm, J_L = 1.02 m/s, $J_{N,G}$ = 0.037 m/s, L/D = 39.2, parameter: range of equivalent bubble diameters

The data recorded by the wire-mesh sensors allow obtaining gas fraction profiles, which are decomposed according to bubble-size classes (Prasser et al., 2002b). In Fig. 5.5 the result of such an analysis is given for a test point which is characterized by a wall peak when the injection head I was used (see Fig. 5.1). It is clearly visible that the wall peak is caused by the bubbles of an equivalent diameter below 5.5 mm (Fig. 5.5, right side). Bubbles bigger than 12.5 mm were hardly found in this test. At the same superficial velocities, injection head K produces a central gas fraction peak. Nevertheless, bubbles of an equivalent diameter of less than 5.5 mm still form a wall

peak (Fig. 5.5, left side). Even in case of a higher superficial gas velocity at which a wall peak was not observed with injection head I, the bubble-size class D_{bub} < 5.5 mm has a pronounced peak close to the pipe wall (Fig. 5.6).

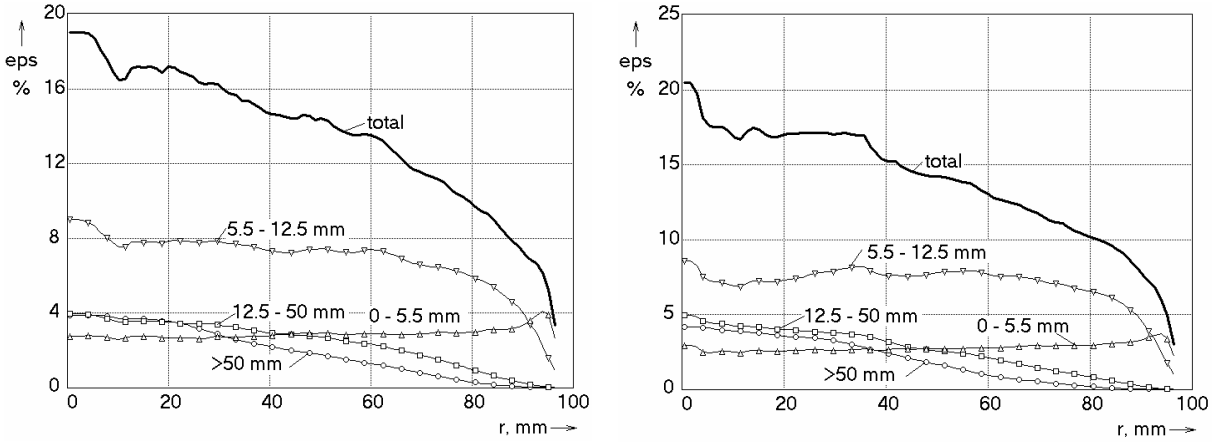

Injection geometry K (60 orifices, ∅ 6 mm) Injection geometry I (152 orifices, ∅ 0.8 mm)

Fig. 5.6 Radial gas fraction profiles decomposed according to bubble-size classes D_{pipe} = 194.1 mm, J_L = 1.02 m/s, $J_{N,G}$ = 0.22 m/s, L/D = 39.2, parameter: range of equivalent bubble diameters

5.2 Convergence of the flow structure at high superficial gas velocities

At higher superficial gas velocities, the flow structure at the measuring position (L/D = 39.2) becomes independent from the kind of the gas injection. This is illustrated in Fig. 5.7, where radial gas fraction profiles and bubble size distributions are presented for a superficial liquid velocity of 1.02 m/s. Differences in the radial profiles and the bubble size distribution caused by a change of the gas injection head vanish starting from a superficial gas velocity ($J_{N,G}$) of about 0.2 m/s. With growing gas flow rate the flow structure becomes more and more independent from the primary bubble size. This is due to the increasing effect of turbulence.

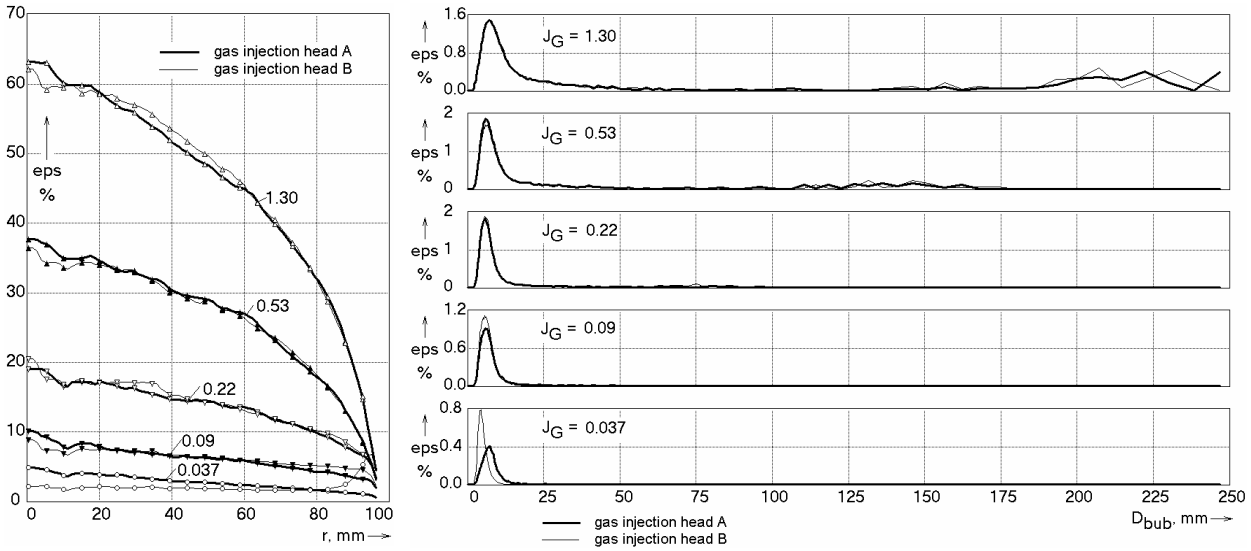

a) Radial gas fraction profiles b) Bubble size distributions

Fig. 5.7 Radial gas fraction profiles and bubble size distributions at higher superficial gas velocities in the 194.1 mm pipe, J_L = 1.02 m/s, varied parameter: $J_{N,G}$, m/s, L/D = 39.2

6. Scale dependence of the flow pattern

6.1 Motivation of the study

Transitions of flow pattern and phase distribution in an upwards gas/liquid flow are subject of numerous papers, the majority of which deals with results obtained in pipes of small diameter (e.g. Hibiki & Ishii, 1999, Kim et al., 2000, Sengpiel 1999). Classical flow maps describe a transition from bubbly to slug, churn-turbulent and, finally, annular flow, when the superficial gas velocity is increased at constant moderate superficial liquid velocities. At higher liquid velocities, most of the authors predict a finely dispersed bubbly flow.

Many researchers, who dealt with drift correlations, found that the average void fraction in a vertical pipe decreases with growing pipe diameter and that this decrease stops at certain diameter, which is correlated with the Bond number. This was the first hint about the presence of scaling effects connected with the pipe diameter. The mentioned effect is reflected in some of the existing drift-flux correlations, which introduce a critical Bond number to distinguish regions with and without an influence of the pipe diameter (Kataoka & Ishii, 1987, Sonnenburg, 1994). As a result of scaling studies, Ohnuki & Akimoto (2000) reported that slug flow, which is established in small pipes, is not found in larger pipes. The authors performed tests in pipes of 200 mm and 480 mm diameter and compared their results with those of Leung et al. (1995) performed at D = 25.4 mm, Liu & Bankoff (1993) at D = 38 mm as well as with the flow maps of Serizawa and Kataoka (Serizawa & Kataoka, 1988). In the large pipes an immediate transition from bubbly to a kind of churn-turbulent flow was found instead of a slug flow. Typical Taylor bubbles that occupy almost the entire cross section occur only in small pipelines. It is assumed that the confining action of the pipe walls stabilize the Taylor bubbles in the small pipes.

6.2 Methodology

Flow patterns studies were performed on basis of the measuring data obtained during air/water tests in the vertical test sections DN50 and DN200, the latter in the configuration with the gas injection through the sparger head at the bottom. In the large pipe, the relative inlet length was kept constant at L/D = 39.2. This is the maximum that can be achieved at TOPFLOW. For the comparison with the small diameter, two inlet lengths were chosen: L/D = 30.6 and L/D = 151.2. In the latter case, the absolute length of the test section DN50 was nearly equal to the inlet length used at the large pipe. This granted the possibility to check whether the relative inlet length or the absolute length is the determining factor for the establishing of the flow pattern.

Two wire-mesh sensors with a matrix of 64x64 measuring points each were applied. Each of these devices delivers 2500 instantaneous gas fraction distributions (frames) per second. A cross-correlation of the data of the first and the second sensor allowed obtaining gas velocity profiles. Using the available bubble recognition techniques bubble size distributions are derived. In this way new insight was brought into the structure of the two-phase flow in large pipes.

6.3 Qualitative analysis of flow patterns

The plots (Fig. 6.1) obtained with the method of virtual side projections (comp. section 4.4.1) seem to confirm the findings of Ohnuki & Akimoto, 2000. Large bubbles appearing in the flow, the magnitude of which grows rapidly with increasing superficial gas velocity, are surrounded by a bubble flow that takes a more and more irregular structure, bubble density becomes very inhomogeneous. At high gas flows, the flow pattern seems to become churn turbulent, i.e. regular structures seem to disappear completely. Finally, large bubbles are hardly visible anymore since the view is obstructed by the irregular swarms of small bubbles. This gives reason to the conclusion that a transition to churn-turbulent flow has taken place.

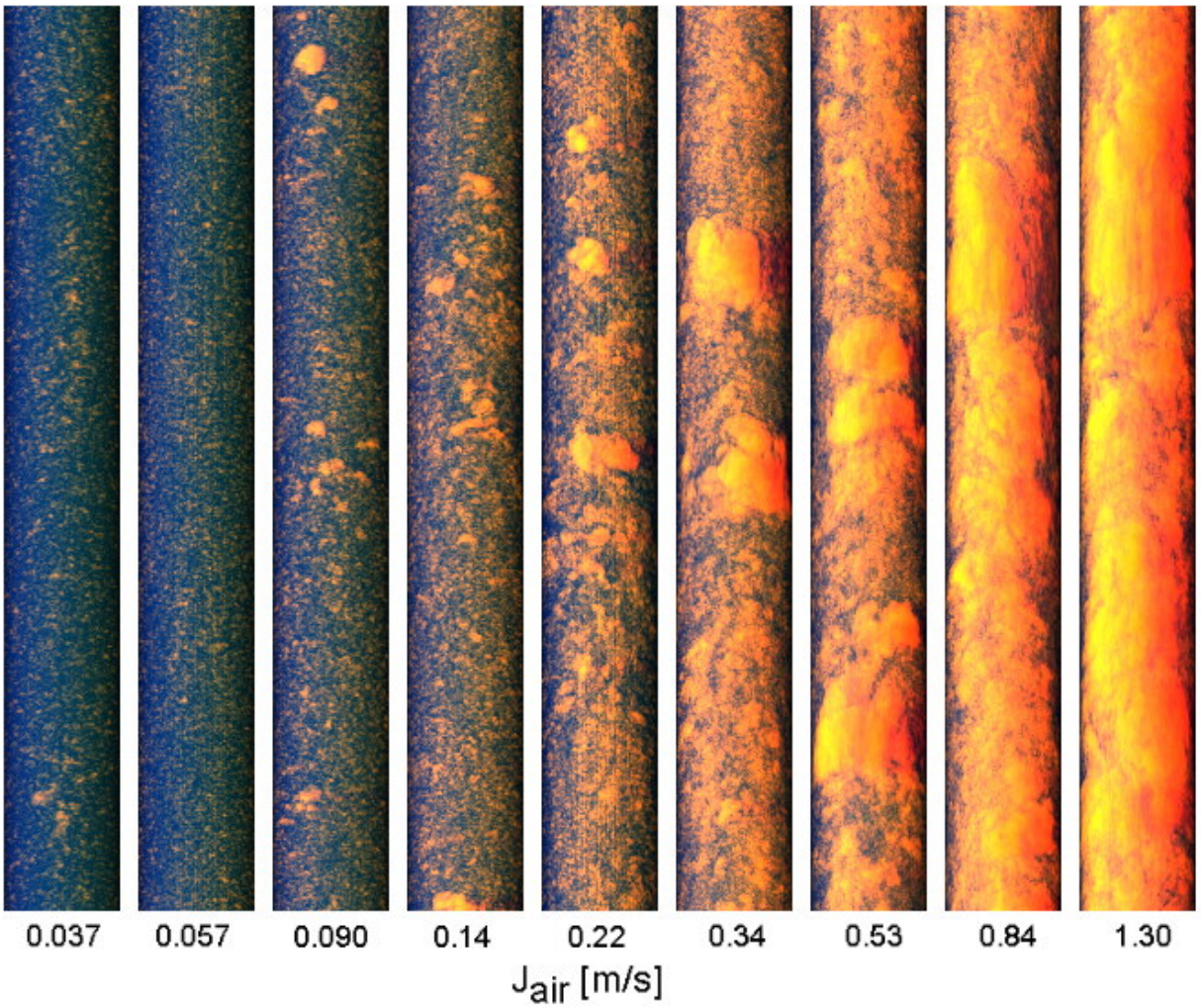

Fig. 6.1 Virtual side projections of the void (colour from red to yellow) distribution in the DN200 test section, J_{water} = 1 m/s, $J_{air} = J_{N,air}$; relation vertical to horizontal scale = 1:1, height scaled according to average gas phase velocity

Virtual sectional side views have the advantage, that they present the flow structure in the mid-plane of the pipe without the view obstruction by bubbles in the region close to the pipe wall. Such plots reveal that large bubbles are still present, their size and the number increases (Fig. 6.2) with growing gas flow. At the same time the observed flow structure is quite different from what is found in the small pipe (Fig. 6.3). Here, it is visible that the bubbly flow transits to slug flow with the characteristic Taylor bubbles referred to in many publications when the gas flow rate is increased.

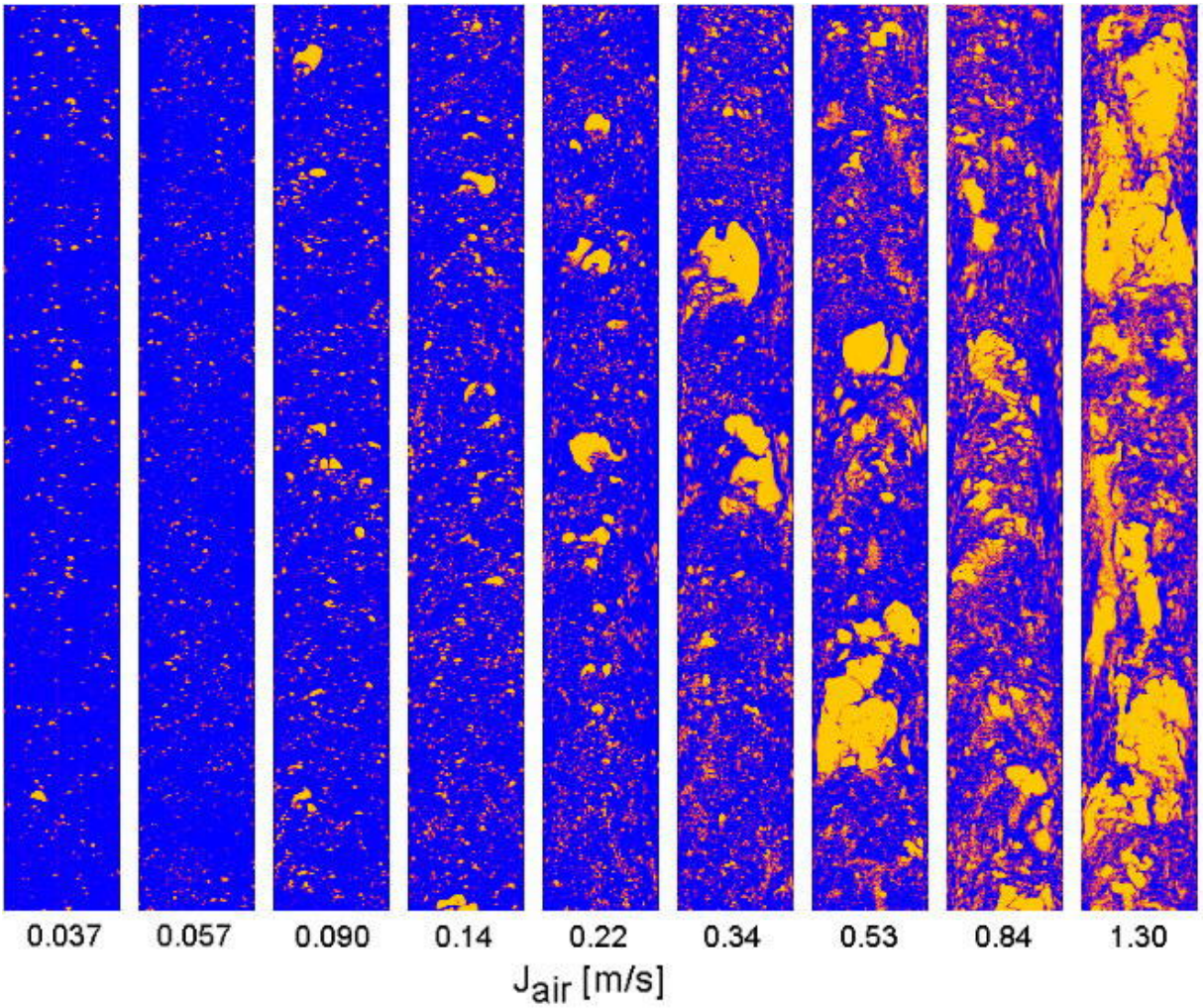

Fig. 6.2 Virtual sectional views of the void distribution in the DN200 test section, J_{water} = 1 m/s, $J_{air} = J_{N,air}$; relation vertical to horizontal scale = 1:1, height scaled according to average gas phase velocity (colours: air = yellow, water = blue)

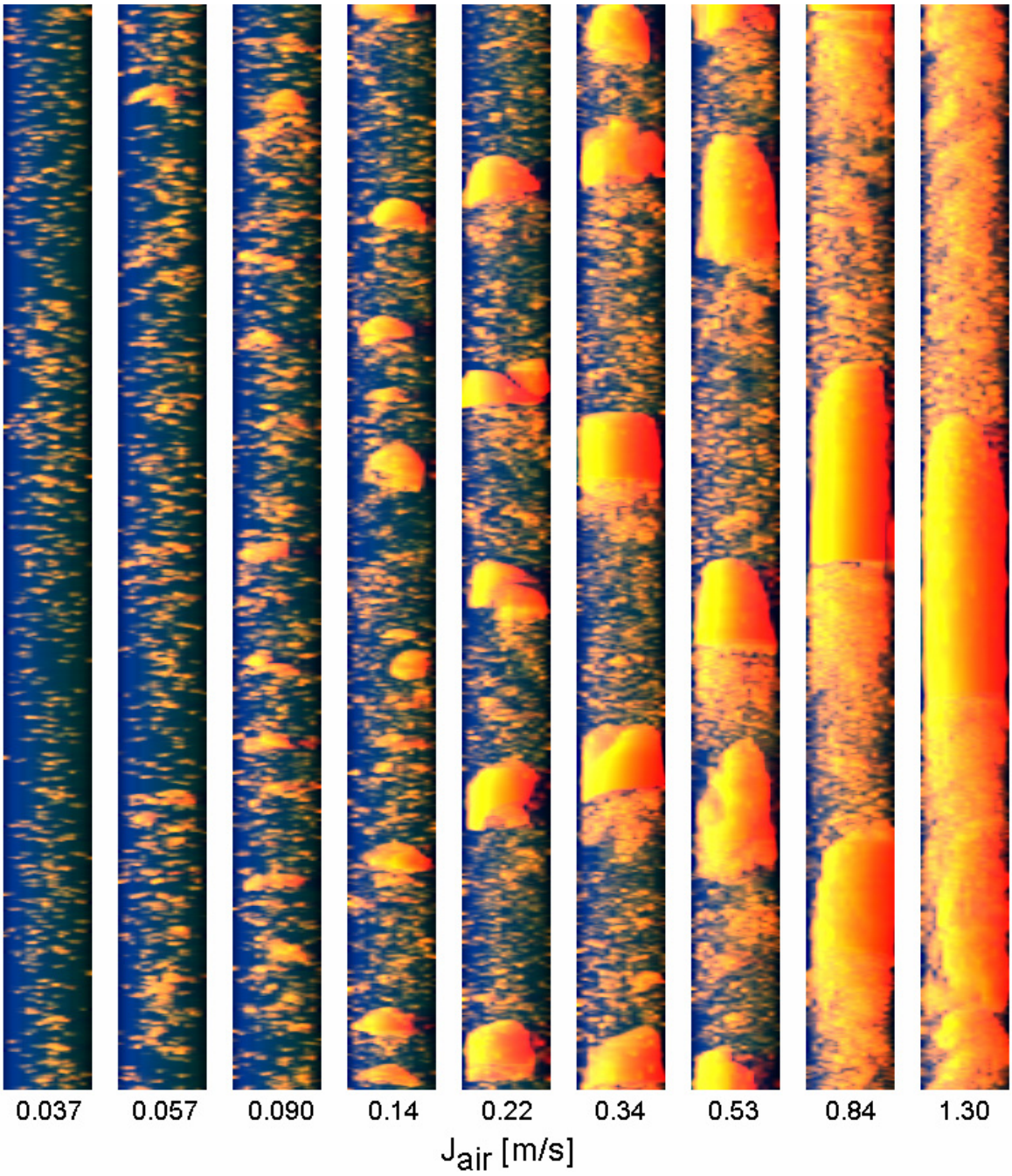

Fig. 6.3 Virtual side projections of the void distribution in the DN50 test section, J_{water} = 1 m/s, J_{air} = $J_{N,air}$; relation vertical to horizontal scale = 1:1, height scaled according to average gas phase velocity

6.4 Scale dependence of radial gas fraction and velocity profiles

Quantitative insides are granted by the radial profiles of the gas fraction and the gas phase velocity (Fig. 6.4 - Fig. 6.7). In all these figures the results obtained in the large pipe (DN200) are compared with the measurements carried in the small pipe at two different inlet lengths (1600 and 7910 mm; see Tab. 2.1). All radial gas fraction profiles (Fig. 6.4 and Fig. 6.5) are characterized by a central peak of the void fraction, which is explained by the large primary bubbles generated by the comparatively large injection nozzles of the applied gas distributors. The presented tests can therefore not contribute to the wall-to-central peak transition problem (Tomiyama, 1998, Lucas et al., 2001).

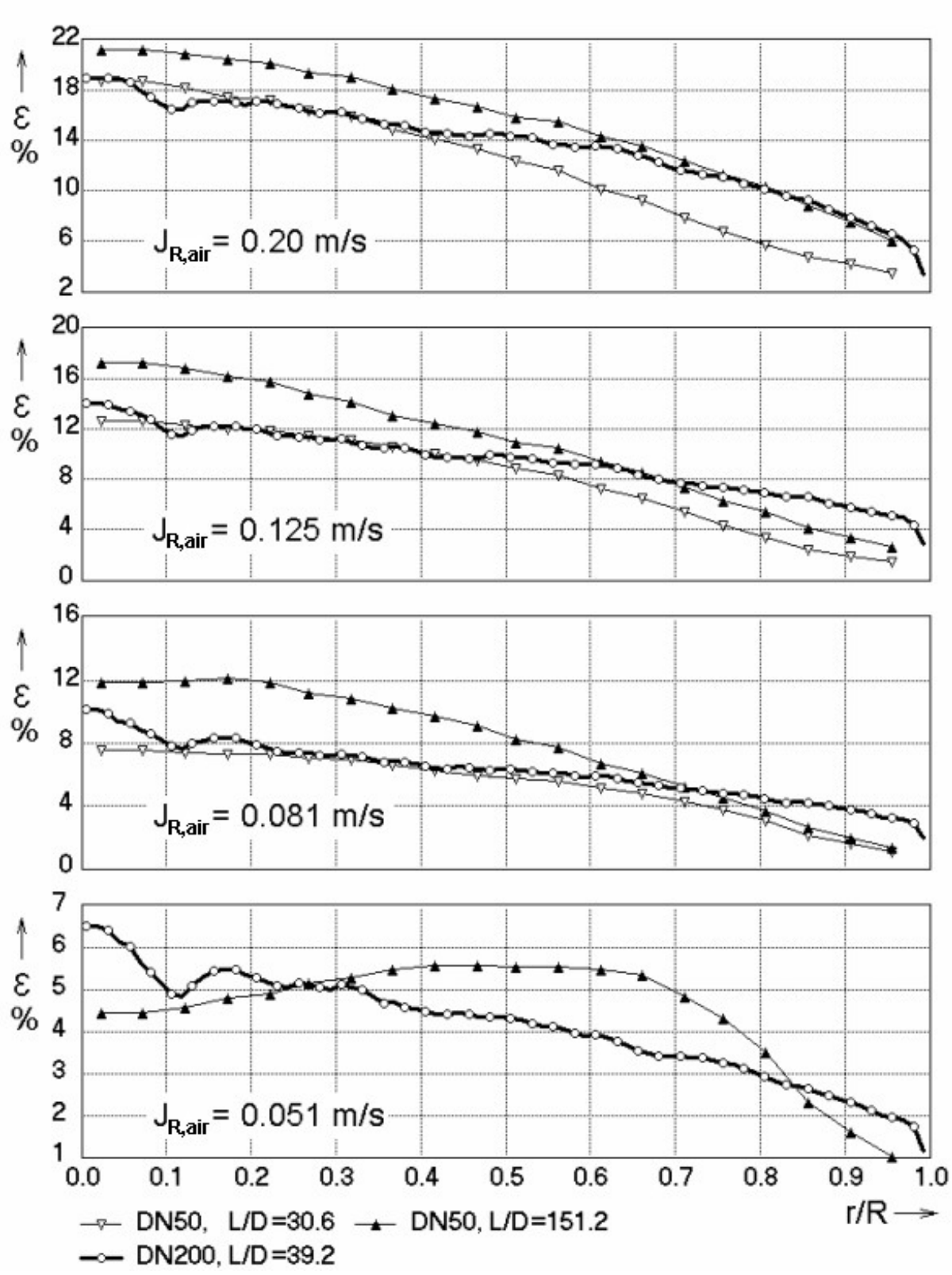

Fig. 6.4 Gas fraction profiles in the test sections DN50 and DN200
J_{water} = 1.015 m/s, $J_{R,air} \leq 0.2$ m/s

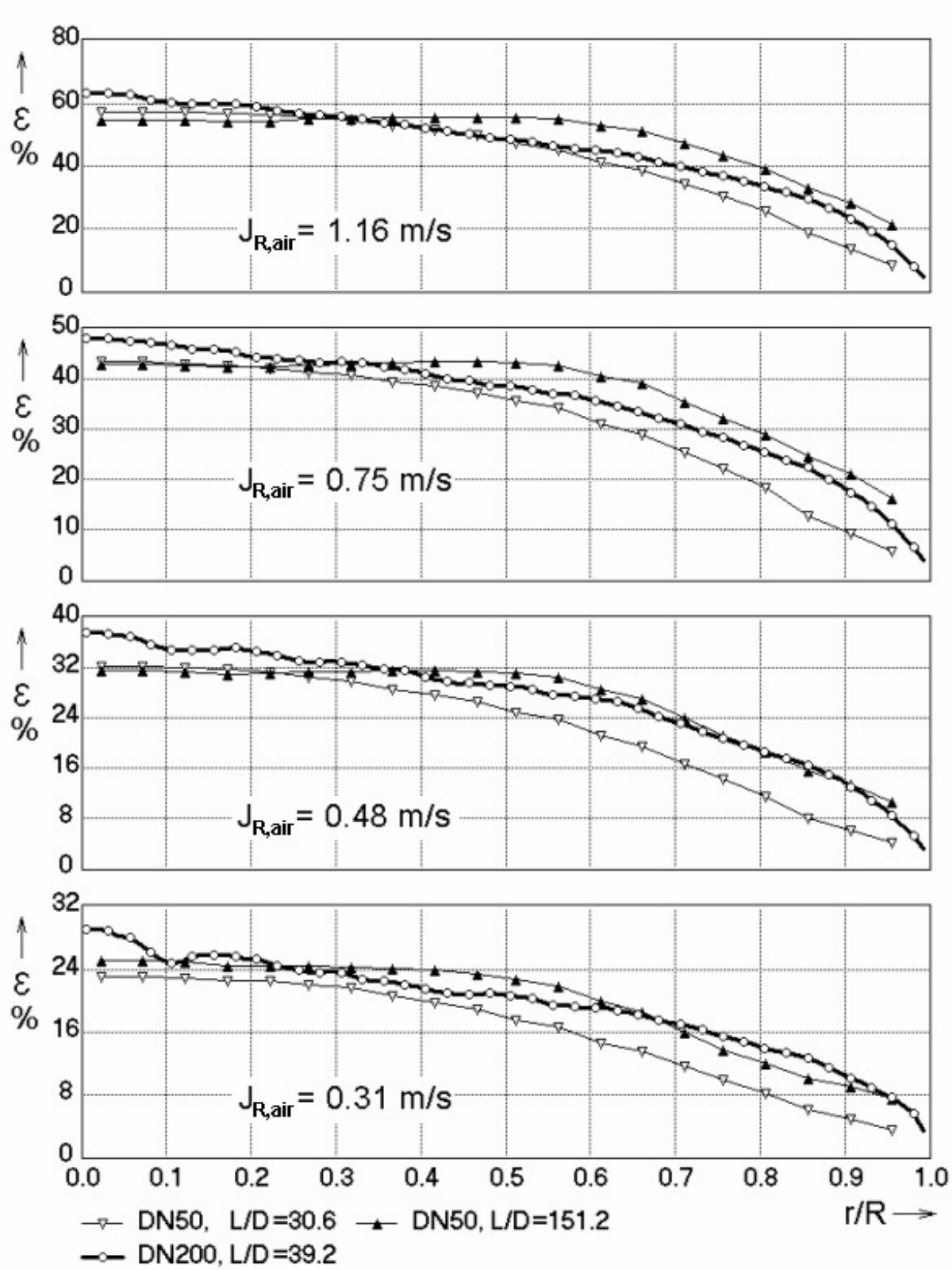

Fig. 6.5 Gas fraction profiles in the test sections DN50 and DN200
J_{water} = 1.015 m/s, $J_{R,air}$ > 0.2 m/s

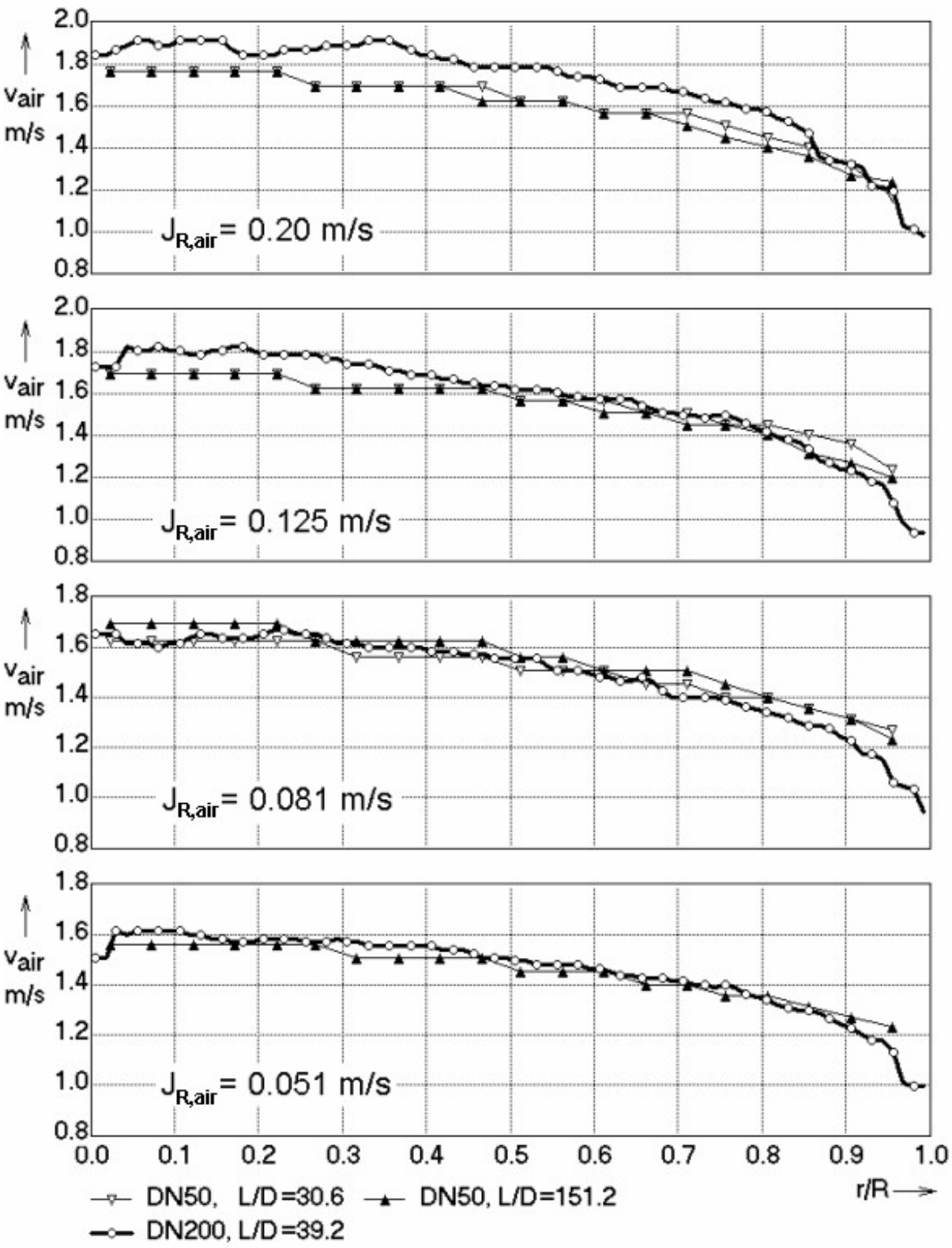

Fig. 6.6 Gas velocity profiles in the test sections DN50 and DN200
J_{water} = 1.015 m/s, $J_{R,air} \leq 0.2$ m/s

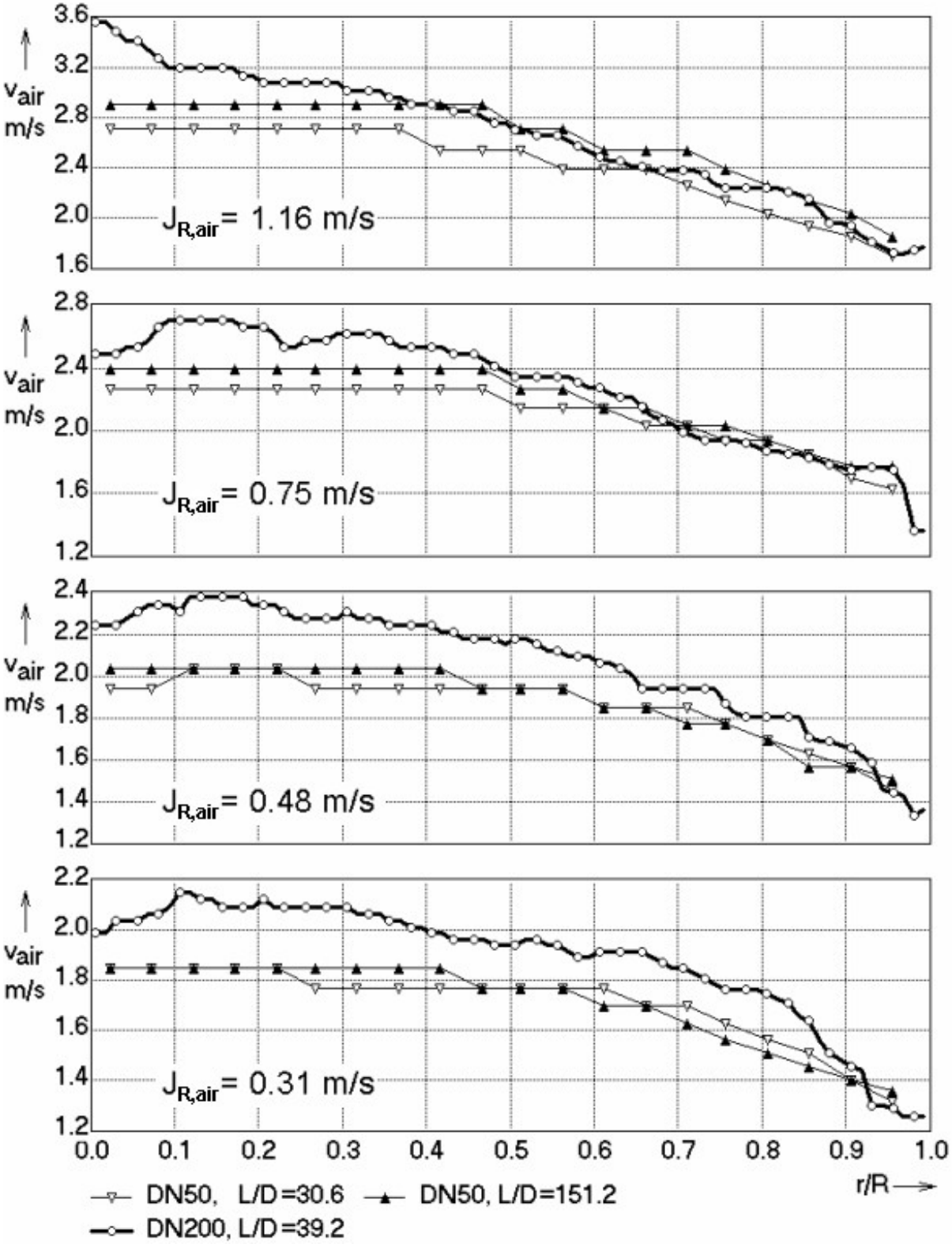

Fig. 6.7 Gas velocity profiles in the test sections DN50 and DN200
J_{water} = 1.015 m/s, $J_{R,air}$ > 0.2 m/s

The profiles for the small and the large pipes show significant differences which are more pronounced for smaller superficial gas velocities (Fig. 6.4). Here, the profiles in the large pipe are more uniform than those in the small pipe. The profiles in the small pipe still change between the relative lengths of L/D = 30.6 and L/D = 151.2, i.e. they become more uniform. The total gas fraction is slightly increasing which is explained by the expansion of the gas phase.

In Fig. 6.6 and Fig. 6.7 the result of the cross-correlation velocity measurement is shown. Compared to the gas fraction profiles (Fig. 6.4 and Fig. 6.5) the velocity profiles are much less dependent from the pipe diameter as well as from the relative inlet length within the investigated range. At higher superficial gas velocities there is a clear tendency of higher gas velocities at the higher pipe diameter.

6.5 Scale dependence of bubble size distributions

Most instructive are the obtained bubble-size distributions. They show the appearance of a bimodal distribution at a superficial gas velocity (J_R) of about 0.20 m/s (Fig. 6.8). The observations in Fig. 6.1 are confirmed quantitatively, since a further increase of the gas flow leads to a continuous growth of the large-bubble peak in the distribution (Fig. 6.8 and Fig. 6.9). The appearing second peak is shifted towards higher diameters, it becomes wider and the amplitude increases. With other words, the growing turbulization of the fluid by the increase of the gas flow does not lead to a dominance of the bubble break-up, i.e. the transition towards churn-turbulent flow is accompanied by a continuous growth of the large bubbles found in the flow.

In this sense, the bubble-size distributions behave similar in the large and the small pipes. The difference consists in the mean diameter of the large bubble fraction, which is much less in the small pipe compared to the large pipe at identical superficial velocities. It is furthermore observed that the peak is narrower and therefore significantly higher than in the large pipe. It is representing the characteristic Taylor bubbles that occupy almost the entire cross section of the pipe, which are clearly visible in Fig. 6.3.

There is a reason to believe that the evolution of the bubble size distribution caused by coalescence and bubble break-up is rather a time-dependent process, for which at given fluid velocities rather the total pipe length than the relative length is the determining factor. Nevertheless, as it can be seen from Fig. 6.8 and Fig. 6.9, the increase of the length of the small pipe from L/D = 30.6 to L/D = 151.2 does not lead to a convergence of the bubble size distributions in the small and the large pipes, though the bubble size continues to grows.

In general we believe that large bubbles in the large pipe can move much more freely, which leads to a higher probability of collisions between them than in the small pipe, where the separating liquid slug has to be drained off, before two Taylor bubbles can coalesce. This hypothesis would explain that bubbles grow up to bigger sizes in the larger pipe.

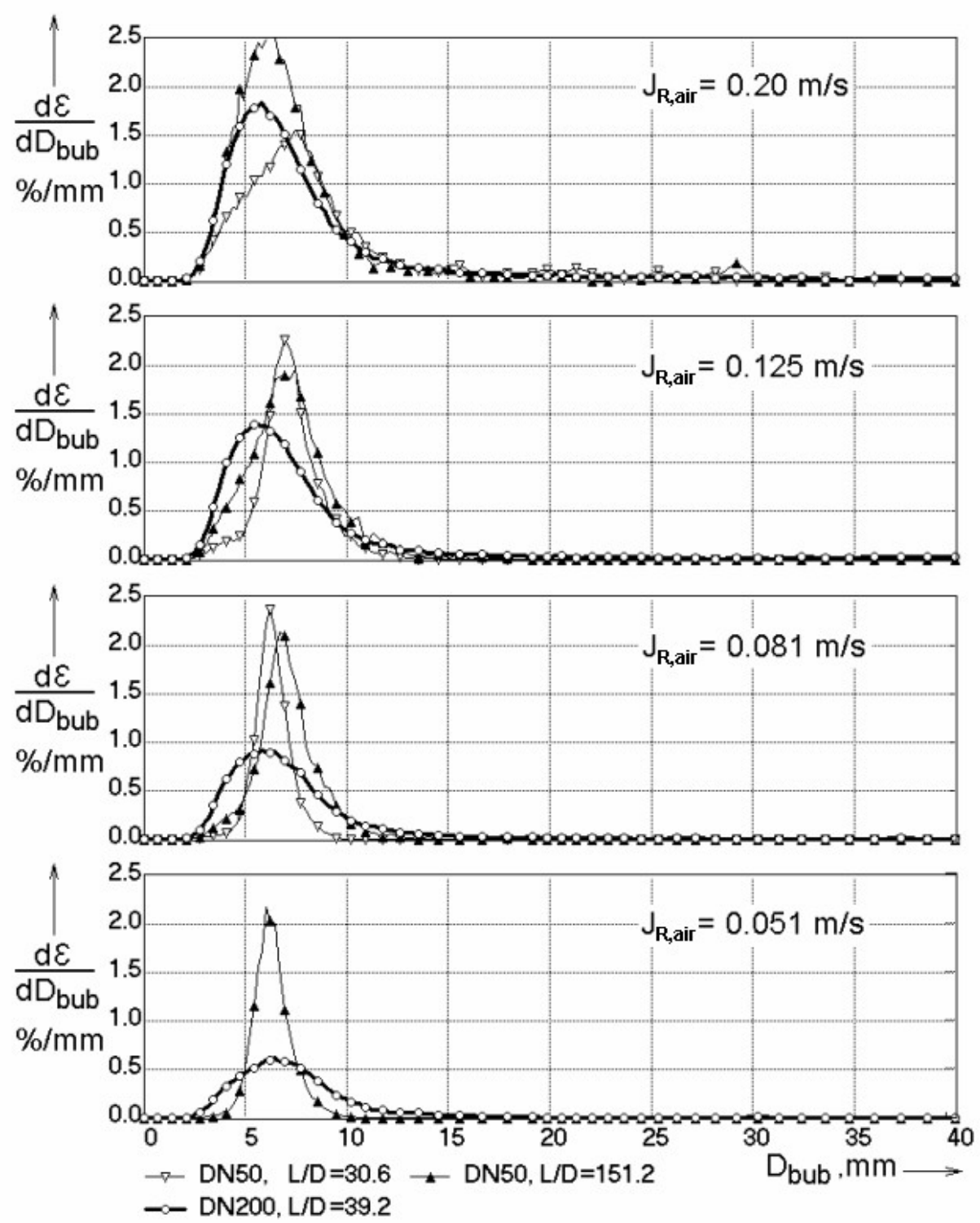

Fig. 6.8 Bubble size distributions in the test sections DN50 and DN200
J_{water} = 1.02 m/s, $J_{R,air} \leq 0.2$ m/s

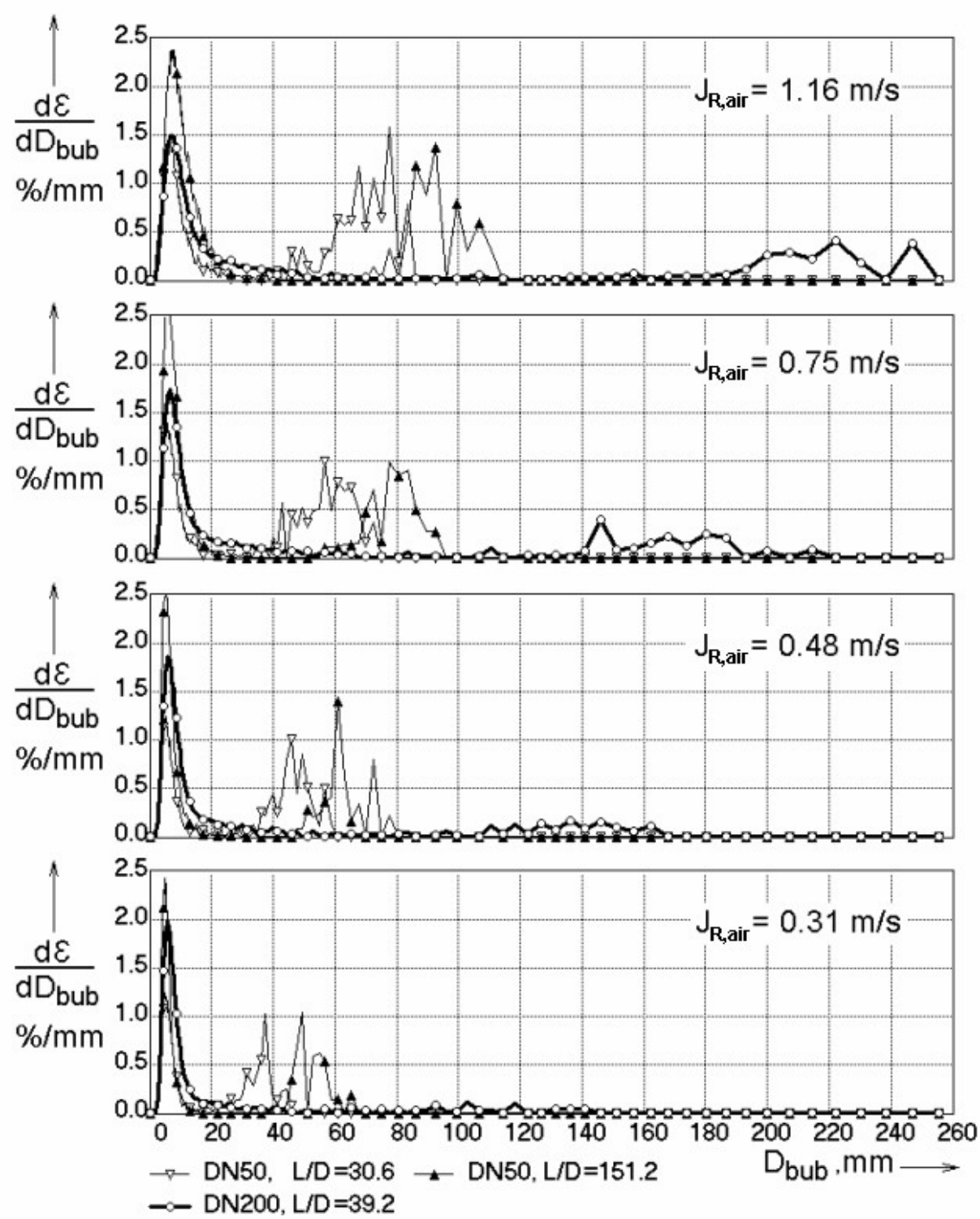

Fig. 6.9 Bubble size distributions in the test sections DN50 and DN200
J_{water} = 1.015 m/s, $J_{R,air}$ > 0.2 m/s

6.6 Shape of large bubbles appearing at high gas flow rates

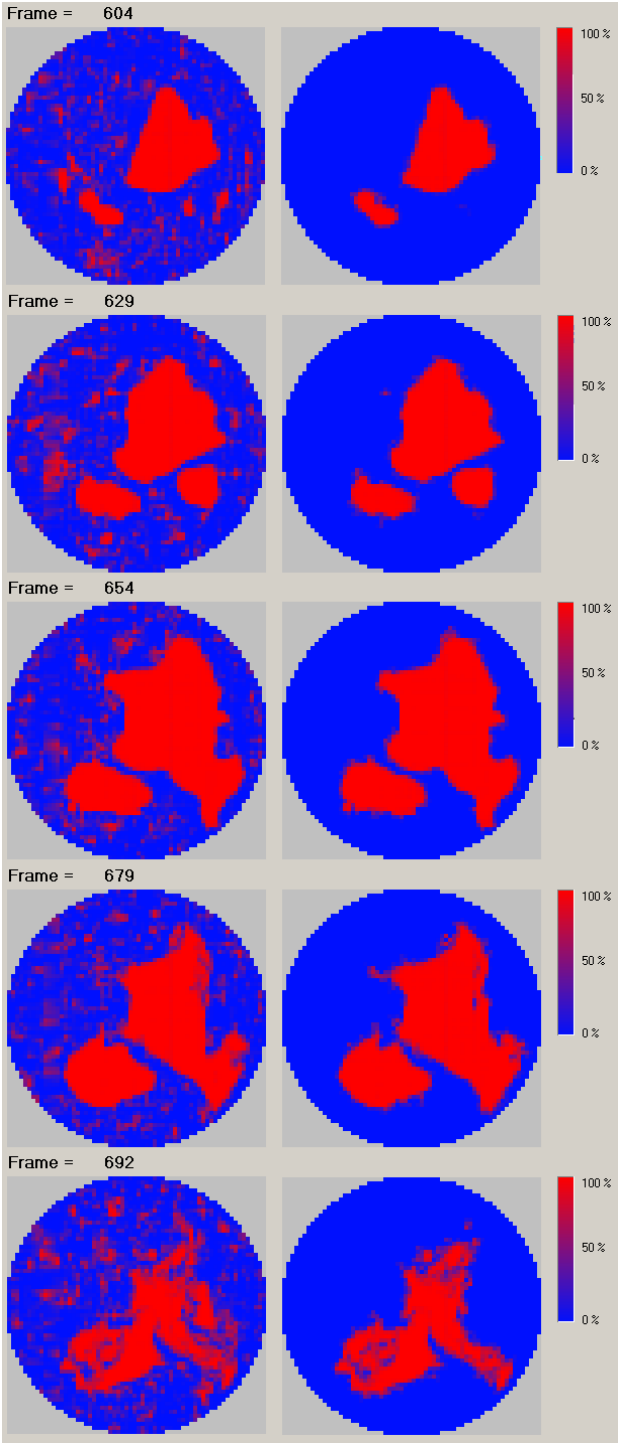

Fig. 6.10 Selected cross-sectional plots of the gas fraction distribution during passage of a large bubble, left: original signal, right: extracted bubble; (J_{air} = 0.53 m/s and J_{water} = 1 m/s) bubble selected in Fig. 6.10.

Beside the calculation of bubble size distributions, the result of the bubble identification procedure can be used to extract single bubbles from the data array and display them individually. For this purpose the local instantaneous gas fractions in all those elements of the distribution $\varepsilon_{i,j,k}$ are put to zero which do not belong to the bubble with the selected number. To demonstrate this method, a series of cross-section plots containing a large bubble are shown in Fig. 6.10, left side. The images demonstrate the large clarity of the sensor signal.

On the right side of this picture, the result of the bubble extraction is presented. In frame 604, three gas-filled areas are visible, which nevertheless belong to the same connected gas volume, as it turns out later (frames 654 and 692). Often it was observed that a large bubble consisted of two or more not connected areas within the cross section, which are connected at the base of the bubble, like in case of the bubble in Fig. 6.10. It is a typical observation, that the side surface of the bubble shows large concave regions, which is not characteristic for the Taylor bubbles in small pipes.

When the resulting new distribution is displayed by one of the mentioned visualization techniques, the selected bubble becomes visible without all the other surrounding bubbles, which otherwise may have obstructed the view. In turn, it is also possible to eliminate a selected bubble and to display only the surrounding bubbles. For this, the gas fractions of elements labelled by the number of the given bubble have to be set to zero. The virtual side projections generated in this way are shown in Fig. 6.11 for the

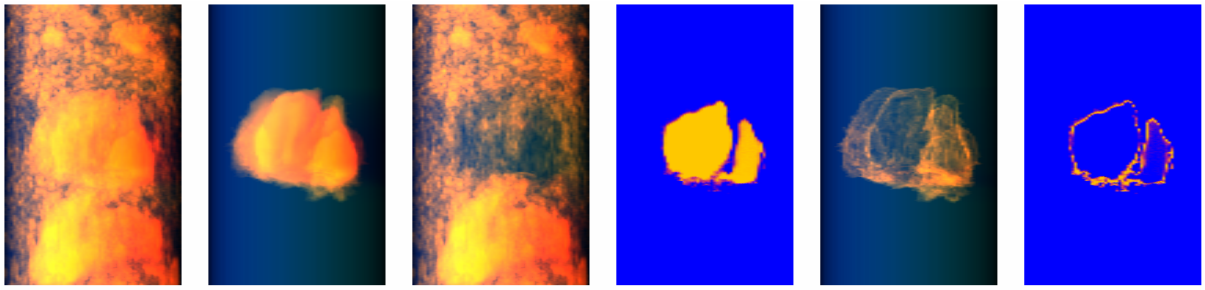

Fig. 6.11 Analysis of a large isolated bubble (flow see Fig. 6.1) extracted from the signal of the wire-mesh sensor ($J_{N,G}$ = 0.53 m/s and J_L = 1 m/s)

This method was applied to extract several large bubbles found in the wire-mesh data at high superficial gas velocities. More examples are shown in the Fig. 6.12 and Fig. 6.13. The columns in each figure show from left to right: (1) the original data, (2) the virtual projection view of the selected bubble, (3) the flow structure remaining after eliminating the selected large bubble, (4) the virtual sectional view of the separated bubble, (5) the virtual side projection view of the gas/liquid interface inside the separated bubble and (6) the virtual central cut of the gas/liquid interface. The shape of the large bubbles becomes more and more complex with increasing superficial gas velocity. Their total height also increases significantly. The bubble depicted in Fig. 6.13, for example, has a total Eulerian height of about 660 mm.

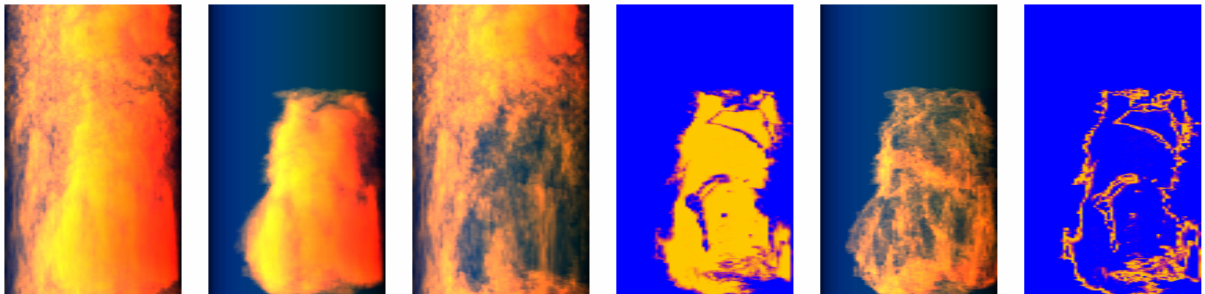

Fig. 6.12 Analysis of a large isolated bubble (flow see Fig. 6.1) extracted from the signal of the wire-mesh sensor ($J_{N,G}$ = 0.84 m/s and J_L = 1 m/s)

It has to be noted that the giant bubble shown in Fig. 6.13 has a pronounced internal structure, which was discovered by preparing a virtual side view of the gas/liquid interface (Fig. 6.13, two right columns). The interface was made visible using the function $\varepsilon' = (1-\varepsilon)\cdot\varepsilon$ instead of the local instantaneous gas fractions, a function that has its maximum at a gas fraction of 50 %, i.e. those points are highlighted, which are semi-filled with the gaseous phase. The bubble contains large quantities of the liquid phase arranged in numerous lamellas. The voids between these liquid films are connected by gas containing holes, through which they are united by the bubble recognition algorithm. This is clearly visible, when the plane of the virtual cut is rotated. It remains open, whether these holes in the liquid lamellas are reality or if the

films become invisible for the sensor due to a thickness below the resolution of the sensor. A final answer can only be given by increasing the resolution of the void measurement.

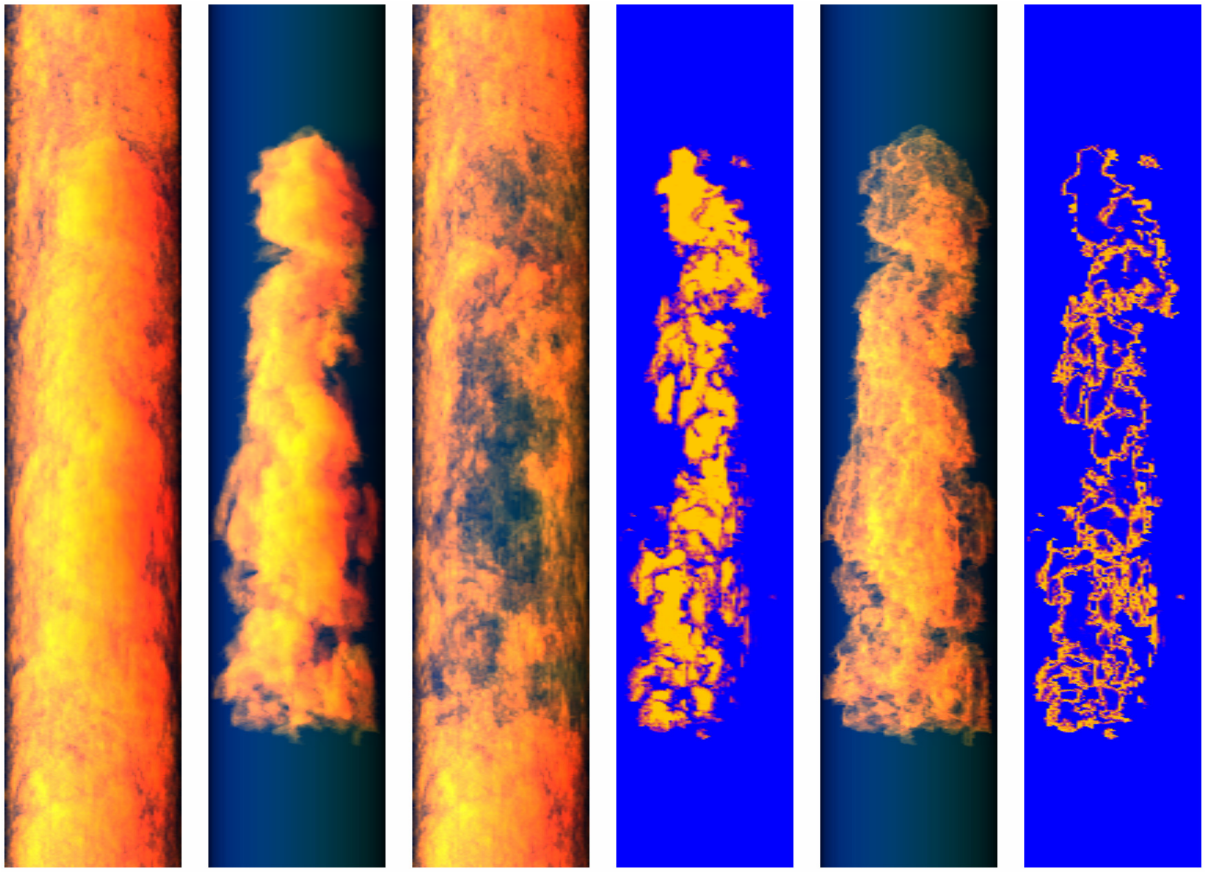

Fig. 6.13 Analysis of a large isolated bubble (flow see Fig. 6.1) extracted from the signal of the wire-mesh sensor ($J_{N,G}$ = 1.3 m/s and J_L = 1 m/s)

The fact, that the amount of liquid inside a large bubble increases with growing superficial gas velocity, supports the hypothesis of an increasing deformation of the gas/liquid interface as the cause of the complicated inner structure. The bubble in Fig. 6.11, for example, found at $J_{N,G}$ = 0.53 m/s consists of two parts divided by a liquid film. Both parts are connected at the bottom of the bubble. With growing air flow the structure becomes more and more complicated.

7. Assessment of the turbulent dispersion coefficient

7.1 Background

An important local phenomenon that has to be taken into consideration by the constitutive equations for the calculation cell of a two-fluid CFD model is the turbulent diffusion, also called turbulent dispersion. It provokes a transport of the gaseous phase in the direction against the void fraction gradient. Depending on the way of averaging of the main conservation equations, it is modelled by a turbulent diffusion term in the mass conservation equation or a turbulent dispersion force in the momen-

tum equation. It is determined by the combination of the eddy diffusivity, independent of the bubbles agitation, and the bubbles induced diffusivity.

TOPFLOW data offers a unique opportunity to asses the turbulence diffusion coefficient in two-phase flow on a wide range of liquid and gas superficial velocities. In the present analysis, the data from the large vertical test section DN200 with gas injection through the sparger heads at the bottom is used. The flow pattern in the air/water experiments ranged from bubbly to slug/churn regime. Only in the air/water tests, a pair of wire-mesh sensors was available, which is essential for the method described below. The turbulence diffusion coefficient has been measured in the central region of the test section, where the gradients of the gas volume fraction and of the liquid velocity are small. Method and results were published by Manera et al. (2006).

Not many models exist in literature, which describe the bubble-induced diffusivity (Sato and Sekoguchi, 1975; Sato *et al*., 1981; Milelli, 2002). Moreover, all the models available have been derived for bubbly flow only. A comparison has been performed between the experimental data and the Sato model (Sato and Sekoguchi, 1975; Sato *et al*., 1981), which is widely used to predict the bubble-induced turbulence in two-phase flow. For the first time this model has been tested beyond the bubbly flow regime.

7.2 The use of cross-correlation techniques to measure bubbles lateral displacement

The motion of gas bubbles in a uniform parallel upward flow (far away from the wall so that wall effects and gradients of the liquid velocity can be neglected) can be described by a combination of a transport term that takes into account the motion of the bubbles in the axial direction and by a diffusion term that characterizes the motion in the radial direction:

$$\frac{\partial \varphi}{\partial t} + v_B \frac{\partial \varphi}{\partial z} = D_B \left(\frac{\partial^2 \varphi}{\partial r^2} + \frac{1}{r} \frac{\partial \varphi}{\partial r} \right), \tag{22}$$

where φ is the bubbles concentration and r is a radial coordinate with the origin located at the position of an assumed input Dirac-shaped bubble concentration disturbance in the axial plane identified with z = 0. The diffusion coefficient D_B is given by a combination of the liquid eddy diffusivity and the bubble-induced diffusivity. The bubble velocity v_B is considered to be constant. This assumption is justified for a fully developed flow.

By applying the Lagrangean coordinates, eq. (22) can be written as:

$$\begin{cases} \dfrac{D\varphi}{Dt} = D_B \left(\dfrac{\partial^2 \varphi}{\partial r^2} + \dfrac{1}{r} \dfrac{\partial \varphi}{\partial r} \right) \\ \dfrac{dz}{dt} = v_B \end{cases} \tag{23}$$

The solution is:

$$\begin{cases} \varphi(r,\tau) = \dfrac{A}{\tau} e^{-\frac{r^2}{4\tau D_B}} \\ \tau = \dfrac{z - z_0}{v_B} = \dfrac{d}{v_B} \end{cases}, \tag{24}$$

where d is the distance travelled by the gas bubbles in a time interval τ. The solution has thus a Gaussian shape. It can be analytically demonstrated that the spatial cross-correlation $CCF_{\varphi,z}$ between the bubble concentrations $\varphi(r,\tau)$ measured at two axial locations z_0 and z is again a Gaussian function in r, having identical exponential term as in eq. (24). Therefore the diffusion coefficient D_B can be evaluated from the dispersion ε of the spatial cross-correlation $CCF_{\varphi,z}$:

$$D_B = \frac{\varepsilon^2}{2\tau} = \varepsilon^2 \frac{v_B}{2d} \tag{25}$$

Local gas fraction signals measured by two wire-mesh sensors are correlated. The spatial cross-correlation between gas fraction signals differs from the cross-correlation $CCF_{\varphi,z}$ since it is biased by the finite dimension of the bubbles and by the spatial resolution of the measuring system. To eliminate this bias, the spatial cross-correlation has first to be deconvoluted on the basis of the auto-correlation function. The deconvolution operation is equivalent to find a function G(r) such that:

$$CCF(r) = \int_{-\infty}^{\infty} G(r) ACF(r - r^*) dr^* \tag{26}$$

Eq. (26) expresses a classical inverse problem that can be rather complex to solve. The problem can be simplified by assuming G(r) to be a Gaussian function. This assumption is fully justified since G(r) is the cross-correlation $CCF_{\varphi,z}$. The dispersion coefficient of G(r) then can be used to evaluate the diffusion coefficient D, as from eq. (25). The spatial correlation computed for the lower sensor is used for the deconvolution.

The evaluation of the diffusion coefficient that describes the lateral motion of the bubbles in the centre of the pipe consists therefore of the following steps:

- Computation of the spatial cross-correlation between the central region of the lower sensor with the upper sensor (since we are interested in studying the later motion of bubbles in the central region of the pipe only);
- Computation of the spatial auto-correlation of the lower sensor and
- Search for a solution of Gaussian shape for equation (25). On the basis of its standard deviation, the diffusion coefficient can be evaluated. The function G(r) is calculated by applying a least square method.

The abovementioned procedure is applied to all experiments represented in grey colour in Fig. 7.1 for both types of gas injection devices K and I.

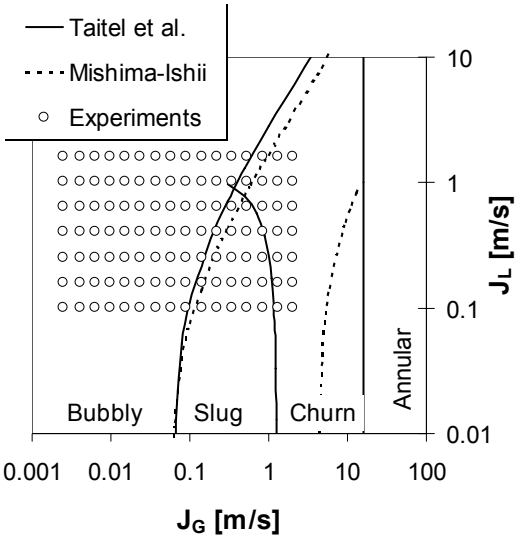

Fig. 7.1 Experimental test matrix and flow maps

For the computation of the spatial cross-correlation (step 1), the signal measured by the lower sensor at a given location A in the centre of the pipe is correlated successively to the signals measured by the upper sensor at different lateral distances. In this way, several time-dependent correlations are obtained, as illustrated in Fig. 7.2 (left). In the figure the correlation between one point of the lower wire-mesh sensor and up to five points of the upper wire-mesh is shown for illustration purpose.

The spatial correlation is then obtained by plotting the maxima of the time-dependent correlations as function of the lateral distance between correlated points, as shown in Fig. 7.2 (right). In the figure the spatial cross-correlation has been normalized with respect to its maximum value.

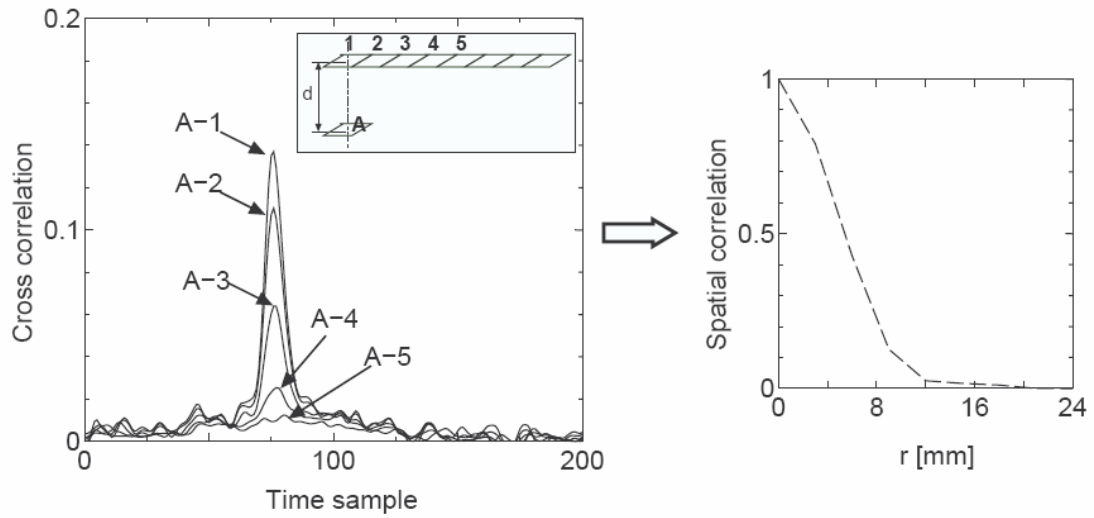

Fig. 7.2 Example of computation of spatial cross-correlation

Similarly, the spatial auto-correlation (step 2) is obtained by correlating points belonging to the same measurement plane (i.e. to the same wire-mesh sensor). Cross- and auto-correlation are normalized with respect to their maximum value before step 3 is performed.

An example of the step 3 of the procedure is shown in Fig. 7.3, where the auto- and cross-correlation and the corresponding convolution function G(r) are presented. The function resulting from the convolution of G(r) with the measured auto-correlation function *ACF* is indicated with black dots and is in very good agreement with the measured cross-correlation *CCF*.

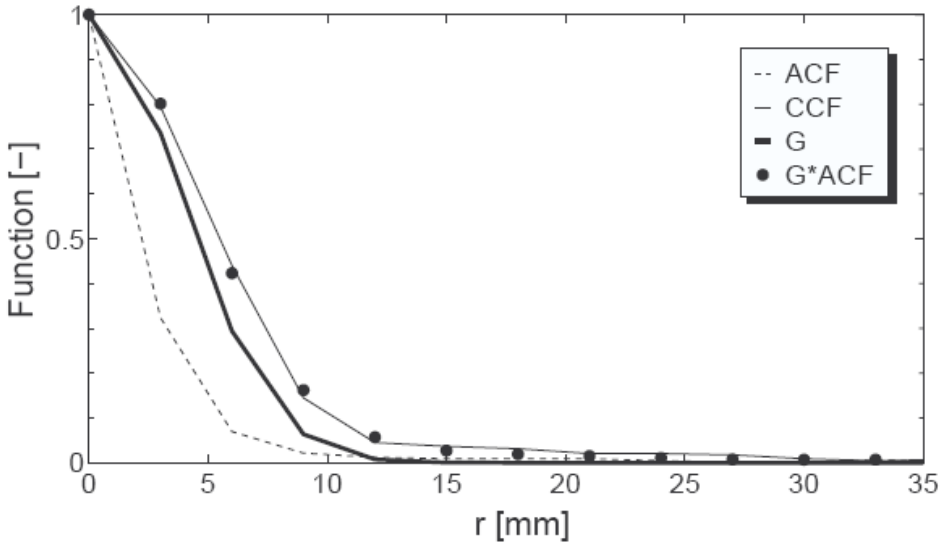

Fig. 7.3 Example of computation of convolution function G(r)

7.3 Spatial correlation from wire-mesh sensors by means of ensemble averaging

As mentioned in section 2.2 and 4.2, at each measuring point of a wire-mesh sensor, a signal of 25000 samples is recorded. To improve the statistics of the correlation procedure, a central region of 4x4 points is selected in the lower sensor instead of a single point. In addition, four directions are selected for the correlation with the upper sensor (see illustration in Fig. 7.4).

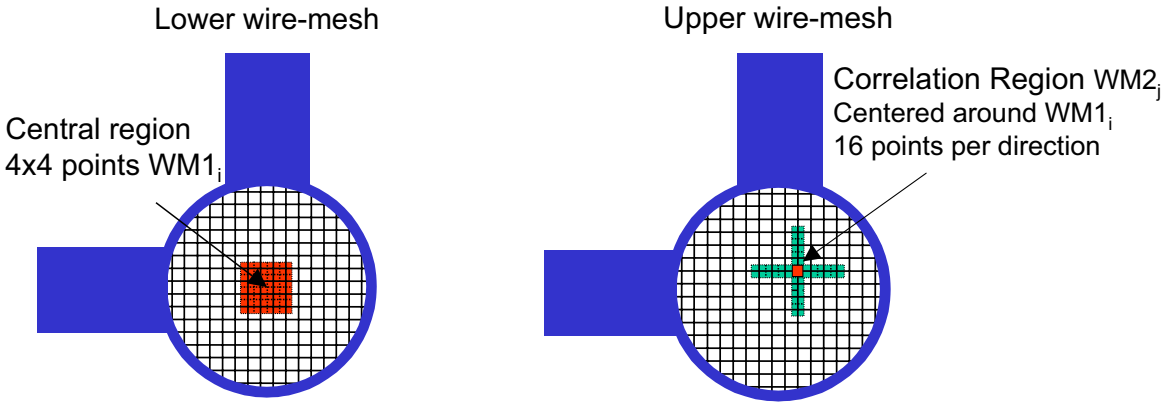

Fig. 7.4 Correlation regions for lower and upper wire-mesh sensor

Therefore each point of discrete coordinates (j_0,k_0) belonging to a 4x4 region at the centre of the lower wire-mesh sensor is correlated with the points of the upper wire-mesh having coordinates (j,k):

$$\begin{cases} j = j_0 - n, \quad k = k_0 \\ \text{or} \qquad\qquad\qquad n \in [-16,16] \\ j = j_0, \quad k = k_0 - n \end{cases} \tag{27}$$

$$j,k,n \in N$$

In this way, for each point (j_0,k_0) 65 cross-correlations are computed (16x4+1). Since a region of 4x4 points is taken into account in the computation, the total number of cross-correlation becomes 1040 (65x4x4).

After computing all time-dependent cross-correlation, the ones obtained for the same value of |n| (see eq. 27) are averaged together. In this way, ensemble-averaged time cross-correlations are obtained for 17 radial positions. Then, the maximum of each correlation is selected to obtain a spatial dependent correlation between the central region of the lower wire-mesh and the upper wire-mesh sensor, as shown in Fig. 7.4. The selection of a 4x4 region in the lower sensor and of the four-direction segments in the second sensor is done to improve the statistics of the spatial correlation, being the ensemble-averaging procedure equivalent to an increase of the effective measuring time of a factor 64 (when compared to the correlation of a single point in the centre of the lower sensor with one radial direction in the upper sensor).

Due to the large number of data to correlate (2080 correlations between signals of 25000 records each), the FFT (Fast Fourier Transform) is used to compute the time-dependent correlation between two given signals. This allows reducing considerably the necessary computational time.

7.4 Results

In Fig. 7.5 the turbulence diffusion coefficient D_B is plotted as function of the gas superficial velocity for different liquid superficial velocities. The analysis of experiments performed with both injection devices are reported in the figure. Error bars of the data are shown in Fig. 7.6 and Fig. 7.7.

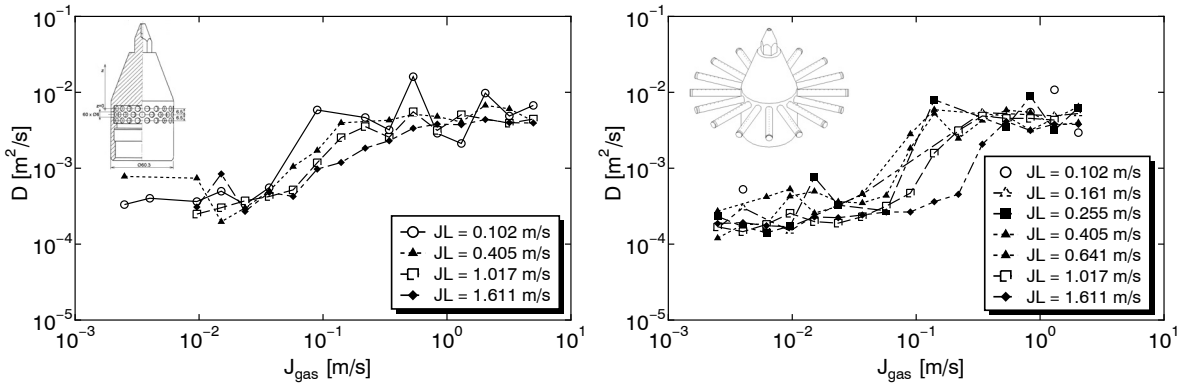

Fig. 7.5 Turbulent diffusion coefficient for experiments with injection device K (left) and I (right).

The derivation of the experimental errors is discussed in appendix A in the article of Manera et al. (2006), while the influence of the wire-mesh sensor is addressed to appendix B of the mentioned paper. The following observations can be derived:

- the turbulence diffusion coefficient exhibits only small variations as function of the liquid superficial velocity and no clear trend can be deduced; the absence of a clear trend might be caused by the presence of two effects acting in opposite direction: at a fixed gas volume flow rate the wall induced (single phase) diffusivity increases with the liquid volume flow rate, but the bubble induced diffusivity decreases because of decreasing gas volume fraction (with increasing liquid flow rate);
- the coefficient strongly depends on the gas superficial velocity;
- for each liquid superficial velocity, a range of gas superficial velocities is found in which an abrupt increase of the turbulence diffusion coefficient takes place;

- for small gas superficial velocities, the effect of the injection device (and thus the size of the primary bubbles) has a strong influence on the turbulence diffusion coefficient. In particular, a larger diffusion coefficient is observed when the sparger with bigger holes is used (Fig. 7.5, left); this effect becomes negligible at high gas superficial velocities;
- the gas injection device has a strong influence on the range of gas superficial velocities in which the sudden increase of the turbulence diffusion coefficient D_B takes place.

All trends described are dominating above uncertainty ranges.

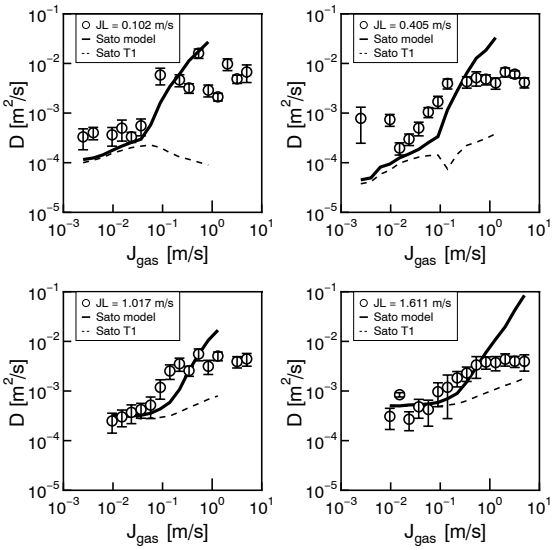

Fig. 7.6 Comparison between experimental turbulence diffusivity and Sato model (injection device K). With *'Sato T1'* the liquid turbulence diffusion coefficient independent of the bubbles agitation is indicated

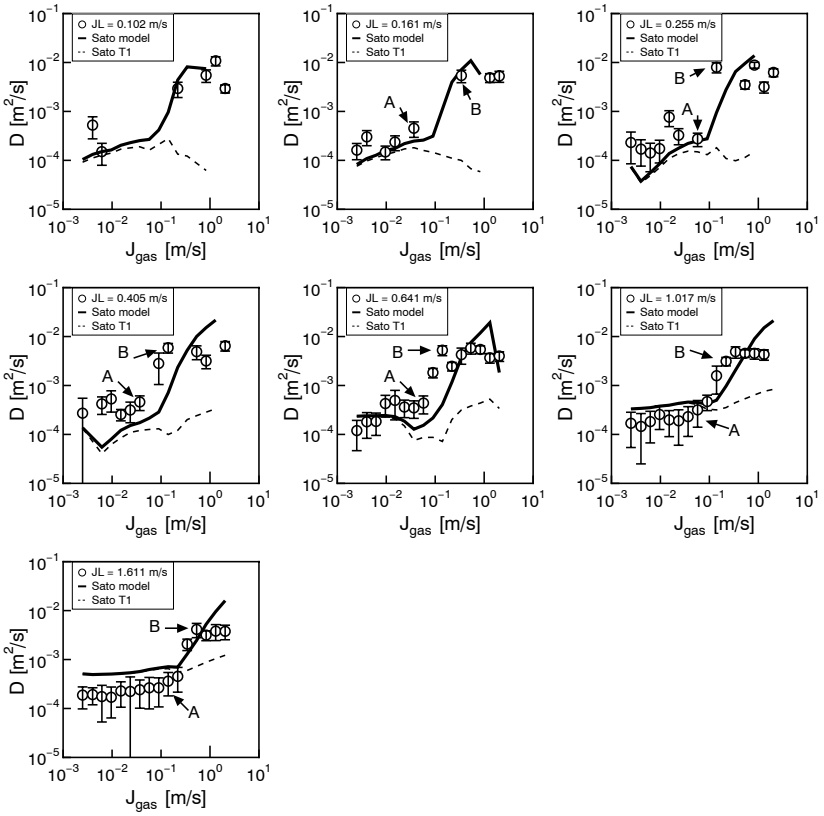

Fig. 7.7 Comparison between experimental turbulence diffusivity and Sato model (injection device I). With *'Sato T1'* the liquid turbulence diffusion coefficient independent of the bubbles agitation is indicated

The experimental results are compared to calculated values obtained with the Sato model (Sato and Sekoguchi, 1975; Sato *et al*., 1981). The experimental bubble size distributions and radial gas fraction profiles are given as input to the model. Sato assumes the turbulence diffusion coefficient to be the result of a linear superposition of two components, the liquid turbulence component T1, independent of bubbles agitation, and the bubble-induced turbulence T2.

The comparison between experimental results and Sato model is reported for the experiments with injection devices K and I in Fig. 7.6 and Fig. 7.7 respectively.

Despite the fact that the Sato model has been developed only for bubbly flow, the general trends agree quite well with the experiments. In agreement with the experimental data, the Sato model predicts a strong variation of the turbulence diffusion coefficient when the gas superficial velocity is increased above a certain value (greater than 0.1 m/s in most of the cases). However, a not fully satisfactory agreement is found when comparing the absolute values of the turbulent diffusion coefficients. At low gas superficial velocity and high liquid superficial velocity the turbulence diffusion coefficient is over-predicted by the model. At high gas superficial velocities, the model over-predicts the coefficient in all cases when the large-holes sparger (device K) is used and only for high liquid superficial velocities when the small-holes sparger is applied (device I).

The reason for the abrupt change of the turbulence diffusion coefficient has been investigated as well. It is found that for high liquid superficial velocities (J_L > 1 m/s) the sudden increase of D_B occurs together with the transition of the radial gas fraction profiles from wall-peaked to centre-peaked. However, for the cases with lower superficial liquid velocity always a centre-peaked profile appears. Examples are shown in Fig. 7.8, where the radial gas fraction profiles (in %) are shown for the transition points A and B indicated in Fig. 7.7.

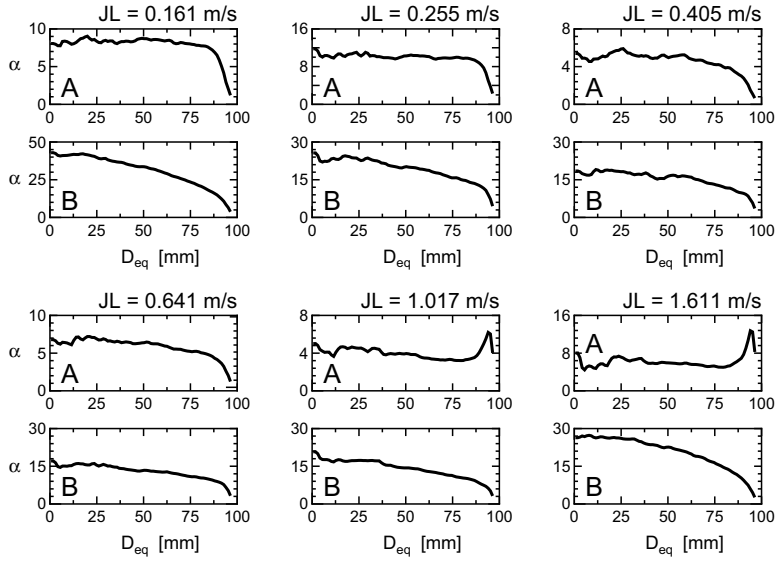

Fig. 7.8 Radial gas fraction profiles for transition points indicated in Fig. 7.7

A further analysis points out that the abrupt increase of turbulence diffusivity occurs together with the transition of the bubble size distribution from mono- to bimodal shape, i.e. when large bubbles/slugs appear in the flow, as shown in Fig. 7.9. In the figure the bubble size distributions (in terms of equivalent diameter) are reported for different liquid superficial velocities in correspondence of the transition points A and

B indicated in Fig. 7.7. The appearance of larger bubbles in the flow causes a sudden increase of the bubble-induced diffusivity, while the wall-induced eddy diffusivity gives a negligible contribution. This can be observed in Fig. 7.6 and Fig. 7.7 as well, where the eddy diffusivity component calculated by means of the Sato model is reported (indicated in the legend as *Sato T1*).

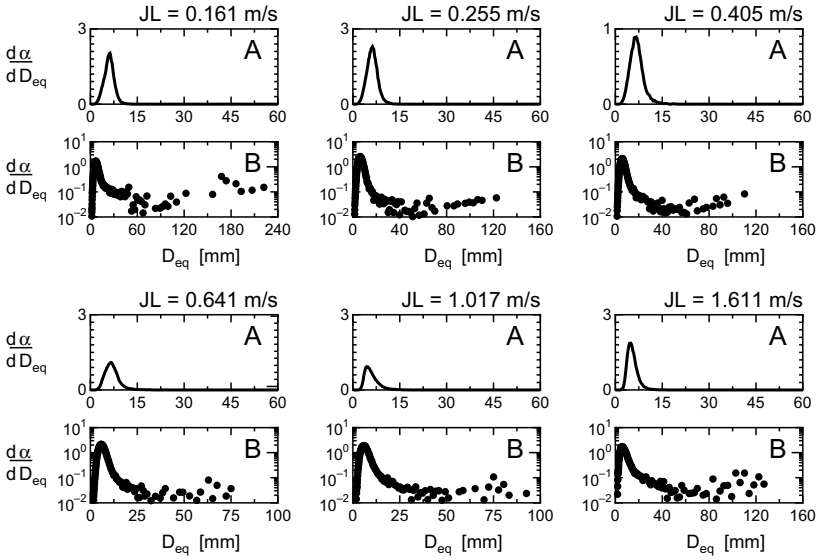

Fig. 7.9 Bubble size distributions for transition points indicated in Fig. 7.7

7.5 Conclusions

The lateral motion of bubbles in the central region of a vertical flow in a pipe of large diameter is studied by means of cross-correlation techniques. The lateral displacement of bubbles is investigated in terms of turbulent diffusion coefficient, which is a combination of the liquid eddy diffusivity (wall induced) and the diffusivity induced by the bubbles themselves. A unique experimental data on this parameter has been collected on a wide range of liquid and gas superficial velocities. It has been found that the turbulence diffusion coefficient exhibits only a weak dependence on the liquid superficial velocity, while a strong dependence has been observed as function of the gas superficial velocity. In particular, it has been found that in bubbly flow regime the turbulent diffusion coefficient increases slightly with the gas superficial velocity. As soon as larger bubbles appear in the flow, i.e. when the bubble size distribution changes from mono- to bimodal, an abrupt increase of the coefficient is observed, this increase being of one or more orders of magnitude. It has been also found that the bubble-induced diffusivity alone contributes to the sudden increase of the turbulent diffusion coefficient, while the wall-induced eddy diffusivity changes only slightly.

The application of the Sato model has shown that the model is able to capture the sudden increase of the turbulence diffusion coefficient with increasing gas superficial velocity, despite the model has been developed for bubbly flow only. The model predictions are even so in the correct range of order of magnitude. However, the model over-predicts the wall-induced eddy diffusivity for high liquid superficial velocities and over-predicts the bubble-induced diffusivity for high gas superficial velocities. It is clear that efforts are still needed for a correct modelling of bubble-induced diffusivity, especially in the case of high gas fractions.

8. Evolution of the structure of an adiabatic two-phase flow in a vertical pipe

8.1 Background

The evolution of the flow structure in the vertical test sections of TOPFLOW is reflected by radial gas fraction and velocity profiles as well as bubble-size distributions measured by wire-mesh sensors at various distance from a gas injection site. The change of the measuring data in axial direction is sensibly depending on the interfacial momentum exchange and the bubble coalescence and break-up. Experiments are carried out on both vertical test sections (DN50 and DN200), both for an air/water and a steam/water flow. In case of the large test pipe, the variable gas injection system described in section 2.3 was used.

Closure laws for CFD models that reflect the bubble forces as well as coalescence and break-up cannot be tested at the data directly. For this, the closure relations have to be embedded into the CFD code. Tests have to be reproduced by calculations and the quality of the closure relations has to be analysed on basis of a comparison between the experimental and theoretical results. This part of the work is presented in the following separate reports:

- *"CFD models for poly-dispersed bubbly flows",*
- *"Turbulent dispersion of bubbles in poly-dispersed gas/liquid flows in a vertical pipe"* and
- *"Validation of the Multiple Velocity Multiple Size Group (CFX10.0 N x M MUSIG) Model for poly-dispersed multiphase flows"*.

An alternative to the use of the CFD code is the application of simplified solvers that take benefit from the radial symmetry and the simple boundary conditions in vertical pipes (Lucas et al., 2001 and 2007a).

These laws can be characterized on the basis of the evolution of bubble-size distributions along the flow path. The flow patterns to be considered in vertical pipes are bubbly flow, vertical slug flow, churn-turbulent flow, wispy-annular flow, annular flow and finely-dispersed flow. All these flow regimes were addressed by experiments performed within the project.

Vertical pipe flow has always been in the centre of the attention of thermal hydraulic research. The experiments at the vertical test sections of TOPFLOW distinguish themselves by a number of novel characteristics, which are outlined in the introduction (section 1). For the first time, gas/liquid flows in large diameter pipes were studied at fluid parameters close to nuclear reactor conditions with instrumentation capable of characterizing the flow structure in the entire cross-section with a resolution in the range of millimetres and sampling frequencies in the range of some kHz.

8.2 Test conditions

For this kind of experiments the test facility was equipped with a special modification of the large vertical test section with an inner diameter of 195.3 mm (DN200). This pipe is equipped with a variable gas injecting system (see section 2.3 and Fig. 2.9) that allows feeding gas or, respectively steam to 18 different vertical positions upstream of the measuring position. By changing the location of the gas supply, it is possible to study the evolution of the flow structure along the flow path in the DN200

vertical pipe. The gas supply to the injection points is realised with a gas riser (DN50) that is mounted instead of the small test section. Experiments can be carried out either with an air/water flow at ambient conditions or with a steam/water flow at saturation conditions and pressures of up to 7 MPa.

In the experiments, the superficial velocities ranged from 0.04 to 7.8 m/s for the gas phase ($J_{N,G}$) and from 0.04 to 1.6 m/s for the liquid. In this way, the full range from bubbly to churn turbulent flow regimes was covered. Information about the separate experiments contains appendix A1: L20, D10 and D11 as well as A2: L01-L08, D12 and D13. A special data evaluation technique allows extracting from the primary wire-mesh sensor data radial gas fraction profiles that are decomposed according to bubble size classes (Prasser et al. 2002b). In this way, the behaviour of bubbles of different diameter can be observed, which experience a displacement in either towards the wall or towards the centre of the pipe, which is caused by bubble-diameter dependent non-drag forces. Furthermore, information on bubble coalescence and break-up frequencies can be obtained from the change of the measured bubble size distributions.

Air/water tests were carried out at ambient pressure and temperatures in the range between 20 and 40 °C. The absolute pressure at the sensor position was usually about 120 kPa due to the pressure drop in the pipe between test section and steam drum (see Fig. 2.1 and Fig. 2.5). Desalinated water with a conductivity of about 2 – 5 µS/cm was used. Steam/water experiments were performed at the following pressure levels: 1, 2, 4, 6.5 MPa and the corresponding saturation temperatures of 180, 212, 250 and 280 °C. The pressure in the heater circuit of TOPFLOW was about 0.5 MPa higher to ensure the necessary driving force for pushing the steam mass flow into the test section. Experiments selected for the presented paper were carried out at a constant superficial liquid velocity of J_L = 1 m/s. The gas superficial velocity was varied in a wide range.

8.3 Results

8.3.1 Air/water experiments

Gas fraction and gas velocity profiles as well as bubble size distributions as function of the inlet lengths for a bubbly flow regime are presented in Fig. 8.1. The air was injected through orifices of 1 mm diameter. Despite of this, the most probable bubble size measured at L/D = 1.1 is about 6 mm. There is a slight tendency of a decreasing bubble size when the gas injection is shifted to lower positions. At low L/D, the gas fraction profiles show a peak close to the pipe wall, which is caused by the gas injection at the periphery. With growing distance from the gas injection, the bubbles are transported towards the centre of pipe. The final gas fraction profile has a pronounced central maximum.

Gas velocity profiles exhibit a maximum close to the wall, as long as there is a gas fraction peak close to the wall, too (the jump to zero at a certain radius is due to the lack of gas bubbles in the central region, see gas fraction profiles). This is due to buoyancy caused by the gaseous phase that accelerates the liquid phase in the near-wall region. The gas velocity is linked with the liquid velocity by the bubble rise velocity that is mainly constant due to the narrow bubble size distribution. At higher L/D the velocity maximum close to the wall vanishes.

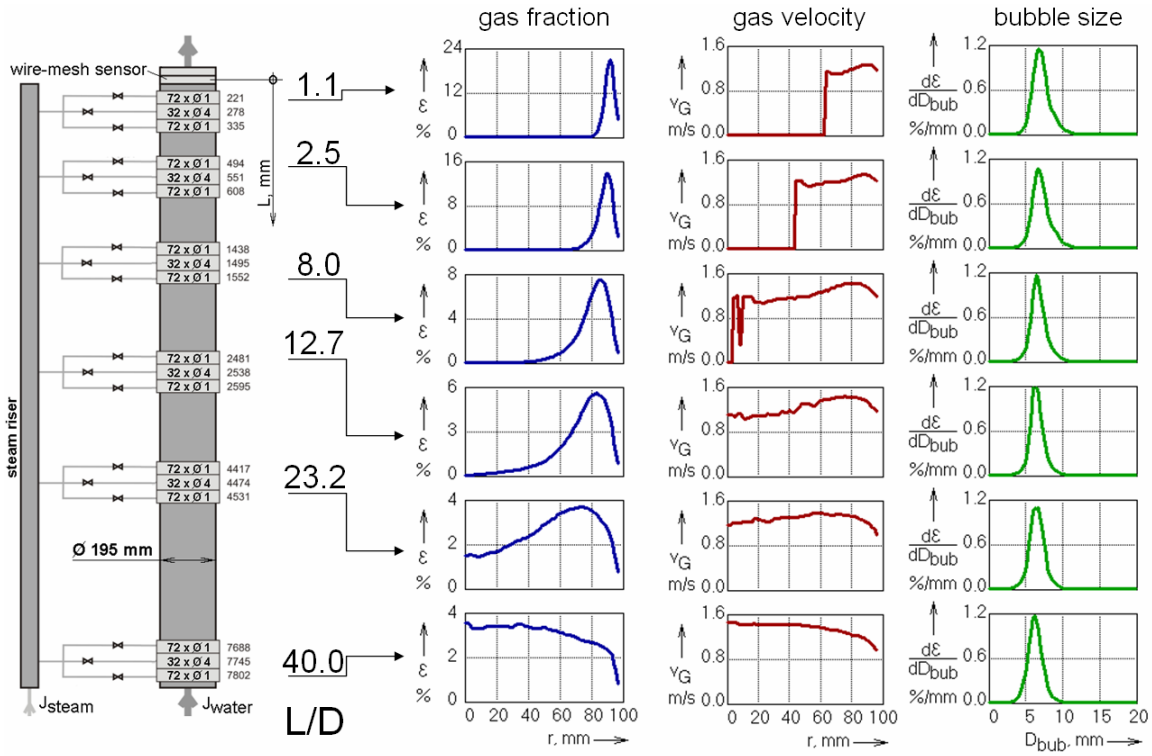

Fig. 8.1 Gas fraction and gas velocity profiles as well as bubble size distributions in the test pipe DN200 in an air/water experiment at J_L = 1 m/s and **$J_{N,G}$ = 0.037 m/s**, T = 30 °C, p = 0.12 MPa at sensor position, gas injection orifices: D_{inj} = 1 mm

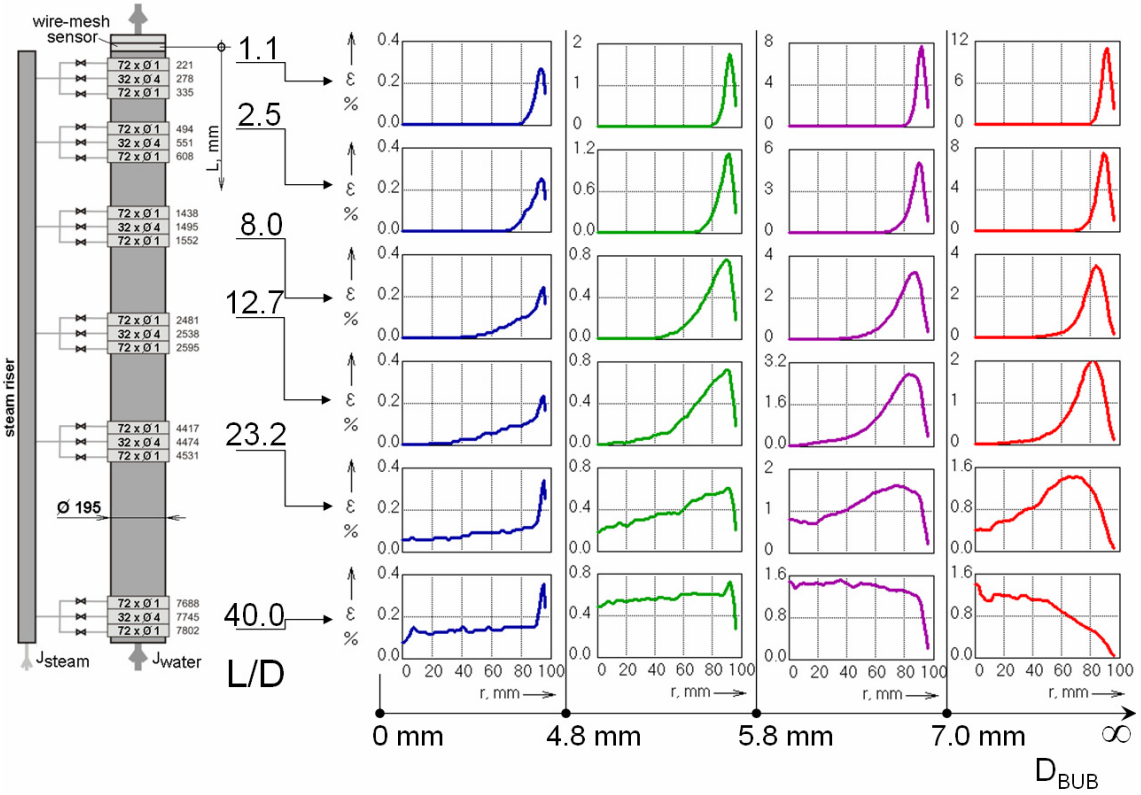

Fig. 8.2 Gas fraction profiles decomposed according to bubble size classes in the test pipe DN200 in an air/water experiment at J_L = 1 m/s and **$J_{N,G}$ = 0.037 m/s**, T = 30 °C, p = 0.12 MPa at sensor position, gas injection orifices: D_{inj} = 1 mm

Gas fraction profiles decomposed according to bubble size classes are shown in Fig. 8.2. Naturally, closely downstream the gas inlet, all four chosen bubble size classes show a maximum close to the wall. The peak vanishes completely for bubbles larger than D_{bub} = 5.8 mm, while smaller bubbles maintain a wall peak over the total available relative length of L/D = 40. Most pronounced is the wall peak for bubbles between 0 and 4.8 mm equivalent diameter.

These findings are inline with the observations of Tomiyama (1998) for single bubbles, which experience an inversion of the direction of the lift force at a certain critical bubble diameter, which is about 5.8 mm for air in water at ambient conditions. In case of upwards flow, small bubbles are pushed in the direction towards the pipe wall, while larger bubbles tend to move towards the centre. The criterion for the change of sign of the lift force is the Eötvös number. Since the bubble size distribution at L/D = 1.1 contains bubbles that are both smaller and larger than the critical diameter, the described effect of a radial bubble separation according to their size is observed.

The observation that the slight decrease in bubble sizes along the flow path is due to a dominating bubble fragmentation has to be discussed with care. As shown in Fig. 8.3, the pressure at the injection site has a significant influence on the bubble size distribution, when the air mass flow respectively the volume flow rate related to normal conditions is kept constant (test run L08 see appendix A2). Naturally, the same mass flow corresponds to a lower volume flow at an increased pressure and the bubbles become smaller (Fig. 8.3). This was found by injecting the gas into the upper distribution chamber at L/D = 1.1 while varying the pressure in the steam drum downstream (Fig. 2.1) of the outlet of the test section.

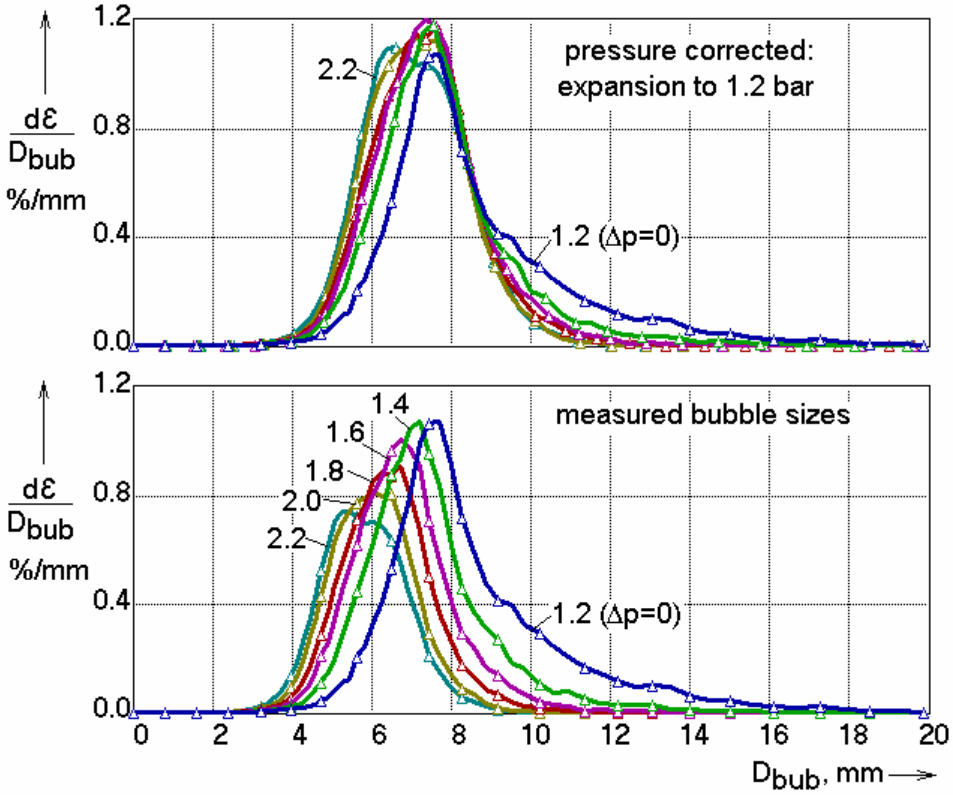

Fig. 8.3 Dependency of bubble sizes from pressure in an air/water flow (J_L = 1 m/s, **$J_{N,G}$ = 0.037 m/s**, T = 30 °C, parameter: pressure at sensor position)

In the same time it is clear that the hydrostatic head grows in downwards direction, i.e. the pressure at the location of the gas injection is significantly higher than the pressure at the measuring position. In the experiment shown in Fig. 8.1 and Fig. 8.2 the pressure at the sensor is 1.2 bar, while the pressure at the gas injection device can reach about 2 bar at the lowest position (L/D = 40). In order to check if the observed tendency of dominating bubble fragmentation along the pipe is realistic, the bubble size distribution generated at the lowest injection position has to be compared to the bubble size distribution measured at the sensor position at equal pressure. However, we did not move the sensor along the flow path, but the gas injection height was changed. In reality, the bubble growth due to the expansion is dominating above weak bubble coalescence and fragmentation effects at the given flow conditions.

In order to eliminate the effect of bubble growth due to expansion, the bubble size distribution measured for L/D = 40 at p = 1.2 bar at the sensor position has to be compared to a bubble size distribution obtained from a measurement for L/D = 1.1 at 2 bar, which is transformed to the distribution that has to be expected at the sensor position, if bubble coalescence and break-up were absent. The numerical transformation has to consider the bubble growth due to expansion from 2 bar down to 1.2 bar, which is performed for each bubble-size class individually. The result is shown in Fig. 8.4 obtained on basis of the data in Fig. 8.3. The expansion was assumed to be isothermal, since the heat capacity of the water dominates at the given low mass fractions of gas and keeps the temperature constant.

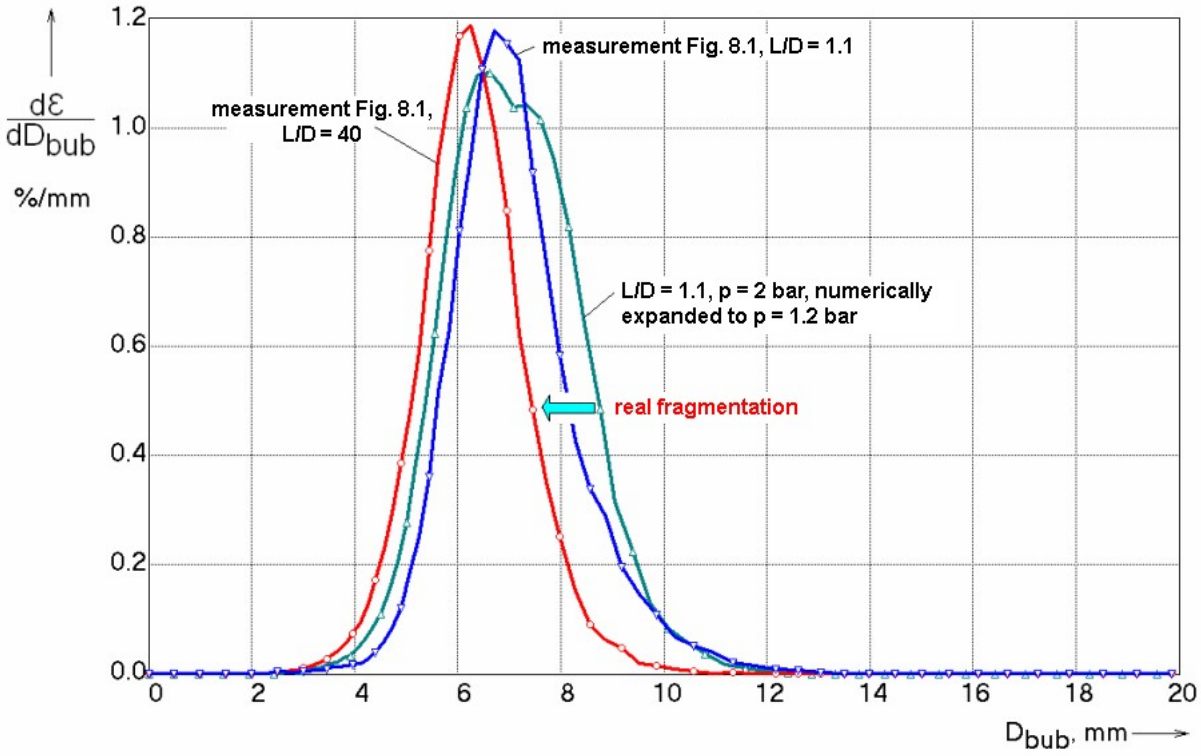

Fig. 8.4 Dependency of bubble sizes from pressure in an air/water flow (J_L = 1 m/s, **$J_{N,G}$ = 0.037 m/s**, T = 30 °C, parameter: pressure at sensor position)

The distribution corrected for the expansion from 2 bar to 1.2 bar is close to the one measured at L/D = 1.1 at a pressure of 1.2 bar. There is a slight tendency towards smaller bubble sizes, but the corrected distribution still shows larger bubble sizes then those measured at L/D = 40. This means that the tendency of a slight bubble

break-up on the way from L/D = 1.1 to L/D = 40 in the test shown in Fig. 8.1 and Fig. 8.2 is real, although smaller than suggested by Fig. 8.1.

In case of higher gas superficial velocities, the effects of coalescence and fragmentation are much more pronounced (Fig. 8.5 - Fig. 8.8). On the way from the distribution observed at L/D = 1.1 to the one found at L/D = 40, both fragmentation and coalescence takes place. With growing superficial air velocity, the inlet length to establish a central peak of the gas fraction is decreasing and a growing number of very large bubbles is present in the flow, the equivalent diameter of which reaches the order of magnitude of the pipe diameter. It is typical for large pipes, that a direct transition from bubbly to the churn-turbulent flow is found (Ohnuki et al, 1996, 2000). As we showed before (section 6.6), the flow contains large bubbles of very irregular shape, that is far from classical Taylor bubbles found in small pipes. The flow regime attributed to the conditions shown in Fig. 8.7 and Fig. 8.8 is therefore indeed churn-turbulent.

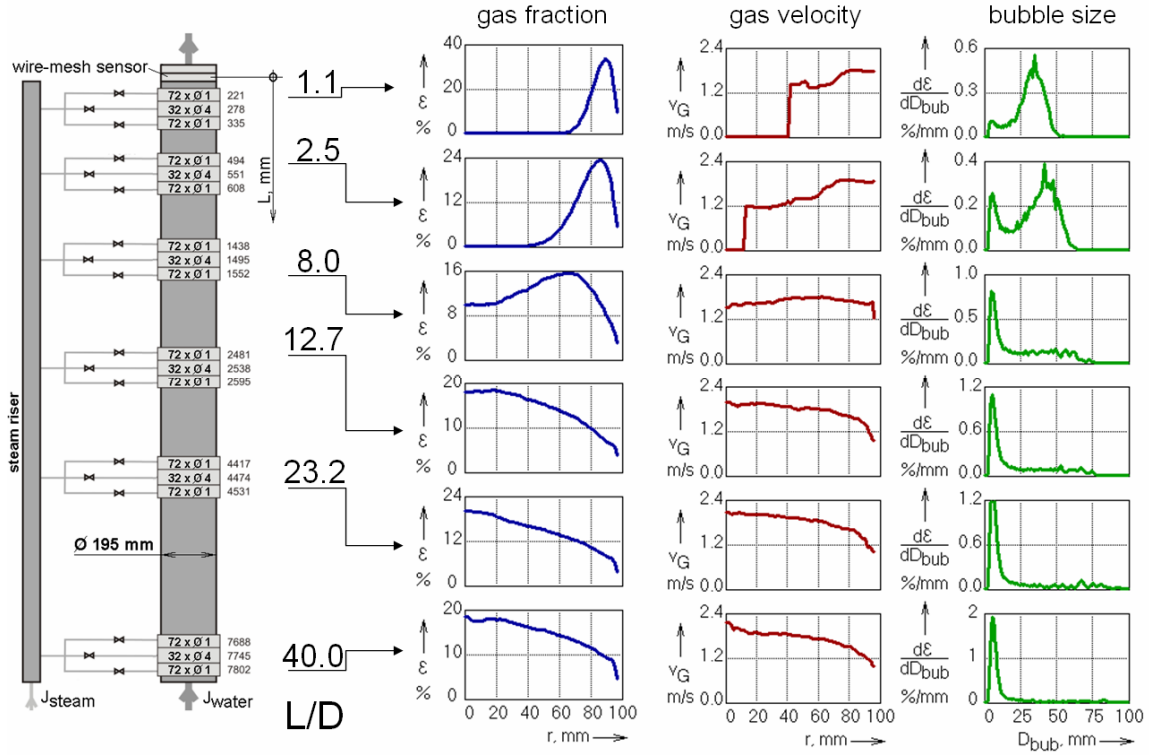

Fig. 8.5 Gas fraction and gas velocity profiles as well as bubble size distributions in the test pipe DN200 in an air/water experiment at J_L = 1 m/s and **$J_{N,G}$ = 0.22 m/s**, T = 30 °C, p = 0.12 MPa at sensor position, gas injection orifices: D_{inj} = 1 mm

Even at those high gas superficial velocities, pronounced wall peaks in the decomposed gas fraction profiles are maintained for the small bubble classes (see Fig. 8.6 and Fig. 8.8), which confirms that the lift force is able to push small bubbles towards the wall even under the conditions of a churn turbulent flow. All radial profiles reach equilibrium at L/D = 12.7 for $J_{N,G}$ = 0.22 m/s and at L/D = 8 for $J_{N,G}$ = 0.53 m/s, while the sizes of the very large bubbles continues to grow.

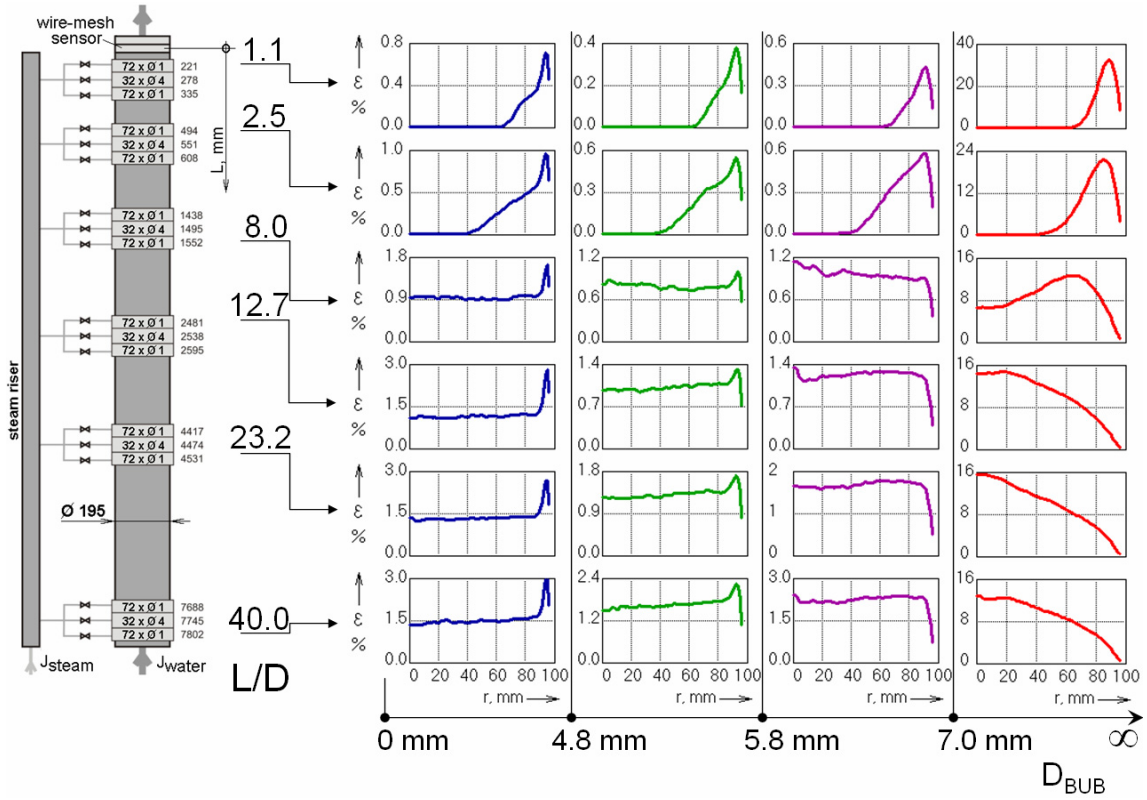

Fig. 8.6 Gas fraction profiles decomposed according to bubble size classes in the test pipe DN200 in an air/water experiment at J_L = 1 m/s and **$J_{N,G}$ = 0.22 m/s**, T = 30 °C, p = 0.12 MPa at sensor position, gas injection orifices: D_{inj} = 1 mm

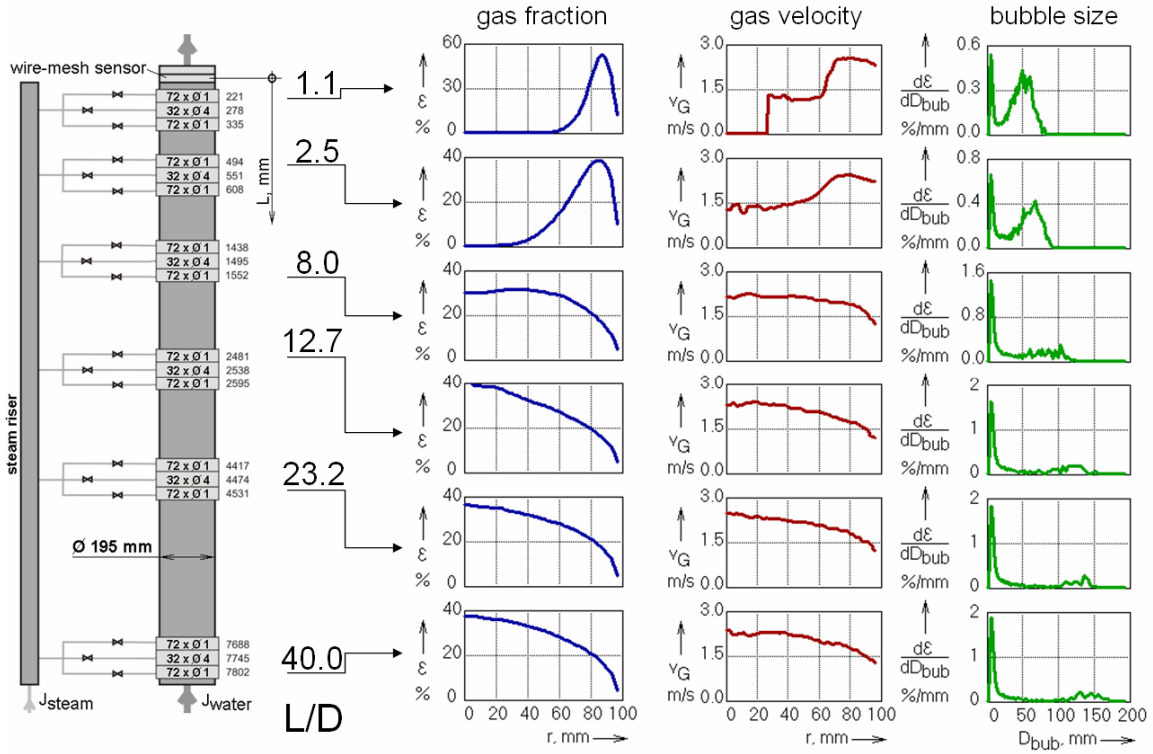

Fig. 8.7 Gas fraction and gas velocity profiles as well as bubble size distributions in the test pipe DN200 in an air/water experiment at J_L = 1 m/s and **$J_{N,G}$ = 0.53 m/s**, T = 30 °C, p = 0.12 MPa at sensor position, gas injection orifices: D_{inj} = 1 mm

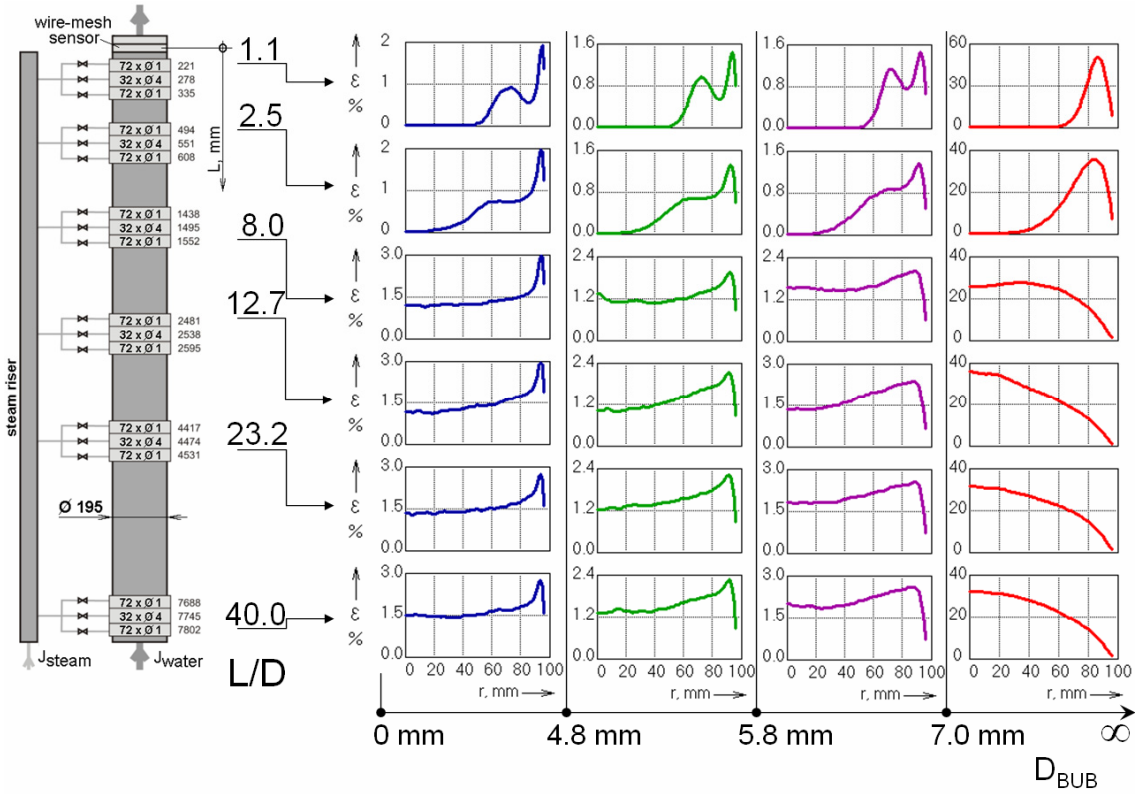

Fig. 8.8 Gas fraction profiles decomposed according to bubble size classes in the test pipe DN200 in an air/water experiment at J_L = 1 m/s and **$J_{N,G}$ = 0.53 m/s**, T = 30 °C, p = 0.12 MPa at sensor position, gas injection orifices: D_{inj} = 1 mm

8.3.2 Steam/water experiments at 65 bar

For the experiments performed at high temperature that we are able to present here, only one wire-mesh sensor (Fig. 8.9) was available, since the second one is still under construction. For this reason, a gas phase velocity measurement could not be performed. The lack of reliable velocity information did not allow extracting distributions of the equivalent diameter of the bubbles, since the velocity has to be known for calculating the correct volume of the gas bubbles identified in the wire-mesh data array. The diameter in a horizontal plane was used instead (see section 4.4.4).

Due to the high efforts represented by the experiments at high pressure at the large test section, the test matrix was focused to the most important combinations of superficial velocities as shown in Fig. 8.10. Main attention was given to the variation of the steam mass flow at a constant superficial liquid velocity of J_L = 1 m/s. For selected points, the liquid superficial velocity was varied in order to study its influence.

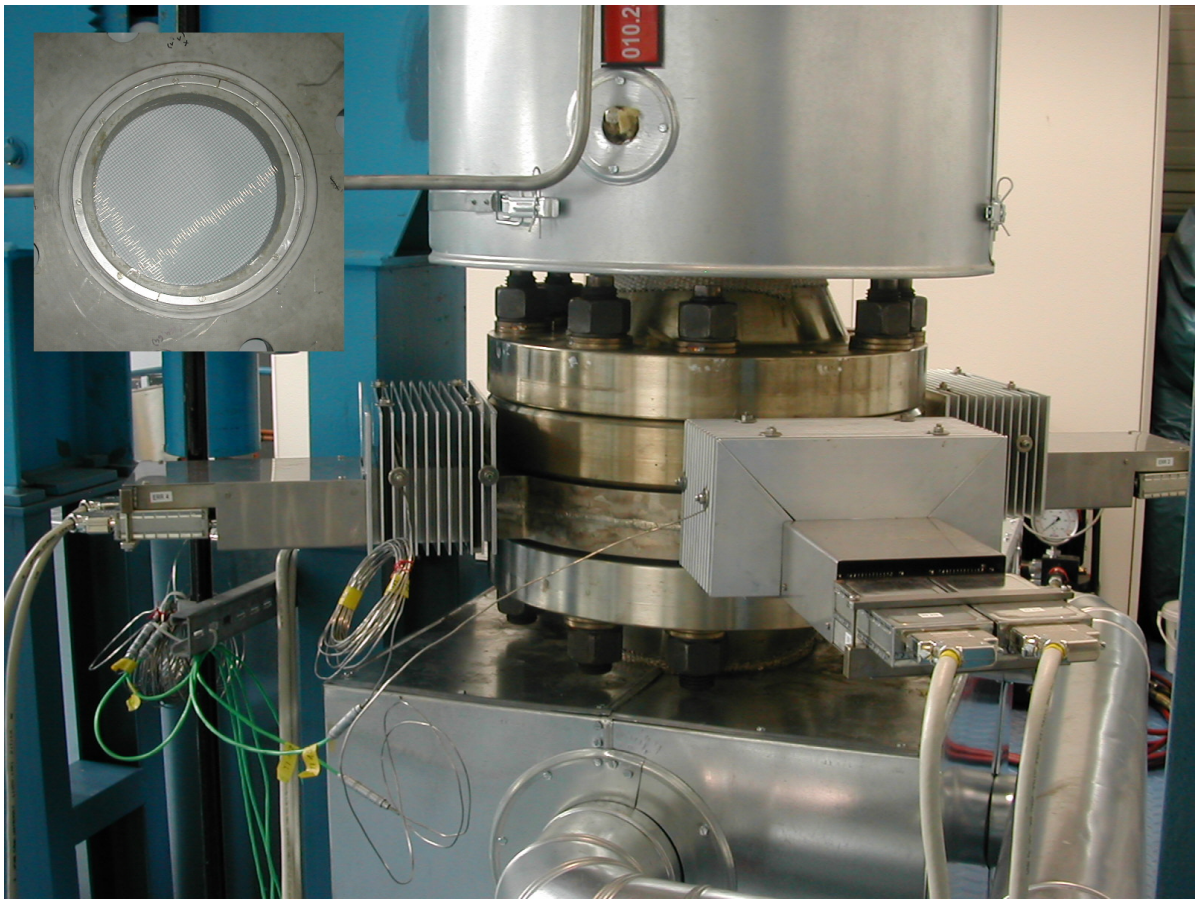

Fig. 8.9 Wire-mesh sensor for high-pressure tests in mounting position at the test pipe DN200

J_{water} m/s \ J_{steam}, m/s	0.0025	0.004	0.0062	0.0096	0.0151	0.0235	0.0368	0.0574	0.0898	0.14	0.219	0.342	0.534	0.835	1.305	2.038	3.185	4.975	7.772	12.14	18.97
4.047	011	022	033	044	055	066	077	088	099	110	121	132	143	154	165	176	187	198	209	220	231
2.554	010	021	032	043	054	065	076	087	098	109	120	131	142	153	164	175	186	197	208	219	230
1.611	009	020	031	042	053	064	075	086	097	108	119	130	141	152	163	174	185	196	207	218	229
1.017	008	019	030	041	052	063	074	085	096	107	118	129	140	151	162	173	184	195	206	217	228
0.641	007	018	029	040	051	062	073	084	095	106	117	128	139	150	161	172	183	194	205	216	227
0.405	006	017	028	039	050	061	072	083	094	105	116	127									
0.255	005	016	027	038	049	060	071	082	093	104	115	126									
0.161	004	015	026	037	048	059	070	081	092	103	114	125									
0.102	003	014	025	036	047	058	069	080	091	102	113	124									
0.0641	002	013	024	035	046	057	068	079	090	101	112	123									
0.0405	001	012	023	034	045	056	067	078	089	100	111	122									

all pressures (1, 2, 4, 6.5 MPa)

6.5 MPa, L/D=40 D_{inj}=0.8 mm

6.5 MPa, all L/D

at selected pressure levels

Fig. 8.10 Test matrix of steam/water experiments performed at the large DN200 test section with the variable gas injection system (detailed information see appendix A2: D12 and D13)

Some of the data was used to perform a qualitative study of the influence of pressure and saturation temperature to the flow pattern. In Fig. 8.11, virtual side projections and virtual sectional views obtained from data measured in the DN50 pipe are shown for a combination of liquid and gas superficial velocities typical for a fully established slug flow at ambient pressure and temperature.

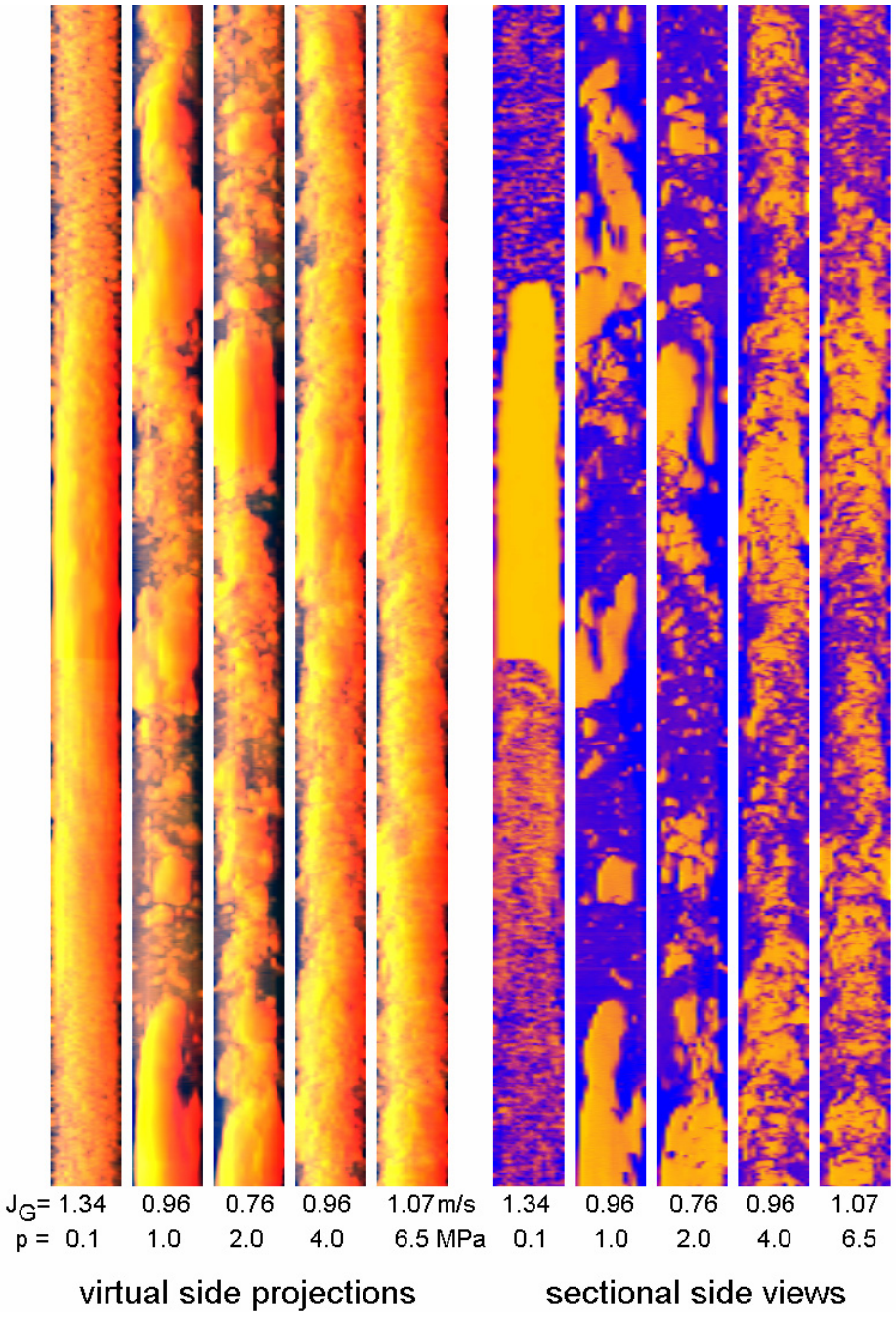

Fig. 8.11 Visualization of wire-mesh sensor data obtained in the pipe ∅ 52.3 mm, J_L = 1 m/s, J_G = $J_{R,G}$; L/D = 151.2

The inlet length was kept constant at the maximum available at the small test section (L/D = 151.2). In steam/water tests, it is not able to fully rely on the injected gas flow rate to provide the superficial gas velocity at the measuring position, since a certain part of the steam is condensed. The superficial gas velocities indicated in the figure were therefore reconstructed from measured gas fraction and gas velocity profiles. In order to match the test point selected for air/water flow, steam/water points with a

higher injected steam flow rate had to be chosen in a way, that the superficial velocities at the measuring position are as close as possible to the value in the air/water test.

It is clearly visible, that the increase of pressure and correspondingly saturation temperature leads to a loss of the slug flow structure with the characteristic large Taylor bubbles. This is due to the decreasing surface tension with growing temperature. The flow structure approaches a churn-turbulent flow regime at p = 6.5 MPa.

A similar tendency was found also in the DN200 pipe (Fig. 8.12). At identical superficial gas and liquid velocities, the slug flow is already not found in the air water case (see section 6.3). With increasing pressure and temperature, the typical large bubble structures found in the air/water flow dissolve into a chaotic gas/liquid mixture, i.e. the churn-turbulent character of the flow pattern becomes more and more pronounced.

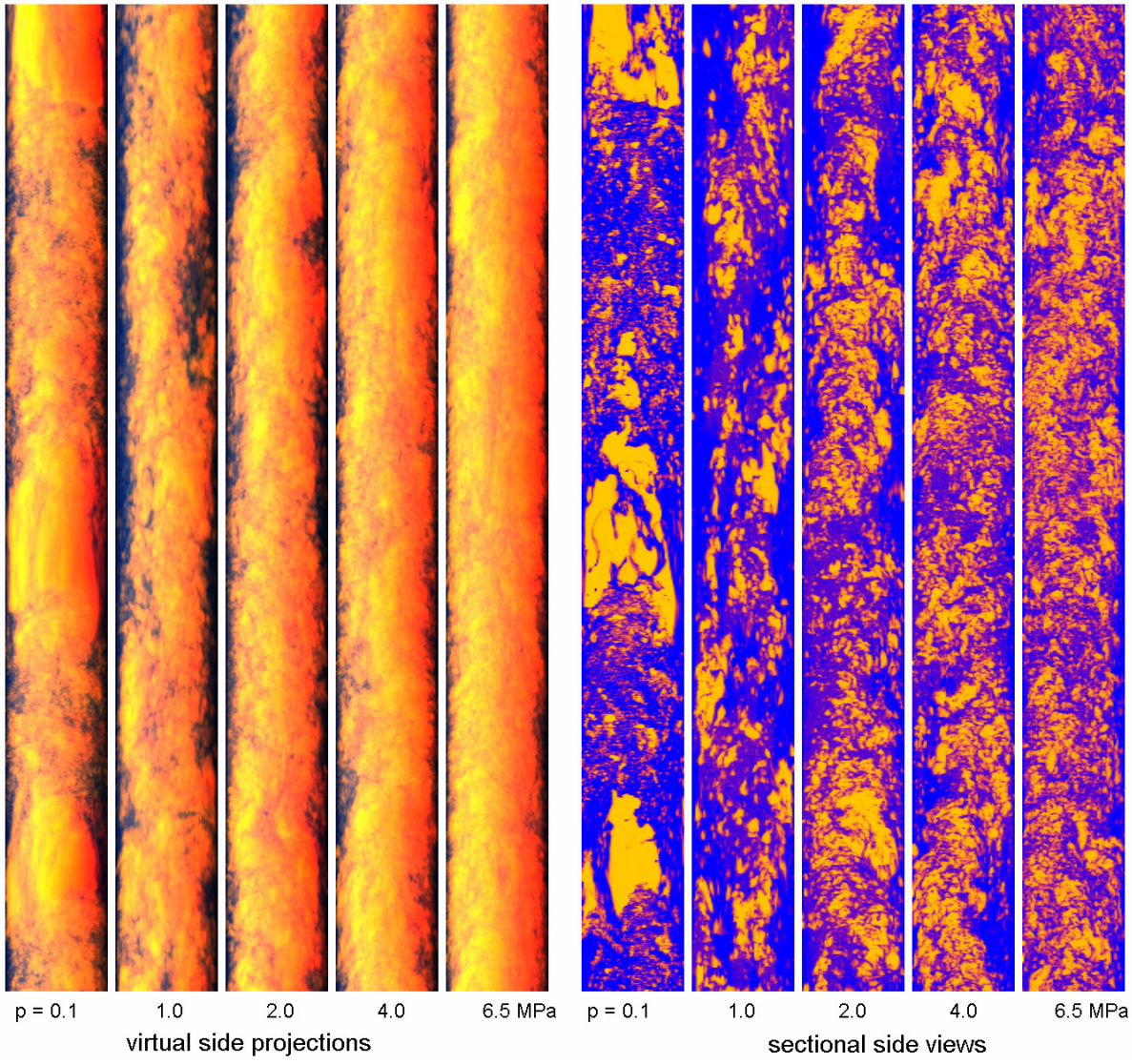

Fig. 8.12 Visualization of wire-mesh sensor data obtained in the pipe ∅195.3 mm; J_L = 1 m/s, $J_{R,G} \cong$ 0.84 m/s, L/D = 39.7

The evolution of radial gas fraction profiles reveal interesting details of the influence of the vapour density on the inertia of the gaseous phase, especially at high gas

injection rates (Fig. 8.13). It the same superficial velocity, the radial profile is much earlier reaching the equilibrium central-peaked shape in case of high pressure. Already starting from L/D = 1.4 a large part of the injected steam arrived at the axis of the DN200 pipe, while the air at ambient pressure does not arrive at radial positions below r = 40 mm at the boundary conditions selected in the figure. The larger density of the pressurized steam leads to a higher inertia and consequently the steam beams injected by the gas injection nozzles in radial direction penetrate much deeper into the main flow than in case of the air injection, despite of the fact, that the injection velocities are identical due to the equal superficial velocities in both cases.

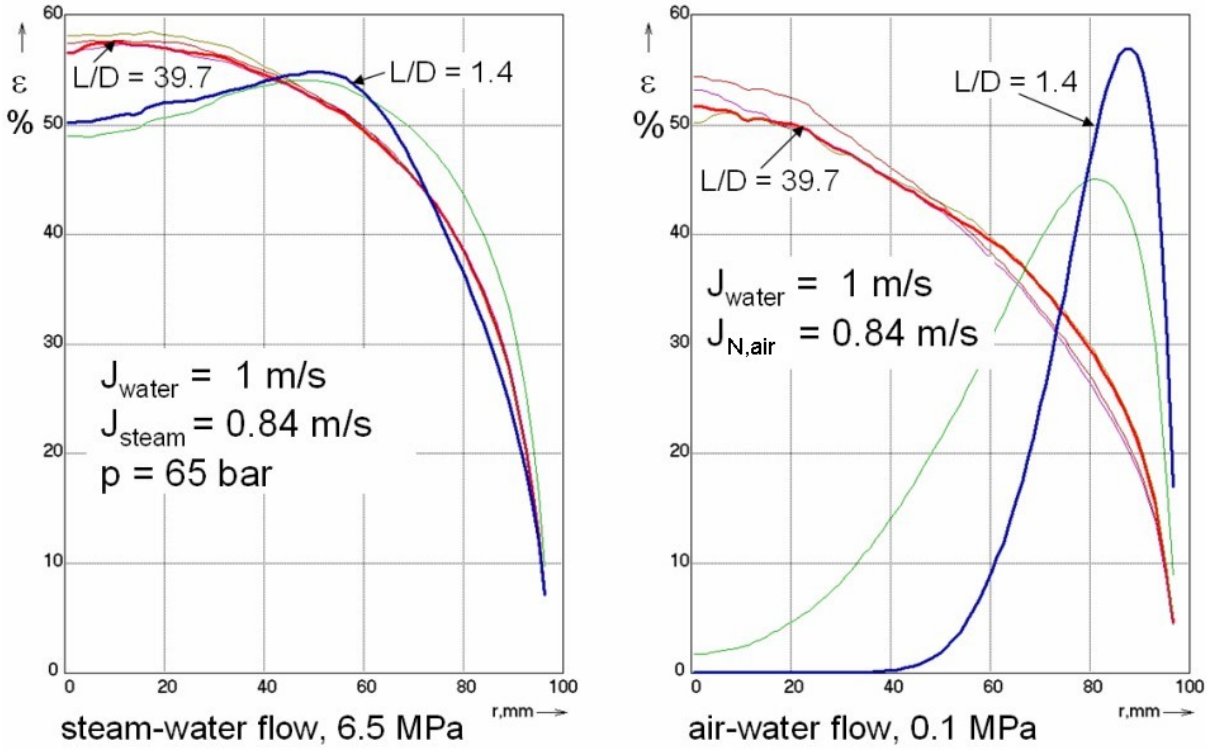

Fig. 8.13 Radial gas fraction profiles - significant pressure influence at high superficial gas velocities

The hypothesis of the dominating effect of inertia on the penetration of the gaseous beams in radial direction can be validated by checking the scalability of the effect with the Wallis parameter. If the superficial air velocity is increased until the Wallis parameter for the gaseous phase is brought close to the value in case of the steam/water experiment at 6.5 MPa, the radial profiles of the void fraction become similar in shape (Fig. 8.14). The increase of the injection velocity compensates the smaller density in the kinetic energy of the injected gas beams. Of course, the absolute void fractions are higher in case of the air injection because of the higher superficial velocity in correspondence with the drift flux model.

The flow regimes at superficial velocities of 1 m/s for liquid and 0.09, 0.34 and 0.84 m/s for the gaseous phase ($J_{N,G}$) have been selected as representative results for illustration of the evolution of bubble-size distributions. Gas was injected through orifices of 1 mm diameter (Fig. 8.15) as well as through orifices of 4 mm diameter (Fig. 8.16 and Fig. 8.17). Significant differences were found compared to the corresponding air/water experiments.

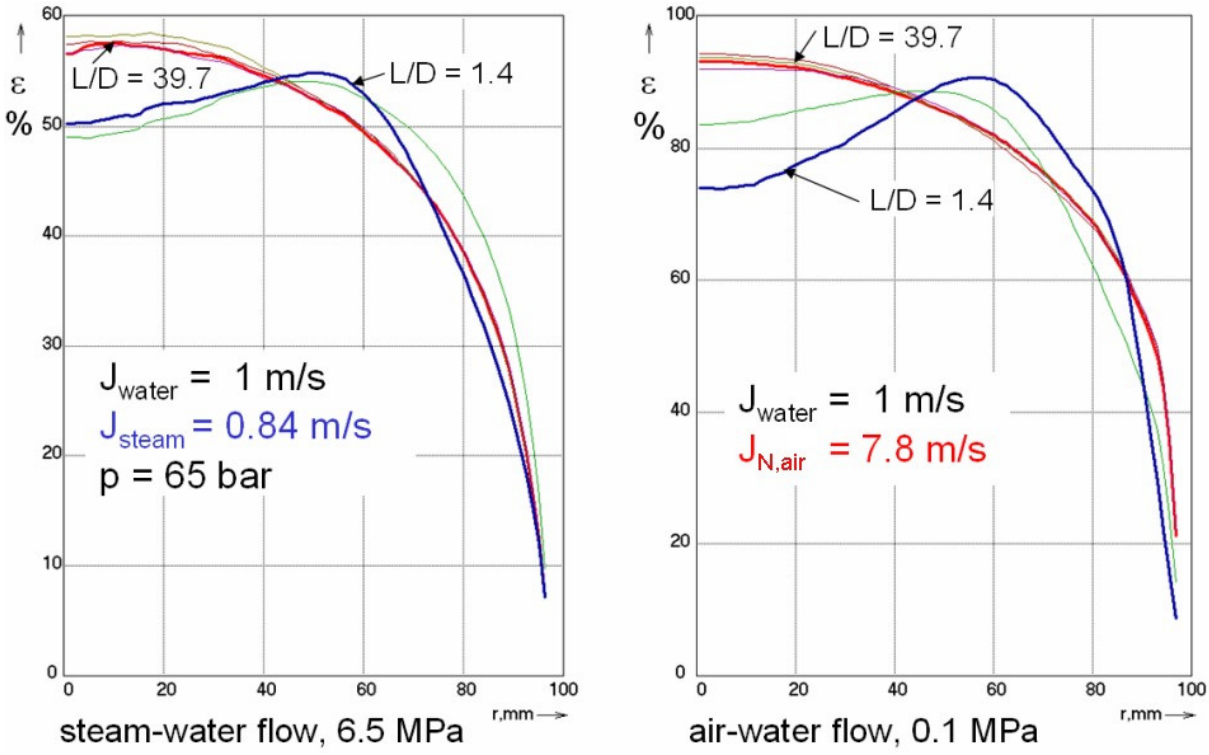

Fig. 8.14 Radial gas fraction profiles - Wallis parameter scales steam penetration depth

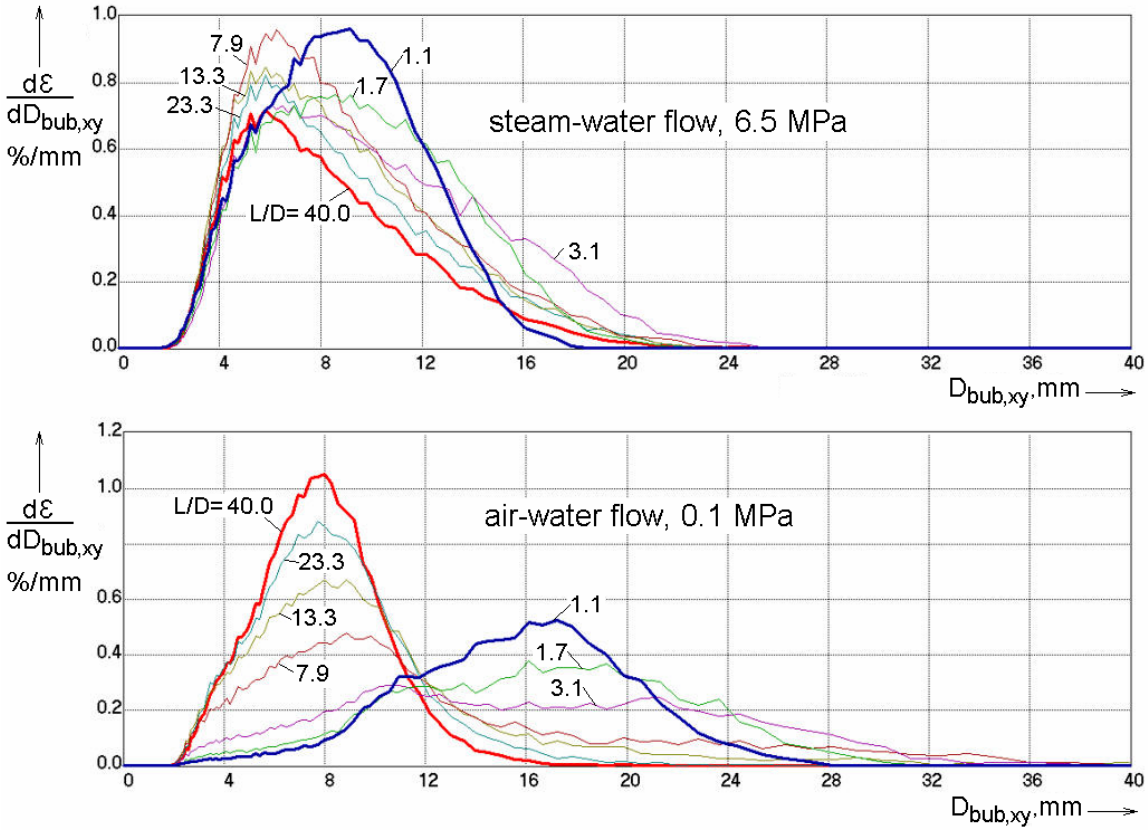

Fig. 8.15 Bubble size distributions in the test pipe DN200 at J_L = 1 m/s and **$J_{steam} = J_{N,air} = 0.09$ m/s**, gas injection orifices: D_{inj} = 1 mm

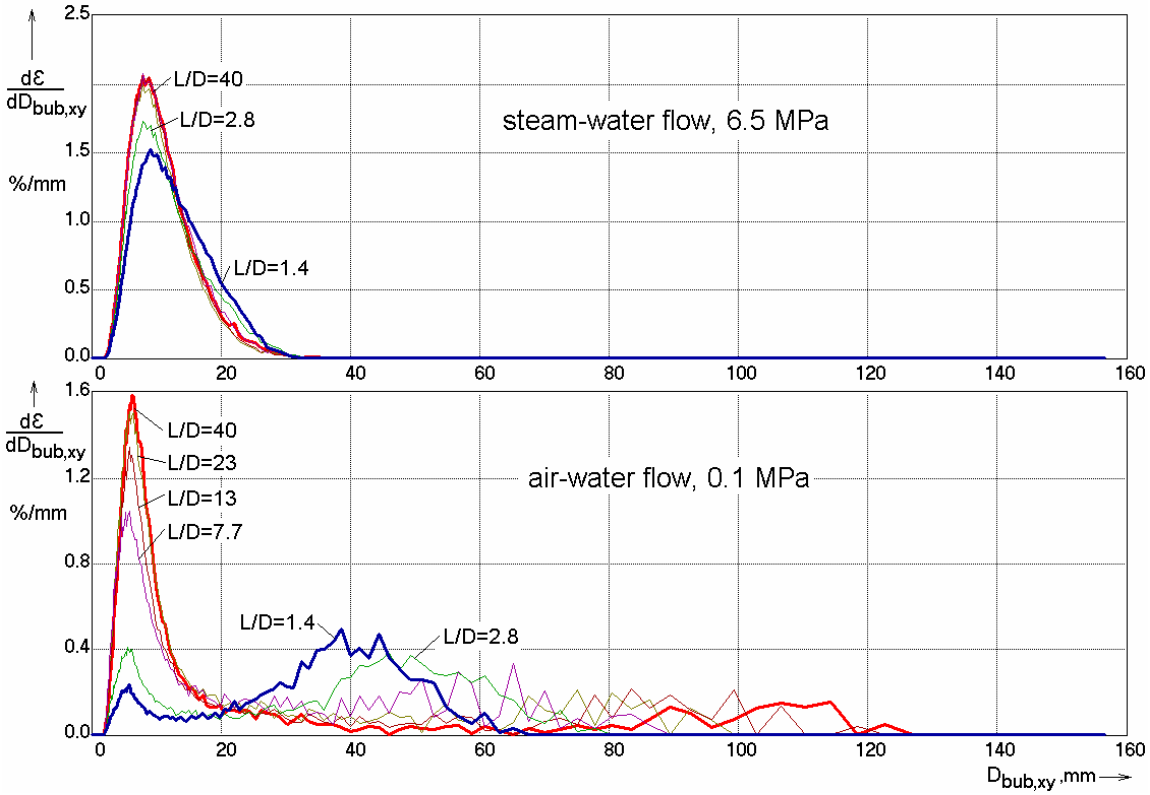

Fig. 8.16 Bubble size distributions in the test pipe DN200 at J_L = 1 m/s and **$J_{steam} = J_{N,air} = 0.22$ m/s**, gas injection orifices: D_{inj} = 4 mm

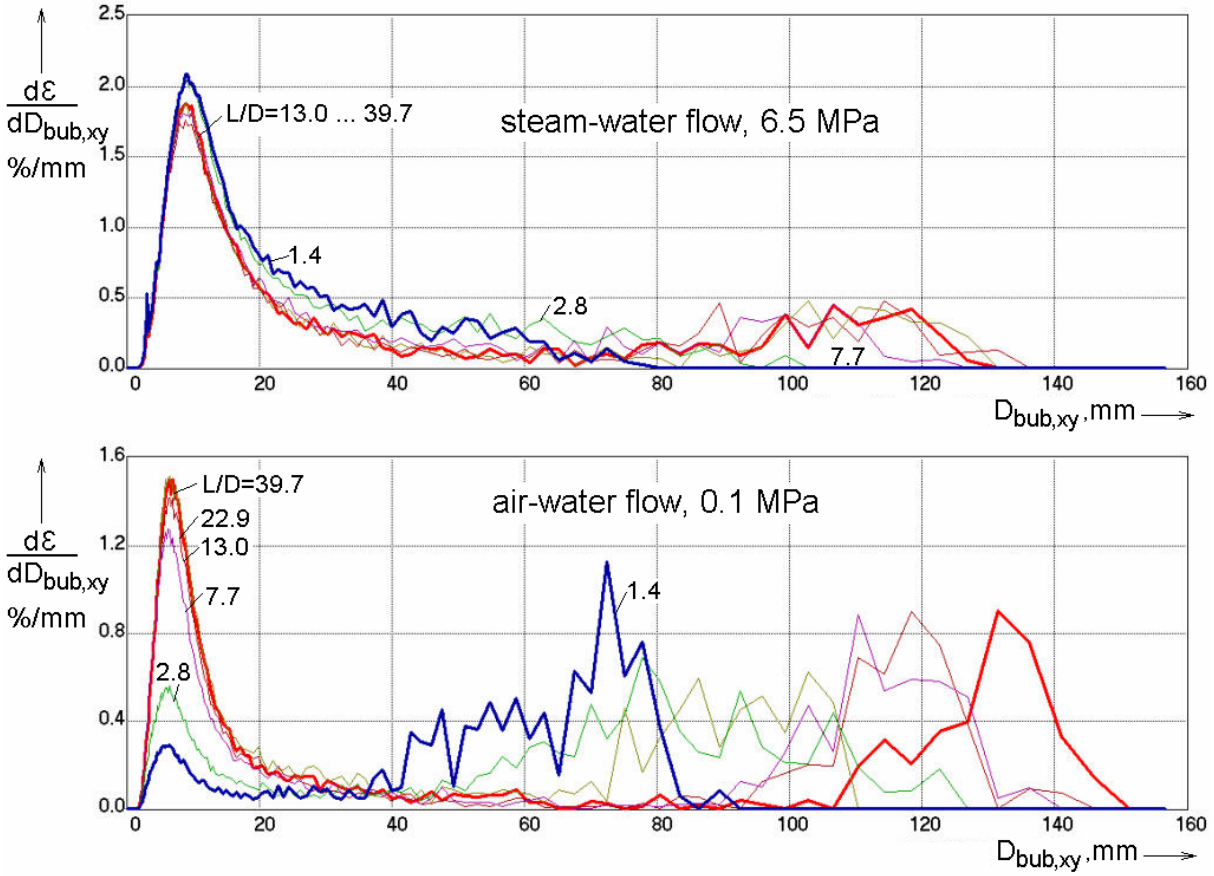

Fig. 8.17 Bubble size distributions in the test pipe DN200 at J_L = 1 m/s and **$J_{steam} = J_{N,air} = 0.84$ m/s**, gas injection orifices: D_{inj} = 4 mm

At all three superficial gas velocities in both the air/water and the steam/water cases, the bubble size distributions converge to equilibrium profiles, although the equilibrium is reached much earlier in case of the steam/water flow at 6.5 MPa. Starting from about L/D = 7 the distributions become identical in all three steam/water tests, while in the air/water experiment there is still a significant evolution even at L/D = 40. In case of J_G = 0.09 m/s this concerns the continuation of a decrease in the bubble sizes (Fig. 8.15, bottom), while at higher gas flow rates large bubble with equivalent diameters above 50 mm continue to grow (Fig. 8.16 and Fig. 8.17, bottom).

Furthermore, it is evident that the steam/water flow at 6.5 MPa shows much less tendency to form large bubbles. The test at J_G = 0.22 m/s is an extreme example. Here, large bubbles with an equivalent diameter of more than 50 mm were formed in the air/water experiment, while such large bubbles are completely missing in the steam/water test (Fig. 8.16). At J_G = 0.84 m/s, which is deeply in the region of churn-turbulent flow, the gas fraction transported by the very large bubble fraction is significantly higher in case of the air/water flow (Fig. 8.17).

On the other hand, the equilibrium bubble sizes in the small bubble fraction are significantly higher in the steam/water tests compared to the air/water experiments. The peak in the bubble size region between 0 and 20 mm is much wider in case of the hot experiments.

Before analysing radial profiles decomposed according to bubble-size classes, it has to be kept in view that the bubble diameter of the inverse of the lift force according to Tomiyama (1998) depends on the physical properties of the fluid, since it is defined by a critical Eötvös number. At high pressure and temperature the surface tension of water is significantly lower than at ambient conditions. The critical bubble diameter therefore decreases with growing saturation pressure (Fig. 8.18). At 6.5 MPa this diameter is $D_{bub,cr}$ = 3.5 mm. Therefore, the boundaries of the bubble size classes were modified in Fig. 8.19 compared to Fig. 8.2, Fig. 8.6 and Fig. 8.8. When the smallest class is defined for bubble diameters from 0 to 3.5 mm again a stable wall peak for small bubbles is detected (Fig. 8.19). The reported case is a flow at J_{steam} = 0.22 m/s. Although the share of bubble of less than 3.5 mm diameter is quite small, the established wall peak is clearly visible. The flow structure is fully developed at about L/D = 13.

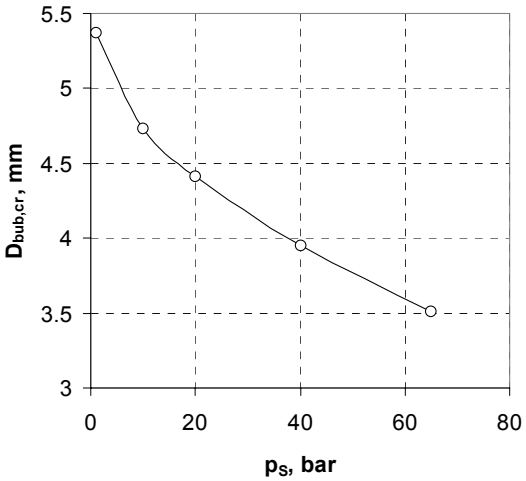

Fig. 8.18 Decrease of the critical equivalent bubble diameter of the lift force inverse with growing saturation pressure

A detailed insight into the conditions close to the wall for fully developed flow conditions (L/D = 40) is given in Fig. 8.20, where the gas fraction profiles are resolved in steps of the diameter in xy-direction of 0.5 mm. The class of the smallest bubbles ranges from 0 to 3.5 mm. It is clearly visible, that the bubble diameters producing a pronounced wall peak are much higher in case of the air/water experiment compared to the steam/water test at 65 bar.

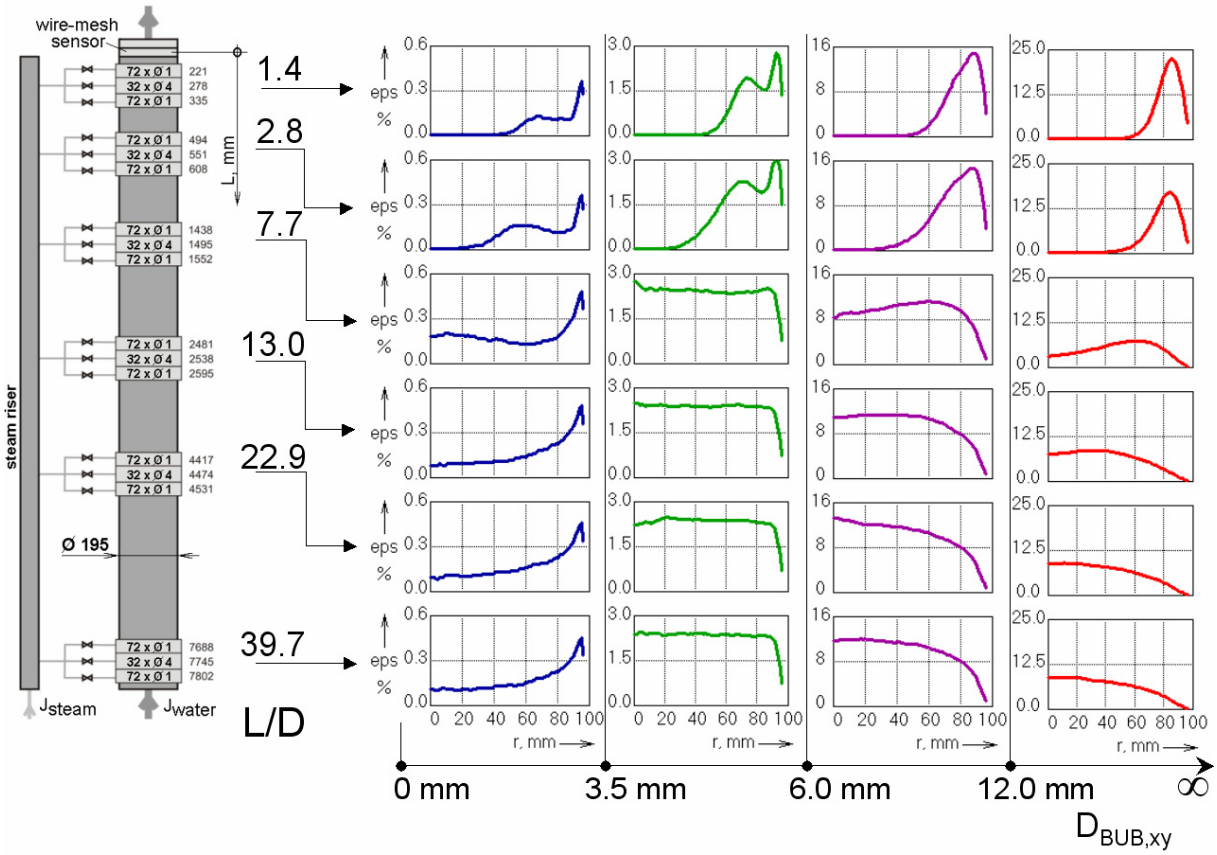

Fig. 8.19 Gas fraction profiles decomposed according to bubble size classes in the test pipe DN200 in a steam/water test at J_L = 1 m/s and **J_{steam} = 0.22 m/s**, T = 280 °C, p = 6.5 MPa at sensor position,
gas injection orifices: D_{inj} = 4 mm

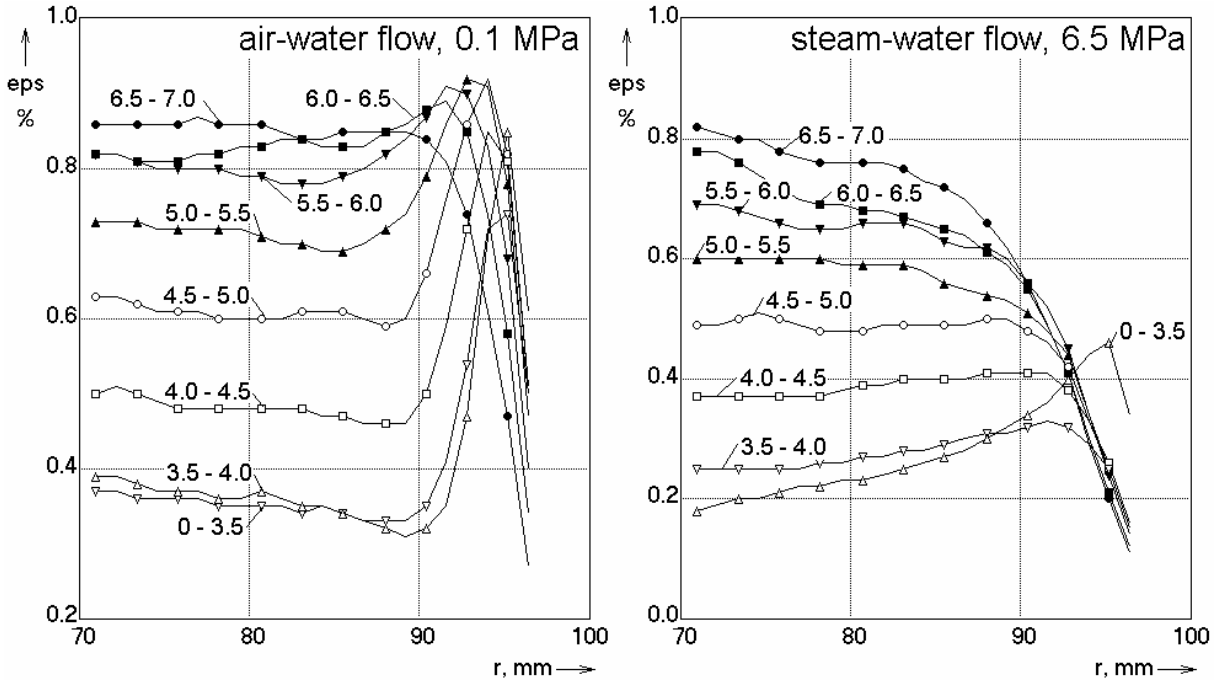

Fig. 8.20 Gas fraction profiles decomposed according to bubble size classes in the test pipe DN200 at J_L = 1 m/s and **$J_{N,G}$ = J_{steam} = 0.22 m/s**, L/D = 40,
gas injection orifices: D_{inj} = 4 mm

The fact that a wall peak is still observed for bubble diameters slightly bigger than the critical ones predicted by the correlation of Tomiyama (1998) can be explained by the permanent production of larger bubbles due to coalescence that still contribute to the profiles while moving away from the wall.

9. Measurement of interfacial area concentrations with wire-mesh sensors

9.1 Literature overview

In two-fluid models, the concept of adding an interfacial area transport equation to the set of conservation equations for mass, momentum and energy is a way to consider the dynamics of the gas/liquid boundary. The local instantaneous formulation of the interfacial area concentration was introduced by Kataoka & Ishii (1986). It is applied in 1D thermal hydraulic codes and seems to be promising to enhance the capabilities of 3D two-phase CFD modelling as well (Prasser, 2006b). The interfacial area density can be divided into bubble-size classes, which increases the accuracy of the predictions (Hibiki & Ishii 2000, Fu & Ishii 2002a, 2002b). The transport equations for either an integral interfacial area concentration or, even more complicated, a set of equations for more than one bubble-size class contain conservation terms as well as source and sink terms that have to reflect bubble coalescence and break-up, two effects that contribute to interfacial area changes and to bubble transition from one class into another. While the conservation terms are easy to formulate, source and sink terms have to be derived from experiments, or obtained by a mechanistic approach and validated against experimental data. Numerous papers deal with the determination of empirical coefficients that take into account phenomena like wake entrainment, random bubble collision, fragmentation due to turbulent impact.

Since the work of Ishii (1975), who demonstrated that the interfacial area concentration is proportional to the sum of the reciprocal individual velocities of the phase boundary passing a given location, double and four tip probes were developed to measure local interfacial area concentrations (Kataoka et al., 1986). Starting from double-tip probes sufficient to measure the velocity of a vertically rising spherical bubble impinged in its centre, the development arrived at four-point probes, where the orientation of the normal vector of the gas liquid interfacial is derived from the pattern of the time delays between the instants of contact of the bubble with the individual tips of the probe. In this way, the method is now applicable to elliptically deformed bubbles as well, which can arrive at the probe tip in an arbitrary direction. Microprobes for such measurements were developed by Kim & Ishii (2001). Numerous papers deal with the measurement of interfacial area concentrations in vertical pipes, annular as well as rectangular channels with both upwards and downwards gas/liquid flow.

There are three motivations for seeking alternatives to needle probes: (1) it is not clear if the concept of Ishii (1975) can be transferred to flows with large and highly deformed bubbles or, with other words, which are the limits of the concept in two-phase flows with high volumetric gas fractions, (2) experiments with local point probes are very time-consuming, when they aim at characterising the flow structure over the entire cross-section of a duct, since they have to be traversed for a complete scan at least over the diameter of a pipe, for example. Beside the required long

experiment runs, it is impossible to obtain information about the flow structure in transient situations, (3) finally both optical and electrical local probes are very delicate devices hardly suitable for high-pressure / high-temperature experiments.

9.2 Methodology

Wire-mesh sensors were applied to measure the interfacial area concentration in a vertical pipe of 195.3 mm inner diameter as an alternative to the mentioned above probes. Its measuring data is represented by a three-dimensional matrix of local instantaneous gas fractions representing a time sequence (sampling frequency 2.5 kHz) of two-dimensional gas fraction distributions (resolution in x-y direction: 3 mm). Velocity information necessary to convert the time axis in an Eulerian z-axis was obtained by cross-correlating the signals of two identical mesh sensors located at a small distance behind each other. Bubbles are identified as regions of connected elements in the data array that are filled with the gaseous phase. The method used to deduce the interfacial area concentration from the wire-mesh sensor data consists in a full reconstruction of the gas/liquid interface. The interfacial area of each bubble is recovered as the sum of the surface area of all surface elements belonging to the given bubble.

The method was applied to a vertical air/water flow. Since the distance between the sensors and the gas injection was varied, it was possible to characterize the change of the interfacial area concentration along the pipe. A combination with bubble size measurements allowed the decomposition of the interfacial area concentration into classes belonging to different bubble sizes. The use of mesh sensors proved to be very efficient, since a bubble-size decomposed interfacial area concentration measurement in an entire pipe cross-section can be performed in a few seconds, which is very efficient compared to the use of local probes.

9.3 Synthetic sensor data

The lack of an accurate reference method for checking the performance of the algorithm developed and described below was compensated using synthetic wire-mesh sensor data. The response of the sensor $\varepsilon_{i,j,k}$ to spherical bubbles was calculated on a grid of 5000 samples of 64x64 elements (i.e. $1 \leq i \leq 64$; $1 \leq j \leq 64$, $1 \leq k \leq 5000$). The lateral pitch was chosen corresponding to the real sensor ($\Delta x = \Delta y = 3$ mm). Bubbles of a well-defined uniform diameter where put onto the three-dimensional domain defined by this grid by choosing their centres with a pseudo-random number generator until either a number of 1000 bubbles was reached or there was no space left for new bubbles. Between all bubbles a gap of at least 5 mm was left. When the arbitrary number generator supplied centre coordinates that result in overlapping of bubbles or in a smaller distance than the given limit, then the corresponding bubble was rejected. In this way, the data domain was filled by detached bubbles, the centres of which are situated on a random position relative to the grid, so that the gas fraction values at the periphery of the bubbles were affected by different discretisation errors.

Depending on the given diameter and the coordinates of the centres of a synthetic spherical bubble, the elements of the array $\varepsilon_{i,j,k}$ are either completely covered or partially touched by bubbles. They were given a gas fraction value according to the part of the element that lies inside the bubble. The calculation of the share of the element filled with gas is performed under the following considerations: (a) the

measuring plane is approximated as indefinitely thin, i.e. it has no extension in axial direction (i.e. in z-direction);

(b) for symmetry reasons, the control volume of a given sensitive crossing point of two wires in the measuring plane is a square spreading between the midlines between the given electrode wire and the neighbouring wires; (c) each bubble that is cut by the measuring plane at a given instant causes a decrease of the measured local current that is approximately proportional to the part of the sensitive square that is covered by the bubble; (d) the bubble moves over a distance of $\Delta z = w_G/f_{sample}$ during the sampling period of the mesh sensor (for the generation of synthetic bubbles, the gas phase velocity w_G is assumed to be constant, while in the evaluation of real measurements the local time-averaged gas velocity was used, which was determined by cross-correlation between two wire-mesh sensors). The assumption of an infinitely thin measuring plane is a good approximation for gas phase velocities around 1 - 2 m/s and a measuring rate of 2500 Hz, because in this case Δz is 0.4 - 0.8 mm, which is much less than the lateral electrode pitches Δx and Δy of 3 mm.

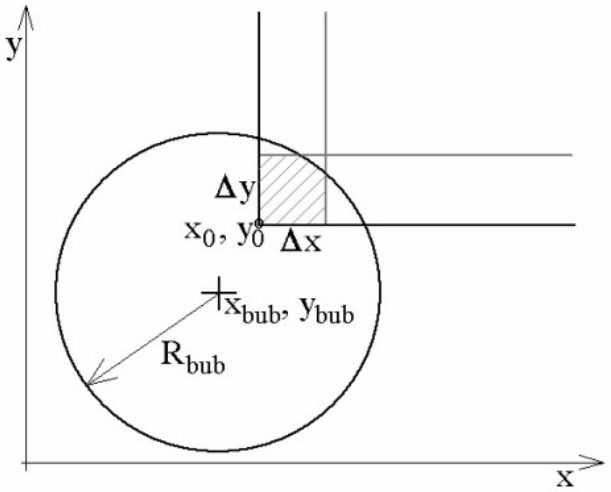

Fig. 9.1 Definition of the area of a part of a square covered by a circle

For the geometrical configuration given in Fig. 9.1 the area that is cut by an 90 deg corner the sides of which is parallel to the x and y axes can be expressed as follows:

$$A_{cor}(x_0, y_0) = \frac{1}{2}\left\{ {R_{bub}}^2 \left[\arccos\left(\frac{\Delta x_0}{R_{bub}}\right) - \arcsin\left(\frac{\Delta y_0}{R_{bub}}\right) \right] - \Delta x_0 \sqrt{{R_{bub}}^2 - \Delta x_0^2} - \Delta y_0 \sqrt{{R_{bub}}^2 - \Delta y_0^2} \right\} + \Delta x_0 \Delta y_0 \qquad (27)$$

where $\Delta x_0 = x_0 - x_{bub} \quad \Delta y_0 = y_0 - y_{bub}$.

When the origin of the corner lies outside the circle, this formula has to be modified to match one out of a four different cases that have to be distinguished depending on the quadrant in which the origin of the corner is situated with respect to the centre of the circle (the corresponding formulas are omitted). The area inside the part of a square with the size equal to the electrode pitches Δx and Δy that is covered by the circle is equal to:

$$A_{sq}(x_0, y_0) = A_{cor}(x_0, y_0) - A_{cor}(x_0 + \Delta x, y_0) - A_{cor}(x_0, y_0 + \Delta y) + A_{cor}(x_0 + \Delta x, y_0 + \Delta y) \qquad (28)$$

The local volumetric gas fraction caused by a bubble is calculated by relating the covered area to the sensitive area of the control volume:

$$\varepsilon(x_0, y_0) = \frac{A_{sq}(x_0, y_0)}{\Delta x \cdot \Delta y} \qquad (29)$$

Selected frames of synthetic gas fraction distributions are shown in Fig. 9.2. Since an instantaneous two-dimensional distribution is displayed, the bubbles appear as circles of different diameters, though the spheres all have the same diameter. This is a result of cutting the bubbles at an arbitrary instant of their passage through the virtual measuring plane. Due to the use of random numbers to define the central co-

ordinates of the bubbles, their boundary is affected by discretisation errors in an individual way. This property of the synthetic data allows a comprehensive study on the contribution of the grid discretisation to the error of the algorithms (b) and (c) to calculate the interfacial area.

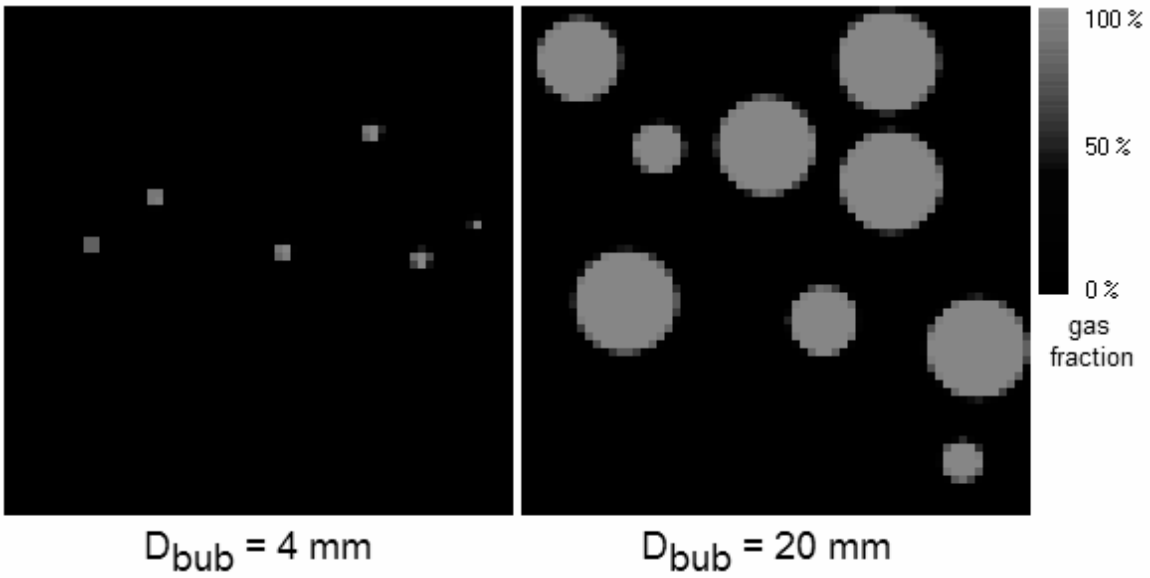

Fig. 9.2 Selected frames from a data sequence of synthetic mono-disperse spherical bubbles

9.4 Interfacial area measurement by full reconstruction of the gas/liquid interface

The full reconstruction of the gas/liquid interface is performed in cuboidal control elements of the dimensions Δx, Δy, Δz ranging from the indexes (i_0, j_0, k_0) to (i_0+1, j_0+1, k_0+1), at the corners of which local instantaneous gas fractions $\varepsilon_{i,j,k}$ are given. The gas/liquid interface is reconstructed for each bubble individually (bubble recognition algorithm see section 4.4.4). For this, the gas fraction is put to zero at those corners of the control element, at which the bubble identificator is unequal to the chosen bubble number:

$$\varepsilon'_{i,j,k,n} = \begin{cases} \varepsilon_{i,j,k} & \text{if} \quad b_{i,j,k} = n \\ 0 & \text{if} \quad b_{i,j,k} \neq n \end{cases} \tag{30}$$

At the bottom ($k = k_0$) and the top ($k = k_0$+1) surface, the length of the bubble boundary ($l_{xy,bub,i,j,k,n}$ for i_0, j_0, k_0) is calculated by connecting points on the edges of the corresponding rectangles at which the gas fraction equals to a threshold value ε_{tr}. For this, the rectangles are divided into triangles by one of the two existing diagonals. The points on the edges of the triangles where the gas fraction is equal to the threshold value are obtained by linear interpolation (Fig. 9.3, left side). From the two existing possibilities for the division into triangles the one with the smaller total lengths of the line representing the bubble boundary is taken (Fig. 9.3, right side). This has proven to supply the best results. Besides $l_{xy,bub,i,j,k,n}$, the part of the area of the rectangle $A_{xy,bub,i,j,k,n}$ that belongs to the bubble is calculated, too. On rectangles, at all four corners of which the gas fraction is either above the threshold, the corresponding length is zero and the area is equal to $\Delta x \cdot \Delta y$, while in case all four gas fractions are below the threshold both length and area are set to zero.

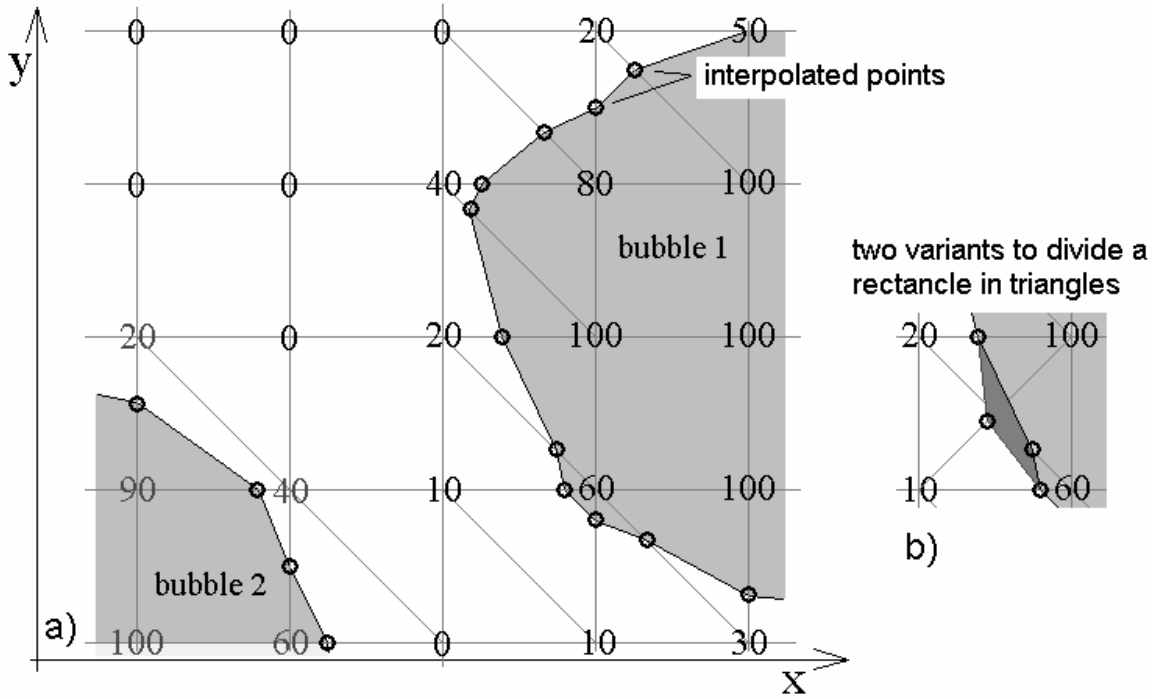

Fig. 9.3 Interpolation of the bubble boundary on the measuring grid for a given threshold

For the calculation of the interfacial area we take benefit from the fact that the height of the control cuboid $\Delta z = w_{bub}/f_{sample}$ is small compared to the extension in x-y directions (compare section 9.3). For such a case, a good approximation for the interfacial area inside the cuboid i, j, k belonging to bubble n is given by:

$$A_{bub,i,j,k,n} \cong \sqrt{\left(\Delta z \frac{I_{xy,bub,i,j,k,n} + I_{xy,bub,i,j,k+1,n}}{2}\right)^2 + \left(A_{xy,bub,i,j,k+1,n} - A_{xy,bub,i,j,k,n}\right)^2} \qquad (31)$$

The interfacial area of a bubble as well as the total interfacial area in the flow domain is obtained by summation:

$$A_{bub,n} = \sum_{i,j,k} A_{bub,i,j,k,n}\,, \quad A_{total} = \sum_{n} A_{bub,n} \qquad (32)$$

At the end, the area A_{total} can again be transformed into an area density by relating it to the total measured volume of the two-phase flow. In case the superficial gas and liquid velocities are known, this leads to the expression:

$$\alpha_{total} = \frac{A_{total}}{(J_G + J_L)\cdot t_{meas}} \qquad (33)$$

It is obvious that the summation in eq. (32) can be restricted to bubbles of a certain bubble size region. In this way, bubble-size resolved interfacial area densities can be obtained.

It has not to be forgotten, that the interfacial area according to eq. (32) and the interfacial area density from eq. (33) depend on the threshold applied to identify the boundary of the bubbles. The definition of an appropriate threshold is therefore an essential task. In case of large bubbles with an extended core region, where the gas fraction is 100 %, a threshold of 50 % seems to be a good choice, while the gas

fraction inside small bubbles may not reach 100 %. The threshold was therefore defined for each bubble individually, i.e. it obtains the bubble identifier as index: $\varepsilon_{tr,n}$. It was proposed to adjust the threshold in a way, that the volume of the three-dimensional region within the boundary defined by the threshold (see Fig. 9.3), further called reconstructed bubble volume, becomes equal to the bubble volume obtained by the sum of the local instantaneous gas fractions in all elements belonging to the bubble (eq. (14)).

The reconstructed volume decreases with growing threshold, since the boundary is shifted towards the centre of the bubble. The part of the volume of each prism in Fig. 9.3 that contributes to the bubble volume can be approximated by multiplying base area by height:

$$V'_{bub,i,j,k,n} \cong \Delta z \cdot \frac{A_{xy,bub,i,j,k,n} + A_{xy,bub,i,j,k+1,n}}{2} \tag{34}$$

The volume of the bubble obtained by surface reconstruction is the sum of all partial volumes belonging to this bubble:

$$V'_{bub,n} = \sum_{i,j,k} V'_{bub,i,j,k,n} \tag{35}$$

The correct value was found by an iterative solution of the following equation that was performed for each bubble individually:

$$V'_{bub,n}\left(\varepsilon_{tr,n}\right) = V_{bub,n} \rightarrow \quad \varepsilon_{tr,n} \tag{36}$$

The reconstruction of the interfacial area of synthetic bubbles with a diameter between 3 to 40 mm is shown in Fig. 9.4. The agreement of the reconstructed surface with the known surface of the synthetic bubbles is nearly perfect. With decreasing bubble size, the scatter characterised by the standard deviation shown in Fig. 9.4 is growing. The scattering of the reconstructed interfacial area is caused by the arbitrary allocation of the centres of the synthetic bubbles within the measuring grid and the resulting variations of the discretisation of the bubble boundary. In general, a slight overestimation of the interfacial area of about 2 % is found for bubbles bigger than 15 mm. The overestimation has its maximum at a bubble diameter of 3 mm, where it reaches about 8 % in the average.

The result of the iteration of the threshold for the determination of the gas/liquid interface is discussed in Fig. 9.5. It can be seen, that the maximum local void fraction ε_{max} inside the synthetic bubbles generally does not reach 100 % for bubble diameters less than 6 - 7 mm, which is likewise true for real bubble signals. This is due to the fact, that these bubbles do not cover the control rectangle completely. The scatter shown in Fig. 9.5 is due to the arbitrary location of the centres of the synthetic bubbles with respect to the discretisation grid, i.e. each individual bubble may have its own maximum gas fraction within a certain range, characteristic for the given diameter. The iteration of the threshold $\varepsilon_{tr,n}$ to fulfil the equation $V'_{bub,n} = V_{bub,n}$, as described above, results in an optimum close to 50 % for large bubbles, while the optimal threshold is significantly below 50 % for smaller bubbles (Prasser & Gregor, 2005c).

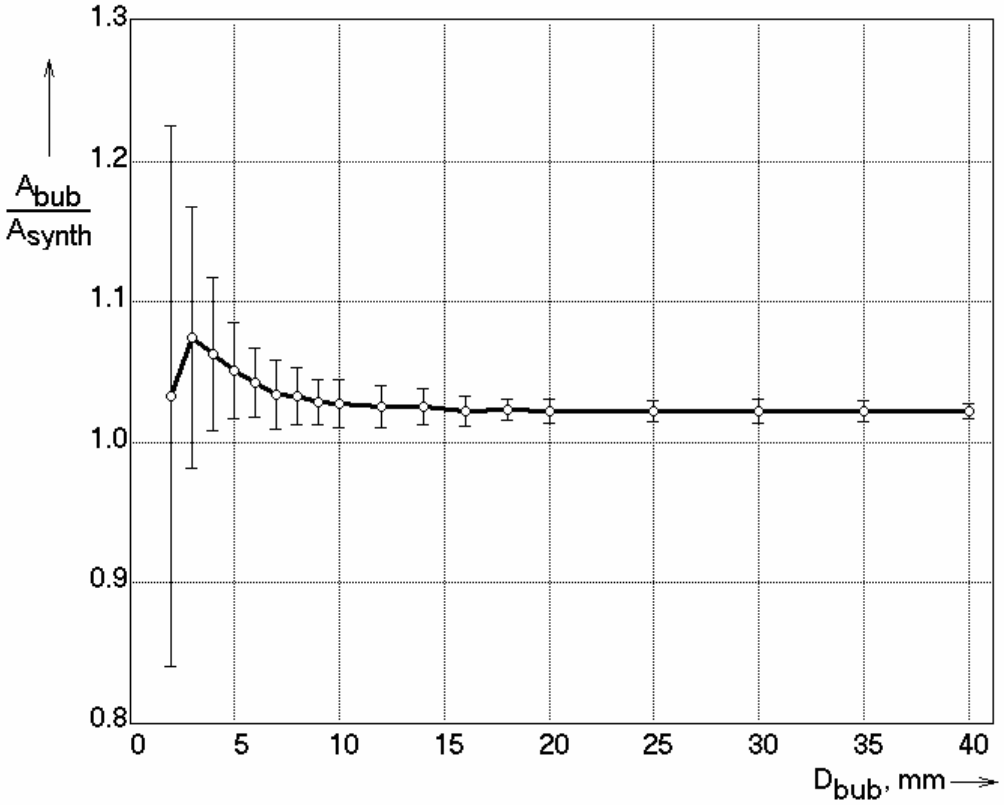

Fig. 9.4 Accuracy of the surface of synthetic bubbles (section 9.3) obtained by full reconstruction of the interface using eq. (32)

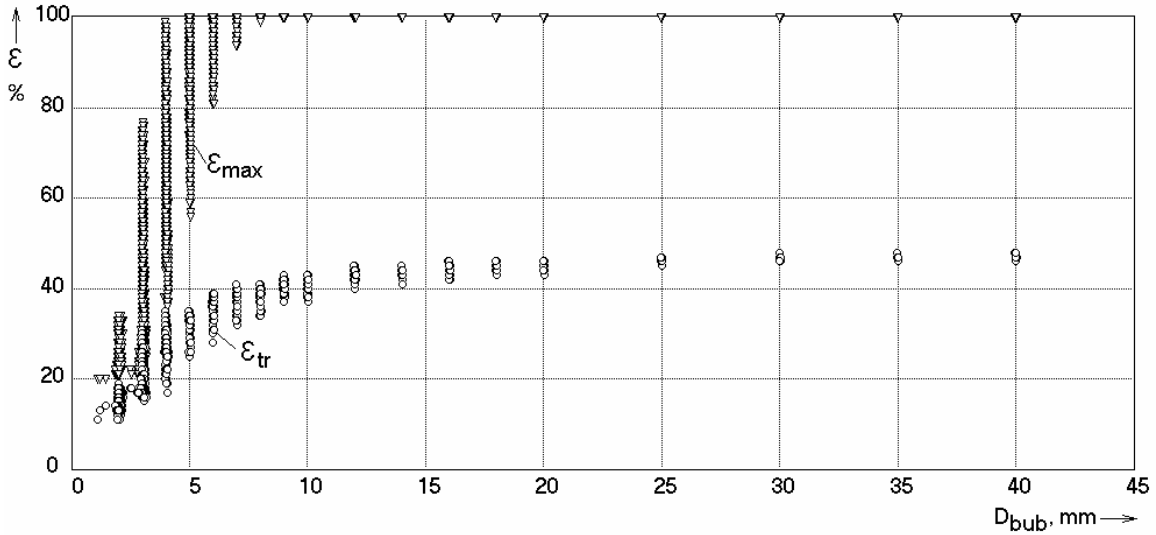

Fig. 9.5 Maximum local instantaneous gas fractions ε_{max} inside synthetic bubbles of selected diameters and the optimal threshold ε_{tr} for the determination of the gas/liquid interface

As an alternative to the described method, it seemed to be convenient to discretize the gas/liquid interface into triangular elements by converting the measuring grid into a grid of tetrahedral elements, the angles of which are identical with the points in which local instantaneous gas fractions are given. This method was found to result in a significant overestimation of the surface area of synthetic bubbles, when

$\Delta z = w_{bub} / f_{sample} << \Delta x$ (or $<< \Delta y$, respectively). It may be a good alternative for nearly cubical control volumes, all the same (Gregor, 2004).

9.5 Experiments

The measuring data analysed origins from the large vertical test section with variable gas injection system (comp. section 2.3). The inlet length between gas injection and mesh sensor was varied from 1.1 to 40. Both air injection diameters are used. The liquid was water at 20 °C at ambient pressure. In all presented tests, the liquid superficial velocity was kept constant at J_L = 1.02 m/s, while the gas superficial velocity was taken from the series $J_{N,G}$ = 0.0096, 0.037, 0.090, 0.22, 0.53 (comp. appendix A2: L01).

A pair of wire-mesh sensors with a matrix of 64x64 measuring points and a sampling frequency of 2500 Hz was used. Samples were taken for periods of 10 s for each flow regime. Velocity profiles were measured by the cross-correlation method.

9.6 Results

The superficial air velocities cover the range from bubbly flow with a wall peaked gas fraction profile to values typical for slug flow with a central void fraction maximum (Fig. 9.6). The bubble-size distributions measured at about L/D = 40 shown in Fig. 9.7 report the appearance of a peak in the range of very large bubbles at $J_{R,G}$ = 0.53 m/s. As shown in section 6.6, these large bubbles do not have a regular shape like Taylor bubbles found in small pipes, but they are heavily deformed by the action of turbulence.

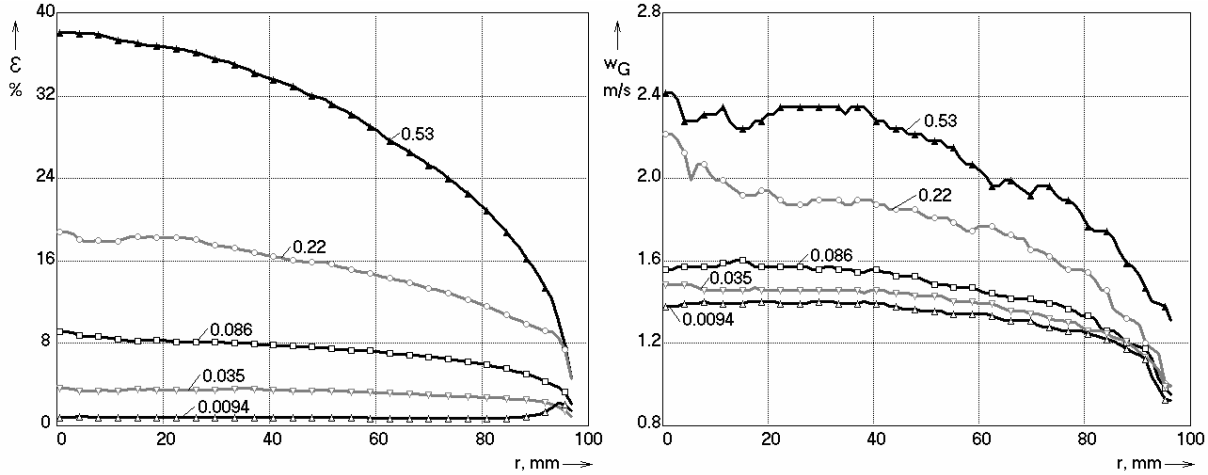

Fig. 9.6 Gas fraction and gas velocity profiles obtained by wire-mesh sensors in the pipe of 195.3 mm inner diameter at L/D ≅ 40 and J_L = 1.02 m/s for different gas superficial velocities $J_{R,G}$ (parameter), gas injection: 72 orifices of 1 mm diameter

The obtained interfacial area density is shown in Fig. 9.8 as a function of the gas superficial velocity for an inlet length of about L/D = 40. As expected, the interfacial area concentration grows with increasing gas superficial velocity. The growth is less steep for superficial gas velocities ($J_{R,G}$) greater than 0.2 m/s. This has to be expected because of the appearance of very large gas bubbles in the flow (see Fig. 9.7).

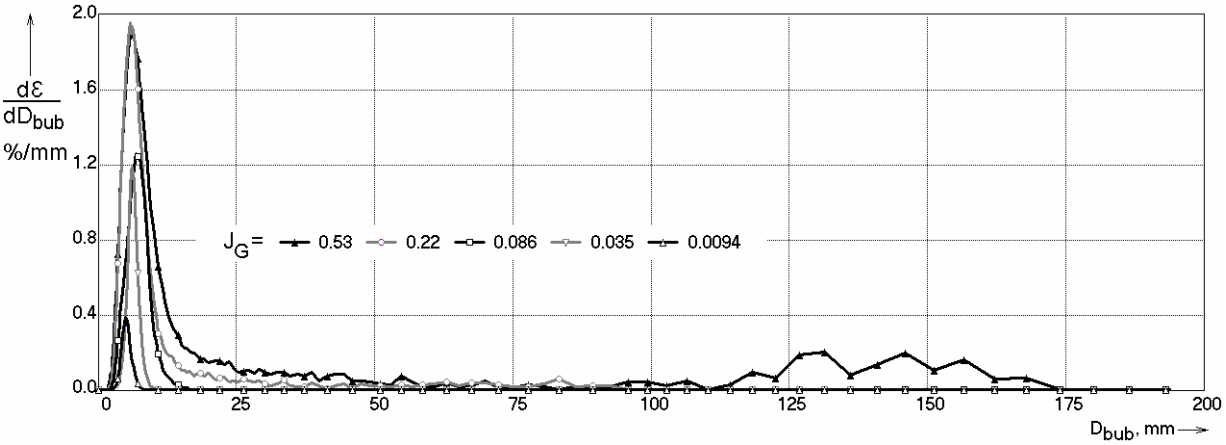

Fig. 9.7 Bubble size distributions obtained by the wire-mesh sensor in the pipe of 195.3 mm inner diameter at L/D ≅ 40 and J_L = 1.02 m/s for different gas superficial velocities $J_{R,G}$

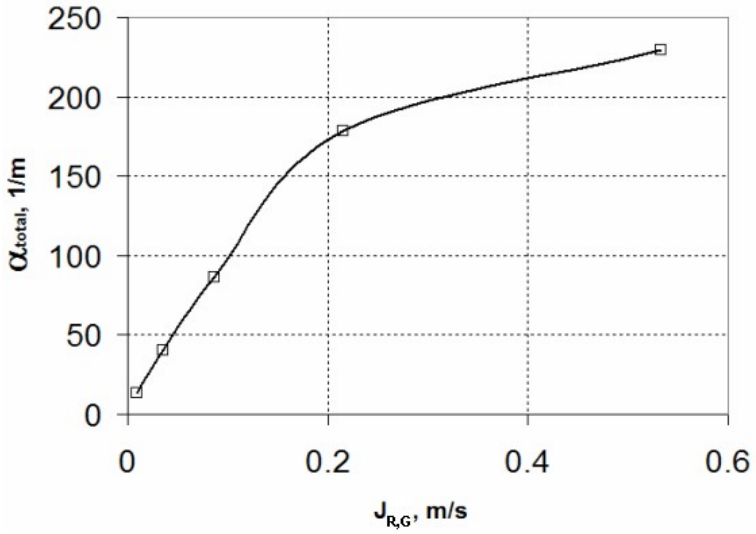

Fig. 9.8 Interfacial area density in the 195.3 mm pipe as a function of the superficial gas velocity, L/D ≅ 40, J_L = 1.02 m/s, gas injection orifices 1 mm

The evolution of the interfacial area density along the pipe is shown in Fig. 9.9. In this figure, the results for both gas injection diameters are compared, too. There is a tendency of convergence between the results for 1 mm and 4 mm injection orifices with growing lengths.

A growing interfacial area density along the pipe is observed at the superficial gas velocities of $J_{R,G}$ = 0.086, 0.22, 0.53 m/s in case of both types of gas injection orifices and also for $J_{R,G}$ = 0.035 m/s for an injection through 4 mm orifices, which points at a preponderance of fragmentation processes in the flow, while the interfacial area density is slightly decreasing for the very small gas flow of $J_{R,G}$ = 0.0094 m/s, which is due to bubble coalescence. It remains nearly constant for $J_{R,G}$ = 0.035 m/s and an injection through 1 mm orifices.

More detailed information can be obtained by calculating interfacial area densities for bubble size classes (Fig. 9.10). Here, for the example of the gas superficial velocity of $J_{R,G}$ = 0.53 m/s, it is illustrated that both coalescence and fragmentation can hide behind a growing total interfacial area density. The area density for bubbles smaller than 15 mm follows the trend for the total area density, while the area density for bigger bubbles decreases. This reflects the fact that the evolution of the flow structure starts from primary bubbles of an intermediate size, which are subject to both break-up and coalescence. This is confirmed, when the bubble size distribution measured close to the gas injection is compared to the distribution established at L/D ≅ 40. The effect of coalescence leads to the appearance of the peak of very large

bubbles, while a peak at about 10 mm is generated by the bubble break-up (Fig. 9.11).

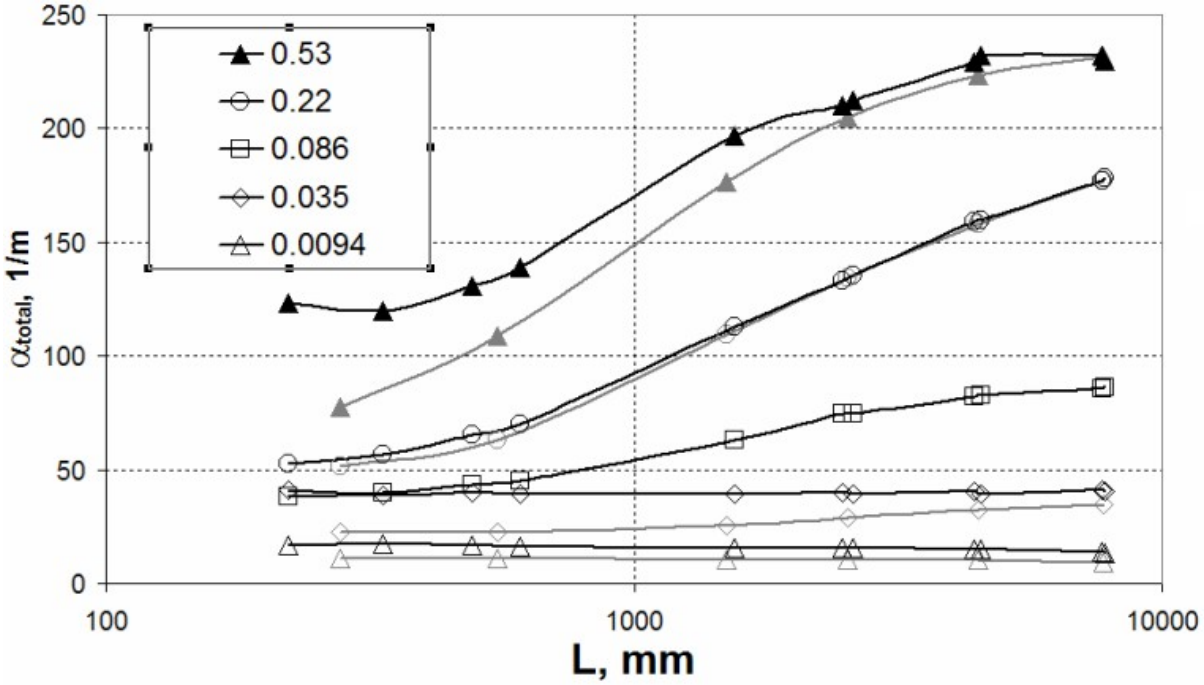

Fig. 9.9 Interfacial area density in the pipe of 195.3 mm inner diameter as a function of the distance between gas injection and measuring position L at J_L = 1.02 m/s for different gas superficial velocities $J_{R,G}$ (parameter), gas injection orifices: bold lines: 1 mm, thin lines: 4 mm

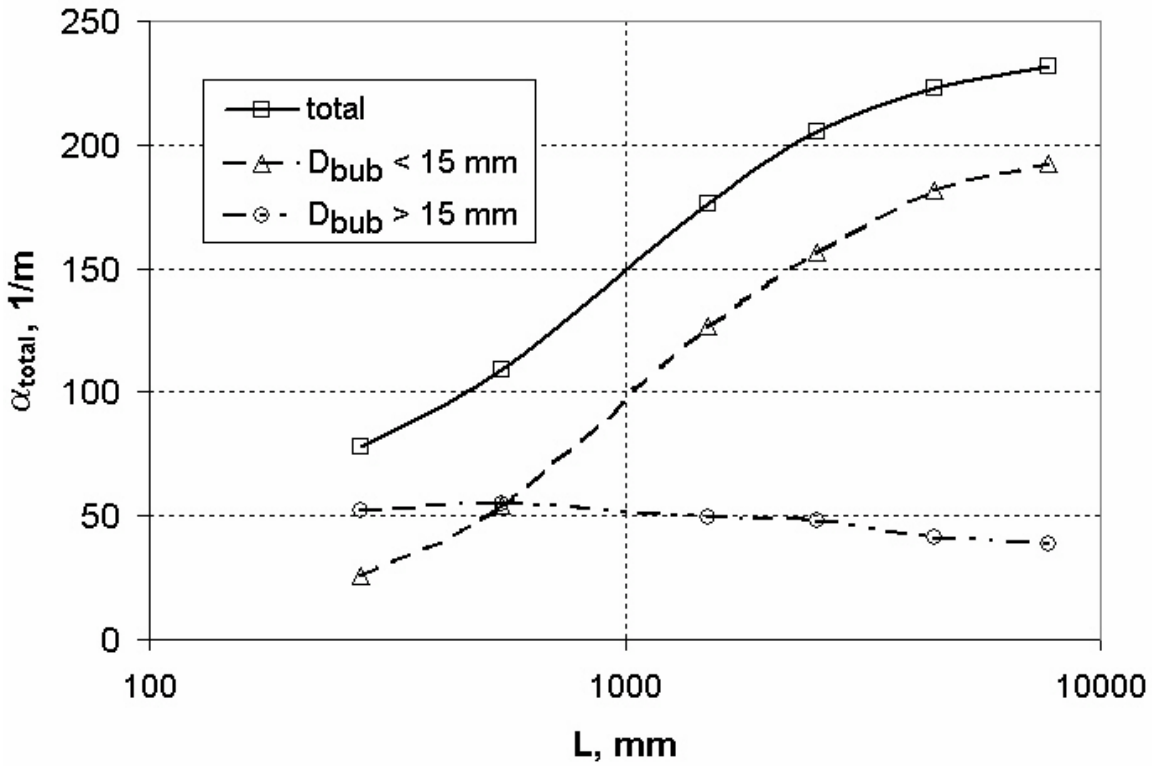

Fig. 9.10 Interfacial area density for two different bubble size classes as a function of the distance between gas injection and measuring position L at J_L = 1.02 m/s, $J_{R,G}$ = 0.53 m/s, gas injection orifices 4 mm

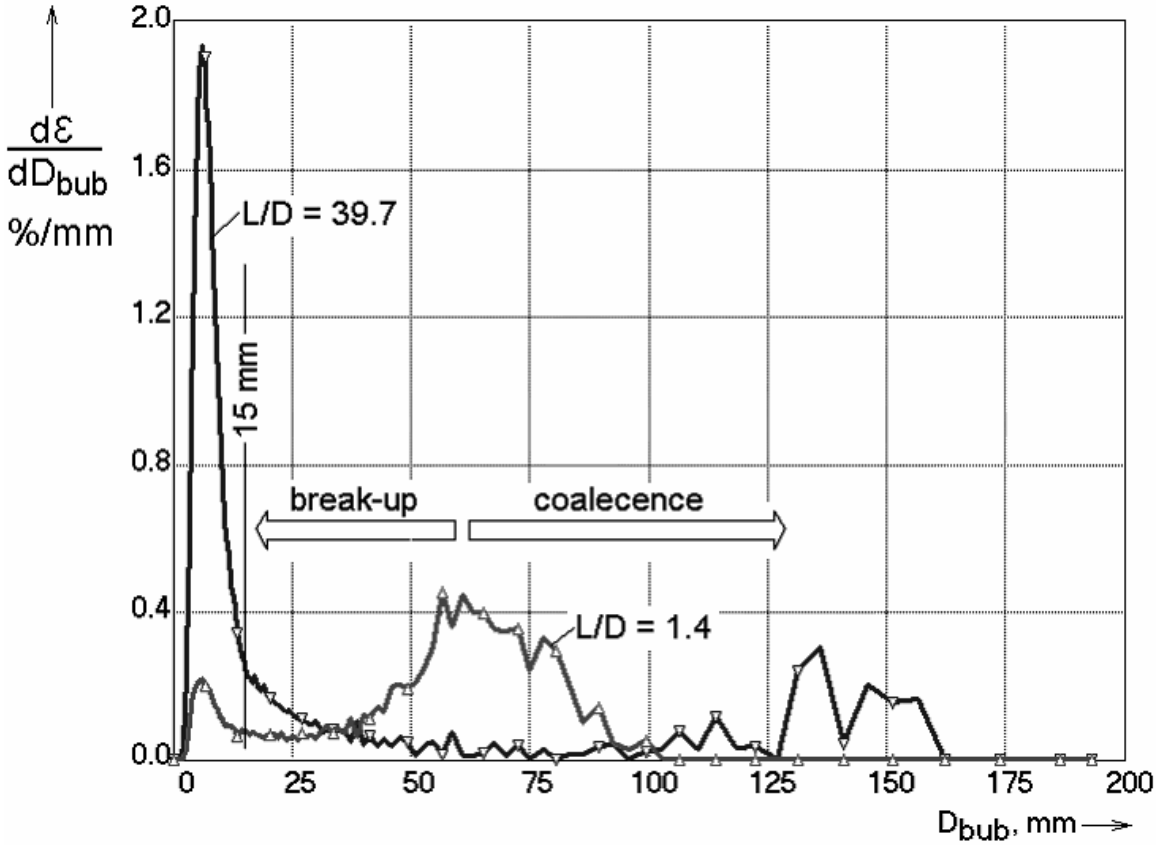

Fig. 9.11 Evolution of the bubble size distribution in the experiment shown in Fig. 9.10, (J_L = 1.02 m/s and $J_{R,G}$ = 0.53 m/s)

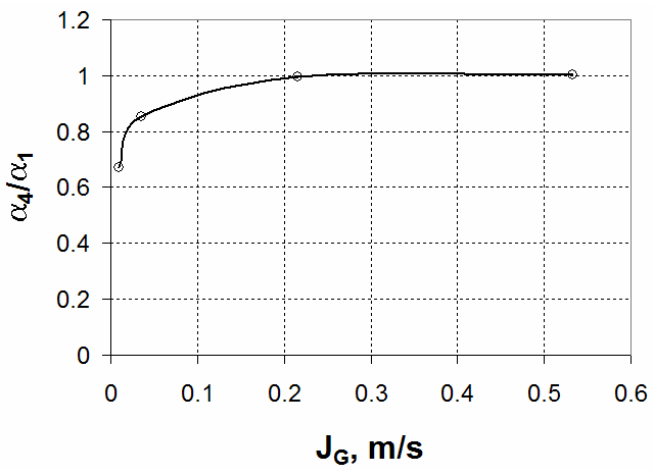

Fig. 9.12 Influence of the diameter of the gas injection orifices on the interfacial area density at L/D ≅ 40

The influence of the gas sparger is still visible at L/D = 40, if the superficial gas velocity is below 0.2 m/s. In Fig. 9.12 the ratio between the total interfacial area concentrations are shown measured with the 4 mm injection orifices (α_4) versus the one measured with the 1 mm orifices (α_1). Larger orifices result in bigger bubbles, which leads to lower interfacial areas and, consequently, to a ratio α_4/α_1 becomes less than 1. This is very important, because the interfacial area density can obviously be very much determined by the kind of the gas injection even at comparatively high inlet lengths when the gas superficial velocity is low.

Concerning the order of magnitude of the obtained interfacial area densities, a comparison with the measurements of Sun et al. (2002) can be performed. This is the only available publication on interfacial area density measurements in a pipe of larger diameter. Unfortunately, the diameter of the pipe was 101.6 mm instead of 195.3 mm in case of TOPFLOW and the experiments were performed at slightly

different superficial velocities. Furthermore, a different gas injection device was used. The comparison has to remain qualitative. It is shown in Fig. 9.13.

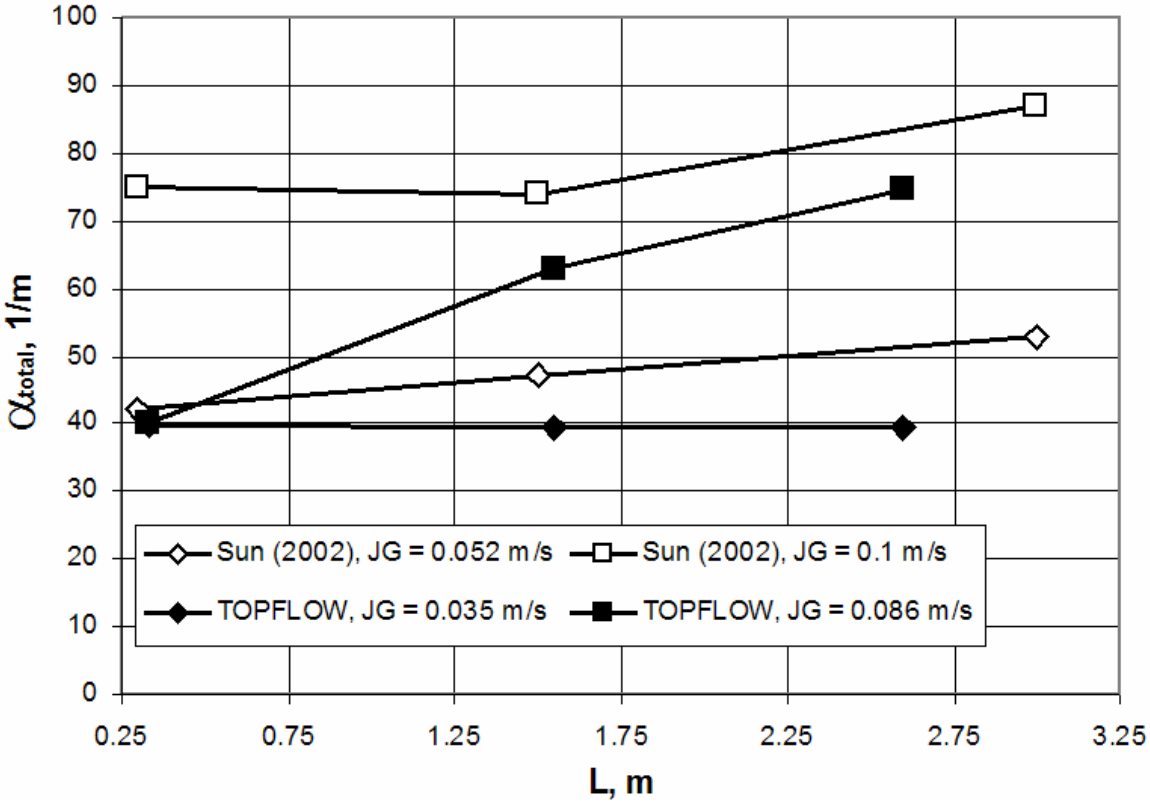

Fig. 9.13 Comparison of total interfacial area densities measured in the 195.3 mm pipe with results of Sun et al. (2002) obtained in a 101.6 mm diameter pipe using a four-sensor conductivity probe, J_L = 1 m/s, $J_G = J_{R,G}$

Despite of the significant deviations in the boundary conditions of both experiments, there is a fairly good agreement even in terms of quantitative values. In general, the measurements of Sun et al. (2002) resulted in greater values of the interfacial area, which can partially be explained by the slightly higher gas superficial velocities.

10. Vertical pipe flow with phase transfer by bulk condensation

10.1 Aim

The experiments described in this chapter aimed at providing experimental data for the modelling of phase transition due to condensation heat exchange at the gas/ liquid interface in CFD codes. The condensation power and therefore the mass transfer rate is determined by the heat transfer coefficient and the magnitude of the interfacial area. The large vertical test pipe of TOPFLOW with the variable gas injection system (comp. section 2.3) was used to set-up experiments, in which the vapour phase experienced condensation due to a sub-cooling of the water. The variation of the distance between sensor and vapour injection allowed tracing the condensation process along the flow path. The ability of the sensor to deliver gas fractions and bubble-size distributions created ideal conditions to separate the effects of the heat transfer and the interfacial area. The method of decomposition of gas fraction profiles according to bubble-size classes supplies very sensitive data for the validation of multi-bubble-size models. In these models, like the proposed and

implemented in CFX-10 Inhomogeneous MUSIG model (see individual technical reports: *"Validation of the Multiple Velocity Multiple Size Group (CFX10.0 N x M MUSIG"* and *"CFD models for poly-dispersed bubbly flows"*), condensation has to be modelled by additional source and sink terms in the mass conservation equations of the bubble-size classes, that transport the bubbles from larger into smaller classes, when their size decreases due to the condensation of vapour.

The new detailed experimental data were used to check the complex interactions between the changes of local gas volume distribution, bubble size distribution and local heat and mass transfer. To do this, the Multi Bubble Class Test Solver, first introduced by Lucas et al. (2001 a) was extended to consider the phase transfer separately for each bubble class (Lucas et al. 2007b). In the present report, the focus is put on the experimental technique and the results.

10.2 Test facility and boundary conditions

The vertical test pipe DN200 with variable gas injection system was used (Prasser et al., 2005d). A sketch is given in Fig. 10.1. The pipe is supplied by water from the steam drum where saturation conditions are present. Saturated steam comes from the electrical steam generator (see Fig. 2.1). A slight sub-cooling of the water flow (max. 6 K) was achieved by throttling the ball valve at the upper end of the vertical test section. Behind this ball valve, saturation conditions are reached by expansion. For this reason, the liquid phase is sub-cooled upstream of the valve. The sub-cooling corresponds to the pressure drop across the valve, which is compensated by the work performed by the test section pump delivering the water phase.

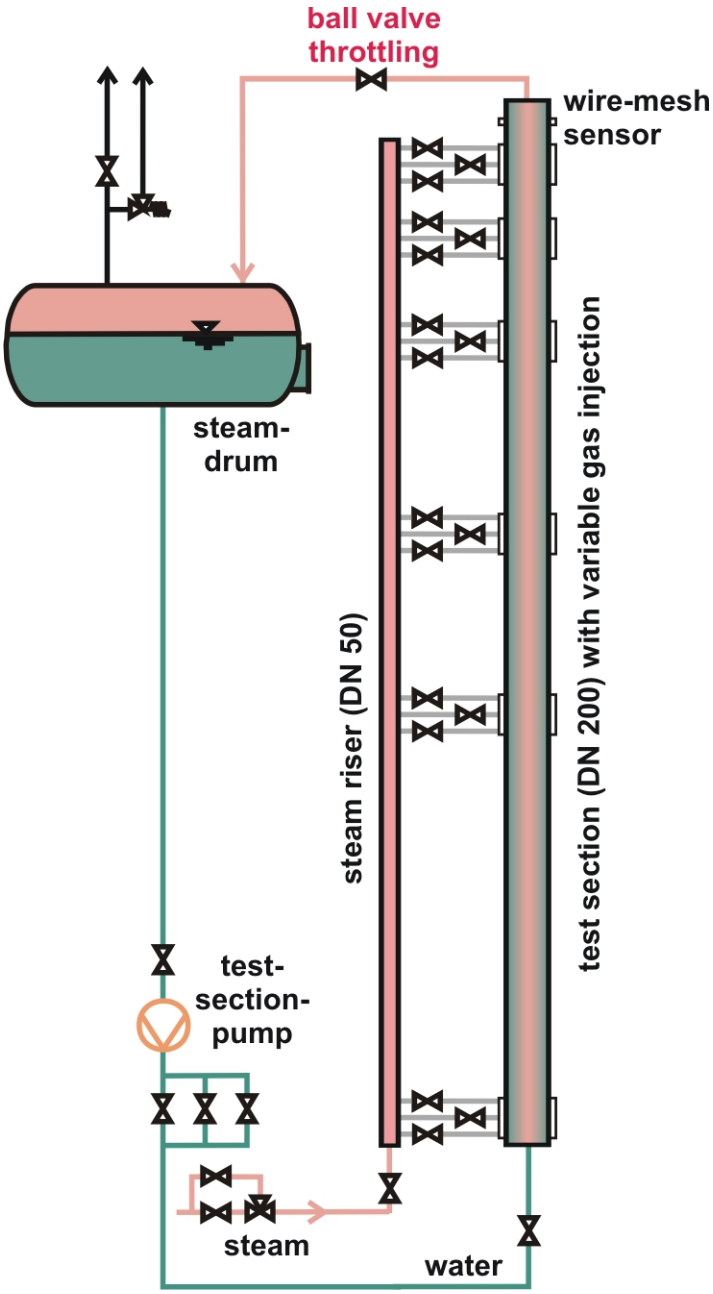

Fig. 10.1 Creation of a sub-cooling in the vertical test section with variable gas injection system by throttling the ball valve at the exit of the test section

Tab. 10.1 Conditions of test runs with sub-cooling and reference experiments

Run	Pressure			Superficial velocity		Temperature		Sub-cooling
	Sensor p_{WMS}[MPa]	Steam drum p_{SEP}[MPa]	Throttle Δp[kPa]	Water [m/s]	Steam [m/s]	Water [°C]	Steam [°C]	Water [K]
1	1.07	1.00	70	1.017	0.534	177.8	182.8	5.0
2	1.10	1.00	100	1.017	0.534	177.8	184.0	6.2
3	2.08	2.00	80	1.017	0.534	210.5	214.4	3.9
4	2.16	2.00	160	1.017	0.534	210.5	216.3	5.8
Ref 1	1.00	1.00	0	1.017	0.534	177.8	179.2	1.4
Ref 2	2.00	2.00	0	1.017	0.534	210.5	211.2	0.7

For each parameter set, shown in Tab. 10.1, mesh sensor signals were recorded over a period of 10 s for each steam injection level and reference experiments were carried out without throttling, i.e. with a much lower sub-cooling that is now only a result of the pressure drop in the pipe connecting the outlet of the test section with the steam drum. The boundary conditions are characterised by two pressures: the pressure in the steam drum (separator) downstream of the throttling valve p_{SEP}, where the fluid is at saturation and which defines the liquid temperature at the inlet of the test section, and the pressure at the mesh sensor position p_{WMS}. The difference Δp determines the sub-cooling at the sensor position. Superficial steam and water velocities were kept constant, while the pressure in the system was varied, as well as the pressure drop across the valve.

10.3 Experimental results

Axial profiles of the cross-section averaged void fractions (Fig. 10.2 and Fig. 10.3) show the decrease of the void fraction in the test runs with sub-cooling. In the reference case, the void fraction is nearly constant in case of pressure of 2 MPa in the steam drum, though the flow is not completely free of condensation, which is due to the presence of pressure drop even when the valve is fully open (Fig. 10.2). This effect is more pronounced in the experiment at p_{SEP} = 1 MPa (Fig. 10.3), because small mass sinks of the steam phase due to condensation result in bigger volume sinks because of the lower steam density compared to the tests at p_{SEP} = 2 MPa.

Both test runs clearly show the effect of the different gas injection diameters. Smaller bubble sizes created by the 1 mm orifices cause the void fraction to decrease more rapidly compared to 4 mm. As expected, condensation progresses faster for higher sub-cooling. In radial gas fraction profiles (Fig. 10.4) the migration of the bubbles from the wall, where they are generated, towards the centre is seen. In the reference test without sub-cooling, an equilibrium profile is reached, while in case of high sub-cooling the gas fraction vanishes before this can happen.

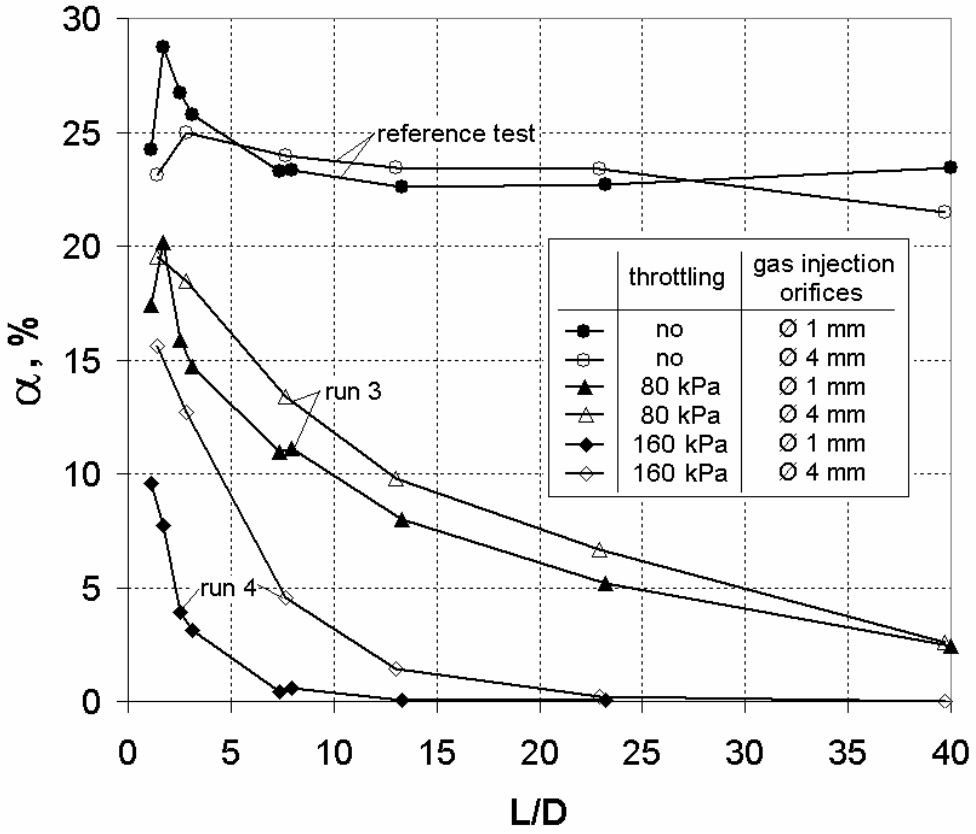

Fig. 10.2 Axial evolution of the average void fraction, test runs 3, 4 and reference case (p_{SEP} = 2 MPa)

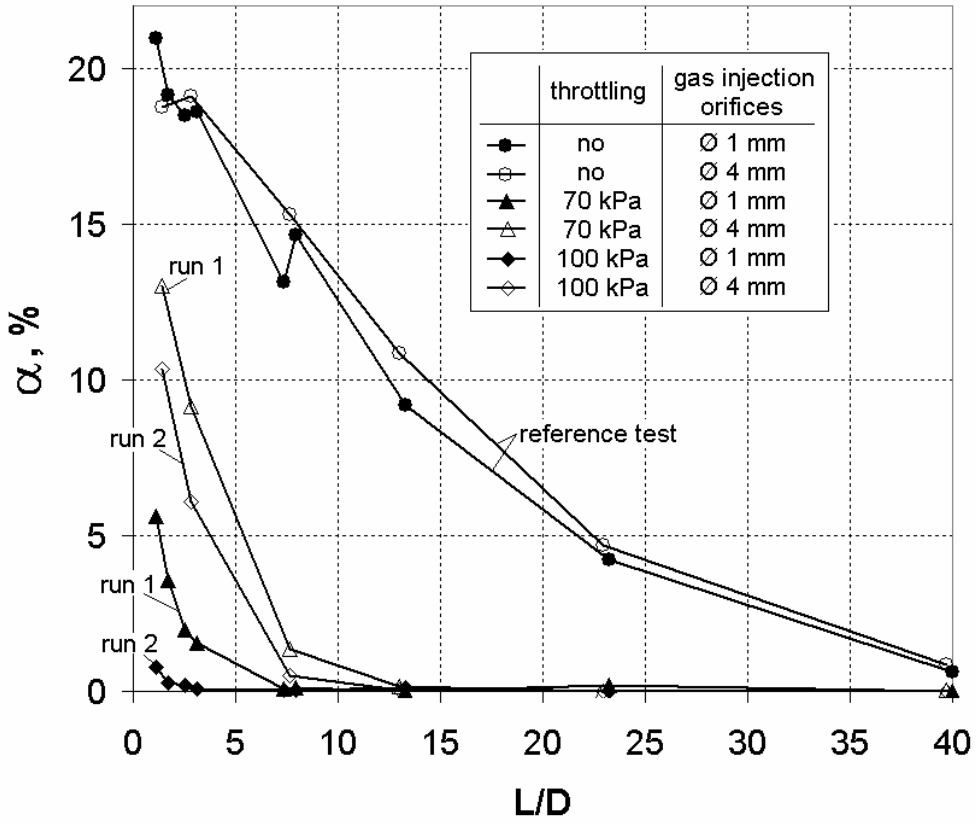

Fig. 10.3 Axial evolution of the average void fraction, test runs 1, 2 and reference case (p_{SEP} = 1 MPa)

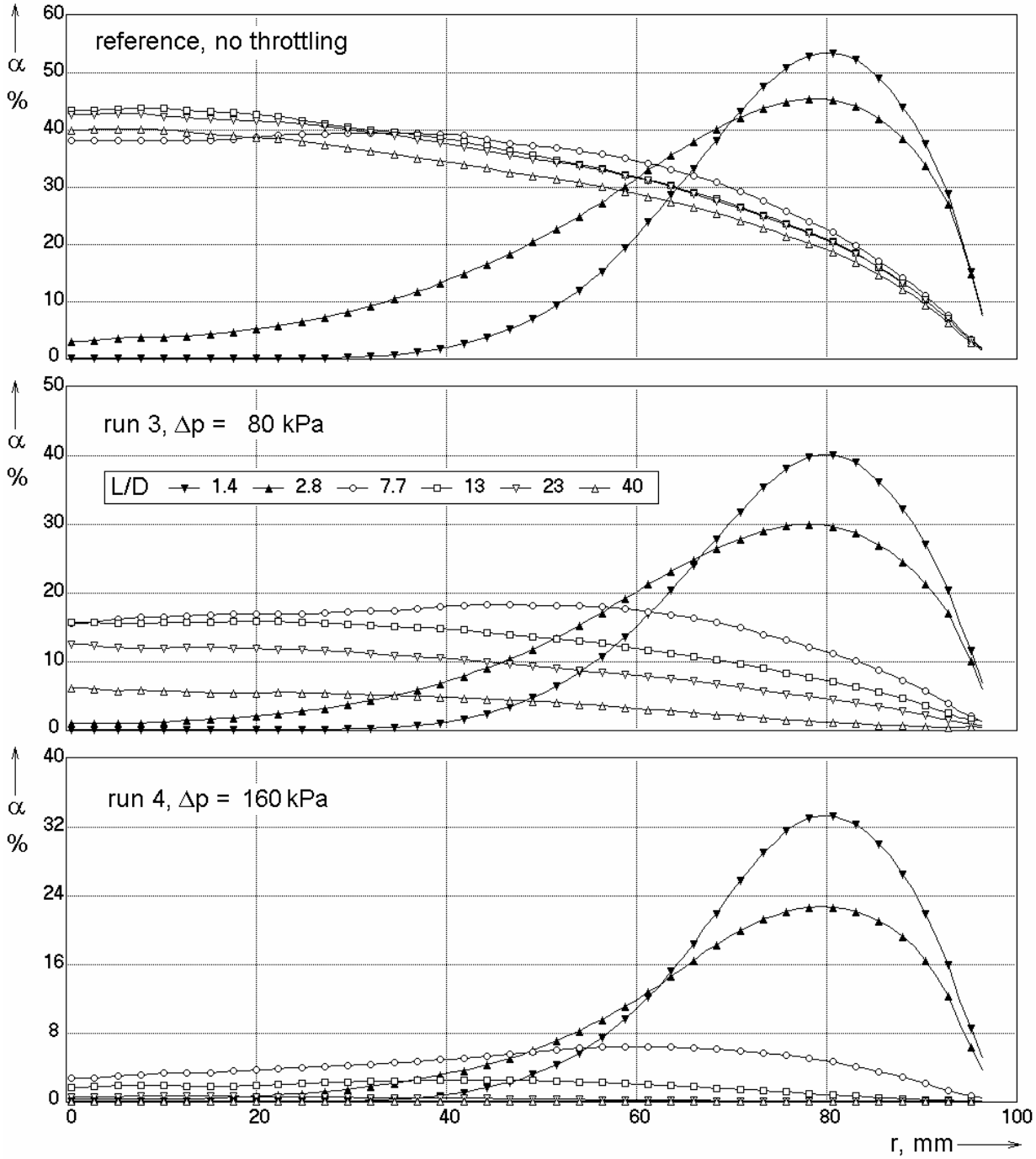

Fig. 10.4 Radial gas fraction profiles for test run 3 and 4, D_{inj} = 4 mm

A visualization (Fig. 10.5) is done by generating virtual side projections and side views of virtual central cuts from the mesh sensor data according to the algorithms described in section 4.4.1. For each mesh sensor data set, virtual side views and virtual central cuts are combined in the same image. The height-to-width relation of the depicted bubbles is nearly respected in this image. It is visible how bubbles injected at the periphery move towards the centre of the pipe in case of the reference experiment without sub-cooling, while in the experiment with condensation the bubble density decreases with growing distance from the injection device.

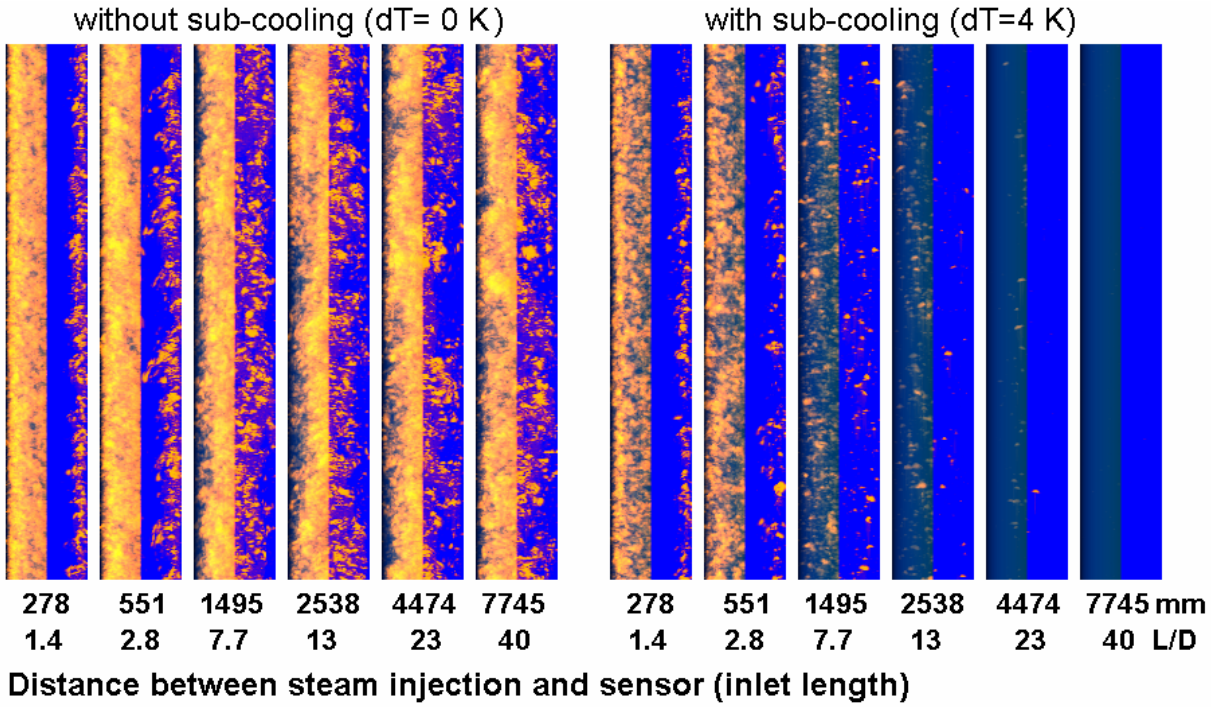

Fig. 10.5 Virtual side projections (left halves of the columns) and side views of virtual central cuts (right halves) of the mesh sensor data, test run 4, D_{inj} = 4 mm

The bubble size measurement requires information on the bubble velocity or at least an approximate value like a local time-averaged gas phase velocity or the cross-section averaged gas phase velocity. None of this velocity information was available in the presented tests. An earlier used method to approximate the velocity by the average gas phase velocity calculated by dividing the superficial gas velocity by the average void fraction was also not applicable, since the superficial gas velocity at the sensor position is unknown. It is not equal to the known superficial velocity at the location of steam injection because it decreases along the pipe due to the progressing condensation.

For this reason, the extension of the bubbles in the horizontal measuring plane (i.e. in x-y direction) was used to characterize the bubble size, which can be obtained without knowing the gas velocity (section 4.4.4).

From the manifold of individual bubble diameters, bubble-size distributions are calculated. Bubble-size distributions found in the reference tests without throttling at the smallest available distances between steam injection and sensor position show clearly the different behaviour of 1 and 4 mm gas injection orifices (Fig. 10.6), which explains the different intensity of the condensation process for both gas injections. The further development of bubble-size distributions are shown in Fig. 10.7 and Fig. 10.8. The vertical axis represents the contribution of bubbles of the given diameter to the overall gas fraction averaged over the pipe cross-section. Without sub-cooling, the bubble-size distribution soon converges to an equilibrium, while an ongoing condensation disturbs the equilibrium, which can therefore not establish. In the consequence, bubble sizes at identical inlet lengths with condensation are significantly lower than without. In the tests at p_{SEP} = 1 MPa, there is a decrease of bubble sizes due to condensation also in the reference experiment performed without explicit throttling (see Fig. 10.8).

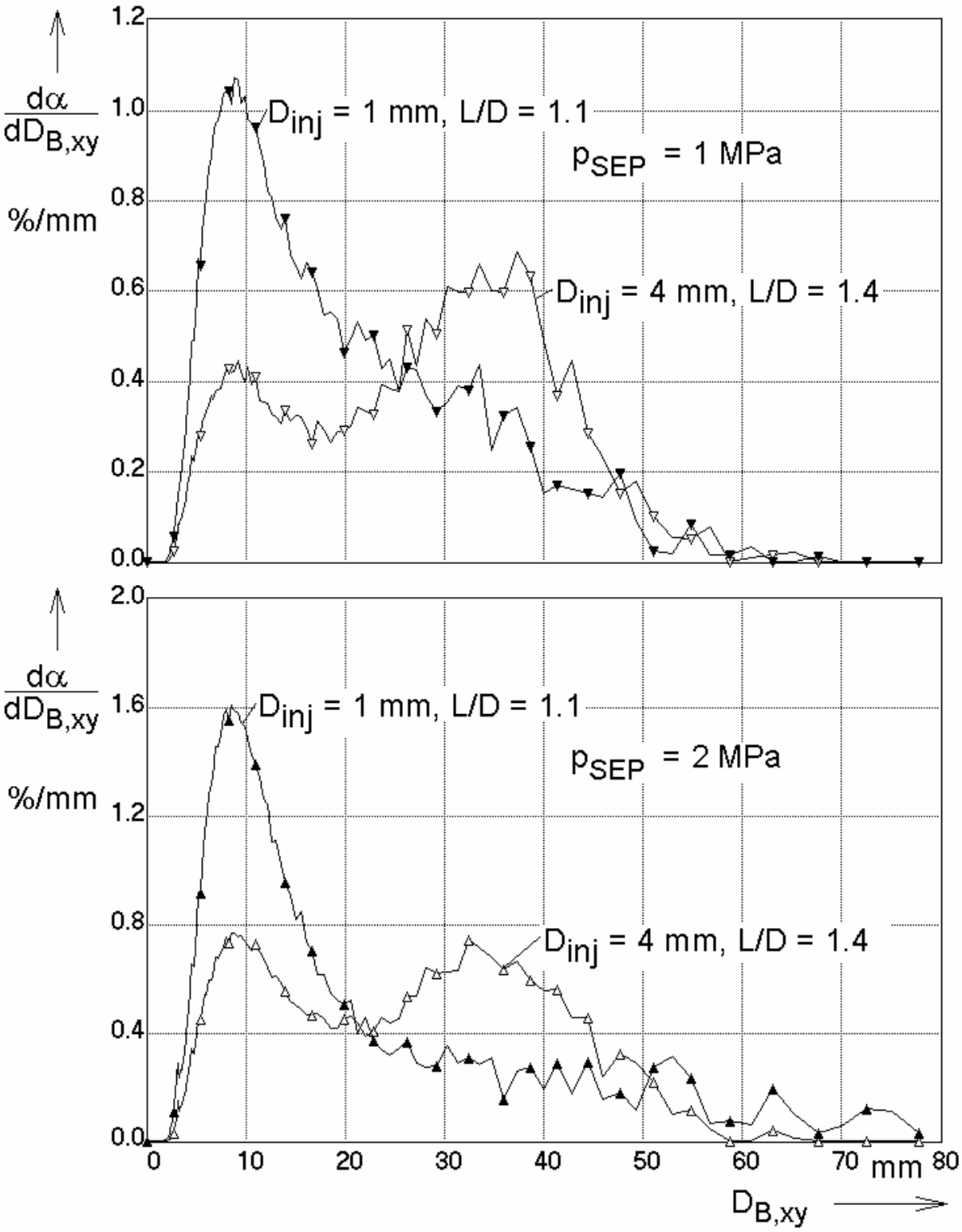

Fig. 10.6 Bubble-size distributions close to the gas injection in the reference tests without throttling

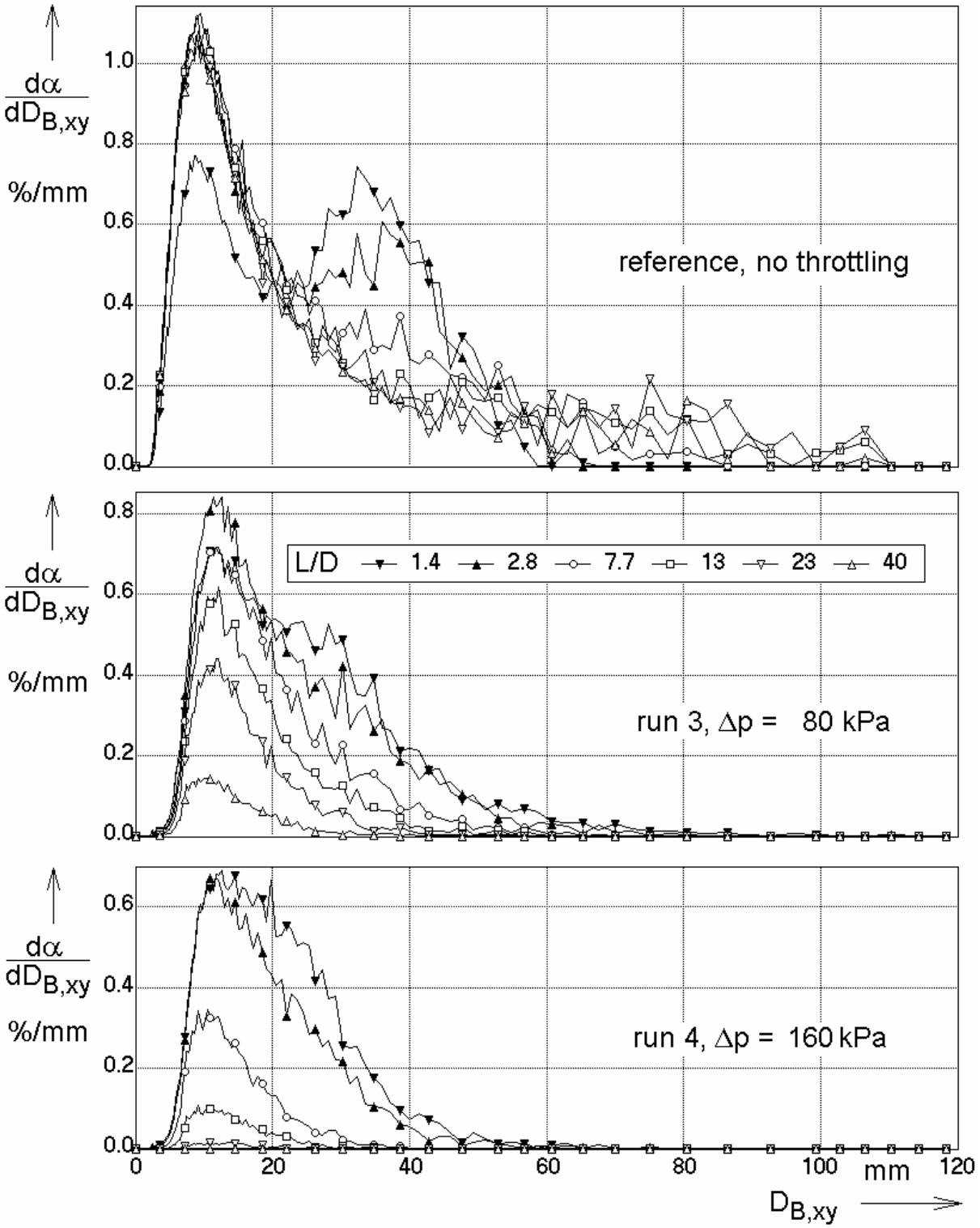

Fig. 10.7 Bubble-size distributions, test run 3 and 4, D_{inj} = 4 mm

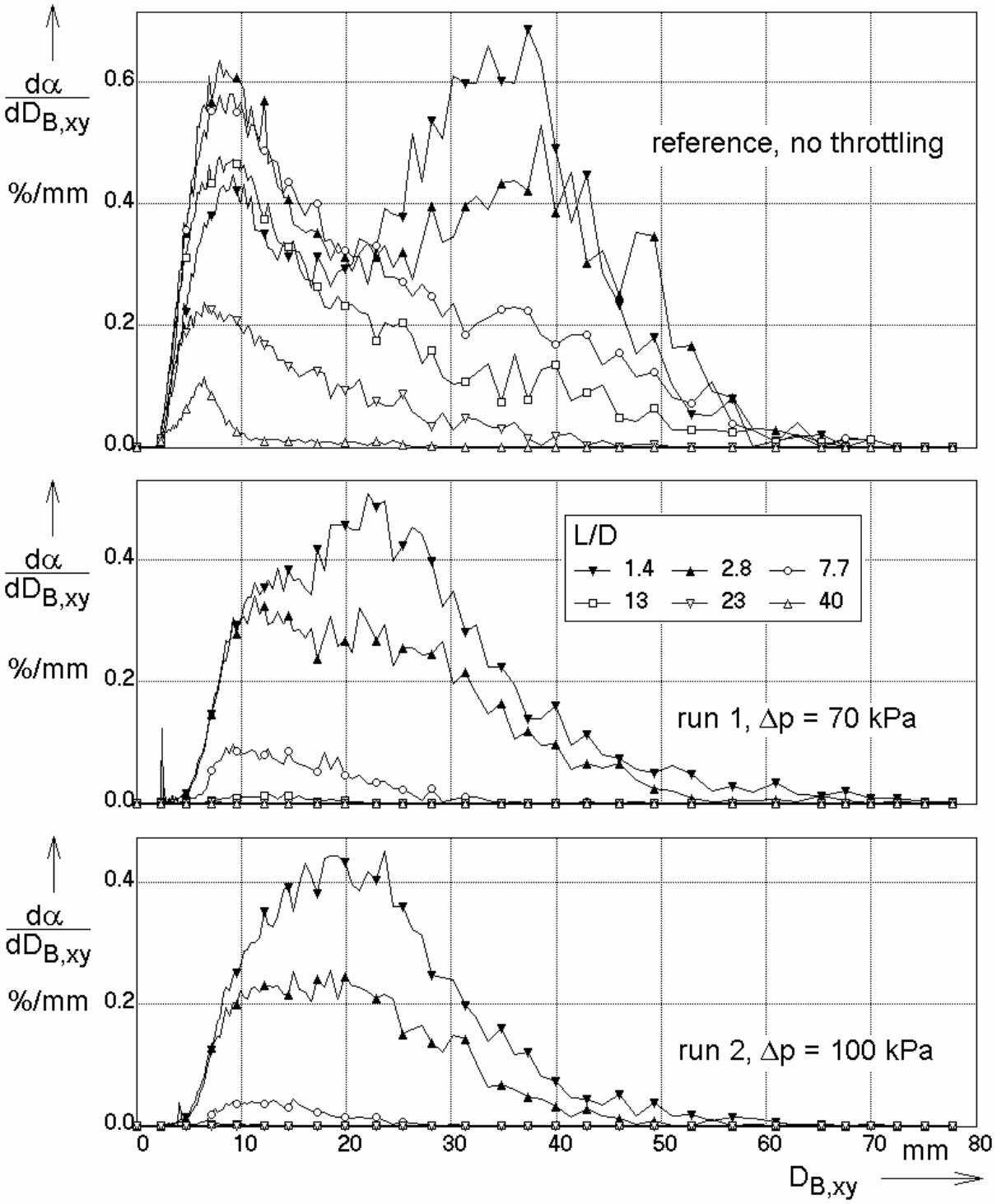

Fig. 10.8 Bubble-size distributions, test run 1 and 2, D_{inj} = 4 mm

11. Summary

The experimental methods and results presented in this report are the basis for the development of the closure relations for the Inhomogeneous MUSIG model, for its validation and for the future extension towards a gas/liquid two-fluid model that can take into account mass transfer at the gas/liquid interface. The analysis of the vast material is still ongoing. Some of the tests have provided data extremely valuable for code development and validation and are therefore widely used by the partners within the German CFD alliance. Compared to the variety, quantity and quality of the experiments at the vertical test sections of TOPFLOW planned in the technical annex to the project application, the obtained results exceed the required in the following main points:

- The spatial resolution of 3 mm achieved by the high pressure sensors is better than the planned by a factor of 2. It was offered to construct mesh sensors with 32x32 crossing points in the measuring cross-section. In reality, the novel design allowed to create a measuring matrix of 64x64 in the cross section of DN200 (Pietruske & Prasser, 2007). The design was patented (Pietruske et al., 2006).
- The construction of the variable gas injection system was not planned. It was foreseen to sidmantle the large test section for the variation of the inlet length. The variable gas injection system allowed increasing significantly the number of test regimes that could be carried out due to an efficient way of the control of the test facility.
- Condensation tests carried out by creating a sub-cooling in the liquid phase were not planned. The availability of preliminary results from these tests allowed to progress with the modelling of interfacial mass transfer in the CFD code, especially within the Inhomogeneous MUSIG model. The experience from the experiments was very valuable for the design of advanced condensation and evaporation tests within the successor project.
- Two novel evaluation methods for wire-mesh sensor data were proposed, tested and applied for the validation of closure relations for two-fluid models: (1) a method to extract turbulent dispersion coefficients in a wide range of superficial velocities and (2) the measurement of interfacial area densities with wire-mesh sensors. Beside this, some progress was made also in visualizing of the wire-mesh data by virtual side projection techniques.

12. References

Delfos, R., Wisse, C.J., Oliemans, R.V.A., (2001). Measurements of air entrainment from a stationary Taylor bubble in a vertical tube. Int. J. Multiphase flow, 27, 1769–1787.

Fu, X. Y. and Ishii, M., (2002a). Two-group interfacial area transport in vertical air/ water flow, I. Mechanistic model. Nuclear Engineering and Design, 219(2002)143-168.

Fu, X. Y. and Ishii, M., (2002b). Two-group interfacial area transport in vertical air/water flow, II. Model evaluation. Nuclear Engineering and Design, 219(2002)169-190.

Giot, M., Seynhaeve, J.-M., (2004). Two-phase flow water hammer transients and induced loads on materials and structures of nuclear power plants. EU project WAHALoads, FIKS-CT-2000-00106, final report, May 2004.

Gregor, S., (2004). Ermittlung der Zwischenphasen-Grenzflächendichte mit Gittersensoren bei unterschiedlichen Strömungsbedingungen. Interdisziplinäre Projektarbeit, TU Dresden, Nr. 2111.

Hibiki, T., Ishii, M., (1999). Experimental study on interfacial area transport in bubbly two-phase flows. International Journal of Heat and Mass Transfer, 42(1999)3019-3035.

Hibiki, T., and Ishii, M., (2000). Two-group interfacial area transport equations at bubbly-to-slug flow transition. Nuclear Engineering and Design, 202(2000)39-76.

Hicken, Enno F., Schaffrath, A., Fethke, M., Jaegers, H., (2002). Der NOKO-Versuchsstand der Forschungszentrum Jülich (FZR) GmbH - Rückblick auf 7 Jahre experimentelle Untersuchungen zur Erhöhung der Sicherheit von Leichtwasserreaktoren. Atomwirtschaft-Atomtechnik 47 (2002), Nr. 5, S. 343-348.

Ishii, M., (1975). Thermo-Fluid Dynamic Theory of Two-Phase Flow. Eyrolles, Paris, 1975.

Johnson, I. D., (1987). Method and Apparatus for Measuring Water in Crude Oil. United States Patent, No 4,644,263, Date of Patent: Feb. 17, 1987.

Kataoka, I., Ishii, M., Serizawa, A., (1986). Local formulation and measurements of interfacial area concentration in two-phase flow. Int. J. Multiphase Flow, 12(1986)505-529.

Kataoka, I., Ishii, M., (1987). Drift flux model for large diameter pipe and new correlation for pool void fraction. International Journal of Heat and Mass Transfer 30(1987), pp. 1927-1939.

Kim, S. et al., (2000). Bubble transport in small diameter pipe flow. 4th International Conference on Multiphase Flow, ICMF-2000, New Orleans, La, USA, May 27 - June 1, 2001.

Kim, S. and Ishii, M., (2001). Micro four-sensor probe measurement of interfacial area transport for bubbly flow in round pipes. Nuclear Engineering and Design, 205(2001)123–131.

Kobayashi, A., Shakutsui, H., Higashine, M., Minagawa, H., (2004). Void fraction in Upward Gas/Liquid Two-Phase Flow in a Large Diameter Vertical Pipe. 5th International Conference on Multiphase Flow, ICMF'04, Yokohama, Japan, May 30 - June 4, 2004, Paper No. 267.

Kockx, J. P., Nieuwstadt, F. T .M., Oliemans, R. V. A., Delfos, R., (2005). Gas entrainment by a liquid film falling around a stationary Taylor bubble in a vertical tube. International Journal of Multiphase Flow, 31, 1–24.

Leung, W. H., Eberle, C. S., Wu, Q., Ueno, T., Ishii, M., (1995). Quantitative characterization of phasic structure developments by local measurement methods in two-phase flow. Proc. of the Second Int. Conf. on Multiphase Flow, 1995, Kyoto, IN2-17-IN2-25.

Liu, T. J., Bankoff, S. G., (1993). Structure of air/water bubbly flow in a vertical pipe - II. Void fraction, bubble velocity and bubble size distribution. Int. J. Heat Mass Transfer, 36(1993)4, pp. 1061 - 1072.

Lucas, D., Krepper, E., Prasser, H.-M., (2001). Prediction of radial gas profiles in vertical pipe flow on basis of the bubble size distribution. International Journal of Thermal Sciences, 40(2001)217-225.

Lucas, D., Krepper, E., Prasser, H.-M., (2007a). Modelling of the evolution of bubbly flow along a large vertical pipe. Nuclear Technology (May 2007).

Lucas, D., Prasser, H.-M., (2007b). Steam bubble condensation in sub-cooled water in case of co-current vertical pipe flow. Nuclear Engineering and Design 237 (2007)497-508.

Manera, A., Prasser, H.-M., van der Hagen, T. H. J. J., Mudde, R. F., de Kruijf, J. M., (2001). A comparison of void-fraction measurements during flashing-induced instabilities obtained with a wire-mesh sensor and a gamma-transmission set-up. 4th International Conference on Multiphase Flow, New Orleans, Lousiana, USA, May 27 - June 1, 2001, Proc. CD-ROM, paper #436.

Manera, A., Prasser, H.-M., Lucas, D., (2006). Experimental investigations on bubble turbulent diffusion in a vertical large-diameter pipe by means of wire-mesh sensors and correlation techniques. NURETH-11, Avignon, France, October 2-6, 2005, Paper: 091.

Milelli M., (2002). A numerical analysis of confined turbulent bubble plumes. Dissertation, Swiss Federal Institute of Technology, Zurich, Switzerland. ETH-14799 (2002).

Miller, N., Mitchie, R., (1970). Measurement of local voidage in liquid/gas two-phase flow systems using a universal probe. J. Brit. Nucl. Energy Soc. 2, 94-100.

Misawa, M., Tiseanu, I., Prasser, H.-M., Ichikawa, N., Akai, M., (2003). Ultra-fast x-ray tomography for multi-phase flow interface dynamic studies. Kerntechnik 68 (2003) 3, pp. 85-90.

Misawa, M., Suzuki, A., Morikawa, Y., Minato, A., Prasser, H.-M., (2004). Nonlinear Characteristics of Gas/Liquid Two-Phase Flow and Verification of Extended Two-Fluid Model. 5th International Conference on Multiphase Flow, ICMF'04, Yokohama, Japan, May 30 - June 4, 2004, Paper No. 213.

Neal, L., Bankoff, S., (1963). A high-resolution resistivity probe for determination of local properties in gas/liquid flow. AIChE J. 9/4, 490-494.

Ohnuki, A., Akimoto, H., (1996). An experimental study on developing air/water two-phase flow along a large vertical pipe: effect of air injection method. Int. J. Multiphase Flow 22, 1143-1154.

Ohnuki, A., Akimoto, H., (2000). Experimental study on transition of flow pattern and phase distribution in upward air/water two-phase flow along a large vertical pipe. International Journal of Multiphase Flow, 26(2000)367-386.

Okawa, T., Yoneda, K., Zhou, S., Tabata, H., (1999). New Interfacial Drag Force Model Including Effect of Bubble Wake, (II) Model Validation Using Experimental Data of Steam/Water Bubbly Flow in Large-Diameter Pipes. J. of Nuclear Science and Technology, 36/11, 1030-1040.

Peters, D., Pietzsch, G., Prasser, H.-M., Taubert, W., Trepte, M., Zschau, J., (1999). Wire-Mesh Sensor - now 10000 Frames per Second. Institute of Safety Research, Annual Report 1999, FZR-284, Feb. 2000, ISSN 1437-322X, pp. 15-18.

Pietruske, H., Sühnel, T., Prasser, H.-M., (2006). Gittersensor. Patentschrift Nr.: DE102005019739B3, angenommen am 26.10.2006.

Pietruske, H., Prasser, H.-M., (2007). Wire-mesh sensors for high-resolving two-phase flow studies at high pressures and temperatures. Flow Measurement and Instrumentation, 2007, in press.

Prasser, H.-M., Böttger, A., Zschau, J., (1998). A new electrode-mesh tomograph for gas/liquid flows. Flow Measurement and Instrumentation, 9 (1998), 111-119.

Prasser, H.-M., Böttger, A., Zschau, J., (1999). Entwicklung von Zweiphasenmeß-technik für vergleichende Untersuchungen zur Beschreibung von transienten Strömungen in Rohrleitungen. Forschungszentrum Rossendorf, FZR-233 Februar 1999, ISSN 1437-322X, Abschlußbericht zum Vorhaben 11ZF9504/1.

Prasser, H.-M., (2000). High-speed measurement of the void fraction distribution in ducts by wire-mesh sensors. International Meeting on Reactor Noise, Oct. 11-13, 2000, Athens, Greece, proc. on CD-ROM, paper_7_1.doc.

Prasser, H.-M., Scholz, D., Zippe, C., (2001). Bubble size measurement using wire-mesh sensors. Flow Measurement and Instrumentation, 12 (2001), 299-312.

Prasser, H.-M., Zschau, J., Peters, D., Pietzsch, G., Taubert, W., Trepte, M., (2002a). Fast wire-mesh sensors for gas/liquid flows - visualization with up to 10000 frames per second. ICAPP 2002, Hollywood, Florida, paper #1055.

Prasser, H.-M., Krepper, E., Lucas, D., (2002b). Evolution of the two-phase flow in a vertical tube - decomposition of gas fraction profiles according to bubble size classes using wire-mesh sensors. International Journal of Thermal Sciences, 41 (2002) 17-28.

Prasser, H.-M., Lucas, D., Krepper, E., Baldauf, D., Böttger, A., Rohde, U., Schütz, P., Weiß, F.-P., Zippe, C., Zippe, W., Zschau, J., (2003). Strömungskarten und Modelle für transiente Zweiphasenströmungen. Wissenschaftlich-Technische Berichte / Forschungszentrum Rossendorf, FZR-379, Juni 2003.

Prasser, H.-M., (2004). Influence of the Gas Injection on the Void Fraction Profiles and Bubble Size Distributions of an Air/Water Flow in Vertical Pipes. 5th International Conference on Multiphase Flow, ICMF'04, Yokohama, Japan, May 30–June 4, 2004, Paper No. 366.

Prasser, H.-M., Beyer, M., Böttger, A., Carl, H., Lucas, D., Schaffrath, A., Schütz, P., Weiß, F.-P., Zschau, J., (2005a). Influence of the pipe diameter on the structure of the gas/liquid interface in a vertical two-phase pipe flow. Nuclear Technology 152(2005)Oct, 3-22.

Prasser, H.-M., Misawa, M., Tiseanu, I., (2005b). Comparison between wire-mesh sensor and ultra-fast X-ray tomograph for an air/water flow in a vertical pipe. Flow Measurement and Instrumentation 16 (2005), 73-83.

Prasser, H.-M., Gregor, S., (2005c). Evolution of interfacial area concentration in a vertical air/water flow measured by wire-mesh sensors. NURETH-11, 2005, Avignon, France, October 2-6, 2005, paper 398.

Prasser, H.-M., Beyer, M., Carl, H., Gregor, S., Lucas, D., Pietruske, H., Schütz, P., Weiss, F.-P., (2005d). Evolution of the structure of a gas/liquid two-phase flow in a large vertical pipe. NURETH-11, 2005, Avignon, France, October 2-6, 2005, paper 399.

Prasser, H.-M., Beyer, M., Carl, H., Manera, A., Pietruske, H., Schütz, P., Weiß, F.-P., (2006a). The multipurpose thermalhydraulic test facility TOPFLOW: an overview on experimental capabilities, instrumentation and results. Kerntechnik 71(2006)4, 163-173.

Prasser, H.-M., (2006b). Novel Experimental Measuring Techniques Required to Provide Data for CFD Validation. International OECD/IAEA workshop CFD4NRS in Garching at 5 – 7 September 2006, keynote lecture.

Reinecke, N., Petritsch, G., Boddem M., Mewes, D., (1998). Tomographic imaging of the phase distribution in two-phase slug flow. Int. J. of Multiphase Flow, 24(1998)4, pp. 617-634.

Saito, T., Ishigaki, Y., Kusano, H., (2004). Measurement and Characterization of Bubbles in a Bubble Column using 4-Tip Optical Fiber Probe. 5th International Conference on Multiphase Flow, ICMF04, Yokohama, Japan, May 30-June 04, 2004, paper 113.

Sato, Y., Sekoguchi, K., (1975). Liquid velocity distribution in two-phase bubble flow. International Journal of Multiphase Flow, 2, 79-95 (1975).

Sato, Y., Sadatomi, M., Sekoguchi, K., (1981). Momentum and heat transfer in two-phase bubble flow. International Journal of Multiphase Flow, 7, 167-177 (1981).

Schaffrath, A., Krüssenberg, A.-K., Weiss, F.-P., Hicken, E. F., Beyer, M., Carl, H., Schuster, J., Schuetz, P., Tamme, M., (2001). TOPFLOW - a new multipurpose thermalhydraulic test facility for the investigation of steady state and transient two-phase flow phenomena. Kerntechnik, 66(2001)4, pp. 209-212.

Schmitz, D. and Mewes, D., (2000). Tomographic imaging of transient multiphase flow in bubble columns. Chemical Engineering Journal, 77(2000)1-2, pp. 99-104.

Scholz, D., Zippe, C., (2000). Variation of bubble size measurements with wire-mesh sensors by high-speed video observation. 5th Workshop on Measurement

techniques of stationary and transient multiphase flow, Rossendorf, November 16 - 17, 2000, Wissenschaftlich-Technische Berichte; Forschungszentrum Rossendorf, FZR-320, Mai 2001, ISSN 1437-322X.

Sengpiel, W., (1999). Messungen der Eigenschaften von kontinuierlicher und disperser Phase in Luft/Wasser-Blasenströmungen, 3. Workshop „Meßtechnik für stationäre und transiente Mehrphasenströmungen“, 14. Oktober 1999, Rossendorf, FZR-281, pp. 25-49.

Serizawa, A., Kataoka, I., (1988). Phase distribution in two-phase flow. N. H. Afgan (Ed.), Transient Phenomena in Multiphase Flow. Hemisphere, 1988, New York. pp. 179-224.

Shen, X., Mishima, K., Nakamura, H., (2005). Two-phase phase distribution in a vertical large diameter pipe. International Journal of Heat and Mass Transfer 48, 211–225.

Sonnenburg, H.-G., (1994). Berechnung der Phasendifferenzgeschwindigkeit von Wasser und Dampf in geometrisch unterschiedlich berandeten Kanälen. Dissertation, TU Berlin, Fachbereich 6, 1994.

Sun, X., Smith T., Kim, S., Ishii, M., Uhle, J., (2002). Interfacial area of bubbly flow in a relatively large diameter pipe. Experimental Thermal and Fluid Science 27(2002)97–109.

Tomiyama, A., (1998). Struggle with computational bubble dynamica. Proceedings of Third International Conference on Multiphase Flow, ICMF 98, Lyon, France, June 8-12, 1998.

13. Nomenclature and indexes

13.1 Symbols

Sign	Unit	Denomination
A	m²	area
a	-	weight factor
b	-	bubble identification number
D	m, m²/s	diameter, diffusion coefficient
d	m	distance
DN	m	nominal diameter
eps	%	volumetric gas fraction
f	Hz	frequency
G		Gaussian function
i, j, k	-	indices
J	m/s	superficial velocity
J_R	m/s	superficial velocity related to reel experimental conditions (p and t)
J_N	m/s	superficial velocity related to nominal conditions (t = 0 °C; p = 1,013 bar)
L	m	length, distance
m	-	number of a ring-shaped square domain
N	-	number of wires in one sensor-plane
n	-	number of frames, number of bubbles
p	MPa	pressure
Q	-	source term for light propagation
R	m	radius of the sensor or pipe, radius of a bubble
r	m	current radius, radial coordinate
t	s	time
T	°C	temperature
V	m³	volume
v	m/s	velocity
w	m/s	velocity
x,y,z	m	coordinates
α	1/m, %	interfacial area density, volumetric gas fraction
Δ	-	difference
ε	%	volumetric gas fraction
Φ	-	light flux
ϕ	-	light flux vector, bubble concentration
Λ	-	absorption coefficient

τ	s	time interval
Ω	-	virtual scattering coefficient

13.2 Indices and abbreviations

Sign	Denomination
0	start value
ACF	auto correlation function
BWR	boiling water reactor
B, bub	bubble
CCF	cross correlation function
CFD	computational fluid dynamics
CFX	commercial CFD code, provided by ANSYS corp.
CM	centre of mass
cor	corner
cr	critical
el	electrode
FFT	Fast Fourier Transformation
FZD	Forschungszentrum Dresden-Rossendorf
G	gas
i	inner
inj	injection
L	liquid
max	maximal
meas	measurement
NOKO	emergency condenser test facility at the Forschungszentrum Jülich
PDF	Probabilistic Density Function
PWR	pressurized water reactor
sq	square
synth	synthetic
TOPFLOW	Transient Two Phase FLOW Test Facility
tr	threshold
VKTA	Verein für Kerntechnik und Analytik
water	water
WM	wire-mesh
xy	related to the cross-section (measurement plane)

13.3 Figures

13.4 Tables

Appendix A: Overview about the test runs

A1 experiments on the vertical test sections (DN50 and DN200)

Averaged inner diameter: DN50: 52.3 mm
DN200: 194.1 mm

LD01

Conditions:

- Two low pressure sensors 64 x 64 wires in DN200
- Injection device: type K 60 x 6 mm orifices (central injection)
- Distance between the injection- and the measuring plane: 7606 mm
- Frequency: 2.5 kHz
- Measuring time: 10 s
- Atmospheric pressure
- Temperature range: 15 – 24 °C

Superficial velocity of the gaseous phase J_G, m/s

Superficial water velocity J_W, m/s	0.0025	0.0040	0.0062	0.0096	0.0151	0.0235	0.0368	0.0574	0.0898	0.140	0.219	0.342	0.534	0.835	1.305	2.038	3.185	4.975	7.772	12.14	18.97
4.047	011	022	033	044	055	066	077	088	099	110	121	132	143	154	165	176	187	198	209	220	231
2.554	010	021	032	043	054	065	076	087	098	109	120	131	142	153	164	175	186	197	208	219	230
1.611	009	020	031	042	053	064	075	086	097	108	119	130	141	152	163	174	185	196	207	218	229
1.017	008	019	030	041	052	063	074	085	096	107	118	129	140	151	162	173	184	195	206	217	228
0.641	007	018	029	040	051	062	073	084	095	106	117	128	139	150	161	172	183	194	205	216	227
0.405	006	017	028	039	050	061	072	083	094	105	116	127	138	149	160	171	182	193	204	215	226
0.255	005	016	027	038	049	060	071	082	093	104	115	126	137	148	159	170	181	192	203	214	225
0.161	004	015	026	037	048	059	070	081	092	103	114	125	136	147	158	169	180	191	202	213	224
0.102	003	014	025	036	047	058	069	080	091	102	113	124	135	146	157	168	179	190	201	212	223
0.0641	002	013	024	035	046	057	068	079	090	101	112	123	134	145	156	167	178	189	200	211	222
0.0405	001	012	023	034	045	056	067	078	089	100	111	122	133	144	155	166	177	188	199	210	221

LD02

Conditions:

- Two low pressure sensors 64 x 64 wires in DN200
- Injection device: type I 152 x 0.8 mm orifices (central injection)
- Distance between the injection- and the measuring plane: 7606 mm
- Frequency: 2.5 kHz
- Measuring time: 10 s
- Atmospheric pressure
- Temperature range: 22 – 28 °C

Superficial velocity of the gaseous phase J_G, m/s

Superficial water velocity J_W, m/s	0.0025	0.0040	0.0062	0.0096	0.0151	0.0235	0.0368	0.0574	0.0898	0.140	0.219	0.342	0.534	0.835	1.305	2.038	3.185	4.975	7.772	12.14	18.97
4.047	011	022	033	044	055	066	077	088	099	110	121	132	143	154	165	176	187	198	209	220	231
2.554	010	021	032	043	054	065	076	087	098	109	120	131	142	153	164	175	186	197	208	219	230
1.611	009	020	031	042	053	064	075	086	097	108	119	130	141	152	163	174	185	196	207	218	229
1.017	008	019	030	041	052	063	074	085	096	107	118	129	140	151	162	173	184	195	206	217	228
0.641	007	018	029	040	051	062	073	084	095	106	117	128	139	150	161	172	183	194	205	216	227
0.405	006	017	028	039	050	061	072	083	094	105	116	127	138	149	160	171	182	193	204	215	226
0.255	005	016	027	038	049	060	071	082	093	104	115	126	137	148	159	170	181	192	203	214	225
0.161	004	015	026	037	048	059	070	081	092	103	114	125	136	147	158	169	180	191	202	213	224
0.102	003	014	025	036	047	058	069	080	091	102	113	124	135	146	157	168	179	190	201	212	223
0.0641	002	013	024	035	046	057	068	079	090	101	112	123	134	145	156	167	178	189	200	211	222
0.0405	001	012	023	034	045	056	067	078	089	100	111	122	133	144	155	166	177	188	199	210	221

L03

Conditions:

- Two low pressure sensors 16 x 16 wires in DN50
- Injection device: type I 24 x 0.8 mm orifices (central injection)
- Distances between the injection- and the measuring plane: 7910 mm
- Frequency: 10 kHz
- Measuring time: 10 s
- Atmospheric pressure
- Temperature range: 22 – 25 °C

Superficial velocity of the gaseous phase J_G, m/s

Superficial water velocity J_W, m/s	0.0025	0.0040	0.0062	0.0096	0.0151	0.0235	0.0368	0.0574	0.0898	0.140	0.219	0.342	0.534	0.835	1.305	2.038	3.185	4.975	7.772	12.14	18.97
4.047	011	022	033	044	055	066	077	088	099	110	121	132	143	154	165	176	187	198	209	220	231
2.554	010	021	032	043	054	065	076	087	098	109	120	131	142	153	164	175	186	197	208	219	230
1.611	009	020	031	042	053	064	075	086	097	108	119	130	141	152	163	174	185	196	207	218	229
1.017	008	019	030	041	052	063	074	085	096	107	118	129	140	151	162	173	184	195	206	217	228
0.641	007	018	029	040	051	062	073	084	095	106	117	128	139	150	161	172	183	194	205	216	227
0.405	006	017	028	039	050	061	072	083	094	105	116	127	138	149	160	171	182	193	204	215	226
0.255	005	016	027	038	049	060	071	082	093	104	115	126	137	148	159	170	181	192	203	214	225
0.161	004	015	026	037	048	059	070	081	092	103	114	125	136	147	158	169	180	191	202	213	224
0.102	003	014	025	036	047	058	069	080	091	102	113	124	135	146	157	168	179	190	201	212	223
0.0641	002	013	024	035	046	057	068	079	090	101	112	123	134	145	156	167	178	189	200	211	222
0.0405	001	012	023	034	045	056	067	078	089	100	111	122	133	144	155	166	177	188	199	210	221

L04

Conditions:

- Two low pressure sensors 16 x 16 wires in DN50
- Injection device: type I 24 x 0.8 mm orifices (central injection)
- Distances between the injection- and the measuring plane: 7910 mm
- Frequency: 10 kHz
- Measuring time: 10 s
- Atmospheric pressure
- Temperature range: 28 – 31 °C

Superficial velocity of the gaseous phase J_G, m/s

Superficial water velocity J_W, m/s	0.0025	0.0040	0.0062	0.0096	0.0151	0.0235	0.0368	0.0574	0.0898	0.140	0.219	0.342	0.534	0.835	1.305	2.038	3.185	4.975	7.772	12.14	18.97
4.047	011	022	033	044	055	066	077	088	099	110	121	132	143	154	165	176	187	198	209	220	231
2.554	010	021	032	043	054	065	076	087	098	109	120	131	142	153	164	175	186	197	208	219	230
1.611	009	020	031	042	053	064	075	086	097	108	119	130	141	152	163	174	185	196	207	218	229
1.017	008	019	030	041	052	063	074	085	096	107	118	129	140	151	162	173	184	195	206	217	228
0.641	007	018	029	040	051	062	073	084	095	106	117	128	139	150	161	172	183	194	205	216	227
0.405	006	017	028	039	050	061	072	083	094	105	116	127	138	149	160	171	182	193	204	215	226
0.255	005	016	027	038	049	060	071	082	093	104	115	126	137	148	159	170	181	192	203	214	225
0.161	004	015	026	037	048	059	070	081	092	103	114	125	136	147	158	169	180	191	202	213	224
0.102	003	014	025	036	047	058	069	080	091	102	113	124	135	146	157	168	179	190	201	212	223
0.0641	002	013	024	035	046	057	068	079	090	101	112	123	134	145	156	167	178	189	200	211	222
0.0405	001	012	023	034	045	056	067	078	089	100	111	122	133	144	155	166	177	188	199	210	221

L05

Conditions:

- Two low pressure sensors 16 x 16 wires in DN50
- Injection device: type K 8 x 4 mm orifices (central injection)
- Distances between the injection- and the measuring plane: 7910 mm
- Frequency: 10 kHz
- Measuring time: 10 s
- Atmospheric pressure
- Temperature range: 27 – 29 °C

Superficial velocity of the gaseous phase J_G, m/s

Superficial water velocity J_W, m/s	0.0025	0.0040	0.0062	0.0096	0.0151	0.0235	0.0368	0.0574	0.0898	0.140	0.219	0.342	0.534	0.835	1.305	2.038	3.185	4.975	7.772	12.14	18.97
4.047	011	022	033	044	055	066	077	088	099	110	121	132	143	154	165	176	187	198	209	220	231
2.554	010	021	032	043	054	065	076	087	098	109	120	131	142	153	164	175	186	197	208	219	230
1.611	009	020	031	042	053	064	075	086	097	108	119	130	141	152	163	174	185	196	207	218	229
1.017	008	019	030	041	052	063	074	085	096	107	118	129	140	151	162	173	184	195	206	217	228
0.641	007	018	029	040	051	062	073	084	095	106	117	128	139	150	161	172	183	194	205	216	227
0.405	006	017	028	039	050	061	072	083	094	105	116	127	138	149	160	171	182	193	204	215	226
0.255	005	016	027	038	049	060	071	082	093	104	115	126	137	148	159	170	181	192	203	214	225
0.161	004	015	026	037	048	059	070	081	092	103	114	125	136	147	158	169	180	191	202	213	224
0.102	003	014	025	036	047	058	069	080	091	102	113	124	135	146	157	168	179	190	201	212	223
0.0641	002	013	024	035	046	057	068	079	090	101	112	123	134	145	156	167	178	189	200	211	222
0.0405	001	012	023	034	045	056	067	078	089	100	111	122	133	144	155	166	177	188	199	210	221

L20

Conditions:

- Two low pressure sensors 16 x 16 wires in DN50
- Injection device: type K 8 x 4 mm orifices (central injection)
- Distances between the injection- and the measuring plane:
  - 100 mm
  - 1600 mm
  - 3100 mm
  - 7910 mm
- Frequency: 2.5 kHz
- Measuring time: 10 s
- Atmospheric pressure
- Temperature range: 16– 45 °C

Superficial velocity of the gaseous phase J_G, m/s

Superficial water velocity J_W, m/s	0.0025	0.0040	0.0062	0.0096	0.0151	0.0235	0.0368	0.0574	0.0898	0.140	0.219	0.342	0.534	0.835	1.305	2.038	3.185	4.975	7.772	12.14	18.97
4.047	011	022	033	044	055	066	077	088	099	110	121	132	143	154	165	176	187	198	209	220	231
2.554	010	021	032	043	054	065	076	087	098	109	120	131	142	153	164	175	186	197	208	219	230
1.611	009	020	031	042	053	064	075	086	097	108	119	130	141	152	163	174	185	196	207	218	229
1.017	008	019	030	041	052	063	074	085	096	107	118	129	140	151	162	173	184	195	206	217	228
0.641	007	018	029	040	051	062	073	084	095	106	117	128	139	150	161	172	183	194	205	216	227
0.405	006	017	028	039	050	061	072	083	094	105	116	127	138	149	160	171	182	193	204	215	226
0.255	005	016	027	038	049	060	071	082	093	104	115	126	137	148	159	170	181	192	203	214	225
0.161	004	015	026	037	048	059	070	081	092	103	114	125	136	147	158	169	180	191	202	213	224
0.102	003	014	025	036	047	058	069	080	091	102	113	124	135	146	157	168	179	190	201	212	223
0.0641	002	013	024	035	046	057	068	079	090	101	112	123	134	145	156	167	178	189	200	211	222
0.0405	001	012	023	034	045	056	067	078	089	100	111	122	133	144	155	166	177	188	199	210	221

D10

Conditions:

- Two high pressure sensors 16 x 16 wires in DN50
- Injection device: type I 24 x 0.8 mm orifices (central injection)
- Distances between the injection- and the measuring plane: 7910 mm
- Frequency: 10 kHz
- Measuring time: 10 s
- Temperature range: saturation conditions

Superficial velocity of the gaseous phase J_G, m/s

Superficial water velocity J_W, m/s	0.0025	0.0040	0.0062	0.0096	0.0151	0.0235	0.0368	0.0574	0.0898	0.140	0.219	0.342	0.534	0.835	1.305	2.038	3.185	4.975	7.772	12.14	18.97
4.047	011	022	033	044	055	066	077	088	099	110	121	132	143	154	165	176	187	198	209	220	231
2.554	010	021	032	043	054	065	076	087	098	109	120	131	142	153	164	175	186	197	208	219	230
1.611	009	020	031	042	053	064	075	086	097	108	119	130	141	152	163	174	185	196	207	218	229
1.017	008	019	030	041	052	063	074	085	096	107	118	129	140	151	162	173	184	195	206	217	228
0.641	007	018	029	040	051	062	073	084	095	106	117	128	139	150	161	172	183	194	205	216	227
0.405	006	017	028	039	050	061	072	083	094	105	116	127	138	149	160	171	182	193	204	215	226
0.255	005	016	027	038	049	060	071	082	093	104	115	126	137	148	159	170	181	192	203	214	225
0.161	004	015	026	037	048	059	070	081	092	103	114	125	136	147	158	169	180	191	202	213	224
0.102	003	014	025	036	047	058	069	080	091	102	113	124	135	146	157	168	179	190	201	212	223
0.0641	002	013	024	035	046	057	068	079	090	101	112	123	134	145	156	167	178	189	200	211	222
0.0405	001	012	023	034	045	056	067	078	089	100	111	122	133	144	155	166	177	188	199	210	221

p in the steam drum: 1 MPa

Superficial velocity of the gaseous phase J_G, m/s

Superficial water velocity J_W, m/s	0.0025	0.0040	0.0062	0.0096	0.0151	0.0235	0.0368	0.0574	0.0898	0.140	0.219	0.342	0.534	0.835	1.305	2.038	3.185	4.975	7.772	12.14	18.97
4.047	011	022	033	044	055	066	077	088	099	110	121	132	143	154	165	176	187	198	209	220	231
2.554	010	021	032	043	054	065	076	087	098	109	120	131	142	153	164	175	186	197	208	219	230
1.611	009	020	031	042	053	064	075	086	097	108	119	130	141	152	163	174	185	196	207	218	229
1.017	008	019	030	041	052	063	074	085	096	107	118	129	140	151	162	173	184	195	206	217	228
0.641	007	018	029	040	051	062	073	084	095	106	117	128	139	150	161	172	183	194	205	216	227
0.405	006	017	028	039	050	061	072	083	094	105	116	127	138	149	160	171	182	193	204	215	226
0.255	005	016	027	038	049	060	071	082	093	104	115	126	137	148	159	170	181	192	203	214	225
0.161	004	015	026	037	048	059	070	081	092	103	114	125	136	147	158	169	180	191	202	213	224
0.102	003	014	025	036	047	058	069	080	091	102	113	124	135	146	157	168	179	190	201	212	223
0.0641	002	013	024	035	046	057	068	079	090	101	112	123	134	145	156	167	178	189	200	211	222
0.0405	001	012	023	034	045	056	067	078	089	100	111	122	133	144	155	166	177	188	199	210	221

p in the steam drum: 2 MPa

D10 continuation

Superficial velocity of the gaseous phase J_G, m/s

Superficial water velocity J_W, m/s	0.0025	0.0040	0.0062	0.0096	0.0151	0.0235	0.0368	0.0574	0.0898	0.140	0.219	0.342	0.534	0.835	1.305	2.038	3.185	4.975	7.772	12.14	18.97
4.047	011	022	033	044	055	066	077	088	099	110	121	132	143	154	165	176	187	198	209	220	231
2.554	010	021	032	043	054	065	076	087	098	109	120	131	142	153	164	175	186	197	208	219	230
1.611	009	020	031	042	053	064	075	086	097	108	119	130	141	152	163	174	185	196	207	218	229
1.017	008	019	030	041	052	063	074	085	096	107	118	129	140	151	162	173	184	195	206	217	228
0.641	007	018	029	040	051	062	073	084	095	106	117	128	139	150	161	172	183	194	205	216	227
0.405	006	017	028	039	050	061	072	083	094	105	116	127	138	149	160	171	182	193	204	215	226
0.255	005	016	027	038	049	060	071	082	093	104	115	126	137	148	159	170	181	192	203	214	225
0.161	004	015	026	037	048	059	070	081	092	103	114	125	136	147	158	169	180	191	202	213	224
0.102	003	014	025	036	047	058	069	080	091	102	113	124	135	146	157	168	179	190	201	212	223
0.0641	002	013	024	035	046	057	068	079	090	101	112	123	134	145	156	167	178	189	200	211	222
0.0405	001	012	023	034	045	056	067	078	089	100	111	122	133	144	155	166	177	188	199	210	221

p in the steam drum: 4 MPa

Superficial velocity of the gaseous phase J_G, m/s

Superficial water velocity J_W, m/s	0.0025	0.0040	0.0062	0.0096	0.0151	0.0235	0.0368	0.0574	0.0898	0.140	0.219	0.342	0.534	0.835	1.305	2.038	3.185	4.975	7.772	12.14	18.97
4.047	011	022	033	044	055	066	077	088	099	110	121	132	143	154	165	176	187	198	209	220	231
2.554	010	021	032	043	054	065	076	087	098	109	120	131	142	153	164	175	186	197	208	219	230
1.611	009	020	031	042	053	064	075	086	097	108	119	130	141	152	163	174	185	196	207	218	229
1.017	008	019	030	041	052	063	074	085	096	107	118	129	140	151	162	173	184	195	206	217	228
0.641	007	018	029	040	051	062	073	084	095	106	117	128	139	150	161	172	183	194	205	216	227
0.405	006	017	028	039	050	061	072	083	094	105	116	127	138	149	160	171	182	193	204	215	226
0.255	005	016	027	038	049	060	071	082	093	104	115	126	137	148	159	170	181	192	203	214	225
0.161	004	015	026	037	048	059	070	081	092	103	114	125	136	147	158	169	180	191	202	213	224
0.102	003	014	025	036	047	058	069	080	091	102	113	124	135	146	157	168	179	190	201	212	223
0.0641	002	013	024	035	046	057	068	079	090	101	112	123	134	145	156	167	178	189	200	211	222
0.0405	001	012	023	034	045	056	067	078	089	100	111	122	133	144	155	166	177	188	199	210	221

p in the steam drum: 6.5 MPa

D11

Conditions:

- Two high pressure sensors 16 x 16 wires in DN50
- Injection device: type K 8 x 4 mm orifices (central injection)
- Distances between the injection- and the measuring plane: 7910 mm
- Frequency: 10 kHz
- Measuring time: 10 s
- Temperature range: saturation conditions

Superficial velocity of the gaseous phase J_G, m/s

Superficial water velocity J_W, m/s	0.0025	0.0040	0.0062	0.0096	0.0151	0.0235	0.0368	0.0574	0.0898	0.140	0.219	0.342	0.534	0.835	1.305	2.038	3.185	4.975	7.772	12.14	18.97
4.047	011	022	033	044	055	066	077	088	099	110	121	132	143	154	165	176	187	198	209	220	231
2.554	010	021	032	043	054	065	076	087	098	109	120	131	142	153	164	175	186	197	208	219	230
1.611	009	020	031	042	053	064	075	086	097	108	119	130	141	152	163	174	185	196	207	218	229
1.017	008	019	030	041	052	063	074	085	096	107	118	129	140	151	162	173	184	195	206	217	228
0.641	007	018	029	040	051	062	073	084	095	106	117	128	139	150	161	172	183	194	205	216	227
0.405	006	017	028	039	050	061	072	083	094	105	116	127	138	149	160	171	182	193	204	215	226
0.255	005	016	027	038	049	060	071	082	093	104	115	126	137	148	159	170	181	192	203	214	225
0.161	004	015	026	037	048	059	070	081	092	103	114	125	136	147	158	169	180	191	202	213	224
0.102	003	014	025	036	047	058	069	080	091	102	113	124	135	146	157	168	179	190	201	212	223
0.0641	002	013	024	035	046	057	068	079	090	101	112	123	134	145	156	167	178	189	200	211	222
0.0405	001	012	023	034	045	056	067	078	089	100	111	122	133	144	155	166	177	188	199	210	221

p in the steam drum: 1 MPa

Superficial velocity of the gaseous phase J_G, m/s

Superficial water velocity J_W, m/s	0.0025	0.0040	0.0062	0.0096	0.0151	0.0235	0.0368	0.0574	0.0898	0.140	0.219	0.342	0.534	0.835	1.305	2.038	3.185	4.975	7.772	12.14	18.97
4.047	011	022	033	044	055	066	077	088	099	110	121	132	143	154	165	176	187	198	209	220	231
2.554	010	021	032	043	054	065	076	087	098	109	120	131	142	153	164	175	186	197	208	219	230
1.611	009	020	031	042	053	064	075	086	097	108	119	130	141	152	163	174	185	196	207	218	229
1.017	008	019	030	041	052	063	074	085	096	107	118	129	140	151	162	173	184	195	206	217	228
0.641	007	018	029	040	051	062	073	084	095	106	117	128	139	150	161	172	183	194	205	216	227
0.405	006	017	028	039	050	061	072	083	094	105	116	127	138	149	160	171	182	193	204	215	226
0.255	005	016	027	038	049	060	071	082	093	104	115	126	137	148	159	170	181	192	203	214	225
0.161	004	015	026	037	048	059	070	081	092	103	114	125	136	147	158	169	180	191	202	213	224
0.102	003	014	025	036	047	058	069	080	091	102	113	124	135	146	157	168	179	190	201	212	223
0.0641	002	013	024	035	046	057	068	079	090	101	112	123	134	145	156	167	178	189	200	211	222
0.0405	001	012	023	034	045	056	067	078	089	100	111	122	133	144	155	166	177	188	199	210	221

p in the steam drum: 2 MPa

D11 continuation

Superficial velocity of the gaseous phase J_G, m/s

Superficial water velocity J_W, m/s	0.0025	0.0040	0.0062	0.0096	0.0151	0.0235	0.0368	0.0574	0.0898	0.140	0.219	0.342	0.534	0.835	1.305	2.038	3.185	4.975	7.772	12.14	18.97
4.047	011	022	033	044	055	066	077	088	099	110	121	132	143	154	165	176	187	198	209	220	231
2.554	010	021	032	043	054	065	076	087	098	109	120	131	142	153	164	175	186	197	208	219	230
1.611	009	020	031	042	053	064	075	086	097	108	119	130	141	152	163	174	185	196	207	218	229
1.017	008	019	030	041	052	063	074	085	096	107	118	129	140	151	162	173	184	195	206	217	228
0.641	007	018	029	040	051	062	073	084	095	106	117	128	139	150	161	172	183	194	205	216	227
0.405	006	017	028	039	050	061	072	083	094	105	116	127	138	149	160	171	182	193	204	215	226
0.255	005	016	027	038	049	060	071	082	093	104	115	126	137	148	159	170	181	192	203	214	225
0.161	004	015	026	037	048	059	070	081	092	103	114	125	136	147	158	169	180	191	202	213	224
0.102	003	014	025	036	047	058	069	080	091	102	113	124	135	146	157	168	179	190	201	212	223
0.0641	002	013	024	035	046	057	068	079	090	101	112	123	134	145	156	167	178	189	200	211	222
0.0405	001	012	023	034	045	056	067	078	089	100	111	122	133	144	155	166	177	188	199	210	221

p in the steam drum: 4 MPa

Superficial velocity of the gaseous phase J_G, m/s

Superficial water velocity J_W, m/s	0.0025	0.0040	0.0062	0.0096	0.0151	0.0235	0.0368	0.0574	0.0898	0.140	0.219	0.342	0.534	0.835	1.305	2.038	3.185	4.975	7.772	12.14	18.97
4.047	011	022	033	044	055	066	077	088	099	110	121	132	143	154	165	176	187	198	209	220	231
2.554	010	021	032	043	054	065	076	087	098	109	120	131	142	153	164	175	186	197	208	219	230
1.611	009	020	031	042	053	064	075	086	097	108	119	130	141	152	163	174	185	196	207	218	229
1.017	008	019	030	041	052	063	074	085	096	107	118	129	140	151	162	173	184	195	206	217	228
0.641	007	018	029	040	051	062	073	084	095	106	117	128	139	150	161	172	183	194	205	216	227
0.405	006	017	028	039	050	061	072	083	094	105	116	127	138	149	160	171	182	193	204	215	226
0.255	005	016	027	038	049	060	071	082	093	104	115	126	137	148	159	170	181	192	203	214	225
0.161	004	015	026	037	048	059	070	081	092	103	114	125	136	147	158	169	180	191	202	213	224
0.102	003	014	025	036	047	058	069	080	091	102	113	124	135	146	157	168	179	190	201	212	223
0.0641	002	013	024	035	046	057	068	079	090	101	112	123	134	145	156	167	178	189	200	211	222
0.0405	001	012	023	034	045	056	067	078	089	100	111	122	133	144	155	166	177	188	199	210	221

p in the steam drum: 6.5 MPa

A2 experiments on the vertical test sections DN200 with variable gas injection system

Averaged inner diameter: DN200: 195.3 mm

L01

Conditions:

- Two low pressure sensors 64 x 64 wires in DN200
- Injection device: variable gas injection system (wall injection)
- Distance between the injection- and the measuring plane: comp. Fig. 2.16
- Frequency: 2.5 kHz
- Measuring time: 10 s
- Atmospheric pressure
- Temperature range: 19 – 31 °C

Superficial velocity of the gaseous phase J_G, m/s

Superficial water velocity J_W, m/s	0.0025	0.0040	0.0062	0.0096	0.0151	0.0235	0.0368	0.0574	0.0898	0.140	0.219	0.342	0.534	0.835	1.305	2.038	3.185	4.975	7.772	12.14	18.97
4.047	011	022	033	044	055	066	077	088	099	110	121	132	143	154	165	176	187	198	209	220	231
2.554	010	021	032	043	054	065	076	087	098	109	120	131	142	153	164	175	186	197	208	219	230
1.611	009	020	031	042	053	064	075	086	097	108	119	130	141	152	163	174	185	196	207	218	229
1.017	008	019	030	041	052	063	074	085	096	107	118	129	140	151	162	173	184	195	206	217	228
0.641	007	018	029	040	051	062	073	084	095	106	117	128	139	150	161	172	183	194	205	216	227
0.405	006	017	028	039	050	061	072	083	094	105	116	127	138	149	160	171	182	193	204	215	226
0.255	005	016	027	038	049	060	071	082	093	104	115	126	137	148	159	170	181	192	203	214	225
0.161	004	015	026	037	048	059	070	081	092	103	114	125	136	147	158	169	180	191	202	213	224
0.102	003	014	025	036	047	058	069	080	091	102	113	124	135	146	157	168	179	190	201	212	223
0.0641	002	013	024	035	046	057	068	079	090	101	112	123	134	145	156	167	178	189	200	211	222
0.0405	001	012	023	034	045	056	067	078	089	100	111	122	133	144	155	166	177	188	199	210	221

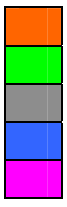

position A – R
position A – R, only 1 mm orifices
position A – R + 1 mm chambers parallel
position A – R, only 4 mm orifices + 1 mm parallel
position A – R, only 4 mm orifices

L02

Conditions:

- Two low pressure sensors 64 x 64 wires in DN200
- Injection device: variable gas injection system (wall injection)
- Distance between the injection- and the measuring plane: comp. Fig. 2.16
- Frequency: 2.5 kHz
- Measuring time: 10 s
- Atmospheric pressure
- Temperature range: 28 – 37 °C

Superficial velocity of the gaseous phase J_G, m/s

Superficial water velocity J_W, m/s	0.0025	0.0040	0.0062	0.0096	0.0151	0.0235	0.0368	0.0574	0.0898	0.140	0.219	0.342	0.534	0.835	1.305	2.038	3.185	4.975	7.772	12.14	18.97
4.047	011	022	033	044	055	066	077	088	099	110	121	132	143	154	165	176	187	198	209	220	231
2.554	010	021	032	043	054	065	076	087	098	109	120	131	142	153	164	175	186	197	208	219	230
1.611	009	020	031	042	053	064	075	086	097	108	119	130	141	152	163	174	185	196	207	218	229
1.017	008	019	030	041	052	063	074	085	096	107	118	129	140	151	162	173	184	195	206	217	228
0.641	007	018	029	040	051	062	073	084	095	106	117	128	139	150	161	172	183	194	205	216	227
0.405	006	017	028	039	050	061	072	083	094	105	116	127	138	149	160	171	182	193	204	215	226
0.255	005	016	027	038	049	060	071	082	093	104	115	126	137	148	159	170	181	192	203	214	225
0.161	004	015	026	037	048	059	070	081	092	103	114	125	136	147	158	169	180	191	202	213	224
0.102	003	014	025	036	047	058	069	080	091	102	113	124	135	146	157	168	179	190	201	212	223
0.0641	002	013	024	035	046	057	068	079	090	101	112	123	134	145	156	167	178	189	200	211	222
0.0405	001	012	023	034	045	056	067	078	089	100	111	122	133	144	155	166	177	188	199	210	221

position A – R
position A – R + 1 mm chambers parallel
position A – R, only 4 mm orifices

L06

Conditions:

- Two low pressure sensors 64 x 64 wires in DN200
- Injection device: variable gas injection system (wall injection)
- Distance between the injection- and the measuring plane: comp. Fig. 2.16
- Frequency: 2.5 kHz
- Measuring time: 10 s
- Pressure at wire-mesh sensor ca. 130 kPa
- Temperature range: 28 – 38 °C

Superficial velocity of the gaseous phase J_G, m/s

Superficial water velocity J_W, m/s	0.0025	0.0040	0.0062	0.0096	0.0151	0.0235	0.0368	0.0574	0.0898	0.140	0.219	0.342	0.534	0.835	1.305	2.038	3.185	4.975	7.772	12.14	18.97
4.047	011	022	033	044	055	066	077	088	099	110	121	132	143	154	165	176	187	198	209	220	231
2.554	010	021	032	043	054	065	076	087	098	109	120	131	142	153	164	175	186	197	208	219	230
1.611	009	020	031	042	053	064	075	086	097	108	119	130	141	152	163	174	185	196	207	218	229
1.017	008	019	030	041	052	063	074	085	096	107	118	129	140	151	162	173	184	195	206	217	228
0.641	007	018	029	040	051	062	073	084	095	106	117	128	139	150	161	172	183	194	205	216	227
0.405	006	017	028	039	050	061	072	083	094	105	116	127	138	149	160	171	182	193	204	215	226
0.255	005	016	027	038	049	060	071	082	093	104	115	126	137	148	159	170	181	192	203	214	225
0.161	004	015	026	037	048	059	070	081	092	103	114	125	136	147	158	169	180	191	202	213	224
0.102	003	014	025	036	047	058	069	080	091	102	113	124	135	146	157	168	179	190	201	212	223
0.0641	002	013	024	035	046	057	068	079	090	101	112	123	134	145	156	167	178	189	200	211	222
0.0405	001	012	023	034	045	056	067	078	089	100	111	122	133	144	155	166	177	188	199	210	221

position A – R

L08

Conditions:

- Two low pressure sensors 64 x 64 wires in DN200
- Injection device: variable gas injection system (wall injection)
- Distance between the injection- and the measuring plane: comp. Fig. 2.16
- Frequency: 2.5 kHz
- Measuring time: 10 s
- Pressure at wire-mesh sensor: 120, 140, 160, 180, 200, 220 kPa
- Temperature range: 31 – 42 °C

Superficial velocity of the gaseous phase J_G, m/s

Superficial water velocity J_W, m/s	0.0025	0.0040	0.0062	0.0096	0.0151	0.0235	0.0368	0.0574	0.0898	0.140	0.219	0.342	0.534	0.835	1.305	2.038	3.185	4.975	7.772	12.14	18.97
4.047	011	022	033	044	055	066	077	088	099	110	121	132	143	154	165	176	187	198	209	220	231
2.554	010	021	032	043	054	065	076	087	098	109	120	131	142	153	164	175	186	197	208	219	230
1.611	009	020	031	042	053	064	075	086	097	108	119	130	141	152	163	174	185	196	207	218	229
1.017	008	019	030	041	052	063	074	085	096	107	118	129	140	151	162	173	184	195	206	217	228
0.641	007	018	029	040	051	062	073	084	095	106	117	128	139	150	161	172	183	194	205	216	227
0.405	006	017	028	039	050	061	072	083	094	105	116	127	138	149	160	171	182	193	204	215	226
0.255	005	016	027	038	049	060	071	082	093	104	115	126	137	148	159	170	181	192	203	214	225
0.161	004	015	026	037	048	059	070	081	092	103	114	125	136	147	158	169	180	191	202	213	224
0.102	003	014	025	036	047	058	069	080	091	102	113	124	135	146	157	168	179	190	201	212	223
0.0641	002	013	024	035	046	057	068	079	090	101	112	123	134	145	156	167	178	189	200	211	222
0.0405	001	012	023	034	045	056	067	078	089	100	111	122	133	144	155	166	177	188	199	210	221

position A, B

L10

Conditions:

- Two low pressure sensors 64 x 64 wires in DN200
- Injection device: type I 152 x 0.8 mm orifices (central injection)
- Distance between the injection- and the measuring plane: 7606 mm
- Frequency: 2.5 kHz
- Measuring time: 10 x 10 s
- Pressure at wire-mesh sensor ca. 120 kPa
- Temperature range: 32 – 35 °C

Superficial velocity of the gaseous phase J_G, m/s

Superficial water velocity J_W, m/s	0.0025	0.0040	0.0062	0.0096	0.0151	0.0235	0.0368	0.0574	0.0898	0.140	0.219	0.342	0.534	0.835	1.305	2.038	3.185	4.975	7.772	12.14	18.97
4.047	011	022	033	044	055	066	077	088	099	110	121	132	143	154	165	176	187	198	209	220	231
2.554	010	021	032	043	054	065	076	087	098	109	120	131	142	153	164	175	186	197	208	219	230
1.611	009	020	031	042	053	064	075	086	097	108	119	130	141	152	163	174	185	196	207	218	229
1.017	008	019	030	041	052	063	074	085	096	107	118	129	140	151	162	173	184	195	206	217	228
0.641	007	018	029	040	051	062	073	084	095	106	117	128	139	150	161	172	183	194	205	216	227
0.405	006	017	028	039	050	061	072	083	094	105	116	127	138	149	160	171	182	193	204	215	226
0.255	005	016	027	038	049	060	071	082	093	104	115	126	137	148	159	170	181	192	203	214	225
0.161	004	015	026	037	048	059	070	081	092	103	114	125	136	147	158	169	180	191	202	213	224
0.102	003	014	025	036	047	058	069	080	091	102	113	124	135	146	157	168	179	190	201	212	223
0.0641	002	013	024	035	046	057	068	079	090	101	112	123	134	145	156	167	178	189	200	211	222
0.0405	001	012	023	034	045	056	067	078	089	100	111	122	133	144	155	166	177	188	199	210	221

D12

Conditions:

- One high pressure sensors 64 x 64 wires in DN200
- Injection device: variable gas injection system (wall injection) and type I 152 x 0.8 mm orifices (central injection)
- Distance between the injection- and the measuring plane: comp. Fig. 2.16 or 7606 mm respectively
- Frequency: 2.5 kHz
- Measuring time: 10 s
- Temperature range: saturation conditions

Superficial velocity of the gaseous phase J_G, m/s

Superficial water velocity J_W, m/s	0.0025	0.0040	0.0062	0.0096	0.0151	0.0235	0.0368	0.0574	0.0898	0.140	0.219	0.342	0.534	0.835	1.305	2.038	3.185	4.975	7.772	12.14	18.97
4.047	011	022	033	044	055	066	077	088	099	110	121	132	143	154	165	176	187	198	209	220	231
2.554	010	021	032	043	054	065	076	087	098	109	120	131	142	153	164	175	186	197	208	219	230
1.611	009	020	031	042	053	064	075	086	097	108	119	130	141	152	163	174	185	196	207	218	229
1.017	008	019	030	041	052	063	074	085	096	107	118	129	140	151	162	173	184	195	206	217	228
0.641	007	018	029	040	051	062	073	084	095	106	117	128	139	150	161	172	183	194	205	216	227
0.405	006	017	028	039	050	061	072	083	094	105	116	127	138	149	160	171	182	193	204	215	226
0.255	005	016	027	038	049	060	071	082	093	104	115	126	137	148	159	170	181	192	203	214	225
0.161	004	015	026	037	048	059	070	081	092	103	114	125	136	147	158	169	180	191	202	213	224
0.102	003	014	025	036	047	058	069	080	091	102	113	124	135	146	157	168	179	190	201	212	223
0.0641	002	013	024	035	046	057	068	079	090	101	112	123	134	145	156	167	178	189	200	211	222
0.0405	001	012	023	034	045	056	067	078	089	100	111	122	133	144	155	166	177	188	199	210	221

p in the steam drum: 1 MPa

position A – R + type I
position Q and R + type I
position Q and P + R
position B, E, H, K, N, Q

D12 continuation

Superficial velocity of the gaseous phase J_G, m/s

Superficial water velocity J_W, m/s	0.0025	0.0040	0.0062	0.0096	0.0151	0.0235	0.0368	0.0574	0.0898	0.140	0.219	0.342	0.534	0.835	1.305	2.038	3.185	4.975	7.772	12.14	18.97
4.047	011	022	033	044	055	066	077	088	099	110	121	132	143	154	165	176	187	198	209	220	231
2.554	010	021	032	043	054	065	076	087	098	109	120	131	142	153	164	175	186	197	208	219	230
1.611	009	020	031	042	053	064	075	086	097	108	119	130	141	152	163	174	185	196	207	218	229
1.017	008	019	030	041	052	063	074	085	096	107	118	129	140	151	162	173	184	195	206	217	228
0.641	007	018	029	040	051	062	073	084	095	106	117	128	139	150	161	172	183	194	205	216	227
0.405	006	017	028	039	050	061	072	083	094	105	116	127	138	149	160	171	182	193	204	215	226
0.255	005	016	027	038	049	060	071	082	093	104	115	126	137	148	159	170	181	192	203	214	225
0.161	004	015	026	037	048	059	070	081	092	103	114	125	136	147	158	169	180	191	202	213	224
0.102	003	014	025	036	047	058	069	080	091	102	113	124	135	146	157	168	179	190	201	212	223
0.0641	002	013	024	035	046	057	068	079	090	101	112	123	134	145	156	167	178	189	200	211	222
0.0405	001	012	023	034	045	056	067	078	089	100	111	122	133	144	155	166	177	188	199	210	221

p in the steam drum: 2 MPa

- position A – R + type I (partially)
- position Q and R + type I
- position Q
- position B, E, H, K, N, Q
- position A – I, K, L, N, O, Q, R + type I

Superficial velocity of the gaseous phase J_G, m/s

Superficial water velocity J_W, m/s	0.0025	0.0040	0.0062	0.0096	0.0151	0.0235	0.0368	0.0574	0.0898	0.140	0.219	0.342	0.534	0.835	1.305	2.038	3.185	4.975	7.772	12.14	18.97
4.047	011	022	033	044	055	066	077	088	099	110	121	132	143	154	165	176	187	198	209	220	231
2.554	010	021	032	043	054	065	076	087	098	109	120	131	142	153	164	175	186	197	208	219	230
1.611	009	020	031	042	053	064	075	086	097	108	119	130	141	152	163	174	185	196	207	218	229
1.017	008	019	030	041	052	063	074	085	096	107	118	129	140	151	162	173	184	195	206	217	228
0.641	007	018	029	040	051	062	073	084	095	106	117	128	139	150	161	172	183	194	205	216	227
0.405	006	017	028	039	050	061	072	083	094	105	116	127	138	149	160	171	182	193	204	215	226
0.255	005	016	027	038	049	060	071	082	093	104	115	126	137	148	159	170	181	192	203	214	225
0.161	004	015	026	037	048	059	070	081	092	103	114	125	136	147	158	169	180	191	202	213	224
0.102	003	014	025	036	047	058	069	080	091	102	113	124	135	146	157	168	179	190	201	212	223
0.0641	002	013	024	035	046	057	068	079	090	101	112	123	134	145	156	167	178	189	200	211	222
0.0405	001	012	023	034	045	056	067	078	089	100	111	122	133	144	155	166	177	188	199	210	221

p in the steam drum: 4 MPa

- position A – R + type I
- position Q and R + type I
- position Q and P + R
- position B, E, H, K, N, Q

D12 continuation

Superficial velocity of the gaseous phase J_G, m/s

Superficial water velocity J_W, m/s	0.0025	0.0040	0.0062	0.0096	0.0151	0.0235	0.0368	0.0574	0.0898	0.140	0.219	0.342	0.534	0.835	1.305	2.038	3.185	4.975	7.772	12.14	18.97
4.047	011	022	033	044	055	066	077	088	099	110	121	132	143	154	165	176	187	198	209	220	231
2.554	010	021	032	043	054	065	076	087	098	109	120	131	142	153	164	175	186	197	208	219	230
1.611	009	020	031	042	053	064	075	086	097	108	119	130	141	152	163	174	185	196	207	218	229
1.017	008	019	030	041	052	063	074	085	096	107	118	129	140	151	162	173	184	195	206	217	228
0.641	007	018	029	040	051	062	073	084	095	106	117	128	139	150	161	172	183	194	205	216	227
0.405	006	017	028	039	050	061	072	083	094	105	116	127	138	149	160	171	182	193	204	215	226
0.255	005	016	027	038	049	060	071	082	093	104	115	126	137	148	159	170	181	192	203	214	225
0.161	004	015	026	037	048	059	070	081	092	103	114	125	136	147	158	169	180	191	202	213	224
0.102	003	014	025	036	047	058	069	080	091	102	113	124	135	146	157	168	179	190	201	212	223
0.0641	002	013	024	035	046	057	068	079	090	101	112	123	134	145	156	167	178	189	200	211	222
0.0405	001	012	023	034	045	056	067	078	089	100	111	122	133	144	155	166	177	188	199	210	221

p in the steam drum: 6.5 MPa

- position A – R + type I
- position Q and R + type I
- position Q
- position B, E, H, K, N, Q

D13

Conditions:

- One high pressure sensors 64 x 64 wires in DN200
- Injection device: variable gas injection system (wall injection) and type I 152 x 0.8 mm orifices (central injection)
- Distance between the injection- and the measuring plane: comp. Fig. 2.16 or 7606 mm respectively
- Frequency: 2.5 kHz
- Measuring time: 10 s
- Temperature range: saturation conditions

Superficial velocity of the gaseous phase J_G, m/s

Superficial water velocity J_W, m/s	0.0025	0.0040	0.0062	0.0096	0.0151	0.0235	0.0368	0.0574	0.0898	0.140	0.219	0.342	0.534	0.835	1.305	2.038	3.185	4.975	7.772	12.14	18.97
4.047	011	022	033	044	055	066	077	088	099	110	121	132	143	154	165	176	187	198	209	220	231
2.554	010	021	032	043	054	065	076	087	098	109	120	131	142	153	164	175	186	197	208	219	230
1.611	009	020	031	042	053	064	075	086	097	108	119	130	141	152	163	174	185	196	207	218	229
1.017	008	019	030	041	052	063	074	085	096	107	118	129	140	151	162	173	184	195	206	217	228
0.641	007	018	029	040	051	062	073	084	095	106	117	128	139	150	161	172	183	194	205	216	227
0.405	006	017	028	039	050	061	072	083	094	105	116	127	138	149	160	171	182	193	204	215	226
0.255	005	016	027	038	049	060	071	082	093	104	115	126	137	148	159	170	181	192	203	214	225
0.161	004	015	026	037	048	059	070	081	092	103	114	125	136	147	158	169	180	191	202	213	224
0.102	003	014	025	036	047	058	069	080	091	102	113	124	135	146	157	168	179	190	201	212	223
0.0641	002	013	024	035	046	057	068	079	090	101	112	123	134	145	156	167	178	189	200	211	222
0.0405	001	012	023	034	045	056	067	078	089	100	111	122	133	144	155	166	177	188	199	210	221

p in the steam drum: 1 MPa

position A – R + type I

D13 continuation

Superficial velocity of the gaseous phase J_G, m/s

Superficial water velocity J_W, m/s	0.0025	0.0040	0.0062	0.0096	0.0151	0.0235	0.0368	0.0574	0.0898	0.140	0.219	0.342	0.534	0.835	1.305	2.038	3.185	4.975	7.772	12.14	18.97
4.047	011	022	033	044	055	066	077	088	099	110	121	132	143	154	165	176	187	198	209	220	231
2.554	010	021	032	043	054	065	076	087	098	109	120	131	142	153	164	175	186	197	208	219	230
1.611	009	020	031	042	053	064	075	086	097	108	119	130	141	152	163	174	185	196	207	218	229
1.017	008	019	030	041	052	063	074	085	096	107	118	129	140	151	162	173	184	195	206	217	228
0.641	007	018	029	040	051	062	073	084	095	106	117	128	139	150	161	172	183	194	205	216	227
0.405	006	017	028	039	050	061	072	083	094	105	116	127	138	149	160	171	182	193	204	215	226
0.255	005	016	027	038	049	060	071	082	093	104	115	126	137	148	159	170	181	192	203	214	225
0.161	004	015	026	037	048	059	070	081	092	103	114	125	136	147	158	169	180	191	202	213	224
0.102	003	014	025	036	047	058	069	080	091	102	113	124	135	146	157	168	179	190	201	212	223
0.0641	002	013	024	035	046	057	068	079	090	101	112	123	134	145	156	167	178	189	200	211	222
0.0405	001	012	023	034	045	056	067	078	089	100	111	122	133	144	155	166	177	188	199	210	221

p in the steam drum: 2 MPa

position A – R + type I

Superficial velocity of the gaseous phase J_G, m/s

Superficial water velocity J_W, m/s	0.0025	0.0040	0.0062	0.0096	0.0151	0.0235	0.0368	0.0574	0.0898	0.140	0.219	0.342	0.534	0.835	1.305	2.038	3.185	4.975	7.772	12.14	18.97
4.047	011	022	033	044	055	066	077	088	099	110	121	132	143	154	165	176	187	198	209	220	231
2.554	010	021	032	043	054	065	076	087	098	109	120	131	142	153	164	175	186	197	208	219	230
1.611	009	020	031	042	053	064	075	086	097	108	119	130	141	152	163	174	185	196	207	218	229
1.017	008	019	030	041	052	063	074	085	096	107	118	129	140	151	162	173	184	195	206	217	228
0.641	007	018	029	040	051	062	073	084	095	106	117	128	139	150	161	172	183	194	205	216	227
0.405	006	017	028	039	050	061	072	083	094	105	116	127	138	149	160	171	182	193	204	215	226
0.255	005	016	027	038	049	060	071	082	093	104	115	126	137	148	159	170	181	192	203	214	225
0.161	004	015	026	037	048	059	070	081	092	103	114	125	136	147	158	169	180	191	202	213	224
0.102	003	014	025	036	047	058	069	080	091	102	113	124	135	146	157	168	179	190	201	212	223
0.0641	002	013	024	035	046	057	068	079	090	101	112	123	134	145	156	167	178	189	200	211	222
0.0405	001	012	023	034	045	056	067	078	089	100	111	122	133	144	155	166	177	188	199	210	221

p in the steam drum: 4 MPa

position AC, DF, GI, JL, MO, PR, B, E, H, K, N, Q +Igel
position AC, DF, GI, JL, MO, PR, B, E, H, K, N, Q

D13 continuation

Superficial velocity of the gaseous phase J_G, m/s

Superficial water velocity J_W, m/s	0.0025	0.0040	0.0062	0.0096	0.0151	0.0235	0.0368	0.0574	0.0898	0.140	0.219	0.342	0.534	0.835	1.305	2.038	3.185	4.975	7.772	12.14	18.97
4.047	011	022	033	044	055	066	077	088	099	110	121	132	143	154	165	176	187	198	209	220	231
2.554	010	021	032	043	054	065	076	087	098	109	120	131	142	153	164	175	186	197	208	219	230
1.611	009	020	031	042	053	064	075	086	097	108	119	130	141	152	163	174	185	196	207	218	229
1.017	008	019	030	041	052	063	074	085	096	107	118	129	140	151	162	173	184	195	206	217	228
0.641	007	018	029	040	051	062	073	084	095	106	117	128	139	150	161	172	183	194	205	216	227
0.405	006	017	028	039	050	061	072	083	094	105	116	127	138	149	160	171	182	193	204	215	226
0.255	005	016	027	038	049	060	071	082	093	104	115	126	137	148	159	170	181	192	203	214	225
0.161	004	015	026	037	048	059	070	081	092	103	114	125	136	147	158	169	180	191	202	213	224
0.102	003	014	025	036	047	058	069	080	091	102	113	124	135	146	157	168	179	190	201	212	223
0.0641	002	013	024	035	046	057	068	079	090	101	112	123	134	145	156	167	178	189	200	211	222
0.0405	001	012	023	034	045	056	067	078	089	100	111	122	133	144	155	166	177	188	199	210	221

p in the steam drum: 6.5 MPa